The impact of dynamic processes on chemistry in atmospheric boundary layers over tropical and boreal forest

H. G. Ouwersloot

Thesis committee

Promotors
Prof. Dr M.C. Krol
Professor of Air Quality and Atmospheric Chemistry
Wageningen University

Prof. Dr J. Lelieveld
Managing director of the Max Planck Institute for Chemistry, Mainz, Germany

Co-promotors
Dr J. Vilà-Guerau de Arellano
Associate professor, Meteorology and Air Quality Group
Wageningen University

Dr L.N. Ganzeveld
Assistant professor, Earth System Science Group
Wageningen University

Other members
Prof. Dr H.J.J. Jonker, Delft University of Technology
Dr E.G. Patton, National Center for Atmospheric Research, Boulder, Colorado, USA
Prof. Dr T. Röckmann, Utrecht University
Prof. Dr R. Uijlenhoet, Wageningen University

This research was conducted under the auspices of the Graduate School for Socio-Economic and Natural Sciences of the Environment (SENSE).

The impact of dynamic processes on chemistry in atmospheric boundary layers over tropical and boreal forest

H. G. Ouwersloot

Thesis

submitted in fulfilment of the requirements for the degree of doctor
at Wageningen University
by the authority of the Rector Magnificus
Prof. Dr M.J. Kropff,
in the presence of the
Thesis Committee appointed by the Academic Board
to be defended in public
on Friday 8 November 2013
at 4 p.m. in the Aula.

H.G. Ouwersloot
The impact of dynamic processes on chemistry in atmospheric boundary layers over tropical and boreal forest,

De impact van dynamische processen op chemie in atmosferische grenslagen boven tropisch en boreaal bos,
216 pages.

PhD thesis, Wageningen University, Wageningen, NL (2013)
With references, with summaries in Dutch and English

ISBN 978–94–6173–661–1

Contents

If I can introduce someone to something new, as is constantly happening to me, then I am elated.

Trevor Dunn

1 Introduction

1.1 Motivation and context

Due to human induced perturbations, such as enhanced CO_2 emissions and land-use change, our environment is changing. In turn, the global tendencies in climate affect local air quality and weather patterns, which subsequently impact on the quality of life in the different geographic regions. Key factors in the current climate evolution are the removal rate of anthropogenic CO_2 from the atmosphere (Baldocchi et al., 2001; Sitch et al., 2007) and the presence of hydrocarbons (e.g. isoprene) in the atmosphere, which control the atmosphere's oxidizing capacity and subsequently the lifetime of atmospheric reactants (Davis et al., 1994; Fuentes et al., 2000; Lelieveld et al., 2008). The exchange of chemical reactants between land and atmosphere is governed by small-scale processes in the lowest layer of the atmosphere (e.g., Ganzeveld et al., 2008), influenced by diurnal variability. Essential to the local and global water cycle, these processes additionally affect evaporation and the formation and properties of clouds (Vilà-Guerau de Arellano et al., 2012). To better understand the intricate relations in our Earth system, and to predict its future evolution, numerical models are widely employed. Climate and air-quality models need to represent all these effects that act on different scales, but cannot simultaneously resolve them numerically due to the computational cost. An additional challenge is that the processes and related feedbacks are affected by

changes in climate (Baldocchi et al., 2001; Vilà-Guerau de Arellano et al., 2012) and changes in the land surface composition due to human activity (Andreae et al., 2002). To study the various contributions to local weather and global climate and to bridge the gap between atmospheric scales, observations have to be combined with numerical analyses using a range of atmospheric models.

In general, the atmospheric studies are subdivided into atmospheric chemistry and dynamics, but both fields are strongly connected through interacting processes. These include the influence of turbulent structures on reactant distributions in the atmosphere, the interaction of reactants with aerosols, which in turn affect the atmospheric dynamics, and radiation. Our aim in this thesis is to strengthen the combination of the atmospheric dynamics and atmospheric chemistry research fields. As the interactions between these processes can have significant contributions to the dynamic and chemical budgets and are not yet well understood and/or represented, further investigation on the interplay between these research areas is still necessary.

In this thesis, we explore the impact of the dynamics on the chemical reactants, limiting ourselves to the diurnal scale in the lowest region of the atmosphere, the so-called atmospheric boundary layer (see Fig. 1.1). This layer is generally turbulent due to convective and mechanical sources, which results in the mixing of air. Mechanical turbulence is caused by the reduction of wind speed near the earth's surface and the resulting wind shear. During daytime conditions over land, the convective boundary layer is common. This type of boundary layer, characterized by convective turbulence that is generated by solar heating of the soil and vegetation, significantly evolves with time. Its height increases non-linearly from values as low as 100 m in the morning to values that can exceed 2 km in the afternoon. This growth is related to entering air that originates from the atmospheric layer aloft, a process called entrainment. On top of this convective boundary layer the potential temperature (i.e. temperature corrected for height dependent cooling) increases with height in the so-called thermal inversion layer (see Fig. 1.1). A proper understanding and representation of the boundary layer, is key for two reasons. First, the boundary layer is the connection between conditions at the earth's surface, where surface exchange of e.g. heat, moisture and biogenic compounds takes place, and in the upper atmosphere, therefore controlling atmospheric reactivity. Second, the conditions in the boundary layer are those that are experienced by all organisms that live on the surface of the planet.

The processes that are investigated in this dissertation are not limited to specific geographic locations. However, the case studies focus on atmospheric boundary layers over forests in boreal regions and in the Amazon as both ecosystems significantly impact global atmospheric chemistry. The Amazon rain forest is particularly important due to its high biogenic volatile organic compound emissions (Zimmerman et al., 1988; Karl et al., 2007). In the boreal forest, a significant part of the total carbon over all combined ecosystems is stored

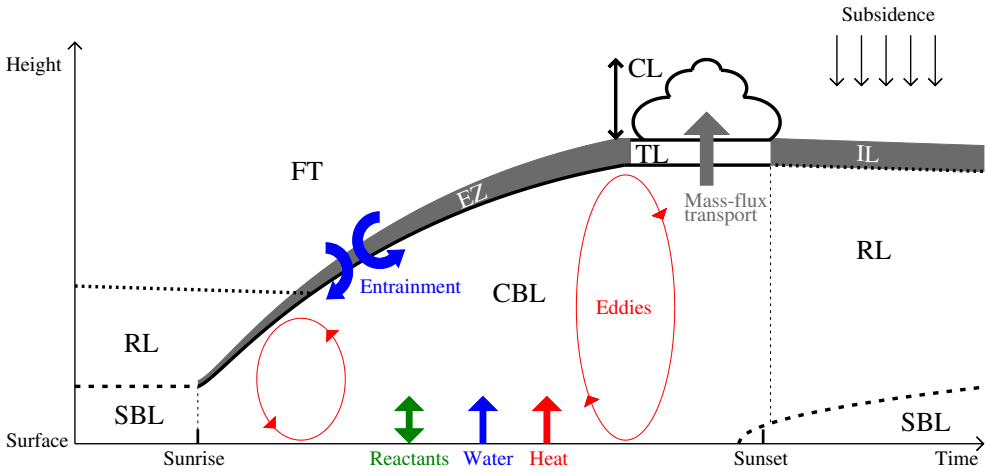

Figure 1.1: Schematic evolution of the atmospheric boundary layer over land, focusing on the daytime properties (inspired by Stull (1988)). Depicted lower atmospheric layers are the (nocturnal) stable boundary layer (SBL), the convective boundary layer (CBL) and the residual layer (RL). On top, the free troposphere (FT) is located. Between the lower and upper atmospheric layers, interface layers are present, which are the entrainment zone (EZ), thermal inversion layer (IL) and the transition layer (TL) that is located between the sub-cloud layer and the cloud layer (CL). Growth of the CBL is the result of entrainment of air from the free troposphere and in this layer, air is mixed by turbulence consisting of eddies of various length and time scales. This turbulence and entrainment are mainly driven by heating at the earth's surface due to solar radiation. Other important surface exchanges are those of moisture and reactants. Furthermore, the influence of air venting by clouds, quantified by the mass-flux transport, and large-scale subsidence are depicted.

(Sellers et al., 1997) and local emissions of reactive organic trace gases, which lead to the formation of aerosols, are high enough to affect the global radiative budget (Williams et al., 2011). Changes in either one of these ecosystems could alter atmospheric chemistry and dynamics at different temporal and spatial scales, potentially affecting global climate.

In this thesis, we aim to bridge the gap between the smaller atmospheric scales ($\sim$ 50 m, 1 s) and the larger ones that are typically resolved by chemistry-transport or climate models ($\sim$ 50 km, 1 day). While the effects under study act on smaller scales and require turbulence resolving models to be fully investigated, they affect the large-scale state of the atmosphere and therefore have to be parametrized (i.e. prescribed by empirical expressions) in larger-scale models. Here, we study in detail a number of processes that are not resolved in these larger-scale models and investigate how to prescribe them. We put special emphasis on how

the local chemistry and dynamics are affected by processes on large scales. An example of such a process is large-scale air flows induced by the different atmospheric properties over separate regions. Therefore, we explore the influences of heterogeneous surface forcings (i.e. the non-uniform exchange of reactants, heat and moisture) on the various interactions between atmospheric chemistry and dynamics.

Considering the current challenges in combining studies on atmospheric chemistry and boundary-layer dynamics, we define the following research objectives:

- Identify the small-scale dynamic processes that significantly affect chemistry in atmospheric boundary layers over forested regions.
- Gain understanding in the underlying mechanisms of these processes and develop parametrizations that could be applied in large-scale chemistry-transport and climate models to account for these influences.
- Investigate alternatives to numerical models in analysing and explaining features in observational data, particularly the impact of surface forcings and boundary-layer dynamics on atmospheric reactant concentrations.
- Characterize how large-scale processes interact with boundary-layer dynamics by studying the effect of land-surface heterogeneity.

1.2 Literature overview

Concentrations of chemical species in the atmosphere are regulated by a combination of surface exchange, chemical processes and physics. That atmospheric chemistry is not detached from the atmospheric dynamics, is already well known from the literature. For example, it was first presented by Davis et al. (1994) that knowledge of the boundary-layer dynamics is fundamental when deriving the surface exchange of reactants from observed vertical profiles. Additionally, multiple studies have been performed on the role of turbulence and mixing on atmospheric reactants, initiated by the theoretical study of Donaldson and Hilst (1972), while Kley (1997) presented how dynamical transport affects chemical compounds in the atmosphere. In turn, the impact of chemistry on turbulent fluxes has been investigated and presented (Fitzjarrald and Lenschow, 1983; Gao et al., 1993; Vilà-Guerau de Arellano and Duynkerke, 1995).

Various numerical studies (e.g., Ganzeveld et al., 2008; Butler et al., 2008; Vilà-Guerau de Arellano et al., 2009, 2011) have demonstrated that it is imperative to understand and correctly account for boundary-layer dynamics in order to represent the atmospheric chemistry. However, since these processes act at scales that are smaller than the typical grid size (i.e.

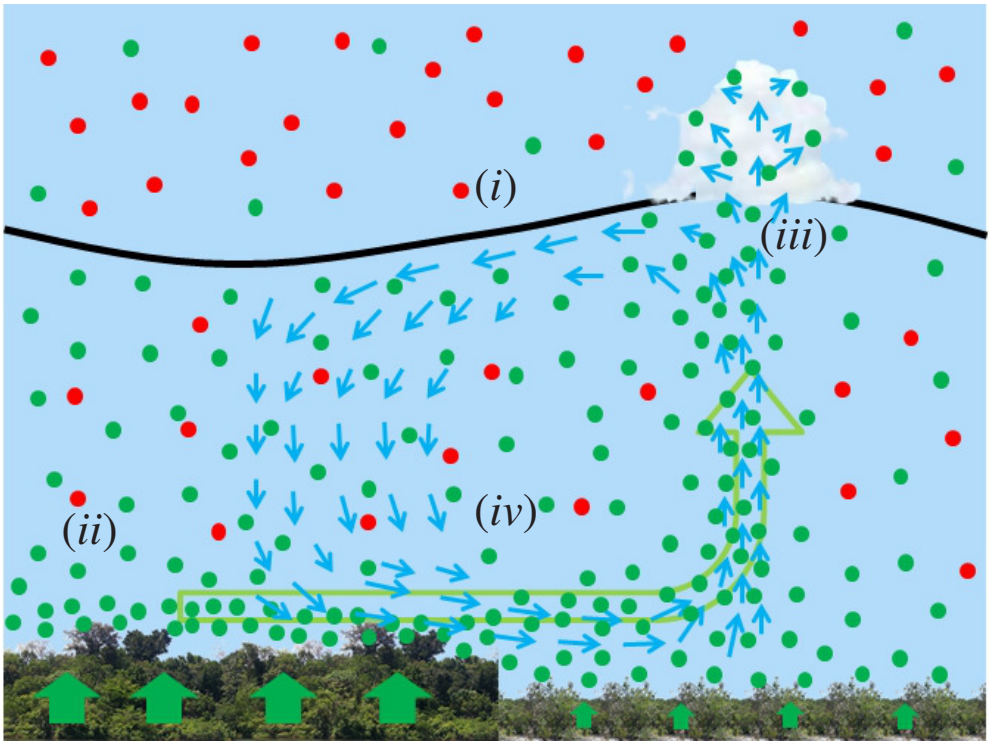

Figure 1.2: Overview of the processes treated in this thesis. Included are the influences of (i) the separation between the atmospheric boundary layer and free troposphere and the height of this separation, treated in Chapters 2, 3 and 4, (ii) the segregation of chemical species within the boundary layer, treated in Chapter 5, (iii) the mass-flux of sub-cloud layer air into the free troposphere by shallow cumulus convection, treated in Chapter 6, and (iv) the large-scale structures in the boundary layer that are related to heterogeneous surface conditions and shallow convection, treated in Chapters 2, 5 and 6.

sub-grid processes) of large-scale models (Ganzeveld et al., 2008; Vilà-Guerau de Arellano et al., 2009; Kim et al., 2012), they have to be parametrized. At the start of this research it was recognized that not all relevant processes were yet properly accounted for. In the following sections, we provide an overview of the literature on the main processes that are investigated in this thesis.

1.2.1 The impact of the boundary-layer height

The evolution of the boundary-layer height governs the dilution and entrainment of atmospheric constituents in the convective boundary layer. Using mixed-layer and large-eddy

simulation models, which respectively prescribe and resolve turbulent mixing and spatial distributions in the boundary layer, it has been demonstrated by Vilà-Guerau de Arellano et al. (2009) that emissions of isoprene, a key atmospheric reactant in boundary layers over the Amazon rain forest, can only be inferred from the concentration evolution in the atmospheric boundary layer if the boundary-layer height evolution is known. Therefore, an accurate representation of the height of the boundary layer is necessary to study the diurnal variability of atmospheric compounds, such as carbon dioxide (e.g., Pino et al., 2012).

For a convectively mixed boundary layer, the dynamics are conveniently described by mixed-layer theory. This theory assumes that properties are well mixed by convective turbulence throughout the boundary layer and that the surface and thermal inversion layers are thin compared to the total boundary layer. The governing equations have first been introduced by Lilly (1968) and expanded since by Betts (1973), Carson (1973) and Tennekes (1973). The resulting numerical models (e.g., Driedonks, 1982a) have been applied to study multiple processes, which include interactions between the land surface and the atmosphere (e.g., de Bruin, 1983; van Heerwaarden et al., 2010), the sensitivity of CO_2 concentrations on entrainment (Culf et al., 1997; Pino et al., 2012), the onset of clouds (Ek and Holtslag, 2004) and the dependence of the boundary-layer height evolution on non-stationary surface heat fluxes (van Driel and Jonker, 2011) and elevated residual layer (Stensrud, 1993). A residual layer is an atmospheric layer that was previously part of a convectively mixed boundary layer (see Fig. 1.1) for which the turbulence has decayed due the decrease in solar heating at the end of the day. As a result, conserved variables are still well mixed in this layer, but there is no active mixing any longer. In the morning, residual layers from the previous day can overlay shallow boundary layers.

Vinuesa and Vilà-Guerau de Arellano (2005) and Vilà-Guerau de Arellano et al. (2009) introduced and developed a mixed-layer model that is coupled with a chemical module, providing the possibility to evaluate the dependence of atmospheric chemistry to the basic boundary-layer dynamics, e.g. the impact of residual atmospheric layers on the chemistry and the interaction between reactants and land surface properties, at a low computational cost. Furthermore, this model can be used to represent and interpret observational data (e.g., van Stratum et al., 2012). In Chapter 2 we study data from boreal forest to gain more insight in the different impacts of the boundary-layer height evolution on chemical species (see (*i*) in Fig. 1.2). Previous studies have been conducted to increase our knowledge about this particular environment, including the extensive Boreal Ecosystem-Atmosphere Study (BOREAS; Sellers et al., 1997). However, even though the boundary-layer dynamics were analysed for that observational campaign (Barr and Betts, 1997; Davis et al., 1997), their impact on atmospheric chemistry was not considered. In the analysed HUMPPA–COPEC–2010 (Hyytiälä United Measurement of Photochemistry and Particles – Comprehensive Organic Particle and Environmental Chemistry; Williams et al., 2011) campaign, the main objective was to obtain

enough data to comprehensively represent the atmospheric chemistry and physics over boreal forest during summer, enabling more thorough analyses.

Complementary to forming the basis for the aforementioned numerical models, the prognostic mixed-layer equations (Lilly, 1968; Tennekes, 1973; Carson, 1973; Betts, 1973) enable a conceptual framework that can be evaluated with analytical expressions. These describe the evolution of the convective boundary-layer dynamics without the need for numerical solving and accommodate the identification and study of the various acting processes. As such, the possibility for sensitivity studies for different driving variables is greatly enhanced. Most of the presented analytical solutions in the literature (e.g., Carson, 1973; Garratt, 1992) are derived by neglecting the influence of the initial conditions and consequently overestimate the boundary-layer height. A complete analytical expression for the height evolution of a boundary layer without moisture is only presented by Driedonks (1982b). However, the presented equation unfortunately contains a typographical error that cannot be discerned by the reader since the derivation is not given.

Next to presenting the correct complete analytical expression, including derivation, for dry conditions, Chapter 3 introduces the solution that includes the effects of moisture and evaporation. The combination of a complete analytical solution for the boundary-layer height evolution and an expression for chemical reactant concentrations as a function of time and the boundary-layer height has not yet been presented in the literature. Finally, considering large-scale dynamics, the influence of subsidence (see Fig. 1.1) on these results, presented in Chapter 4, is generally not taken into account in the analytical derivations with the exception of Carson (1973). However, it should be noted that he does not consider the influence of the initial conditions or moisture.

1.2.2 Representing shallow cumulus convection

On top of convectively mixed boundary layers over land, shallow cumulus (fair weather) clouds often appear during the day (Hahn and Warren, 2007). These clouds form above and are rooted to thermals in the mixed layer (LeMone and Pennell, 1976). In some air parcels with saturated air, the buoyancy is higher than in their environment (starting from their lifting condensation level) due to the latent heat release by condensation, which results in an upward acceleration. These so-called active clouds transport air from the sub-cloud layer to the cloud layer (see (*iii*) in Fig. 1.2). The flow rate of this vertical transport is expressed by the kinematic mass flux.

A first effect of this mass flux on chemistry is that consequently atmospheric reactants are vented from the sub-cloud layer to the cloud layer, too. This process was suggested by Karl et al. (2007) as an explanation for relatively low ratios of isoprene oxidation products compared to isoprene itself that were observed in the lower free troposphere under cloudy

conditions. Additionally, the sub-cloud layer chemistry is affected if the air that is transported to the cloud layer by the mass flux is characterized by different reactant concentrations than the average values in the sub-cloud layer (see (*iii*) in Fig. 1.2). Next to studying the impact of UV radiation modification by clouds, the resulting transport of chemical species by the shallow-cumulus convection has been confirmed by Vilà-Guerau de Arellano et al. (2005) and Kim et al. (2012).

As the processes related to shallow cumulus clouds, including mass-flux transport, occur at scales that are not resolved by regional and global chemistry-transport and climate models (Kim et al., 2012), parametrizations have to be developed to represent this transport in those models. The most suitable technique to study the transport and subsequently derive these expressions is to make use of a 3-dimensional turbulence resolving model, such as a large-eddy simulation model. Using this type of model, Siebesma and Cuijpers (1995) expanded on the work of Tiedtke (1989) and Gregory and Rowntree (1990), who treated shallow convection in the parametrizations for their large-scale models as part of a more general convection scheme. Siebesma and Cuijpers (1995) confirmed that the vertical transport of the dynamical variables (specific humidity and potential temperature) is dominated by the organized transport in the clouds that is related to the kinematic mass flux. This research was expanded by studying the impact of subsiding cloud shells on the mass flux (Heus and Jonker, 2008; Jonker et al., 2008) and by confirming that in the cloud layer the vertical flux of chemical species, particularly NO_2, is well represented by the mass-flux transport (Vilà-Guerau de Arellano et al., 2005). In Chapter 6 we further extend on existing studies by deriving parametrizations to reproduce the mass-flux transport of atmospheric constituents in large-scale models.

Neggers et al. (2006) parametrized the kinematic mass flux by shallow-cumulus convection, based on the sub-cloud layer conditions (Neggers et al., 2004), and applied it to a bulk model to represent the dynamics of a marine sub-cloud layer. The associated mass-flux transport of dynamical and chemical properties from the sub-cloud to the cloud layer was not investigated as this seminal study focused on the impact of the shallow-cumulus convection on the sub-cloud layer height evolution. In a companion study to the work presented in Chapter 6 (van Stratum et al., Submitted), this parametrization is expanded to represent a boundary layer over land. Their results account for the vertical transport of specific humidity, using expressions that are derived from large-eddy simulation data. However, the representation of chemical transport by shallow-cumulus convection is investigated for the first time in this dissertation.

1.2.3 Accounting for segregation of chemical species

Another important sub-grid scale process in chemistry-transport and climate models that can be studied by large-eddy simulation models is the segregation of chemical species. If tur-

bulent mixing is not efficient enough to uniformly distribute chemical species, sub-regions appear where the presence of different species are correlated or anti-correlated (see (*ii*) in Fig. 1.2), which modifies the mean chemical reactivity in the boundary layer. This adaptation of the chemical reactivity is quantified by the intensity of segregation (Danckwerts, 1952) and has been connected to turbulent flows (in reactors) by Toor (1969).

The intensity of segregation was first associated to atmospheric chemistry by Donaldson and Hilst (1972). They concluded, using an analytical model, that segregation could significantly affect chemical depletion in the atmosphere if turbulence is not able to mix the reactants rapidly enough. To quantify this effect, numerical simulations have been performed, using large-eddy simulation models. The pioneering studies (e.g. Schumann, 1989; Sykes et al., 1992) were limited to idealized cases with only a single binary reaction, but already indicated that segregation is most significant if the chemical life time and the turbulent time scale are of similar magnitude. Further analyses, considering more complex chemistry and heterogeneous surface emissions of reactants, were performed by Krol et al. (2000) for a general convective boundary layer and by Auger and Legras (2007) for urban conditions. These studies indicated that non-uniform emissions significantly enhance the intensity of segregation, although large-scale spatial structures in the reactant distribution were already reported to emerge for homogeneous surface conditions as well (Jonker et al., 1999, 2004). Petersen et al. (1999) attempted to link the horizontal intensity of segregation to the division between updrafts and downdrafts within the convective boundary layer, related to coherent dynamical structures (see (*iv*) in Fig. 1.2), but concluded that the covariances that were parametrized by his plume budget did not explain most of the covariances observed in the large-eddy simulation data. As an alternative to numerical simulations with models that simultaneously resolve turbulence and chemistry, the horizontal segregation was studied using more basic second-order closure models (Verver et al., 1997, 2000).

Recently, it has been recognized that the segregation of species could be a relevant process to take into account in observational analyses and numerical model predictions (Butler et al., 2008; Pugh et al., 2010a, 2011). Butler et al. (2008) even considered it the main contributor to the large discrepancies between model results and observations of isoprene and the hydroxyl radical over tropical forest, assuming a decrease of 50 % in the chemical reactivity in order to reconcile the results from their employed numerical model with measurements. However, direct intensity of segregation observations that were presented in the aforementioned studies and by Dlugi et al. (2010) generally correspond to reductions of only 10 to 15 %.

It should be noted that the aforementioned observations only consider data that is sampled at one point per time interval, while the segregation of chemical species within the atmospheric boundary layer is a 3-dimensional effect. A large-eddy simulation model, which explicitly resolves chemistry and turbulence and generates 3-dimensional fields of data at every time interval, provides the opportunity to investigate whether the suggested 50 % re-

duction in chemical reactivity is plausible for the conditions under study. In Chapter 5, the influences of chemical conditions and of heterogeneous surface exchange of reactants, heat and moisture on the intensity of segregation are systematically investigated.

1.2.4 The influence of heterogeneous land surfaces

Heterogeneity in the properties of the land surface can have significant impact on the dynamics in the boundary layer. In spite of this, it has been a challenge to identify related dynamical structures in field observations that focused on sensible and latent heat fluxes (e.g., LeMone et al., 2003; Górska et al., 2008), although the impact on the mean state variables could be discerned. Using numerical models, the main characteristics related to heterogeneous land surfaces can be reproduced and studied in more detail. Ookouchi et al. (1984), using a mesoscale model with 5 km horizontal resolution, indicated that non-uniform heat fluxes caused by soil moisture heterogeneities could induce mesoscale circulations (see (*iv*) in Fig. 1.2) that are comparable in magnitude to a sea breeze. This finding was corroborated by Avissar and Liu (1996), using a regional model with finer (250 m) horizontal resolution. Furthermore, they indicated that the upward motions in the mesoscale circulations, located over the dry surface, are stronger than vertical motions induced by turbulence. As a result, related to the transport of warm, moist air by these circulations, the cloud formation is enhanced and mainly located over the dry areas (see (*iii*) in Fig. 1.2). These effects occur at sub-grid scales of chemistry-transport and climate models. After these seminal analyses, further numerical studies made use of large-eddy simulation models to resolve turbulent motions and expand on the knowledge that was gained.

The dependence of the mesoscale circulations and resulting boundary-layer dynamics on the different properties of the heterogeneous surface heat fluxes was further investigated numerically. Avissar and Schmidt (1998) made a first characterization of the effect of non-uniform surface heat fluxes with different horizontal averages and amplitudes and wavelengths of heterogeneity. This was expanded upon by Raasch and Harbusch (2001), who also investigated the dependence on the length scale of heterogeneity, focusing on small-scale heterogeneities with length scales no larger than the boundary-layer height. They found that significant effects only occurred for the largest length scales they investigated (i.e. equal to the boundary-layer height), confirming the blending-height considerations for short length scales of heterogeneity posed by Mahrt (2000). Further research on this dependence (Patton et al., 2005) focused on length scales between 1 and 18 times the boundary-layer height. It was demonstrated that the strongest effects for the mesoscale circulations and the boundary-layer dynamics were obtained for length scales between 4 and 9 times the boundary-layer height. Additionally, a first characterization was made for the dependency of the entrainment velocity, associated to boundary-layer growth, on the length scale of heterogeneity (Patton

et al., 2005) and the amplitude in the prescribed surface heat fluxes (van Heerwaarden and Vilà-Guerau de Arellano, 2008).

The cloud formation over relatively dry regions has been confirmed by data from aircraft observations (e.g., Garcia-Carreras et al., 2010) and by numerical studies with turbulence resolving models, e.g. by evaluating relative humidity as an indicator for cloud formation (van Heerwaarden and Vilà-Guerau de Arellano, 2008). In turn, aircraft studies (LeMone and Pennell, 1976) indicated that, even over homogeneous terrain, the presence of cumulus clouds is related to roll vertices in the sub-cloud layer, which suggests that the large-scale structures in this atmospheric layer are not only related to heterogeneous surface heat fluxes, but also to shallow convection. It has been confirmed by numerical studies (Kim et al., 2012) that shallow-cumulus clouds indeed enhance vertical motions and drive large-scale circulations in the sub-cloud layer.

Expanding on the results of Avissar and Schmidt (1998), Raasch and Harbusch (2001) and Kim et al. (2004) investigated the dependency of the induced mesoscale circulations and the boundary-layer dynamics on the direction and magnitude of the background wind. Their results showed that the influence of background wind can be significant and is highly dependent on the direction relative to the direction of surface heterogeneity. Additionally, Courault et al. (2007) studied a configuration with 2-dimensional heterogeneity (chessboard pattern), demonstrating that such a non-uniform distribution of surface heat fluxes leads to weaker induced circulations than 1-dimensional heterogeneity.

The influence of heterogeneous heat and moisture fluxes on atmospheric chemistry in the boundary layer has not yet been investigated. Although Krol et al. (2000) and Auger and Legras (2007) considered heterogeneously distributed reactant emissions in their studies on the intensity of segregation, they dealt with uniform surface heat and moisture fluxes. In this context, the combined response of boundary-layer dynamics and chemistry to spatial heterogeneities in the surface exchange of reactants, heat and moisture is investigated in Chapter 6. Special attention is devoted to the spatial distribution and resulting chemical reactivity of isoprene.

1.3 Research strategy

In this thesis, the various impacts of dynamic processes on the atmospheric chemistry in the convective boundary layer are mainly studied by analysing numerical data from models that simultaneously resolve chemistry and dynamics. For this purpose we design idealized numerical experiments that are constrained by data from observational campaigns. By doing so, realistic conditions are examined while controlling the acting large-scale influences and removing complexities that would obscure the signals that we aim to investigate. This enables

us to identify the most important processes and quantify their impact. In our study, we base our analyses on a chemical reaction scheme that is optimized to represent the essential reactions of the O_3–NO_x–VOC–HO_x system that is especially typical for the diurnal boundary layer over the Amazon rain forest.

For a first-order representation of the boundary-layer height evolution and its effect on chemistry, we employ a mixed-layer model. This model is based on the zeroth-order mixed layer assumption that during the day turbulent mixing is vigorous enough to result in a well-mixed atmospheric boundary layer and therefore represents the essential processes that govern the time evolution of the diurnal convective boundary layer. Second-order effects, such as a thermal inversion layer on top of the boundary layer with a significant depth (see Fig. 1.1) or the presence of large-scale dynamical structures are not taken into account. However, the low computational cost allows for sensitivity analyses and executing a multitude of case studies. The mixed-layer model is constructed in a modular way, which enables toggling the representation of different dynamical and chemical processes on and off. By doing so, both the effects of individual processes and their interactions can be systematically investigated.

By analysing the numerical data, the effects of different dynamical and chemical processes can be identified and quantified. As a result, these studies can contribute to the interpretation of observational data from which those processes cannot be directly determined. This is demonstrated for the evolution of atmospheric reactants that is observed in observational data from the HUMPPA–COPEC–2010 campaign. For example, the observed morning peak in the temporal evolution of NO_x is explained by accounting for the morning transition of the boundary-layer.

For idealized conditions the governing equations of the mixed-layer model can be solved analytically. We present these solutions as well as their derivations. Using these expressions, the evolution of the boundary-layer height and its impact on the other boundary-layer characteristics (e.g. the concentration of atmospheric compounds like CO_2) can be investigated without the need for numerical models. These expressions hold for chemically reactive species if the chemical production rate and life time are constant. After deriving the appropriate analytical expressions, the only computational power that is needed for an analysis (e.g. a sensitivity study) considers producing the corresponding graphics.

Finally, more complex dynamical and chemical effects are accounted for by using a large-eddy simulation model as they are explicitly resolved at horizontal grid resolutions finer than 100 m. This allows for analyses of the spatial distribution of chemical species in the boundary layer, the formation and properties of clouds and the impact of heterogeneous surface exchange of heat, moisture and atmospheric compounds. Additionally, the availability of 3-dimensional data fields for every time step results in robust statistics.

1.4 Thesis outline

The influence of the boundary-layer height evolution (see Fig. 1.1 and (*i*) in Fig. 1.2) is first analysed in Chapter 2. Using a mixed-layer model, the role of large-scale atmospheric dynamics and residual boundary layers for this evolution is investigated. Furthermore, it is shown that the observational data from the HUMPPA–COPEC–2010 observational campaign can be well reproduced, demonstrating how this model can assist in interpreting observational data. In Chapter 3, analytical expressions are derived for the evolution of the boundary-layer height and the associated evolution of chemical species mixing ratios under idealized chemistry (assuming a constant production rate and chemical life time). These equations are then expanded to include the effect of the large-scale atmospheric subsidence in Chapter 4.

After exploring the influence of idealized boundary-layer dynamics, 3-dimensional effects, such as turbulent fluctuations, are investigated using a large-eddy simulation model in Chapter 5. The focus is on the influence of heterogeneous surface exchange on the boundary-layer dynamics (including height of this atmospheric layer), the spatial distributions of scalars within the boundary-layer and the resulting altered chemical reactivity due to enhanced segregation of chemical species (see (*i*), (*ii*) and (*iv*) in Fig. 1.2). A natural extension of this study on a clear convective boundary layer is to investigate additional processes in mixed layers that are topped by shallow-cumulus clouds. Using the same numerical model, the influence of reactant transport by the venting of air from the sub-cloud layer to the cloud layer (see (*iii*) in Fig. 1.2) is examined and parametrized in Chapter 6. In this analysis special attention is paid to the interaction between this venting of sub-cloud layer air by shallow convection and large-scale dynamical structures (see (*iv*) in Fig. 1.2). Finally, a summary of the main results of this thesis and an outlook for future research are presented in Chapter 7.

Our observation of nature must be diligent, our reflection profound, and our experiments exact. We rarely see these three means combined; and for this reason, creative geniuses are not common.

Denis Diderot

2

Characterization of a boreal convective boundary layer and its impact on atmospheric chemistry during HUMPPA-COPEC-2010

We studied the atmospheric boundary layer (ABL) dynamics and the impact on atmospheric chemistry during the HUMPPA-COPEC-2010 campaign. We used vertical profiles of potential temperature and specific moisture, obtained from 132 radio soundings, to determine the main boundary layer characteristics during the campaign. We propose a classification according to several main ABL prototypes. Further, we performed a case study of a single day, focusing on the convective boundary layer, to analyse the influence of the dynamics on the chemical evolution of the ABL. We used a mixed layer model, initialized and constrained by observations. In particular, we investigated the role of large scale atmospheric dynamics (subsidence and advection) on the ABL development and the evolution of chemical species concentrations. We find that, if the large scale forcings are taken into account, the ABL dynamics are represented satisfactorily. Subsequently, we studied the impact of mixing with a residual layer aloft during the morning transition

This chapter is published as Ouwersloot et al. (2012).

on atmospheric chemistry. The time evolution of NO_x and O_3 concentrations, including morning peaks, can be explained and accurately simulated by incorporating the transition of the ABL dynamics from night to day. We demonstrate the importance of the ABL height evolution for the representation of atmospheric chemistry. Our findings underscore the need to couple the dynamics and chemistry at different spatial scales (from turbulence to mesoscale) in chemistry-transport models and in the interpretation of observational data.

2.1 Introduction

The atmospheric boundary layer (ABL) dynamics and their impact on atmospheric chemistry are studied by combining field observations, taken during the HUMPPA-COPEC-2010 campaign (Williams et al., 2011), with a modelling study. HUMPPA-COPEC-2010 took place in the boreal forest. This ecosystem, located roughly between 50° and 65° N, covers 8 % of the global land surface and 27 % of the forested area, extending over 15×10^6 km^2 (Williams et al., 2011). Therefore, its impact on the global atmospheric chemistry and physics is significant. Since it contains over 10 % of the total carbon present in the combined ecosystems on Earth, perturbations in the climate of the Northern Hemisphere could lead to changes in the carbon cycle (including emissions of volatile organic compounds, VOCs) and aerosol formation and consequently alter the atmospheric composition (Sellers et al., 1997). Considering the large extent of the boreal forest, perturbations in this ecosystem may alter the dynamics and chemistry at different temporal and spatial scales, possibly up to the entire globe. Therefore, it is relevant and timely to study the atmospheric processes over the boreal forest at a range of scales in order to understand the interactions between the dynamics and chemistry. Here, we largely focus on the processes occurring at smaller spatial scales, which are influenced by the diurnal variability of the ABL.

During the HUMPPA-COPEC-2010 campaign, which took place at the Finnish SMEAR II station from 12 July to 12 August 2010, special emphasis was placed on obtaining a complete data set of surface and atmospheric measurements to comprehensively characterize the atmospheric physics and chemistry. Guided and constrained by this data, we focus on the influence of large scale forcings and transitions in the morning from nocturnal to daytime conditions on the boreal atmospheric boundary layer dynamics and the associated atmospheric chemistry. Our research extends the analyses of previous campaigns, like the Boreal Ecosystem-Atmosphere Study (BOREAS) (Sellers et al., 1997). BOREAS was conducted in the Canadian forest, aimed at improving the understanding of interactions between the boreal forest biome and the lower atmosphere (Sellers et al., 1997). Observations included dynamical, ecological and biogeochemical variables. The latter included observations of the trace gases CO_2, CH_4 and non-methane hydrocarbons. Even though the boundary layer dynamics were analysed (Barr and Betts, 1997; Davis et al., 1997), their evolution was not represented

using models to identify and quantify the driving processes. In addition, their impact on the atmospheric chemistry was not considered.

At the SMEAR II station in Hyytiälä (61°51° N, 24°17° E, 181 m a.s.l.) continuous observations are performed (Hari and Kulmala, 2005). The station is designed to study the transport of aerosols (Kulmala et al., 2001), gases, energy and momentum between the soil, the air within the canopy and the ABL. Due to the focus of SMEAR II, all observations are performed in the soil, the canopy and the lower part of the ABL. Previous observational campaigns at this site mostly focused on aerosol studies (Nilsson et al., 2001).

During the HUMPPA-COPEC-2010 campaign the standard instruments of the SMEAR II site were complemented with additional equipment. An overview of the gas and aerosol measurement instruments is given in Table 1 of Williams et al. (2011). To be able to characterize the ABL evolution, additional observations were made to obtain vertical profiles of the meteorological variables, using a Cessna aircraft and radiosondes. The campaign turned out to be of particular interest due to anomalously high temperatures that might be representative of future boreal climates (Williams et al., 2011). Since the atmospheric temperature affects the surface latent and sensible heat fluxes (van Heerwaarden et al., 2010), future climates may be characterized by different ABL dynamics.

Concentrations of chemical species in the atmosphere are governed by surface exchange, chemical processes and dynamics in the ABL. Therefore, it is imperative to correctly represent the ABL dynamics when interpreting or predicting atmospheric chemistry (Davis et al., 1994; Ganzeveld et al., 2008; Vilà-Guerau de Arellano et al., 2011). A primary goal of our research is to determine how the growth of the ABL influences atmospheric chemistry. The ABL height development influences the chemical evolution of the boundary layer in two ways. First, the actual height of the ABL can be considered as a mixing volume in which reactive compounds are released and interact. During the day, the height of this layer increases non-linearly from values as low as 100 m in the morning to values that can exceed 2 km in the afternoon. Second, the growth of the boundary layer determines the entrainment of air from the free troposphere into the boundary layer. This entrained air generally has different thermodynamic and chemical properties than air in the ABL.

In this paper we classify different boundary layer prototypes that correspond to the most representative vertical potential temperature profiles. These prototypes correspond to stable, convectively mixed and conditionally unstable boundary layers. This classification of the structure of the ABL enables the identification of important processes for atmospheric chemistry during HUMPPA-COPEC-2010, like the intensity of mixing, turbulent time scales, the atmospheric dilution capacity and the entrainment of free tropospheric air. An overview of these processes is given in Table 1 of Ouwersloot et al. (2011).

We further examine the boundary layer dynamics for a single day with particularly intensive observations, using a mixed layer model (MXL). Emphasis is placed on how atmospheric

chemistry is affected by the ABL height evolution. The day is selected because important processes took place that can be easily overlooked when analysing the impact of the boundary layer dynamics on chemistry. These processes, associated with temporal transitions and large-scale forcings, include subsidence, the advection of air masses and, in the morning, the connection with a residual boundary layer from the previous day. We complete the study by evaluating the effectiveness of the applied observational strategy during HUMPPA-COPEC-2010 in characterizing the ABL dynamics.

The next section addresses the methodology of this study. Subsequently, the representation of the boundary layer height during one representative day in the HUMPPA-COPEC-2010 campaign is presented. This is followed by an illustration of its importance for accurately modelling atmospheric chemistry. Finally, the strategy for obtaining meteorological data during field campaigns is discussed.

2.2 Methods

In this study, meteorological and atmospheric chemistry observations are combined with numerical experiments. Some observations serve as initial and boundary conditions, while others are compared to the numerical model results. The upper atmospheric conditions are determined by radiosondes. These observations encompass both the boundary layer and free troposphere. The evolution of the atmospheric conditions near the Earth's surface is monitored at the SMEAR II measuring station. The chemical observational techniques used are described in Table 1 of Williams et al. (2011). We focus on the O_3 observations with the ultraviolet absorption/fluorescence (UV) method and the NO and NO_2 observations with the chemiluminescence (CLD) method, which were all performed by the Max Planck Institute for Chemistry at a height of 24 m above the ground, approximately 9 m above the canopy (Mammarella et al., 2009). Since no observations are made in the mixed layer above the surface layer, this data is used as first estimates for the boundary layer average values.

Two complementary numerical techniques are used: the mixed layer model is applied to characterize the boundary layer dynamics and their role in atmospheric chemistry, while vertical profiles generated in the numerical experiments with a Large-Eddy Simulation (LES) model act as virtual radio soundings for the discussion of the observed radiosonde profiles. More specific information is given in the following sections.

2.2.1 Radiosondes

During the campaign, 175 GRAW DFM-06 radiosondes were launched from a clear area at approximately 300 m distance from the main observational site. In principle, five radiosondes were launched per day at the local daylight saving times (LT, UTC + 3) 03:00,

09:00, 12:00, 15:00 and 21:00. The local daylight saving time is ahead of the local solar time by 1 h 29 min. During intensive observation periods (IOP), the frequency of radiosonde launches was increased to intervals of maximum two hours. These events took place from 16 July 21:00 to 17 July 18:00, from 21 July 21:00 to 22 July 18:00, from 28 July 21:00 to 29 July 18:00 and from 5 August 18:00 to 6 August 18:00. The observations of 6 August will be analysed in more detail.

Data transmitted by the sonde each second was received by an antenna placed at a nearby building. As well as a GPS device, each sonde included a temperature and a humidity sensor. The GPS coordinates were used to determine the altitude and geographical location of the sonde, as well as the wind velocities. The determined position is accurate within 10 m. The temperature sensor measured with an accuracy of 0.2 °C and the humidity sensor measured the relative humidity with an accuracy of 2 %. The software of the ground station determined the pressure profile by combining these observations with the surface pressure. From the combination of altitude, pressure, temperature and relative humidity data, the profiles of the potential temperature, θ, and specific humidity, q, are determined. This study focuses on the lowest 3000 m of these profiles.

2.2.2 SMEAR II data

Data near the surface was collected at the boreal forest observational station SMEAR II (Hari and Kulmala, 2005). The standard observations include meteorological data, aerosols and the concentrations of several chemical species (CO_2, H_2O, CO, O_3, SO_2, NO and NO_2). In addition, the turbulent fluxes of temperature, moisture, momentum, aerosols, CO_2, O_3 and several volatile organic compounds are measured. For this study, the heat fluxes, surface pressure, relative humidity and temperature observations are used.

The sensible heat flux, H, and the latent heat flux, LE, were determined using 30-min averages of 10 Hz Eddy Covariance measurements at a height of 23 m (Mammarella et al., 2009). The observations were made above the canopy top, which was located at approximately 15 m height. As such they can be considered as appropriate surface forcings for the development of the ABL and can be directly related to the ABL dynamics observed from the radiosonde profiles.

The observational data of surface pressure and the relative humidity and temperature at 50 m height originate from the SMEAR smartSearch database (Junninen et al., 2009). These data are converted to potential temperature and specific humidity in a similar way as the radiosonde data.

Table 2.1: Chemical reaction scheme solved by the MXL model, based on van Stratum et al. (2012). T is the absolute temperature in K and χ is the solar zenith angle. The unit of first-order reaction rate coefficients is s^{-1} and that of second-order reaction rate coefficients is $cm^3\,molec^{-1}\,s^{-1}$. Reactions (R15), (R24) and (R25) have more comprehensive expressions for their reaction rates[1,2,3]. For these expressions, c_{air} and c_{H_2O} are the concentrations in molec cm^{-3} for air and H_2O, respectively. Reactions (R1), (R5) and (R6) are photolysis reactions. MVK is the acronym of methyl vinyl ketone and REST stands for products and/or secondary fast reactions with reactants in the ambient air that are not specified.

Name	Chemical equation	Reaction rate constant
R1	$O_3 + h\nu \rightarrow O^{1D} + O_2$	$3.83\times10^{-5} \cdot e^{-\frac{0.575}{\cos(\chi)}}$
R2	$O^{1D} + H_2O \rightarrow 2\ OH$	$1.63\times10^{-10} \cdot e^{\frac{60}{T}}$
R3	$O^{1D} + N_2 \rightarrow O_3 + REST$	$2.15\times10^{-11} \cdot e^{\frac{110}{T}}$
R4	$O^{1D} + O_2 \rightarrow O_3$	$3.30\times10^{-11} \cdot e^{\frac{55}{T}}$
R5	$NO_2 + h\nu \rightarrow NO + O_3 + REST$	$1.67\times10^{-2} \cdot e^{-\frac{0.575}{\cos(\chi)}}$
R6	$CH_2O + h\nu \rightarrow HO_2 + REST$	$1.47\times10^{-4} \cdot e^{-\frac{0.575}{\cos(\chi)}}$
R7	$OH + CO \rightarrow HO_2 + CO_2 + REST$	2.40×10^{-13}
R8	$OH + CH_4 \rightarrow CH_3O_2 + REST$	$2.45\times10^{-12} \cdot e^{\frac{-1775}{T}}$
R9	$OH + C_5H_8 \rightarrow RO_2$	1.00×10^{-10}
R10	$OH + MVK \rightarrow HO_2 + CH_2O + REST$	2.40×10^{-11}
R11	$HO_2 + NO \rightarrow OH + NO_2$	$3.50\times10^{-12} \cdot e^{\frac{250}{T}}$
R12	$CH_3O_2 + NO \rightarrow HO_2 + NO_2 + CH_2O + REST$	$2.80\times10^{-12} \cdot e^{\frac{300}{T}}$
R13	$RO_2 + NO \rightarrow HO_2 + NO_2 + CH_2O + MVK$	1.00×10^{-11}
R14	$OH + CH_2O \rightarrow HO_2 + REST$	$5.50\times10^{-12} \cdot e^{\frac{125}{T}}$
R15	$2\ HO_2 \rightarrow H_2O_2 + O_2$	k^1
R16	$CH_3O_2 + HO_2 \rightarrow REST$	$4.10\times10^{-13} \cdot e^{\frac{750}{T}}$
R17	$RO_2 + HO_2 \rightarrow REST$	1.50×10^{-11}
R18	$OH + NO_2 \rightarrow HNO_3$	$3.50\times10^{-12} \cdot e^{\frac{340}{T}}$
R19	$NO + O_3 \rightarrow NO_2 + O_2$	$3.00\times10^{-12} \cdot e^{-\frac{1500}{T}}$
R20	$OH + HO_2 \rightarrow H_2O + O_2$	$4.80\times10^{-11} \cdot e^{\frac{250}{T}}$
R21	$OH + H_2O_2 \rightarrow H_2O + HO_2$	$2.90\times10^{-12} \cdot e^{\frac{-160}{T}}$
R22	$NO + NO_3 \rightarrow 2\ NO_2$	$1.80\times10^{-11} \cdot e^{\frac{110}{T}}$
R23	$NO_2 + O_3 \rightarrow NO_3 + O_2$	$1.40\times10^{-13} \cdot e^{\frac{-2470}{T}}$
R24	$NO_2 + NO_3 \rightarrow N_2O_5$	k^2
R25	$N_2O_5 \rightarrow NO_2 + NO_3$	k^3
R26	$N_2O_5 + H_2O \rightarrow 2\ HNO_3$	2.50×10^{-22}
R27	$N_2O_5 + 2\ H_2O \rightarrow 2\ HNO_3 + H_2O$	1.80×10^{-39}
R28	$HO_2 + O_3 \rightarrow OH + 2\ O_2$	$2.03\times10^{-16} \cdot \left(\frac{T}{300}\right)^{4.57} \cdot e^{\frac{693}{T}}$

[1] $k = (k_1 + k_2)\,k_3,\ k_1 = 2.2\times10^{-13} \cdot e^{\frac{600}{T}},\ k_2 = 1.9\times10^{-33} \cdot e^{\frac{980}{T}} \cdot c_{air},\ k_3 = 1 + 1.4\times10^{-21} \cdot e^{\frac{2200}{T}} \cdot c_{H_2O}$

[2] $k = 0.35 \cdot (k_1 \cdot k_2)\,/\,(k_1 + k_2),\ k_1 = 3.6\times10^{-30} \cdot \left(\frac{T}{300}\right)^{-4.1} \cdot c_{air},\ k_2 = 1.9\times10^{-12} \cdot \left(\frac{T}{300}\right)^{0.2}$

[3] $k = 0.35 \cdot (k_1 \cdot k_2)\,/\,(k_1 + k_2),\ k_1 = 1.3\times10^{-3} \cdot \left(\frac{T}{300}\right)^{-3.5} \cdot e^{\frac{-11000}{T}} \cdot c_{air},\ k_2 = 9.7\times10^{14} \cdot \left(\frac{T}{300}\right)^{0.1} \cdot e^{\frac{-11080}{T}}$

2.2.3 Mixed layer model (MXL)

To represent and subsequently interpret the observational data, a mixed layer model is used that is coupled to a chemical module (Tennekes, 1973; Vilà-Guerau de Arellano et al., 2009). This model is based on the zeroth-order mixed layer assumption that during the day turbulent mixing is vigorous enough to result in a well-mixed ABL. Thus, the model is similar to a chemical box model with an evolving upper boundary. Mixed layer theory assumes that conserved scalar variables are uniformly distributed in the vertical direction and that their fluxes are therefore characterized by linear profiles. A thermal inversion layer caps the ABL and separates it from the free troposphere. Both the thermal inversion layer and the surface layer (lowest 10 % of the boundary layer, Stull, 1988) are considered to be thin compared to the total boundary layer. This approach has first been used by Lilly (1968), Tennekes (1973), Carson (1973) and Betts (1973). The vertical profiles of the evaluated quantities show a discontinuity at the height of the inversion, above which they linearly change with height in the free troposphere according to their free tropospheric gradients. This simplified representation of the ABL, which nevertheless incorporates the processes under study, allows for numerical experiments in which atmospheric chemistry and basic ABL dynamics are simultaneously solved at very low computational costs. A model that is similar to the one used here, including chemistry, is described by Vinuesa and Vilà-Guerau de Arellano (2005). Further development includes expanding the chemical module and taking the influence of specific humidity on the entrainment rate into account (Vilà-Guerau de Arellano et al., 2009). The chemical module is flexible and enables the use of different chemical schemes. In previous work it has mostly been used to represent the O_3-NO_x-VOC-HO_x system that is typical for the Amazonian rain forest. The currently applied chemical scheme, which is based on van Stratum et al. (2012), is presented in Table 2.1. The scheme is expanded with a more detailed representation of NO_x and N_2O_5 chemistry (Galmarini et al., 1997). The model acts as a support for the observational data, enabling to study the evolution of the main properties of the boundary layer dynamics.

More information about the governing equations is given in Appendix 2A.

2.2.4 LES model (DALES)

To evaluate the use of radio soundings to obtain vertical profiles of temperature and moisture, numerical experiments were performed with the modified version 3.2 of the Dutch Atmospheric Large-Eddy Simulation (DALES) model (Heus et al., 2010). This model explicitly resolves dynamical (and selected chemical) processes in the boundary layer at grid resolutions finer than 100 m. Therefore, the resulting data can be compared to local observations. In addition, DALES enables us to study how atmospheric flows that are induced by heterogeneous surface forcings influence the distribution of both thermodynamic and chemical

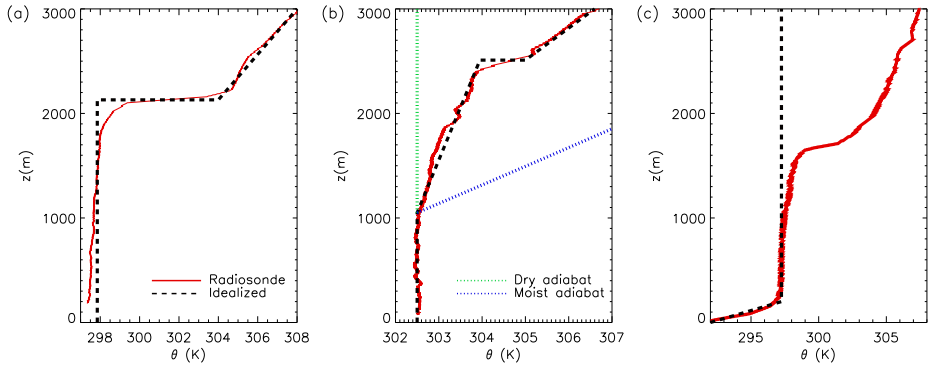

Figure 2.1: Characteristic vertical potential temperature profiles for ***(a)*** *a mixed layer,* ***(b)*** *a mixed layer topped with a conditionally unstable layer and* ***(c)*** *a stable boundary layer. In red an example from the radiosondes is presented, while in black an idealized profile is depicted. In* ***(b)*** *the profile of the potential temperature in the conditionally unstable layer is situated between the dry adiabat and the moist adiabat. In* ***(c)*** *a residual mixed layer from the previous day is present. The data is obtained at* ***(a)*** *16:00 LT on 17 July,* ***(b)*** *18:00 LT on 13 July and* ***(c)*** *03:00 LT on 7 August.*

variables.

This specific LES model has first been used by Nieuwstadt and Brost (1986) and further developed and improved since (e.g., Cuijpers and Duynkerke, 1993; Dosio et al., 2003). Processes are explicitly resolved on scales larger than a set filter width and parametrized on the smaller scales at which the eddies contain less energy. The resolved equations are the filtered Navier-Stokes equations upon which the Boussinesq approximation is applied (Heus et al., 2010). Typically, the filter width is chosen such that over 90 % of the turbulent energy is contained in the resolved scales. The subfilter-scale parametrization is based on the one-and-a-half-order closure assumption (Deardorff, 1973). Periodic boundary conditions are applied in the horizontal directions.

The version of DALES used for this study is modified to enable studies of ABL flows characterized by heterogeneous boundary conditions at the surface (Ouwersloot et al., 2011) and to generate local instantaneous vertical profiles of the chemical species mixing ratios and the dynamical variables. This allows for a comparison between radiosonde profiles and the profiles that are predicted by numerical experiments

2.3 Results

2.3.1 Boundary layer prototypes

Our interpretation of the radiosonde observations indicates that during HUMPPA-COPEC-2010 no clear trend due to synoptic influences is present and that the characteristics of the ABL significantly differ each day. Therefore, the boundary layer dynamics and their influence on atmospheric chemistry have to be analysed on a day-to-day basis. To support this analysis, it is convenient to have a first classification of the ABL dynamics during HUMPPA-COPEC-2010 and associate the radiosonde measurements to boundary layer prototypes. By performing this classification by inspection, the observations can thus be compared to the representations in combined chemistry-meteorology models. The prototypes are characterized by specific vertical profiles and the associated dynamical processes (e.g., Stull, 1988). During the campaign, three different prototypes were observed that correspond to the most representative vertical potential temperature profiles. Out of the 175 radiosondes 43 could not be classified by these prototypes, either due to instrumental errors or different (often transitional) characteristics in the observed vertical profiles. We select three potential temperature profiles from the radiosonde observations to describe their main characteristics. These profiles are similar to those of the virtual potential temperature, which are used for our classification. The profiles are presented in Fig. 2.1.

Figure 2.1a shows the potential temperature profile observed at 16:00 LT on 17 July. It is characterized by a relatively constant potential temperature with height, topped by a layer of a few hundred meters in which the vertical gradient of the potential temperature gradually increases. The location of the maximum potential temperature gradient marks the height of the boundary layer (Sullivan et al., 1998), in this case at approximately 2150 m. From the top of the ABL, the potential temperature linearly increases with height, following its free tropospheric gradient. This increasing potential temperature profile indicates a region that is characterized by a stably stratified flow. The potential temperature is approximately equal in the entire boundary layer due to convective mixing. The jump in potential temperature at the top of the boundary layer, i.e. the thermal inversion, acts as a cap and limits the exchange of air between the ABL and the free troposphere. This measured profile is associated with the convective boundary layer that is usually formed by active convective turbulence during the day. As mentioned in Sect. 2.2.3, a commonly used approximation, the zeroth-order jump assumption (Garratt, 1992), assumes the inversion layer as infinitesimally small, resulting in a jump in the potential temperature at the top of the boundary layer. The resulting theoretical profile is plotted with dashed lines. This very common boundary layer prototype, especially in spring and summer, is evaluated further using the MXL model. ABL profiles of this kind are most clearly discernible during high pressure synoptic systems. During HUMPPA-

COPEC-2010, the SMEAR II station was located in a high pressure region (Williams et al., 2011).

The profile of 18:00 LT on 13 July, as presented in Fig. 2.1b, is similar to the previously discussed one, but contains an extra layer. Until a height of 1050 m the potential temperature is again constant. However, in this case this mixed layer is topped with a conditionally unstable layer. The transition between the two layers is signified by a change in the potential temperature gradient by more than an order of magnitude. This type of ABL is frequently observed with active shallow cumulus (fair weather) clouds (Stull, 1988). The conditionally unstable layer is located between the mixed layer and the inversion layer and is characterized by an increase with height of the potential temperature that is stronger than the dry and weaker than the moist adiabatic lapse rate. The dry adiabatic lapse rate is defined as the increase of potential temperature that an unsaturated rising air parcel would experience under adiabatic conditions, while the moist adiabatic lapse rate describes this increase for a saturated rising air parcel. In short, the conditionally unstable layer acts as a turbulence suppressing stable layer for unsaturated air parcels and as a turbulence generating unstable layer for saturated air parcels. In the first case (clear air), this layer can be considered as part of the thermal inversion layer, while in the latter case (clouds) air parcels that enter the layer rise to its top. When this profile was observed, the humidity was too low to result in condensation (below 70 % relative humidity) and clouds. If under such conditions condensation would have occurred for local air parcels in the conditionally unstable layer, the resulting clouds would become active and grow. Above the conditionally unstable layer, the thermal inversion is located at a height of 2500 m. Above the inversion, the potential temperature rises according to the free tropospheric profile. The corresponding boundary layer prototype, shown by the black dashed line, is a mixed layer topped with a conditionally unstable layer.

The third radiosonde profile is depicted in Fig. 2.1c and is based on data obtained at 03:00 LT on 7 August. It shows a potential temperature that increases with height in a layer that reaches up to a few hundred meters above the surface. Aloft the potential temperature is relatively constant with height. On top, a thermal inversion at 1700 m and a free tropospheric profile are present. This data is characteristic for nocturnal stable boundary layers that are formed after an afternoon transition (e.g., Kaimal et al., 1976; Nieuwstadt and Brost, 1986). During the evening transition and at night, the air near the surface cools, driven by the emission of longwave radiation. This leads to stratification and a stable boundary layer. A residual mixed layer from the previous day can be present above the stable boundary layer, as is the case in this example. However, this is not the case for all stable boundary layers and residual layers can disappear as time progresses (Kaimal et al., 1976). After sunrise, the Earth's surface warms and convective turbulence mixes the air. The stable boundary layer characteristics are then dissipated and a new convectively mixed boundary layer is formed. If a residual layer is still present, the new mixed layer develops until the potential temperature

Table 2.2: Occurrence of atmospheric boundary layer prototypes during HUMPPA-COPEC-2010 according to the radiosonde observations. Listed are the local daylight saving times (UTC+3). Times printed in bold correspond to radiosonde profiles used in this study. The three distinguished prototypes are the mixed layer, ML, the mixed layer topped with a conditionally unstable layer, UC, and a stable boundary layer, SL.

Type	Time of observation				
ML	09:00, 12 Jul	15:00, 12 Jul	21:00, 12 Jul	09:00, 13 Jul	12:00, 13 Jul
	12:00, 15 Jul	15:00, 15 Jul	09:00, 16 Jul	12:00, 16 Jul	15:00, 16 Jul
	21:00, 16 Jul	22:00, 16 Jul	23:00, 16 Jul	00:00, 17 Jul	01:00, 17 Jul
	02:00, 17 Jul	03:00, 17 Jul	04:00, 17 Jul	10:00, 17 Jul	12:00, 17 Jul
	14:00, 17 Jul	**16:00**, **17 Jul**	18:00, 17 Jul	21:00, 17 Jul	09:00, 18 Jul
	21:00, 18 Jul	09:00, 19 Jul	21:00, 19 Jul	12:30, 20 Jul	15:15, 21 Jul
	21:00, 21 Jul	00:00, 22 Jul	09:00, 22 Jul	10:00, 22 Jul	12:00, 22 Jul
	14:00, 22 Jul	18:00, 22 Jul	21:00, 22 Jul	03:00, 23 Jul	09:00, 23 Jul
	12:00, 23 Jul	15:00, 23 Jul	03:00, 24 Jul	16:00, 24 Jul	21:00, 24 Jul
	03:00, 25 Jul	12:00, 26 Jul	21:00, 26 Jul	09:00, 27 Jul	12:00, 27 Jul
	21:00, 27 Jul	12:00, 28 Jul	15:00, 28 Jul	12:00, 29 Jul	14:00, 29 Jul
	16:00, 29 Jul	18:00, 29 Jul	21:00, 30 Jul	09:00, 1 Aug	15:00, 2 Aug
	18:00, 2 Aug	12:00, 3 Aug	18:00, 3 Aug	12:00, 4 Aug	16:00, 4 Aug
	00:00, 5 Aug	09:00, 5 Aug	12:00, 5 Aug	**10:00**, **6 Aug**	**12:00**, **6 Aug**
	14:00, **6 Aug**	**16:00**, **6 Aug**	**18:00**, **6 Aug**	**21:00**, **6 Aug**	12:00, 7 Aug
	15:00, 8 Aug	09:00, 10 Aug	18:00, 10 Aug		
UC	15:00, 13 Jul	**18:00**, **13 Jul**	12:00, 18 Jul	15:45, 18 Jul	15:00, 20 Jul
	21:00, 20 Jul	13:30, 21 Jul	22:00, 21 Jul	23:00, 21 Jul	12:00, 24 Jul
	15:00, 27 Jul	9:00, 30 Jul	15:00, 30 Jul	15:00, 31 Jul	21:00, 31 Jul
	12:00, 1 Aug	18:00, 1 Aug	18:00, 4 Aug	22:00, 4 Aug	15:00, 5 Aug
	18:00, 5 Aug	20:00, 5 Aug	22:00, 5 Aug	15:00, 7 Aug	18:00, 8 Aug
SL	03:00, 12 Jul	03:00, 13 Jul	21:00, 13 Jul	03:00, 14 Jul	09:00, 14 Jul
	16:00, 14 Jul	03:00, 18 Jul	03:00, 19 Jul	04:00, 22 Jul	05:00, 22 Jul
	06:00, 22 Jul	21:00, 25 Jul	03:00, 26 Jul	09:00, 26 Jul	03:00, 27 Jul
	21:00, 28 Jul	22:00, 28 Jul	00:00, 29 Jul	02:00, 29 Jul	06:00, 29 Jul
	08:00, 29 Jul	03:00, 1 Aug	03:00, 2 Aug	11:00, 4 Aug	14:00, 4 Aug
	06:00, **6 Aug**	**08:00**, **6 Aug**	**03:00, 7 Aug**	21:00, 8 Aug	

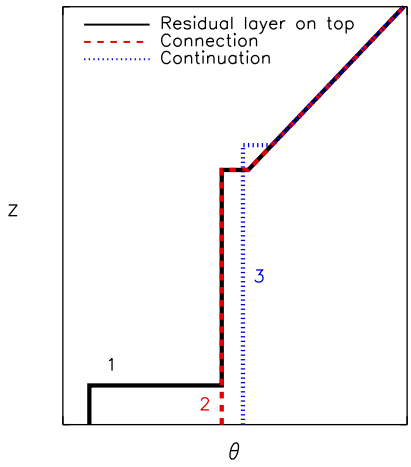

*Figure 2.2: Vertical potential temperature profiles during a transition from a mixed boundary layer topped with a residual boundary layer to a combined ABL. Initially **(1)** a shallow boundary layer develops under the influence of surface heat fluxes. When the potential temperatures in this layer and in the residual layer are equal, both layers connect **(2)**. After both layers are connected, the combined ABL further develops as usual **(3)**.*

is equal in both layers. When this happens, buoyant thermals that originate at the surface enter the residual layer without passing through a stable atmospheric layer, a process called overshooting. It results in an almost instantaneous mixing of the new boundary layer with the air masses in the residual layer. From that moment on, mixed layer theory can be applied to study the evolution of the combined ABL. This process of connecting a shallow boundary layer with a residual layer is depicted in Fig. 2.2. Its impact will be analysed in more detail in Sect. 2.3.4, putting special emphasis on the evolution of the concentrations of the chemical species NO_2 and O_3.

An overview of the occurrence of all three boundary layer prototypes during HUMPPA-COPEC-2010 is given in Table 2.2. Note that the radiosonde profiles in Fig. 2.1 are selected based on their unambiguous structure. In general, due to the instantaneous measurements, deviations of the radiosonde profile compared to the domain averaged profile occur, caused by different atmospheric processes. One of these, which is often overlooked, is the influence of land surface heterogeneity on the distribution of temperature, moisture and chemical species. To show that these deviations are realistic, Fig. 2.3 presents local instantaneous potential temperature profiles as generated by DALES. This simulation is based on the period between 12:00 and 15:00 LT of the MXL case that is treated in more detail in Sect. 2.3.2. The resolution of the domain is 50 m in the horizontal direction and 20 m in the vertical direction. The

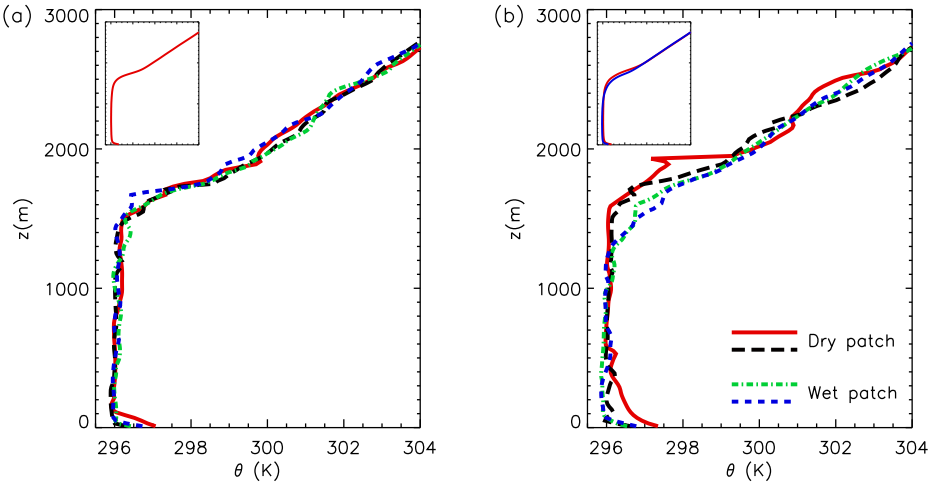

Figure 2.3: Instantaneous and local potential temperature profiles as generated by DALES after 3 h of simulation. ***(a)*** *shows 4 profiles at different locations, while its inset shows the instantaneous horizontal average over the total domain. In* ***(b)****, 2 instantaneous profiles are displayed for the dry patch and 2 profiles for the wet patch. Its inset presents the horizontal averages over the dry and wet patch separately.*

numerical grid spans $256 \times 256 \times 175$ cells in, respectively the x, y and z directions, resulting in a domain of 12.8 km $\times$ 12.8 km $\times$ 3.5 km. Constant surface heat and moisture fluxes are imposed for 3 h after which the local instantaneous profiles are generated. The kinematic surface heat flux and moisture flux are 0.24 K m s^{-1} and 0.087 g kg^{-1} m s^{-1}, corresponding to a sensible and latent heat flux of 295 W m^{-2} and 262 W m^{-2}, respectively. In case of heterogeneous surface forcings, the domain is split into two patches in the x-direction, the *dry* and the *wet* patch. The kinematic surface heat flux is increased (decreased) by 0.04 K m s^{-1} and the kinematic surface moisture flux is decreased (increased) by 0.017 g kg^{-1} m s^{-1} for the *dry* (*wet*) patch. It appears from Fig. 2.3a that for the homogeneous surface forcings, even though the domain averaged profile is smooth (inset), the individual profiles slightly differ from each other and show more random behaviour due to the turbulent character of the ABL, i.e. local warm and cold parcels of air. As demonstrated by the blue dashed line, this can result in observed boundary layer heights that differ from the domain average. Figure 2.3b shows that the differences between local instantaneous profiles are enhanced for heterogeneous surface forcings, especially over the patch with the higher sensible heat flux. This is due to the generated mesoscale circulations (Ouwersloot et al., 2011) in the ABL. These local differences should be kept in mind during the analysis of the radiosonde profiles.

2.3.2 Diurnal evolution of the ABL

To describe the boundary layer dynamics in greater depth, a specific day is selected, characterized by a boundary layer of the mixed layer type. The chosen day, 6 August 2010, was scheduled as an IOP, so multiple radio soundings were performed at relatively short time intervals (every 2 h) during the day. The profiles of θ and q show clear mixed layer prototype behaviour (Fig. 2.1a) for these soundings, enabling the analysis of the data using the MXL model. Most instruments for chemical observations were functioning and the weather conditions were typical. Therefore, chemical data is available for this day under conditions that are representative for the campaign. Closely related to our research questions, additional dynamical processes, which are often disregarded, are also important in interpreting atmospheric chemistry. These processes include advection of air masses, subsidence and the coupling of a dynamically evolving boundary layer with a residual layer aloft during the morning transition. The advection and subsidence are both related to forcings on the meso- and synoptic scale. Note that under typical conditions for which subsidence occurs (high pressure and temperature), the emissions of primary biogenic compounds are usually larger (e.g., Guenther et al., 2006; Yassaa et al., 2012). The advection is assumed to have an equal impact on both the boundary layer and the free troposphere.

Figure 2.4 shows the time evolution of the boundary layer dynamics as observed by the radiosondes. The vertical profiles of potential temperature and specific humidity are displayed in Fig. 2.4a and b, respectively. For clarity, only four profiles (at 06:00, 10:00, 14:00 and 18:00 LT) are presented out of the eight available ones (at 06:00, 08:00, 10:00, 12:00, 14:00, 16:00, 18:00 and 21:00 LT). We omit the radiosonde profiles near the surface (until 100–300 m) due to the poor reception of the sonde data by the antenna of the ground station if the sonde is near the surface. At higher altitudes, the signal is less perturbed and data is received regularly. In Fig. 2.4c, the evolution of the boundary layer height is presented. Boundary layer heights are denoted by asterisks, while the top of the residual layer (in the morning) is denoted by circles.

To initialize the MXL model, the vertical profiles of the potential temperature and specific humidity for an initial point in time are applied. For this study, the residual layer in the observations at 08:00 LT is chosen as an initial profile. Since the residual layer is much deeper than the underlying shallow mixed layer (975 m and 150 m, respectively) and both layers connect and mix within the first hours of the day (between 08:00 and 10:00 LT), considering the residual layer as a start of a new mixed layer seems a valid approximation.

The radiosonde observations are also used to derive the effects of large scale subsidence (descending air) and advection. These effects can not be observed directly, but by using the radiosonde observations as a reference for the predicted evolution of the ABL dynamics, one can obtain a first order estimation. To determine the subsidence velocity, the observed growth

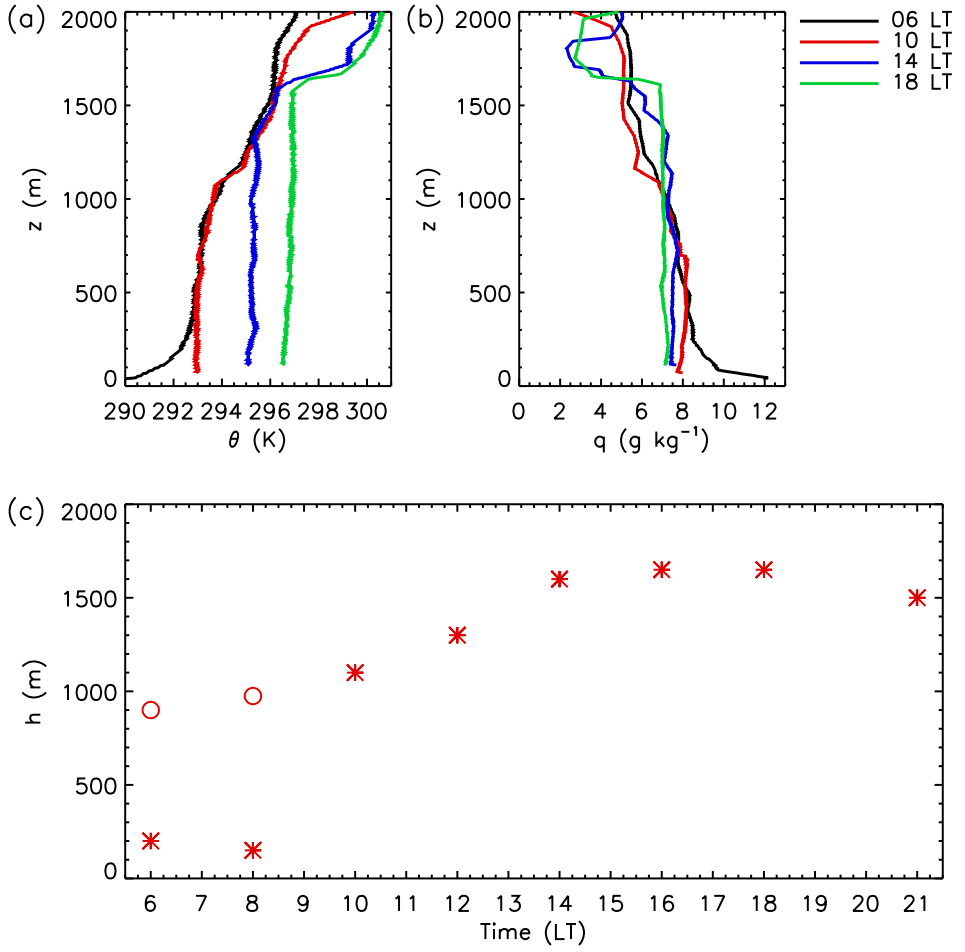

*Figure 2.4: Evolution of the vertical profiles of **(a)** the potential temperature and **(b)** specific humidity as measured by radiosondes on 6 August 2010 (06:00, 10:00, 14:00 and 18:00 LT). In **(c)** the evolution of the boundary layer height is presented, derived from all vertical profiles observed during that day. Asterisks indicate the height of the boundary layer, while circles represent the height of the residual layer in the morning. The shallow boundary layer connects with the residual layer between 08:00 and 10:00 LT.*

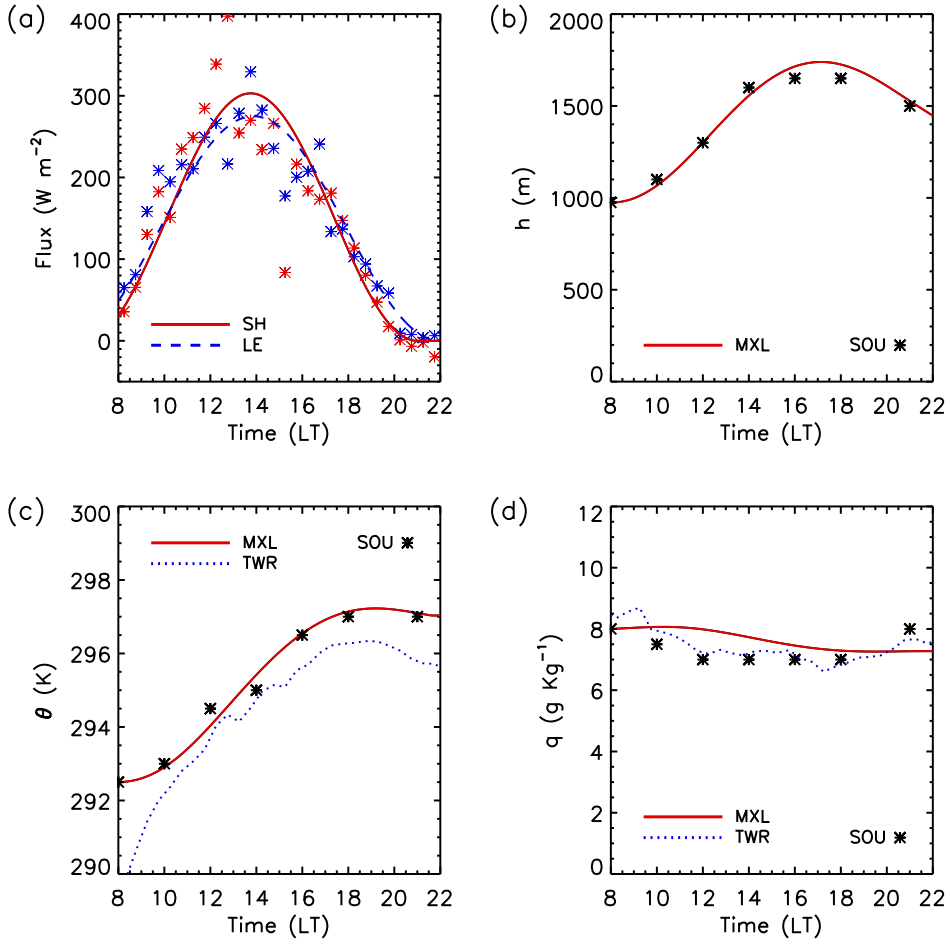

*Figure 2.5: Applied surface forcings **(a)** and simulated evolution of ABL characteristics **(b, c, d)** by the MXL model. The ABL characteristics include the boundary layer height **(b)**, potential temperature **(c)** and specific humidity **(d)**. In **(a)**, the lines represent the sensible heat flux, SH, and latent heat flux, LE, surface forcings applied to the model and the asterisks represent the corresponding observations from the tower. In **(b, c, d)**, solid red lines depict model results and the asterisks symbolize radiosonde observations. Tower observations (TWR) are expressed by dotted blue lines.*

Table 2.3: Overview of the prescribed initial and boundary conditions. Presented are the initial values (subscript 0) for h, θ and q, the initial differences between the free troposphere and boundary layer (additional prefix Δ) and the free tropospheric gradients (denoted by γ) for θ and q, the surface fluxes (subsript s), the large scale divergence, Div_U, and the advection of heat, Adv_θ, and moisture, Adv_q, for the MXL model. The time, t, is expressed in hours local daylight saving time. $\rho = 1.2$ kg m^{-3}, $c_p = 1.0 \times 10^3$ J kg^{-1} K^{-1} *and* $L_v = 2.5 \times 10^6$ J kg^{-1}. *The MXL model is run for 14 h.*

Property	Value
t_0 (h)	8
h_0 (m)	975
Div_U (s^{-1})	1.5×10^{-5}
$\langle\theta\rangle_0$ (K)	292.5
$\Delta\theta_0$ (K)	0.5
γ_θ (K m^{-1})	4.7×10^{-3}
Adv_θ (K s^{-1})	-3×10^{-5}
q_0 (g kg^{-1})	8
Δq_0 (g kg^{-1})	–0.5
γ_q (g kg^{-1} m^{-1})	-2.7×10^{-3}
Adv_q (g kg^{-1} s^{-1})	0
$\rho\, c_p\, \overline{w'\theta'}_s$ (W m^{-2})	$310\left(\frac{1}{2} - \frac{1}{2}\cos\left(2\pi\frac{t-6.5}{14.5}\right)\right)$
$\rho\, L_v\, \overline{w'q'}_s$ (W m^{-2})	$275\left(\frac{1}{2} - \frac{1}{2}\cos\left(2\pi\frac{t-5.75}{16.25}\right)\right)$

of the boundary layer height is compared to the modelled evolution velocity due to entrainment. The subsidence velocity is calculated as the difference between these two velocities, as expressed by Eq. (A4). To derive the contribution of the horizontal advection of air masses we take a different approach. The horizontal advection of air, with different dynamical and/or chemical properties, results in an increase or decrease in the mixed layer averaged scalars. In our model this rate of change is considered to be constant in time. Therefore, a difference between the observed and modelled scalar values that increases linearly in time is considered to be caused by advection. For the case study we find that the advection of cooler air is of importance for temperature (with a cooling rate of 0.108 K h^{-1} resulting in a maximum difference of 1.5 K), whereas there is no significant contribution of advection to humidity. This approach cannot be directly applied to the advection of chemical species, since the free tropospheric concentrations are unknown. In addition, differences can be caused by unaccounted chemical pathways.

The prescribed sensible and latent heat fluxes in the MXL model are determined by fitting sinusoids through the observed fluxes, as shown in Fig. 2.5a. The complete set of initial conditions and forcings is presented in Table 2.3. In Fig. 2.5b–d, the simulated evolutions of the main dynamical ABL characteristics are shown together with the observations. This

Table 2.4: Overview of the prescribed initial mixing ratios (ppbv) and the emissions at the surface (mg m^{-2} h^{-1}) of the reactive species for Sect. 2.3.3 for both boreal and Amazonian chemical conditions. Not listed are the values for species without emissions and zero initial mixing ratio and the values for O_2 and N_2. These latter two species have constant mixing ratios of 2×10^8 and 8×10^8 ppbv, respectively. For the emissions, the functions $f_1 = \left(\frac{1}{2} - \frac{1}{2}\cos\left(2\pi\frac{t-4}{18}\right)\right)$ and $f_2 = \sin\left(2\pi\frac{t-4}{18}\right)$ can be used with t in hours local daylight saving time. The conversion factors for the NO and C_5H_8 emissions from ppbv m s^{-1} to mg m^{-2} h^{-1} are 4.4 and 10, respectively.

	O_3	NO	NO_2	CH_4	CH_2O	MVK	C_5H_8	CO	H_2O_2
Boreal chemical conditions									
Initial mixing ratio	24.5	0.07	0.224	1759	0.171	0.0877	0.17	101.95	0.0266
Prescribed emission	0	$1.76 \times 10^{-2}\, f_1$	0	0	0	0	$0.1\, f_2$	0	0
Amazonian chemical conditions									
Initial mixing ratio	10	0	1	1724	0	1.3	2	124	0
Prescribed emission	0	2.2×10^{-3}	0	0	0	0	6.5	0	0

shows that the model reproduces the radiosonde observations for temperature, moisture and boundary layer heights well. Until approximately 17:00 LT, entrainment most strongly influences the ABL height development, resulting in a deepening ABL. When the boundary layer reaches its maximum height of 1740 m, the subsidence velocity for that height is equal in magnitude as the entrainment velocity. By that time the entrainment process is still very active, as the driving heat fluxes are still greater than 50 % of their maximum values. Since the surface sensible and latent heat fluxes continuously decrease after 14:00 LT, the entrainment fluxes weaken as well. Consequently, after 17:00 LT the subsidence becomes stronger than the rate of the boundary layer growth by entrainment and the ABL height decreases with time. This can be seen in Fig. 2.5b. The potential temperature, shown in Fig. 2.5c, increases with time due to surface fluxes and the related entrainment of relatively warm air from the free troposphere. After sunset, the surface buoyancy flux becomes negligible and, as a result, the convective boundary layer type (Fig. 2.1a) is not longer applicable. A stable boundary layer appears with a residual layer aloft (Fig. 2.1c). During the whole day, the advection of relatively cool air results in a decrease of the potential temperature. After 18:00 LT this effect is stronger than the heating effect of the surface fluxes and entrainment, explaining the temperature decline. As shown by the time evolution in Fig. 2.5d, the specific humidity remains approximately constant, since the effects of the surface moisture flux and the entrainment of relatively dry air cancel each other ($\frac{\partial \langle q \rangle}{\partial t} \approx 0$).

To determine the importance of advection and subsidence, four different cases have been simulated. The three cases other than the previously derived standard MXL case differ by having the subsidence and/or advection disabled. We omit the effect of subsidence by set-

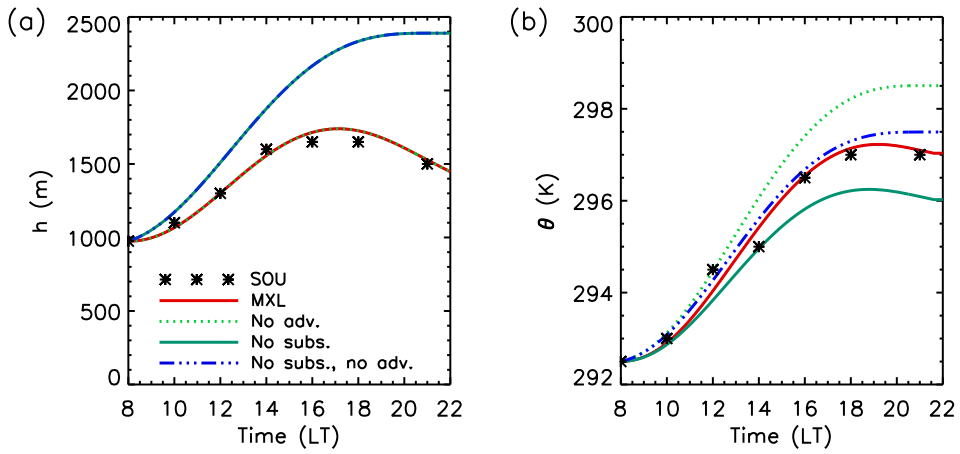

*Figure 2.6: Different evolutions of **(a)** the ABL height and **(b)** the potential temperature predicted by the MXL model. Subsidence and advection are separately enabled and disabled for the different numerical experiments, resulting in four cases. The results are compared to radiosonde observations, SOU. The most accurate case, with advection and subsidence enabled, is labelled MXL. Note that the advection does not significantly affect the boundary layer height evolution. Therefore, the curves are superposed in **(a)** for the cases with and without prescribed advection.*

ting $\mathrm{Div}_U = 0\ \mathrm{s}^{-1}$ and the horizontal advection of air with a different temperature by setting $\mathrm{Adv}_\theta = 0\ \mathrm{K\,s}^{-1}$ (Appendix 2A). First we discuss the impact of subsidence. From Fig. 2.6a we find that subsidence is significant for the boundary layer height development on 6 August 2010. In the cases without subsidence the boundary layer grows like a standard convectively mixed boundary layer until approximately 20:00 LT. Subsequently, the surface heat flux does not remain positive and the growth stops. Since this layer is no longer actively mixed, it remains as a residual layer on top of the stable nocturnal boundary layer. When subsidence occurs, the boundary layer growth slows down, resulting in lower ABL heights. As mentioned earlier, after 18:00 LT the boundary layer height decreases as the subsidence is stronger than the ABL height increase due to entrainment and the ABL becomes shallower. The rate of boundary layer height decrease reaches its maximum when entrainment ceases. The subsidence does not influence the incoming heat fluxes, but does result in shallower boundary layers. Therefore, subsidence promotes a warmer ABL. This is discernible in Fig. 2.6b.

Figure 2.6a shows that the advection of relatively cold air from other regions does not affect the boundary layer height evolution. The reason is that the advection is assumed to be equal in the free troposphere and the boundary layer, hence the strength of the thermal in-

version remains virtually unaltered. The difference in potential temperature due to advection increases linearly in time up to 1.5 K after the 14 h of simulated time, as depicted in Fig. 2.6b. During the day, the impacts of advection and subsidence on the potential temperature roughly cancel in the case under study. Therefore, if both effects are ignored, the resulting potential temperature evolution is similar to that when both effects are concurrently considered. Our results indicate that the effects of both subsidence and horizontal advection are important to take into account.

2.3.3 Importance of the ABL height representation for atmospheric chemistry

After determining the evolution of the ABL dynamics, we study how it influences the mixing ratios of reactive species. Here we focus on the importance of a correct representation of the boundary layer height. Note that we solely study the primary effect of the boundary layer height evolution on the mixing ratio of chemical species, i.e. the ratios between surface exchange and mixing height (first term on the r.h.s. of Eq. 2A.1). To prevent biases due to a combination of dilution and entrainment (e.g., Vilà-Guerau de Arellano et al., 2011), the initial mixing ratios are set equal in the boundary layer and the free troposphere. Two atmospheric chemistry cases are evaluated to show the impacts of the ABL dynamics and surface emissions depending on the region under study. For the first case the initial conditions and surface forcings are based on boreal conditions, while a second case, with a higher isoprene emission and initial mixing ratio, is formulated to contrast the boreal forest to the tropical Amazon rainforest chemical conditions. Especially the initial mixing ratios can significantly affect the chemistry. The initial mixing ratios, in ppbv, and the emissions at the surface, in mg m^{-2} h^{-1}, are set to 0, except for the values listed in Table 2.4.

We designed three different numerical experiments: a "*realistic*" case, a *constant* case and a case that considers the residual layer part of the free troposphere (by *ignoring the residual layer*). The three corresponding boundary layer height evolutions are shown in Fig. 2.7a. The first case corresponds with that described in the previous section, though complemented by the chemistry calculations. Thus the boundary layer height evolution is equal to the one presented above, which represents the observations. The second case represents a boundary layer with a constant height, mimicking the performance of chemical box models. For the third case, the initial profile is taken from the radiosonde at 08:00 LT, but the difference between the residual layer and the free troposphere aloft is ignored. Therefore, this layer is considered to be part of the free troposphere only and the prescribed initial mixed layer conditions and the free tropospheric gradients both change. The effect of subsidence is not considered for this situation. The altered settings for this case are listed in Table 2.5.

In Fig. 2.7b the resulting evolutions of the hydroxyl radical (OH) mixing ratio are presen-

Table 2.5: Overview of the altered initial and boundary conditions for the case in which the residual layer is ignored compared to the standard case in Table 2.3. Listed are initial values (subscript 0), free tropospheric gradients, γ, and the large scale velocity divergence, Div_U.

Property	Value
h_0 (m)	100
Div_U (s^{-1})	0
$\langle\theta\rangle_0$ (K)	290
$\Delta\theta_0$ (K)	1
γ_θ ($\mathrm{K\,m}^{-1}$)	6.3×10^{-3}
q_0 ($\mathrm{g\,kg}^{-1}$)	9
Δq_0 ($\mathrm{g\,kg}^{-1}$)	0
γ_q ($\mathrm{g\,kg}^{-1}\,\mathrm{m}^{-1}$)	-2.2×10^{-3}

Table 2.6: The prescribed initial values (subscript 0) and free tropospheric gradients, γ, for three different numerical experiments with the MXL model. The initial time, t_0, is expressed in hours local daylight saving time and the runtime of the model is expressed by t_{run} in hours.

Property	Standard run	Lower layer	Connected layers
t_0 (h)	8	8	9.5
t_{run} (h)	14	1.5	12.5
h_0 (m)	975	150	1027
$\langle\theta\rangle_0$ (K)	292.5	290.0	292.73
$\Delta\theta_0$ (K)	0.5	2.0	0.73
γ_θ ($\mathrm{K\,m}^{-1}$)	4.7×10^{-3}	1.5×10^{-3}	4.7×10^{-3}
q_0 ($\mathrm{g\,kg}^{-1}$)	8	9	8.06
Δq_0 ($\mathrm{g\,kg}^{-1}$)	-0.5	0	-0.91
γ_q ($\mathrm{g\,kg}^{-1}\,\mathrm{m}^{-1}$)	-2.7×10^{-3}	-2.2×10^{-3}	-2.7×10^{-3}

ted for the boreal conditions. Since the emissions of isoprene (C_5H_8) are relatively low, and its background concentration is negligible, the depletion of OH is governed by other chemical species (especially CO). As we prescribe uniform initial profiles in the ABL and the free troposphere and neglect surface exchanges for these other chemical species, the resulting time evolutions of OH are very similar. As presented in Fig. 2.7c, it becomes different for our case with Amazonian conditions. In this case, the initial concentration and the emission of isoprene are higher and the depletion of OH due to isoprene is significant. During the first six hours of simulated time, if the emitted isoprene is distributed over a smaller mixing volume, the isoprene concentrations become higher and, consequently, the depletion of OH is enhanced. The *constant* boundary layer height case, which has the larger mixing volume, therefore starts with the highest OH concentration. The ABL height and OH mixing ratio are

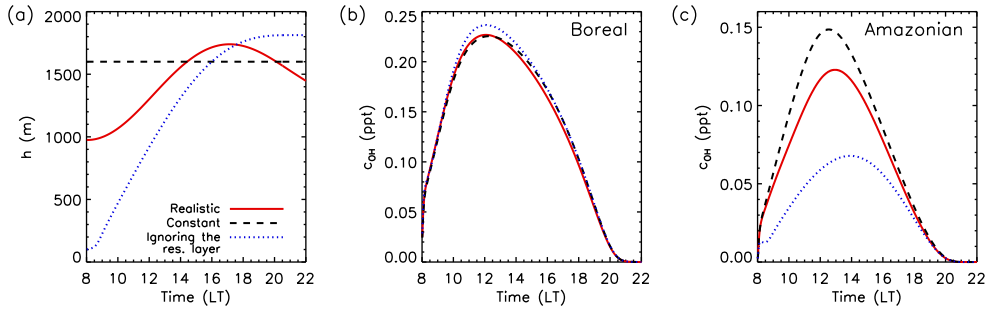

*Figure 2.7: Impact of **(a)** the ABL height development on **(b, c)** the mixing ratio of OH. Panels **(b)** and **(c)** present the results for initial chemical conditions and surface exchanges typical for boreal (as in HUMPPA-COPEC-2010) and Amazonian (**Ouwersloot et al., 2011**) conditions, respectively. Three cases are presented: (1) the boundary layer height as determined by the MXL model for 6 August 2010, (2) a constant boundary layer height and (3) a boundary layer height as determined by the MXL model if the residual layer would be considered as part of the free troposphere.*

lowest for the case that ignores the residual layer. Due to the additionally produced secondary reactants (e.g. through RO_2) this effect remains even after the boundary layers reach the same height for two cases. Because of this non-linear effect, the OH mixing ratio remains highest in the case with the constant boundary layer height and lowest in the case where the influence of the residual layer is ignored. Our findings show that for an adequate model representation of atmospheric chemistry in the boundary layer, it is important to represent the boundary layer height evolution throughout the day. This holds especially for cases in which emitted chemical compounds significantly affect the chemical conditions. Note that the differences in OH between different boundary layer height representations can be over a factor 2, which is similar to the differences seen between observed and modelled OH (Butler et al., 2008). In previous work, changes in chemical mechanisms were proposed to help explain these differences (Lelieveld et al., 2008).

2.3.4 Representation of the morning transition

As discussed in Sect. 2.3.1, in the early morning a residual mixed layer from the previous day is frequently observed above the stable boundary layer and the shallow boundary layer that follows when convection starts. Due to the initially weak surface heat fluxes, the potential temperature in the shallow boundary layer increases until it is similar to the residual mixed layer (in our case around 09:30 LT). Then both layers merge and become one mixed boundary layer, as illustrated in Fig. 2.2. In the MXL model this merging of two atmospheric layers

into one is instantaneous. However, in reality it can take some time due to inhomogeneous ABL conditions and the time it takes for thermals to rise from the surface to the top of the residual layer. In this section we will show that this process can explain specific patterns in the chemistry observations during the morning transition. Note that these numerical experiments do not aim for a perfect representation of the boreal atmospheric chemistry, for example by not accounting for dry deposition (Ganzeveld et al., 2002), though demonstrate that this merger of two atmospheric layers is an important process that may explain certain features in the observations of chemical species in the morning.

Three numerical experiments were designed. The first, the *standard* case, corresponds to that previously defined in Sect. 2.3.2, except for the chemical conditions. This case assumes the residual layer to be part of the mixed layer. The second experiment, the *lower layer*, is based on the initial shallow boundary layer. This corresponds to situation (1) in Fig. 2.2. The initial values for potential temperature, specific humidity and ABL height are again obtained from the radiosonde observation of 08:00 LT. This numerical experiment is run for 1.5 h. After that the buoyant thermals that originate from the shallow boundary layer enter the residual layer and the two layers mix almost instantaneously, resulting in situation (2) in Fig. 2.2. The third numerical experiment represents the ensuing combined mixed layer. This case is referred to as *connected layers* and is labelled situation (3) in Fig. 2.2. The dynamical settings that differ per numerical experiment are listed in Table 2.6 for all three cases. Dynamical settings not mentioned explicitly are equal to the case prescribed in Sect. 2.3.2 and Table 2.3. The prescribed emissions and initial mixing ratios, presented in Table 2.7 if non-zero, are chosen such that the observations of the isoprene, NO, NO_2 and O_3 mixing ratios are reproduced.

The observed and modelled mixing ratios of NO_2 and O_3 are presented in Fig. 2.8a and b, respectively. The time evolution of NO (not shown) has similar features as that of NO_2. The observations show that in the early morning (until 9:30 LT) the NO_2 mixing ratio rises quickly. This is due to the emission of NO_x into the shallow boundary layer. Subsequently, the two atmospheric layers merge. Since the air in the residual layer has lower mixing ratios of NO and NO_2, the mixing ratios in the combined mixed layer are lower than the mixing ratios in the previous shallow boundary layer. Because in reality the conditions of the ABL are not fully horizontally homogeneous, this mixing does not occur simultaneously everywhere, resulting in a transition that takes approximately one hour. After the mixing of the two layers, the NO_x contributions of emission and entrainment are still positive, but are distributed over a larger mixing volume. Therefore, their impact becomes weaker and, due to chemical destruction by OH, the NO_2 mixing ratio slightly decreases with time. The morning peak in NO_2 can not be reproduced by the MXL model if only one numerical experiment is performed. However, by combining two numerical experiments, one for the shallow boundary layer and one for the final combined mixed layer, this peak can be reproduced and explained.

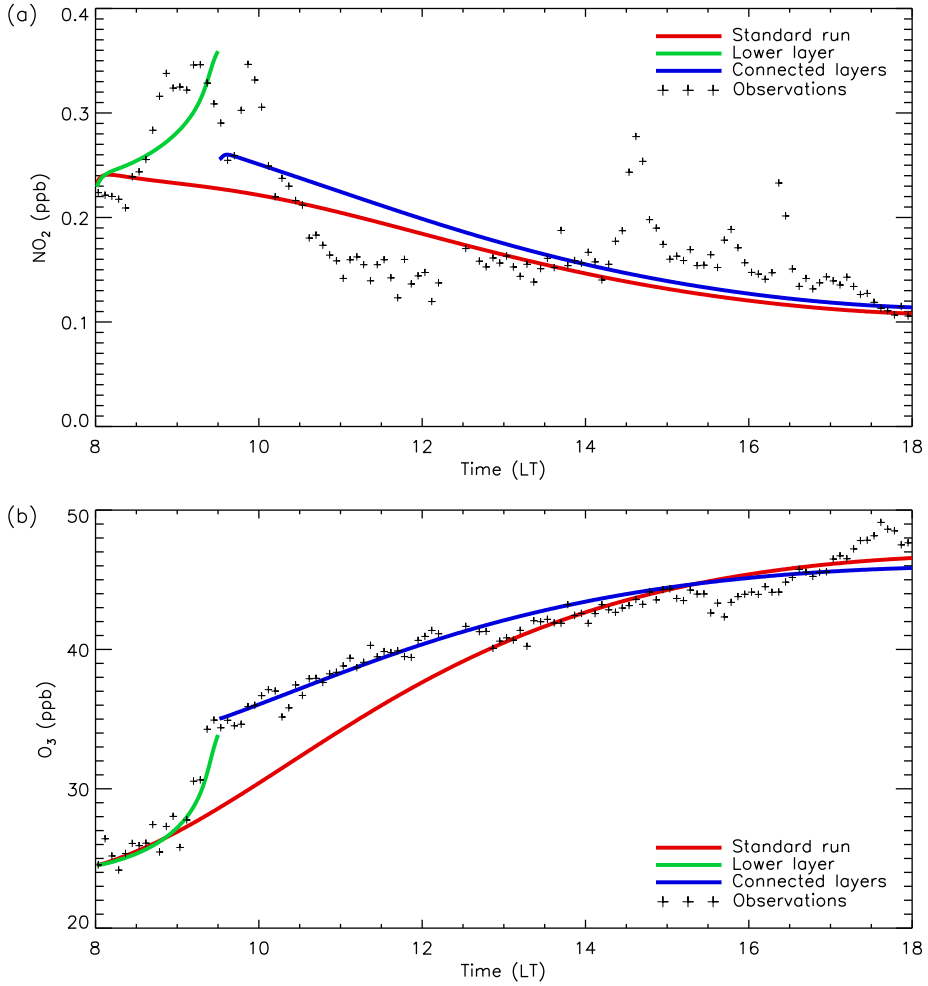

Figure 2.8: Comparison between the observations and MXL model results for the ***(a)*** NO_2 *and* ***(b)*** O_3 *mixing ratios during 6 August 2010. The numerical experiments are the standard case, the case for the lower shallow boundary layer until 09:30 LT and the case where a residual layer and the lower shallow boundary layer are connected and become one mixed layer from 09:30 LT onward. The latter two cases correspond to situation* ***(1)*** *and situation* ***(3)*** *in Fig. 2.2, respectively.*

Table 2.7: The prescribed initial mixing ratios (ppbv) and the emissions at the surface ($\mathrm{mg\,m^{-2}\,h^{-1}}$*) of the reactive species for the numerical experiments discussed in Sect. 2.3.4. The conversion factors for the NO and* C_5H_8 *emissions from* $\mathrm{ppbv\,m\,s^{-1}}$ *to* $\mathrm{mg\,m^{-2}\,h^{-1}}$ *are 4.4 and 10, respectively. The initial conditions are listed for the boundary layer, BL, and the atmospheric layer aloft, TOP. Maximum emissions are denoted by EM and emission patterns by PAT. COS corresponds to an emission of* $EM\left(\frac{1}{2} - \frac{1}{2}\cos\left(2\pi\frac{t-4}{18}\right)\right)$ *and SIN to an emission of* $EM\sin\left(2\pi\frac{t-4}{18}\right)$*. Not listed are the values for species without emissions and zero initial mixing ratio and those for* CH_4*,* O_2 *and* N_2*. These latter three species have constant mixing ratios of 1759,* 2×10^8 *and* 8×10^8 ppbv*, respectively.*

	O_3	NO	NO_2	CH_2O	MVK	C_5H_8	CO	H_2O_2
Standard run								
BL:	24.5	0.07	0.224	0.171	0.0877	0.170	101.95	0.0266
TOP:	52.0	0.10	0.500	0.000	0.0000	0.000	101.95	0.0000
EM:	0.0	1.76×10^{-2}	0.0	0.0	0.0	0.1	0.0	0.0
PAT:	–	COS	–	–	–	SIN	–	–
Lower layer								
BL:	24.5	0.07	0.224	0.171	0.0877	0.170	101.95	0.0266
TOP:	38.0	0.19	0.500	0.000	0.0000	0.000	101.95	0.0000
EM:	0.0	1.76×10^{-2}	0.0	0.0	0.0	0.1	0.0	0.0
PAT:	–	COS	–	–	–	SIN	–	–
Connected layers								
BL:	35.0	0.07	0.26	0.645	0.0765	0.176	101.95	0.0841
TOP:	47.0	0.10	0.42	0.000	0.0000	0.000	101.95	0.0000
EM:	0.0	1.76×10^{-2}	0.0	0.0	0.0	0.1	0.0	0.0
PAT:	–	COS	–	–	–	SIN	–	–

It is worthwhile to note that the longer the separation between shallow boundary layer and residual layer remains present, the stronger this morning peak is. Additionally, due to storage in the canopy under a stable boundary layer, NO_x could accumulate near the surface during the night. When turbulence sets in, the canopy and ABL air masses interact, which could cause pulses in the surface exchange in the early morning (Ganzeveld et al., 2002).

The O_3 mixing ratio in Fig. 2.8b does not show a sudden decrease or increase. However, it is apparent that the time evolution changes after the morning transition from a shallow to a merged boundary layer. The increase in O_3 over time is not driven by surface exchange but mainly by entrainment. In this case chemistry has a smaller impact on the evolution of O_3. In the shallow boundary layer the O_3 mixing ratio is lower than in the residual layer. Therefore, entrainment causes the mixing ratio to rise in the growing shallow boundary layer. During the transition both layers are combined into one mixed layer. The rate of change of O_3 in this merged boundary layer is altered due to two reasons: the mixing ratio in the atmospheric layer above the original residual layer is different and the entrained air is mixed over a larger

mixing volume after the combination. In effect this results in a slower increase of the O_3 mixing ratio. Note that the assumption of one well-mixed boundary layer from the start enables us to get a reasonable first approximation of the mixing ratio evolution. However, the representation in the morning is off and the differences in the rate of change of O_3 before and after 09:30 LT can not be explained. By using the first order approximation to consider in succession the *lower layer* and *connected layers* cases, the time evolution of O_3 can be explained and reproduced.

Our findings show that by using a relatively basic modelling tool, the mixed layer model, and using a first order approximation for the combining of a shallow boundary layer with a residual layer aloft, important features in the morning observations of chemical species can be reproduced and explained. We therefore conclude that the interpretation of atmospheric chemistry observations using a numerical model requires that dynamical processes are accounted for, including the boundary layer height evolution and the connection to a residual layer. This supports previous budget studies using the MXL model (Vilà-Guerau de Arellano et al., 2011; van Stratum et al., 2012) and a single column model (e.g., Ganzeveld et al., 2008).

2.4 Reflection on the observational strategy during HUMPPA-COPEC-2010

In this section, we extend the previous analysis to formulate recommendations for the observational strategy during campaigns such as HUMPPA-COPEC-2010. The experience during the HUMPPA-COPEC-2010 campaign enables us to improve the strategy for future campaigns, resulting in an even more comprehensive set of atmospheric data.

As presented in Fig. 2.3, local observations can result in variations of the measured scalars under the influence of the boundary layer dynamics. For the potential temperature, the largest variations occur in the surface layer and near the inversion layer. The variability of the scalars is even enhanced by heterogeneous surface forcings (Ouwersloot et al., 2011). Thus, we conclude that for representative observations of the boundary layer dynamics it would be recommendable to launch multiple radiosondes simultaneously at key moments (e.g., morning transition, noon and evening transition) to account for the influences of heterogeneous terrain and local, instantaneous observations. In addition, these multiple radiosondes would provide important information about the spatial variations in the dynamical variables, which could be used to evaluate results of numerical models, including large scale chemistry-transport models.

Furthermore, the lowest few hundred meters of the atmosphere are important to characterize in detail. Within a convective boundary layer a surface layer is present in which the

profiles of potential temperature, specific humidity and concentrations of chemical species can have significant vertical gradients. The nocturnal boundary layer, characterized by stable stratification, has a similar height as well. However, the observations during HUMPPA-COPEC-2010 did not suffice to fully characterize this part of the ABL. The observations at the towers are only performed at six fixed locations below 67 m and the radiosonde profiles near the surface are occasionally omitted due to limited transmission of the sonde data. To enable the characterization of the nocturnal boundary layer and the surface layer during the day, it is recommended to operate kytoons (tethered balloons) (Stull, 1988) with the relevant instruments for at least these lower areas. Due to the tether, no data will be lost and the speed of the ascend/descend during the profiling can be controlled.

As discussed in Sect. 2.3.2, another possible improvement to the employed observational strategy is to obtain information about large scale forcings, i.e. the subsidence velocity and horizontal advection of air masses. The information about subsidence could be estimated by comparing the boundary layer heights for subsequent observed profiles. This could be achieved by launching radiosondes within very short time intervals (maximum 1 h). After calculating the entrainment velocity from the observed inversion layer properties and surface heat fluxes (Eq. 2A.5), it can be subtracted from the observed ABL growth rate to determine the subsidence velocity (Eq. 2A.4). In combination with the horizontal wind direction and velocity, the advection can be calculated from the horizontal gradients of the different scalars (Eq. 2A.1). The influence of horizontal advection for potential temperature and specific humidity can therefore be determined by simultaneously launching at least 3 radiosondes around the observational site to obtain the horizontal distribution of these scalars. This approach has previously been applied to tower observations (e.g., Aubinet et al., 2003).

As presented in Fig. 2.4c, the observations during HUMPPA-COPEC-2010 enable a characterization of the development of ABL dynamics. However, for most days observations were limited to 5 radiosonde launches. During the intensive observation periods additional measurements were performed at relatively short time intervals, but even then continuous measurements are not available. A continuous representation of the ABL height would be relevant input for chemical box models as discussed in Sect. 2.3.3 and demonstrated in Fig. 2.7. Continuous observations could be obtained using a ceilometer, sodar (Nilsson et al., 2001), wind profiler (Bianco et al., 2011) or lidar (Gibert et al., 2007). This would also enable that the morning transition can be studied in greater detail, and more specifically the mixing of a shallow boundary layer with a residual layer aloft. Another advantage of continuous observations would be that fluctuations in the measurements due to local observations can be filtered by time averaging the data, according to Taylor's frozen turbulence hypothesis (Stull, 1988).

2.5 Conclusions

By combining observations, both near the surface and in the free troposphere, with a mixed layer model, we studied the atmospheric boundary layer dynamics as observed over the Finnish boreal forest during the HUMPPA-COPEC-2010 campaign. Particular emphasis is placed on the role of atmospheric dynamics at different scales on the boreal atmospheric chemistry. We investigated the influence of large scale forcings (subsidence and advection) and the transition from nocturnal to daytime turbulent conditions on the development of the ABL.

The meteorological data has been classified by identifying boundary layer prototypes based on the vertical potential temperature profiles. During the campaign three different types were observed: the stable boundary layer, the convectively mixed boundary layer and the conditionally unstable layer above a mixed layer. Of these three types, the convective boundary layer was observed most often, 78 out of the 132 classified soundings. Illustrated by Large-Eddy Simulation model results, we discuss how instantaneous observed profiles can deviate from these prototypes.

By selecting a single day, characterized by a convective boundary layer, 6 August 2010, we studied in detail the key dynamic contributions that influence atmospheric chemistry. This analysis could be applied to other cases observed during HUMPPA-COPEC-2010. It is shown that by using a relatively basic numerical model, the mixed layer model (MXL), the evolution of the boundary layer dynamics can be reproduced and explained. A residual mixed layer in the early morning and the effects of two different large scale forcings, subsidence and horizontal advection, have been shown to be important. During this day, the horizontal advection of cold air results in a decrease of the temperature at the measurement site. Subsidence inhibits the boundary layer growth, causing a lower boundary layer height and consequently, due to a smaller mixing volume and unaltered sensible and latent heat fluxes, higher temperatures. By accounting for both subsidence and cold air advection, the modelled evolution for temperature is shown to remain approximately equal, though the resulting atmospheric boundary layer height evolution was significantly reduced.

It is demonstrated that the representation of atmospheric chemistry with a numerical model requires accurate knowledge of the ABL height evolution. Due to the dependency of the chemical reaction rates on the concentrations of chemical species, knowledge about the initial (early morning) chemical conditions, the surface emissions/deposition and the boundary layer height at one specific point in time does not suffice to accurately predict the concentrations of chemical species at that point in time.

The morning transition from a shallow boundary layer, merging with a residual mixed layer aloft into a combined mixed boundary layer, has been represented by combining two numerical experiments with the mixed layer model. The results show that by using this

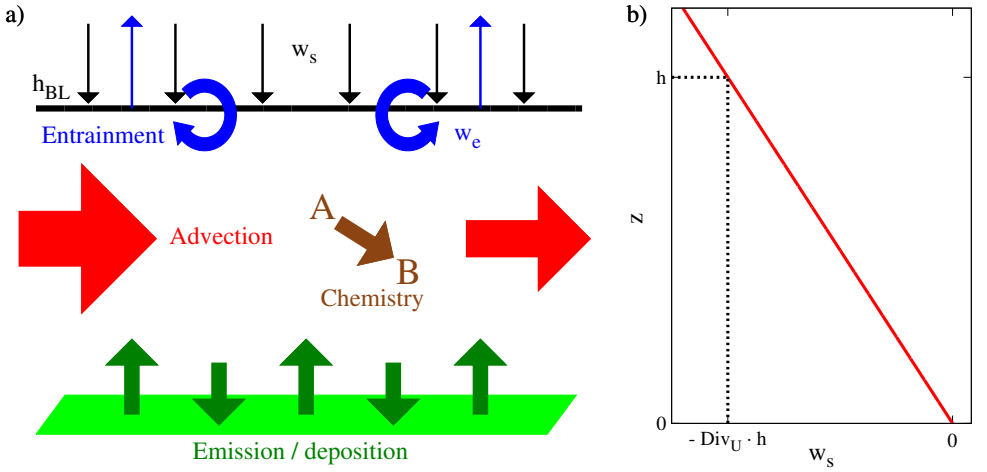

Figure 2A.1: ***(a)*** *Schematic overview of the different terms that affect the evolution of scalars and the boundary layer height. Shown are the emissions and deposition near the surface, advection, entrainment, additional sources and sinks (e.g. due to chemical conversion) and subsidence. The dependence of the subsidence velocity on height is presented in* ***(b)****.*

assumption, we are able to explain and represent an observed morning peak in the NO_x concentrations and the increase of O_3 concentrations with time.

By using the mixed layer model, several processes are identified that require attention during observational field campaigns if measured data is to be reproduced. We find that emphasis should be placed on continuous observations of the atmospheric boundary layer height, combined with model analyses. Using this combined information, the effects of mixing with the residual layer and the entrainment and dilution of chemical species can be evaluated. A continuous representation could be achieved by using radiosondes and (occasionally consecutive) simulations with a numerical model, although this method assumes a boundary layer that is characterized by the convective boundary layer prototype and requires knowledge of the large scale forcings. Therefore, we suggest the use of a ceilometer, sodar or lidar in future campaigns.

2A Appendix: Mixed layer equations

The prognostic equations are solved by the mixed layer model for multiple conserved scalar variables, S. These variables are the potential temperature, θ, specific humidity, q, and the mixing ratios of chemical species, c_{species}. θ and q influence the evolution of the ABL height. Since the ABL is well mixed during the day, the averages of the variables over

the whole boundary layer, $\langle S \rangle$, can be used for the evaluation. The difference between the value at the bottom of the free troposphere and the value in the boundary layer is symbolized by ΔS. The system of prognostic equations that solves $\langle S \rangle$ and ΔS is expressed by (Vilà-Guerau de Arellano et al., 2009):

$$\frac{\partial \langle S \rangle}{\partial t} = \frac{\overline{w'S'}_s}{h} - \frac{\overline{w'S'}_e}{h} - \left(U \frac{\partial \langle S \rangle}{\partial x} + V \frac{\partial \langle S \rangle}{\partial y} \right) + R_S, \tag{2A.1}$$

$$\frac{\partial \Delta S}{\partial t} = \gamma_S w_e - \frac{\partial \langle S \rangle}{\partial t}. \tag{2A.2}$$

An illustration of the different contributions to the boundary layer height development and to the prognostic equation for the boundary layer averaged scalars is presented in Fig. 2A.1. The different terms are explained in more detail below.

$\overline{w'S'}_s$ and $\overline{w'S'}_e$ are the surface and entrainment fluxes, respectively. The height of the mixed layer is h. U and V are the wind velocities in the x and y direction and the total term $-\left(U \frac{\partial \langle S \rangle}{\partial x} + V \frac{\partial \langle S \rangle}{\partial y}\right)$ is the advection of S, Adv_S. The advection is positive if it leads to an increase in S. R_S expresses additional sources or sinks for scalar S. In the case of a chemical species, R_S is equal to the chemical production minus the chemical destruction of that species, based on the applied chemical mechanism. The vertical gradient in the free troposphere is expressed by γ_S. The velocity at which free tropospheric air is entrained into the boundary layer is symbolized by w_e.

The surface fluxes are prescribed, though for the zeroth-order jump assumption the entrainment flux at the top of the mixed layer is expressed by

$$\overline{w'S'}_e = -w_e \Delta S. \tag{2A.3}$$

Next to the scalar variables, the boundary layer height evolution is included by applying

$$\frac{\partial h}{\partial t} = w_e + w_s. \tag{2A.4}$$

Here, w_s is the large scale vertical velocity. If it is negative, $-w_s$ is the subsidence velocity. It is related to the boundary layer height by $w_s = -\mathrm{Div}_U \, h$, where Div_U is the velocity divergence in s^{-1}. Note that this represents a linear profile with $w_s = 0$ at the surface, as presented in Fig. 2A.1b. The entrainment velocity is diagnosed by solving

$$w_e = -\frac{\overline{w'\theta'_v}_e}{\Delta \theta_v} \tag{2A.5}$$

together with the closure assumption that $\overline{w'\theta'_v}_e = -\beta \overline{w'\theta'_v}_s$, where usually $\beta = 0.2$, even though more precise and complicated parametrisations exist (e.g., Pino et al., 2003). The

virtual potential temperature, θ_v, that appears in this set of equations, is equal to

$$\theta_v = \theta\,(1 + 0.61q)\,, \tag{2A.6}$$

which results in

$$\overline{w'\theta'_v} \approx (1 + 0.61\,\overline{q})\;\overline{w'\theta'} + 0.61\,\overline{\theta}\,\overline{w'q'}, \tag{2A.7}$$

$$\Delta\theta_v = \Delta\theta + 0.61\;(\langle q\rangle\,\Delta\theta + \langle\theta\rangle\,\Delta q + \Delta\theta\Delta q)\,. \tag{2A.8}$$

Note that while using these equations, one should take units into account and therefore represent values for q in $\mathrm{kg\,kg^{-1}}$.

If people do not believe that mathematics is simple, it is only because they do not realize how complicated life is.

John Louis von Neumann

3

Analytical solution for the convectively-mixed atmospheric boundary layer

Based on the prognostic equations of mixed-layer theory assuming a zeroth order jump at the entrainment zone, analytical solutions for the boundary-layer height evolution are derived with different degrees of accuracy. First, an exact implicit expression for the boundary-layer height for a situation without moisture is analytically derived without assuming any additional relationships or specific initial conditions. It is shown that to expand the solution to include moisture, only minor approximations have to be made. Second, for relatively large boundary-layer heights, the implicit representation is simplified to an explicit function. Third, a hybrid expression is proposed as a reasonable representation for the boundary-layer height evolution during the entire day. Subsequently, the analysis is extended to present the evolution of any boundary-layer averaged scalar, either inert or under idealized chemistry, as an analytical function of time and boundary-layer height. Finally, the analytical solutions are evaluated. This evaluation includes a sensitivity analysis of the boundary-layer height for the entrainment ratio, the free tropospheric lapse rate of the potential temperature, the time-integrated surface flux and the

This chapter, except for Appendix 3A.1, is published as Ouwersloot and Vilà-Guerau de Arellano (2013a).

initial boundary-layer height and potential temperature jump.

Symbols

h	Boundary-layer height
q	Specific humidity
θ	Potential temperature
θ_v	Virtual potential temperature
$\overline{w'q'}$	Vertical kinematic moisture flux
$\overline{w'\theta'}$	Vertical kinematic heat flux
$\overline{w'\theta'_v}$	Buoyancy flux
c_p	Specific heat capacity of air
D_0	Initial temperature deficit
$D_{v,0}$	Initial virtual temperature deficit
I	Time-integrated surface buoyancy flux
Q	Heat
t	Time
z_0	Roughness length
α	Accuracy
β	Entrainment constant
ρ	Density of dry air
ϕ	Conserved scalar
$\langle\psi\rangle$	Mixed-layer average of arbitrary variable ψ
ψ_{FT}	Value of ψ in the free troposphere
$\Delta\psi$	Jump of ψ at the inversion, $\psi_{\mathrm{FT}} - \langle\psi\rangle$
γ_ψ	Free tropospheric gradient of ψ
$\overline{w'\psi'}_0$	Vertical kinematic surface flux of ψ
$\overline{w'\psi'}_h$	Vertical kinematic entrainment flux of ψ
$\hat{H}$	Dimensionless boundary-layer height
$\hat{J}$	Dimensionless virtual potential temperature jump at the inversion
$\hat{F}$	Dimensionless surface buoyancy flux

3.1 Introduction

The evolution of the atmospheric boundary layer (ABL) has been the subject of study for decades, since this region is the part of the atmosphere that is directly influenced by the presence of the earth's surface (Stull, 1988; Garratt, 1992). For the convective boundary layer

(CBL), which is common during daytime conditions over land, prognostic equations have been derived by Lilly (1968) to calculate the CBL height, the potential temperature and the inversion between the ABL and the free troposphere for maritime conditions. These equations, based on mixed-layer theory, have been further expanded since (Betts, 1973; Carson, 1973; Tennekes, 1973). The prognostic equations enable a conceptual view of the CBL to identify acting processes and study their interactions.

The system of equations resulted in the development of mixed-layer models, which are numerical models that, based on the available boundary and initial conditions, predict the evolution of the boundary-layer dynamics. The mixed-layer models have been applied to study multiple individual processes such as interactions between land and the atmosphere (e.g., de Bruin, 1983; van Heerwaarden et al., 2010), the onset of clouds (Ek and Holtslag, 2004), the impact of entrainment on carbon dioxide concentrations (Culf et al., 1997) and the influence of both non-stationary surface fluxes (van Driel and Jonker, 2011) and elevated residual layers (Stensrud, 1993) on the boundary-layer evolution. Furthermore, mixed-layer theory has been employed to interpret observational data, e.g. for the DOMINO, Diel Oxidant Mechanisms in relation to Nitrogen Oxides (van Stratum et al., 2012) and HUMPPA-COPEC-2010, Hyytiälä United Measurement of Photochemistry and Particles - Comprehensive Organic Particle and Environmental Chemistry - 2010 (Ouwersloot et al., 2012) campaigns.

Using the mixed-layer model, it has been demonstrated that boundary-layer dynamics and, in particular, the evolution of the boundary-layer height can significantly affect atmospheric chemistry (e.g., Vilà-Guerau de Arellano et al., 2009). This shows that an accurate knowledge of the evolution of boundary-layer dynamics is valuable and that an analytical expression for this evolution is relevant and useful to determine how these dynamics govern the diurnal variability of the thermodynamic variables and the atmospheric constituents such as carbon dioxide (e.g., Pino et al., 2012). Analytical expressions allow for extra insight into the driving processes by identifying dimensionless variables and expressing the boundary-layer height evolution as a function of these variables. Additionally, the analytical expressions provide continuous functions for the sensitivities of the boundary-layer properties to the different initial and boundary conditions. As a consequence, the expressions enable us to identify the distinct phases in the boundary-layer height evolution and quantify when those phases occur.

To the authors' knowledge, no complete analytical solutions including the effect of humidity have been published yet without assuming specific initial conditions. Most presented solutions (e.g., Carson, 1973; Garratt, 1992) neglect the non-linear dependence of the potential temperature jump at the inversion on the boundary-layer height. A complete analytical expression for a situation without moisture is presented by Driedonks (1982b). In his manuscript its derivation is not shown, but it is important to note that his expression can only be obtained when this non-linear dependence is included. Here we independently obtain the

same analytical solution and in addition include the effects of specific humidity. We further complete the study by presenting the evolutions of inert species concentrations and the accuracy of the explicit simplification for the boundary-layer height. Additionally, we performed a sensitivity analysis for the final boundary-layer height as a function of the driving initial and boundary conditions. The influence of subsidence is not taken into account, as is common for the published analytical solutions, with the exception of Carson (1973). It will be shown that, by adding subsidence, no solution for the equations can be derived with the applied mathematical techniques.

For the sake of clarity, the solutions and their implications are discussed in the main text, while the full derivations are given in the Appendix. First, we introduce the prognostic equations for the convectively mixed boundary layer without including the moisture effects. Special emphasis is put on the role of the initial conditions and the non-linear dependence of the potential temperature on the boundary-layer height. Subsequently, we discuss the derivation of the analytical solutions for a convective boundary layer without specific humidity. After that, we show the modification of the solutions due to the specific humidity. We then extend the analysis to express how the evolution of the scalars in the CBL responds to the evolution of the boundary-layer dynamics. These scalars include chemical species for idealized chemistry. Finally, the derived relationships are evaluated and an improved explicit approximation of the boundary-layer height evolution is presented. The evaluation includes an analysis of the sensitivity of the final boundary-layer height to the variables that govern its evolution.

3.2 Results

3.2.1 Governing equations

The governing equations for boundary-layer dynamics without including moisture can be derived from the conservation of heat. In this derivation it is assumed that the vertical profiles of conservative scalars (e.g., potential temperature and specific humidity) are characterized by a uniform value with height, $\langle\theta\rangle$, in the boundary layer, a discontinuity, $\Delta\theta$, in an infinitesimally thin inversion layer at the top of the boundary layer and a constant vertical gradient with height and in time, γ_θ, in the free tropospheric layer aloft. This assumption, as well as the resulting governing equations for a case without moisture, were previously presented by Tennekes (1973). The governing equations for a situation without the influence of subsidence,

cloud processes (e.g. radiation and phase changes) or advection read

$$\frac{\mathrm{d}h}{\mathrm{d}t} = -\frac{\overline{w'\theta'}_h}{\Delta\theta}, \tag{3.1}$$

$$\frac{\mathrm{d}\langle\theta\rangle}{\mathrm{d}t} = \frac{\overline{w'\theta'}_0 - \overline{w'\theta'}_h}{h}, \tag{3.2}$$

$$\frac{\mathrm{d}\Delta\theta}{\mathrm{d}t} = \gamma_\theta \frac{\mathrm{d}h}{\mathrm{d}t} - \frac{\mathrm{d}\langle\theta\rangle}{\mathrm{d}t}, \tag{3.3}$$

where h is the boundary-layer height, characterized by extremes in the vertical fluxes and discontinuities in the vertical profiles, $\overline{w'\theta'}_0$ is the Reynolds-averaged surface heat flux, which here is considered to be prescribed, and $\overline{w'\theta'}_h$ is the Reynolds-averaged heat flux at the top of the CBL due to entrainment. Additionally, the potential temperature profile in the free troposphere is described by

$$\theta_{\mathrm{FT}} = \langle\theta\rangle_0 + \Delta\theta_0 + \gamma_\theta (z - h_0)\,. \tag{3.4}$$

A common closure assumption (Stull, 1988) to solve the set of three governing equations with four unknown variables $\left(h, \langle\theta\rangle, \Delta\theta, \overline{w'\theta'_h}\right)$ is to relate the entrainment heat flux at the top of the CBL to the surface flux by

$$\overline{w'\theta'}_h = -\beta\overline{w'\theta'}_0, \tag{3.5}$$

where β is the entrainment constant, where we usually assume $\beta = 0.2$. Equation (3.2) then becomes

$$\frac{\mathrm{d}\langle\theta\rangle}{\mathrm{d}t} = (1+\beta)\frac{\overline{w'\theta'}_0}{h}. \tag{3.6}$$

The adaptation of these governing equations to include moisture will be discussed in Sect. 3.2.3.

3.2.2 Analytical solutions

First, we discuss the dependencies of the boundary-layer averaged potential temperature, $\langle\theta\rangle$, and the potential temperature jump at the inversion, $\Delta\theta$, on the boundary-layer height, which are derived in Appendix 3A.2. Second, these relations are used to derive the expression for the boundary-layer height evolution in Appendix 3A.3. It is important to note that we include all the terms without assumptions about the initial conditions of Eqs. (3.1-3.3) to obtain the analytical solution presented below, as opposed to previous solutions presented in the

literature (e.g., Betts, 1973; Garratt, 1992; Porporato, 2009). As shown by Eq. (3A.38),

$$\Delta\theta = \frac{\beta}{1+2\beta}\gamma_\theta h + \left(\Delta\theta_0 h_0^{\frac{1+\beta}{\beta}} - \frac{\beta}{1+2\beta}\gamma_\theta h_0^{\frac{1+2\beta}{\beta}}\right) h^{-\frac{1+\beta}{\beta}}. \tag{3.7}$$

A set of assumptions that, with the exception of Driedonks (1982b), is commonly made in the analysis of the temporal evolutions in the ABL, results in ignoring the non-linear dependence of the potential temperature jump at the inversion on the boundary-layer height, i.e. the second term on the right-hand site (r.h.s.) in Eq. (3.7). This restricts the resulting solutions to be valid only for idealized situations. One of these assumptions is a priori considering that the ratio of the potential temperature jump over the boundary-layer height is fixed. In that case, Eq. (3A.25) becomes $\Delta\theta = \left(\frac{\beta}{1+2\beta}\right)\gamma_\theta h$ (Betts, 1973; Garratt, 1992). Another assumption is stating as an initial condition that h and $\Delta\theta$ are both zero (e.g., Porporato, 2009), resulting in $c_3 = 0$ in Eq. (3A.25) and again resulting in $\Delta\theta = \left(\frac{\beta}{1+2\beta}\right)\gamma_\theta h$. This latter assumption would be valid if every day the boundary layer would start its growth from the Earth's surface ($h_0 = 0$). It therefore omits the morning transition from a nocturnal boundary layer to a daytime boundary layer, which starts with a height, h_0, equal to the nocturnal boundary-layer height.

To study the contribution of the non-linear term to $\Delta\theta$ and its importance, the dependency of $\Delta\theta$ on h is shown for different conditions in Fig. 3.1. The situation evaluated in Fig. 3.1a considers $\beta = 0.2$, $\gamma_\theta = 0.007$ K m^{-1} and an initial boundary-layer height of $h_0 = 500$ m. The three situations correspond to an initial potential temperature jump of 0.25 K, 0.5 K and 0.75 K. Under these conditions, the second term on the r.h.s. of Eq. (3.7) is zero for $\Delta\theta_0 = 0.5$ K and the potential temperature jump increases linearly with height. For the other two cases, the potential temperature jump gradually moves to the linear profile with increasing boundary-layer height according to the second term on the r.h.s. of Eq. (3.7). From this expression it follows that, for $\beta = 0.2$, the difference between the actual potential temperature jump and the potential temperature jump from the linear profile decreases with the ABL height according to a h^{-6} function.

Using the classification proposed by Tennekes (1973), three different phases can be distinguished in the figure in case the non-linear contribution to $\Delta\theta(h)$ is significant. Here we focus on the situation with a stronger initial potential temperature jump at the top of the ABL. The three phases are the break-up of the morning inversion, a transitional phase and pure convective growth. During the first phase, the boundary layer grows only very slowly due to the strong inversion that formed during night and most energy due to the surface heating is used to erode this inversion and reach the $\Delta\theta(h)$ that corresponds with the linear approximation. The dependence of $\Delta\theta$ on h is governed by the term $\left(\Delta\theta_0 h_0^{\frac{1+\beta}{\beta}} - \left(\frac{\beta}{1+2\beta}\right)\gamma_\theta h_0^{\frac{1+2\beta}{\beta}}\right) h^{-\frac{1+\beta}{\beta}}$ in Eq. (3.7), which falls with h^{-6}. Even though this phase only holds for a limited range

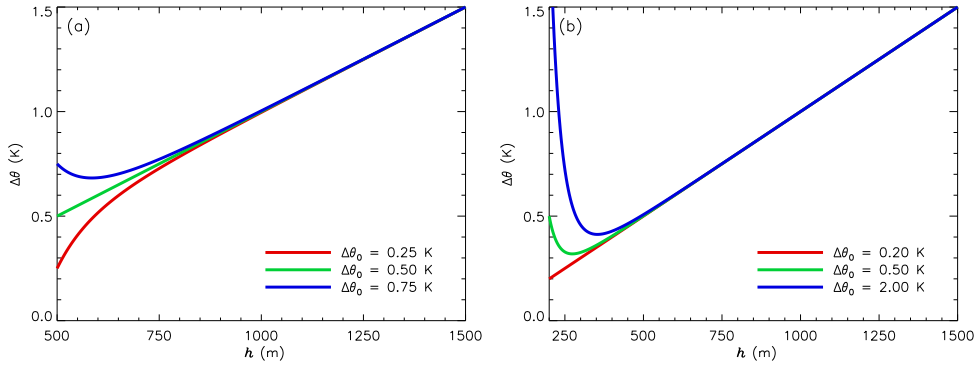

Figure 3.1: Dependency of the potential temperature jump on the ABL height for **a)** *an initial height, h_0, of 500 m, and* **b)** *an initial height of 200 m. For $\Delta\theta_0 = 0.5$ K in* **a)***, the potential temperature jump increases linearly with the ABL height under the chosen set of initial conditions. In* **b)***, with its lower initial height, the potential temperature jump only increases linearly with the ABL height for $\Delta\theta_0 = 0.2$ K .*

of h values, depending on the surface heat flux it can last for several hours as the boundary-layer growth is slow. The stronger the initial potential temperature jump, the slower is the initial boundary-layer growth. In the second phase, the evolution of the boundary-layer dynamics and, consequently, $\Delta\theta(h)$ is significantly influenced by both the initial conditions and convective growth. The value of $\Delta\theta$ does not strongly change with h. However, since the convective growth is less limited by the initial conditions, the boundary-layer growth increases strongly and this phase does not last for a long period. In the third and final phase, $\Delta\theta(h)$ has reached the linear profile that is associated with simplified initial conditions. By then the tendencies of the CBL properties are only governed by the convective growth of the boundary layer and not by the initial conditions. Note that this only holds for the tendencies and not for the actual values of the CBL properties themselves. As an example, in a situation that starts with a stronger nocturnal inversion, the final boundary-layer height at the end of the afternoon will still be lower than in a situation that starts with a weaker nocturnal inversion. At the start of this third phase, the boundary layer grows more rapidly, since the morning inversion no longer influences the entrainment velocity. However, as time progresses and the boundary layer becomes deeper, keeping $\Delta\theta$ small enough when the ABL grows requires relatively more energy. Consequently, the rate of growth of the ABL decreases with increasing boundary-layer height. As the final boundary-layer height is lower and the heat fluxes are unaltered, the final mixed-layer averaged θ is larger.

The evolution of $\Delta\theta$ is dominated by the second term on the r.h.s. of Eq. (3.7) in the first phase and by the first term on the r.h.s. of Eq. (3.7) in the third phase. From Eq. (3.7) we

derive

$$\frac{\mathrm{d}\Delta\theta}{\mathrm{d}h} = Grad_{Conv} + Grad_{IC}, \tag{3.8}$$

$$Grad_{Conv} = \frac{\beta}{1+2\beta}\gamma_\theta, \tag{3.9}$$

$$Grad_{IC} = -\frac{1+\beta}{\beta}\left(\Delta\theta_0 h_0^{\frac{1+\beta}{\beta}} - \frac{\beta}{1+2\beta}\gamma_\theta h_0^{\frac{1+2\beta}{\beta}}\right)h^{-\frac{1+2\beta}{\beta}}, \tag{3.10}$$

where $Grad_{IC}$ is the evolution of $\Delta\theta$ due to the initial conditions and $Grad_{Conv}$ is the evolution of $\Delta\theta$ due to convective growth. In the first phase, $|Grad_{Conv}| \gg |Grad_{IC}|$ and in the third phase $|Grad_{Conv}| \ll |Grad_{IC}|$. The exact timing of the transition between two phases is arbitrary. Here, the criterion we use for a phase is that the one contribution is X times as strong as the other. In that case it follows from Eqs. (3.9) and (3.10) that

$$h < \left(\frac{1}{X}\frac{\left|\Delta\theta_0 h_0^{\frac{1+\beta}{\beta}} - \left(\frac{\beta}{1+2\beta}\right)\gamma_\theta h_0^{\frac{1+2\beta}{\beta}}\right|}{\gamma_\theta}\frac{1+3\beta+2\beta^2}{\beta^2}\right)^{\frac{\beta}{1+2\beta}} \qquad \text{for phase 1,} \tag{3.11}$$

$$h > \left(X\frac{\left|\Delta\theta_0 h_0^{\frac{1+\beta}{\beta}} - \left(\frac{\beta}{1+2\beta}\right)\gamma_\theta h_0^{\frac{1+2\beta}{\beta}}\right|}{\gamma_\theta}\frac{1+3\beta+2\beta^2}{\beta^2}\right)^{\frac{\beta}{1+2\beta}} \qquad \text{for phase 3.} \tag{3.12}$$

For the examples of Fig. 3.1, when taking $X = 2$, the transition from phase 1 to phase 2 is at $h = 530$ m and 320 m for Fig. 3.1a and Fig 3.1b, respectively. The transition from phase 2 to phase 3 for these values is at $h = 646$ m and 390 m, respectively. These ABL heights can be related to the elapsed time by using Eq. (3A.68) if the time evolutions of the surface fluxes are known.

After discussing the influence of $\Delta\theta_0$ for situations in which $h_0 = 500$ m, the influence of h_0 itself is explored. In Fig. 3.1b a case with a more prominent nocturnal inversion is shown. Over land, nocturnal boundary layers with even larger potential temperature jumps, of the order of several K, can occur due to e.g. advection of air masses (Vilà-Guerau de Arellano, 2007). As the nocturnal boundary-layer growth is inhibited increasingly by stronger inversions (Garratt, 1992), the final nocturnal boundary-layer height will be lower as well. Therefore, for these situations the initial boundary-layer height for the CBL of the consecutive day will be lower and the initial potential temperature inversion of the CBL will be stronger than for more moderate nocturnal inversions. For the situations in Fig. 3.1b, h_0 is set equal to 200 m and the initial potential temperature jumps are 0.2 K, 0.5 K and 2 K. For an initial boundary-layer height this low $\Delta\theta_0$ of a few K is common, while 0.2 K is the initial po-

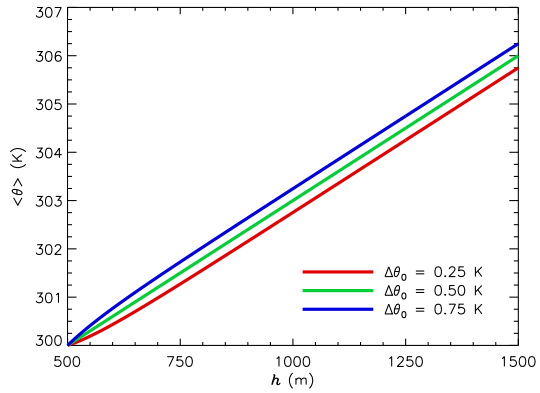

Figure 3.2: Dependency of the mixed-layer averaged potential temperature on the ABL height. For $\Delta\theta_0 = 0.5$ K, the potential temperature increases linearly with the ABL height under the chosen set of initial conditions. For other $\Delta\theta_0$, $\langle\theta\rangle(h)$ approaches with increasing h a linear asymptote that does not cross the initial conditions, but is offset by the difference in $\Delta\theta_0$.

tential temperature inversion that corresponds to the linear approximation of $\Delta\theta = \left(\frac{\beta}{1+2\beta}\right)\gamma_\theta h$. The figure shows that, therefore, the effect of the initial conditions on $\Delta\theta(h)$ become more significant for the lower boundary-layer heights. As a consequence, the three aforementioned regimes are more easily recognizable in Fig. 3.1b compared to Fig. 3.1a. Since the non-linear part of Eq. (3.7) can be written as $\left(\Delta\theta_0 - \left(\frac{\beta}{1+2\beta}\right)\gamma_\theta h_0\right)\left(\frac{h}{h_0}\right)^{-\frac{1+\beta}{\beta}}$ and h_0 is smaller, its influence is significant for lower values of h compared to situations with larger h_0. On the other hand, the accompanying stronger $\Delta\theta_0$ inhibits the boundary-layer growth to a greater degree, so that the boundary layer remains shallow for a longer period. In total, also for lower h_0 the initial conditions are significant for the evolution of the boundary-layer dynamics.

Using the knowledge of $\Delta\theta(h)$ and $\theta_{\mathrm{FT}}(h)$, i.e. the potential temperature at the bottom of the free troposphere, Eq. (3A.40) is derived. This expression for $\langle\theta\rangle(h)$ reads

$$\langle\theta\rangle = \langle\theta\rangle_0 - \gamma_\theta h_0 + \Delta\theta_0 + \left(\frac{1+\beta}{1+2\beta}\right)\gamma_\theta h - \left(\Delta\theta_0 h_0^{\frac{1+\beta}{\beta}} - \left(\frac{\beta}{1+2\beta}\right)\gamma_\theta h_0^{\frac{1+2\beta}{\beta}}\right)h^{-\frac{1+\beta}{\beta}}. \tag{3.13}$$

Note that, for relatively large h (larger than ± 750 m for the conditions of Fig. 3.1), if all other initial conditions are kept the same, $\langle\theta\rangle(h)$ is a linear function whose offset depends on the initial potential temperature jump. This agrees with Fig. 3.1, since for large h, $\Delta\theta(h)$ becomes independent of the initial conditions. According to Eq. (3.4), $\theta_{\mathrm{FT}}(h)$ is offset by differences in $\Delta\theta_0$ and, consequently, so is $\langle\theta\rangle(h)$ for large h. This relationship is demonstrated in Fig. 3.2 for the same conditions as Fig. 3.1a.

As an expression for $\Delta\theta\frac{\mathrm{d}h}{\mathrm{d}t}$ is known from Eq. (3A.22) and $\Delta\theta(h)$ is provided by Eq. (3.7), a differential equation for h is found that is independent of $\Delta\theta$ and $\langle\theta\rangle$. The result, given by Eq. (3A.44), is

$$h^2 - \left(\frac{2+4\beta}{\gamma_\theta}\right)\left(\Delta\theta_0 h_0^{\frac{1+\beta}{\beta}} - \left(\frac{\beta}{1+2\beta}\right)\gamma_\theta h_0^{\frac{1+2\beta}{\beta}}\right)h^{-\frac{1}{\beta}} = h_0^2 - \left(\frac{2+4\beta}{\gamma_\theta}\right)\left(\Delta\theta_0 h_0 - \left(\frac{\beta}{1+2\beta}\right)\gamma_\theta h_0^2\right) + \left(\frac{2+4\beta}{\gamma_\theta}\right)\int_{t_0}^{t}\overline{w'\theta'}_0\mathrm{d}t. \tag{3.14}$$

This solution is implicit and cannot be solved explicitly for general values of β. However, for relatively large h, the second term on the left-hand side (l.h.s.) becomes small and can be ignored. This results in the explicit approximation of Eq. (3A.47),

$$h \approx \sqrt{\underbrace{h_0^2 - \left(\frac{2+4\beta}{\gamma_\theta}\right)\left(\Delta\theta_0 h_0 - \left(\frac{\beta}{1+2\beta}\right)\gamma_\theta h_0^2\right)}_{-\frac{2+4\beta}{\gamma_\theta}D_0} + \left(\frac{2+4\beta}{\gamma_\theta}\right)\int_{t_0}^{t}\overline{w'\theta'}_0\mathrm{d}t}. \tag{3.15}$$

Equation (3.15) matches the equations previously presented by Driedonks (1982b). Apart from notation, the only small difference the reader might note, is found in the second term on the l.h.s. of the implicit solution (Eq. (8) in his manuscript) where a multiplication with β is omitted. The sum of the first two terms in the square root is identified as $-\frac{2+4\beta}{\gamma_\theta}$ times the initial temperature deficit, D_0. This initial temperature deficit describes how much heat is needed to fill the nocturnal inversion that is present at the start of the day. Note that Eq. (3.15) confirms that, for $h \gg h_0$, even though $\Delta\theta(h)$ is unaffected by the initial conditions, $h(t)$ and, consequently, $\Delta\theta(t)$ remain affected by the initial temperature deficit during the entire day. The explicit approximation of Eq. (3.15) is evaluated in more detail in Sect. 3.3.

From Eqs. (3.7), (3.13), (3.14) and (3.15) it is clear that for the chosen conditions the evolutions $h(t)$, $\langle\theta\rangle(t)$ and $\Delta\theta(t)$ are only dependent on time through the integrated surface heat flux, $\int_{t_0}^{t}\overline{w'\theta'}_0\mathrm{d}t$. This is independent of the distribution of the surface heat flux over time and the amount of time needed to reach that value of integrated surface heat flux. This will be confirmed in Sect. 3.3.3.

3.2.3 Including the effects of moisture

If moisture is present, the specific humidity, q, has to be accounted for in the expression of the boundary-layer height evolution. The variable that drives convection is then the virtual potential temperature, θ_v, instead of the potential temperature. This virtual potential temperature

and its transport are expressed by (Stull, 1988)

$$\theta_v = \theta\,(1 + 0.61q)\,, \tag{3.16}$$

$$\overline{w'\theta'_v} \approx 0.61\,\overline{\theta}\,\overline{w'q'} + (1 + 0.61\,\overline{q})\,\overline{w'\theta'}. \tag{3.17}$$

The closure assumption of Eq. (3.5) is altered to

$$\overline{w'\theta'_{vh}} = -\beta\overline{w'\theta'_{v0}}. \tag{3.18}$$

As shown in Appendix 3A.5, the new governing equations are derived by assuming a vertical profile of the specific humidity that, just like the potential temperature, is constant in the boundary layer, has a discontinuity at the inversion and is linear in the free troposphere. In contrast to the case without moisture, two approximations have to be used before obtaining the expressions. To justify these approximations, typical values for variables in the CBL will be applied. The first approximation holds that $|\Delta\theta\Delta q| \ll \Delta\theta_v$, considering that q in these equations should be expressed in the dimensionless kg kg^{-1}. For the clear boundary layer over land, this is valid as $\Delta\theta$ is of similar magnitude as $\Delta\theta_v$, and Δq is of the order of 10^{-3} kg kg^{-1}.

The second approximation is to consider the virtual potential temperature lapse rate in the free troposphere, $\gamma_{\theta_v} = \frac{\mathrm{d}\theta_v}{\mathrm{d}z}$, to be constant with height, while actually

$$\gamma_{\theta_v}(z) = (1 + 0.61q(z))\,\gamma_\theta + 0.61\theta(z)\gamma_q. \tag{3.19}$$

The approximation that is applied considers $\gamma_{\theta_v}(z) \approx \gamma_{\theta_v}(h_0)$. For the first term in Eq. (3.19), $0.61q(z)$ is of the order of 10^{-3} kg kg^{-1}, so that

$$1 + 0.61q(h_0) \approx 1 + 0.61q(z)$$

for all heights considered when evaluating the atmospheric boundary layer. For the second term, $\theta \approx 300$ K and γ_q describes changes in specific humidity with height, which are of the order of g kg^{-1} km^{-1}. This results in a contribution to γ_{θ_v} of the order of 10^{-1} K km^{-1}, which can be significant. However, for an evolving CBL the change in $\theta(z)$ just above the mixed layer is only of the order of 10 K. Because of that, using $\theta(h_0)$ instead of $\theta(z)$ results in a change in γ_{θ_v} of the order of 10^{-2} K km^{-1}. Therefore,

$$0.61\,(\theta(z) - \theta(h_0))\,\gamma_q \ll \gamma_\theta.$$

As an example to show that we can indeed assume γ_{θ_v} to be constant, consider the situation described in Table 3.1 that includes moisture. We consider γ_q to be $\pm$ 0.001 g kg^{-1} m^{-1}. We

compare γ_{θ_v} and θ_v at 2000 m height as calculated with the approximation and as calculated with the prescribed θ and q profiles. For $\gamma_q = 0.001$ g kg^{-1} m^{-1}, the true γ_{θ_v} at 2000 m height is 0.18 % larger than the approximated value of $6.2{\times}10^{-3}$ K m^{-1}, which is a difference of $1.1{\times}10^{-5}$ K m^{-1}. The change has the same magnitude but negative sign if $\gamma_q = -0.001$ g kg^{-1} m^{-1}. Finally, θ_v at 2000 m only differs by 8.2×10^{-3} K.

The resulting set of governing equations that replaces Eqs. (3.1-3.3) becomes

$$\frac{\mathrm{d}h}{\mathrm{d}t} = -\frac{\overline{w'\theta'_{v}}_h}{\Delta\theta_v}, \tag{3.20}$$

$$\frac{\mathrm{d}\left\langle\theta_v\right\rangle}{\mathrm{d}t} = \frac{\overline{w'\theta'_{v}}_0 - \overline{w'\theta'_{v}}_h}{h}, \tag{3.21}$$

$$\frac{\mathrm{d}\Delta\theta_v}{\mathrm{d}t} = \gamma_{\theta_v}\frac{\mathrm{d}h}{\mathrm{d}t} - \frac{\mathrm{d}\left\langle\theta_v\right\rangle}{\mathrm{d}t}. \tag{3.22}$$

The surface flux, $\overline{w'\theta'_{v}}_0$, is again considered to be prescribed. These relations show that to include moisture, the equations of Sect. 3.2.2 can be used by replacing θ by θ_v. Therefore

$$\begin{aligned} h^2 - \left(\frac{2+4\beta}{\gamma_{\theta_v}}\right)\left(\Delta\theta_{v,0}h_0^{\frac{1+\beta}{\beta}} - \left(\frac{\beta}{1+2\beta}\right)\gamma_{\theta_v}h_0^{\frac{1+2\beta}{\beta}}\right)h^{-\frac{1}{\beta}} = \\ h_0^2 - \left(\frac{2+4\beta}{\gamma_{\theta_v}}\right)\left(\Delta\theta_{v,0}h_0 - \left(\frac{\beta}{1+2\beta}\right)\gamma_{\theta_v}h_0^2\right) + \left(\frac{2+4\beta}{\gamma_{\theta_v}}\right)\int_{t_0}^{t}\overline{w'\theta'_{v}}_0\mathrm{d}t, \end{aligned} \tag{3.23}$$

which is approximated as

$$h \approx \sqrt{h_0^2 - \left(\frac{2+4\beta}{\gamma_{\theta_v}}\right)\left(\Delta\theta_{v,0}h_0 - \left(\frac{\beta}{1+2\beta}\right)\gamma_{\theta_v}h_0^2\right) + \left(\frac{2+4\beta}{\gamma_{\theta_v}}\right)\int_{t_0}^{t}\overline{w'\theta'_{v}}_0\mathrm{d}t}. \tag{3.24}$$

As shown in this section, the approximations that were made to derive this result only lead to insignificant changes. Analogous to Eq. (3.15), the sum of the first two terms in the square root of Eq. (3.24), $h_0^2 - \left(\frac{2+4\beta}{\gamma_{\theta_v}}\right)\left(\Delta\theta_{v,0}h_0 - \left(\frac{\beta}{1+2\beta}\right)\gamma_{\theta_v}h_0^2\right)$, describes how much buoyancy needs to be added by the surface buoyancy flux to fill the initial excess inversion in the virtual potential temperature profile.

As before, the evolutions of $h(t)$, $\langle\theta_v\rangle(t)$ and $\Delta\theta_v(t)$ are only dependent on time through the integrated surface buoyancy flux, $\int_{t_0}^{t}\overline{w'\theta'_{v}}_0\mathrm{d}t$. As a result, if two different cases have the same initial conditions and time-integrated surface buoyancy flux at certain points in time, the values of h, $\langle\theta_v\rangle$ and $\Delta\theta_v$ at those times are equal as well. For evaluating cases it is important to note that equipment that measures the sensible and latent heat fluxes can return the buoyancy flux as well.

If $h(t)$ is known, the individual time evolutions $\langle\theta\rangle(t)$ and $\langle q\rangle(t)$, and consequently $\Delta\theta(t)$ and $\Delta q(t)$, can be determined if additionally the corresponding surface fluxes are known. This

will be treated in Sect. 3.2.4.

By defining the dimensionless groups

$$\hat{H} = \frac{h}{h_0}, \tag{3.25}$$

$$\hat{J} = \frac{\Delta\theta_{v,0}}{\gamma_{\theta_v} h_0}, \tag{3.26}$$

$$\hat{F} = \frac{\int_{t_0}^{t} \overline{w'\theta'_{v0}}\mathrm{d}t}{\gamma_{\theta_v} h_0^2}, \tag{3.27}$$

Equations (3.23) and (3.24) can be written in the dimensionless forms

$$\hat{H}^2 - 2\left((1+2\beta)\,\hat{J} - \beta\right)\hat{H}^{-\frac{1}{\beta}} = 1 - 2\left((1+2\beta)\,\hat{J} - \beta\right) + 2\,(1+2\beta)\,\hat{F}, \tag{3.28}$$

$$\hat{H} \approx \sqrt{1 - 2\left((1+2\beta)\,\hat{J} - \beta\right) + 2\,(1+2\beta)\,\hat{F}}, \tag{3.29}$$

$$\hat{H} \approx \sqrt{1+2\beta}\sqrt{1 + 2\left(\hat{F} - \hat{J}\right)}. \tag{3.30}$$

$\hat{H}$ is related to the boundary-layer height compared to its initial value, $\hat{J}$ expresses the relative strength of the initial virtual potential temperature jump at the inversion and $\hat{F}$ denotes the scaled time-integrated surface buoyancy flux. Equation (3.30) shows that for relatively large $\hat{H}$ the growth of the boundary layer is governed by the difference between the scaled time-integrated surface buoyancy flux and the relative strength of the initial virtual potential temperature jump compared to the free tropospheric virtual potential temperature profile. Equations (3.29) and (3.30) are valid for a large range of $\hat{H}$, as already for e.g. $\hat{H} = 2$ in Eq. (3.28), $\hat{H}^2 = 128\hat{H}^{-\frac{1}{\beta}}$ if $\beta = 0.2$.

3.2.4 Evolution of conserved scalars

Appendix 3A.4 demonstrates that, as long as an arbitrary scalar, ϕ, is conserved, has no significant additional sources/sinks in the boundary layer (e.g., radiation divergence, phase changes or chemical production/loss), is not horizontally advected or influenced by subsidence, and has a vertical profile in the free troposphere that is characterized by a constant gradient, γ_ϕ, the evolution of the boundary-layer averaged scalar, $\langle\phi\rangle$, can be expressed as a function of time, the current boundary-layer height and the integral of the emissions after the initial conditions. As the current boundary-layer height, $h(t)$, can be calculated with Eq. (3.23) or approximated using Eq. (3.24), only knowledge about the initial conditions and the evolutions of the surface buoyancy flux and scalar emission/deposition are needed to know

$\langle\phi\rangle(t)$. According to Eq. (3A.50),

$$\langle\phi\rangle(t) = \langle\phi\rangle_0 + \frac{h(t)-h_0}{h(t)}\Delta\phi_0 + \frac{\gamma_\phi}{2}\frac{(h(t)-h_0)^2}{h(t)} + \frac{1}{h(t)}\int_{t_0}^{t}\overline{w'\phi'}_0 \mathrm{d}t. \tag{3.31}$$

If the scalar under consideration is chemically active, there is additional production or loss and this equation does not hold. However, in idealized conditions the chemical production, P, is constant with time and height. If the chemical reactions that deplete the chemical species are of the first-order with respect to that species, the chemical loss, L, scales linearly with the mixing ratio under consideration. L is then expressed by

$$L = -\frac{\langle\phi\rangle}{\tau}, \tag{3.32}$$

where τ is the lifetime of the chemical species. The governing equation for $\langle\phi\rangle$ becomes

$$\frac{\mathrm{d}\langle\phi\rangle}{\mathrm{d}t} = \frac{\overline{w'\phi'}_0 - \overline{w'\phi'}_h}{h} + P - \frac{\langle\phi\rangle}{\tau} \tag{3.33}$$

and it can be shown that

$$\begin{aligned}\langle\phi\rangle(t) = \langle\phi\rangle_0\, \mathrm{e}^{\frac{t_0-t}{\tau}} + \frac{h(t)-h_0}{h(t)}\Delta\phi_0\, \mathrm{e}^{\frac{t_0-t}{\tau}} + \frac{\gamma_\phi}{2}\frac{(h(t)-h_0)^2}{h(t)}\mathrm{e}^{\frac{t_0-t}{\tau}} + \\ P\tau\left(1-\mathrm{e}^{\frac{t_0-t}{\tau}}\right) + \frac{1}{h(t)}\int_{t_0}^{t}\overline{w'\phi'}_0\, \mathrm{e}^{\frac{t'-t}{\tau}}\mathrm{d}t'.\end{aligned} \tag{3.34}$$

In this equation, the chemical destruction is introduced by the occurrences of $\mathrm{e}^{\frac{t_0-t}{\tau}}$. The factor $\mathrm{e}^{\frac{t_0-t}{\tau}}$ in the first three terms on the r.h.s. shows that the initial mixing ratio profile decays with the lifetime τ. If the species is inert, the profile should not decay at all. This is reflected in the equations, since in that case $\tau \to \infty$, which results in $\mathrm{e}^{\frac{t_0-t}{\tau}} \approx 1 + \frac{t_0-t}{\tau} \approx 1$. Therefore, for $\tau \to \infty$, the first three terms on the r.h.s. in Eq. (3.34) are equal to the first three terms on the r.h.s. in Eq. (3.31). For highly reactive chemical species, τ is small and in a short time, e.g. seconds for the hydroxyl radical, $\mathrm{e}^{\frac{t_0-t}{\tau}}$ approaches zero. In that case, the initial conditions are not important for the time evolution of the mixing ratio.

The fourth term on the r.h.s. of Eq. (3.34) describes an equilibrium between chemical production and destruction. If there is no production, $P = 0$ and this term disappears. If not much time has elapsed relative to the chemical lifetime, i.e. $t - t_0 \ll \tau$, then $\tau\left(1-\mathrm{e}^{\frac{t_0-t}{\tau}}\right) \approx \tau - \tau\left(1+\frac{t_0-t}{\tau}\right) = t - t_0$. In these situations the chemical contribution results in a linear increase in time of the mixing ratio, according to $P(t-t_0)$. For inert chemical species, $\tau \to \infty$ and this always holds true.

For chemical species that do not have an extremely short or long lifetime, this balance

between chemical production and destruction first increases linearly with time. When $t - t_0$ becomes of the same order as τ, the rate of increase starts to decrease. Finally, for $t - t_0 \gg \tau$ the balance between chemical production and chemical destruction reaches an asymptote. At that moment, $e^{\frac{t_0-t}{\tau}} \approx 1 + \frac{t_0-t}{\tau} \approx 1$ and thus $P\tau\left(1 - e^{\frac{t_0-t}{\tau}}\right) \approx P\tau$. This shows that the chemical balance results in a mixing ratio that is equal to the chemical production rate times the lifetime of the chemical species.

The final term on the r.h.s. of Eq. (3.34) expresses the influence of the surface exchange (emission or deposition) on the mixing ratio. Greater boundary-layer heights result in a weaker impact of this term. Due to chemical destruction, emissions that took place a longer time ago have less impact on the current mixing ratio than recent emissions. This is quantified by the factor $e^{\frac{t'-t}{\tau}}$ in the integral.

3.3 Evaluation

3.3.1 Accuracy of the explicit approximation

The explicit expression of Eq. (3.24) is a simplification of Eq. (3.23) by neglecting its second term on the l.h.s. As this term falls with $h^{\frac{-1}{\beta}}$, the explicit approximation is valid for relatively large h, but not for relatively small h. For instance, at $t = t_0$ the resulting h is expressed by

$$h = \sqrt{h_0^2 - \left(\frac{2+4\beta}{\gamma_{\theta_v}}\right)\left(\Delta\theta_{v,0}h_0 - \left(\frac{\beta}{1+2\beta}\right)\gamma_{\theta_v}h_0^2\right)} \tag{3.35}$$

instead of $h = h_0$. The difference between the explicit approximation and the real boundary-layer height, as obtained from the implicit expression, becomes smaller for increasing h. An analysis of the l.h.s. of Eq. (3.23) shows that the accuracy of the explicit solution,

$$\alpha = \frac{\left|h_{\text{explicit}} - h_{\text{implicit}}\right|}{h_{\text{implicit}}}, \tag{3.36}$$

is related to the boundary-layer height in such a way that the height can be found for which a certain accuracy is obtained. The explicit simplification of the boundary-layer height is within a certain accuracy of the true (implicitly determined) boundary-layer height if

$$\begin{cases} h(\alpha) \geq (1-\alpha)\left(\left(\frac{2+4\beta}{\gamma_{\theta_v}}\right)\frac{\Delta\theta_{v,0}h_0^{\frac{1+\beta}{\beta}} - \left(\frac{\beta}{1+2\beta}\right)\gamma_{\theta_v}h_0^{\frac{1+2\beta}{\beta}}}{\alpha(2-\alpha)}\right)^{\frac{\beta}{1+2\beta}} & \text{if } \Delta\theta_{v,0} > \left(\frac{\beta}{1+2\beta}\right)\gamma_{\theta_v}h_0, \\ h(\alpha) \geq (1+\alpha)\left(\left(\frac{2+4\beta}{\gamma_{\theta_v}}\right)\frac{\left(\frac{\beta}{1+2\beta}\right)\gamma_{\theta_v}h_0^{\frac{1+2\beta}{\beta}} - \Delta\theta_{v,0}h_0^{\frac{1+\beta}{\beta}}}{\alpha(2+\alpha)}\right)^{\frac{\beta}{1+2\beta}} & \text{if } \Delta\theta_{v,0} < \left(\frac{\beta}{1+2\beta}\right)\gamma_{\theta_v}h_0. \end{cases}$$

Illustrative values are presented for two different situations in Sect. 3.3.3.

3.3.2 Hybrid explicit expression

The mismatch of Eq. (3.24) for small h would be removed if the true h were substituted in the second term on the l.h.s. of Eq. (3.23). Although no perfect explicit solution exists, the previously published boundary-layer height development (Garratt, 1992), which assumes $\Delta\theta_v$ to be linearly dependent on h, could be used for this substitution to decrease the mismatch. The expression for this evolution, $\hat{h}$, is

$$\hat{h} = \sqrt{h_0^2 + \left(\frac{2+4\beta}{\gamma_{\theta_v}}\right)\int_{t_0}^{t} \overline{w'\theta'_{v0}}\,\mathrm{d}t} \tag{3.37}$$

and results in $\hat{h} = h_0$ at $t = t_0$. Furthermore, in reality the typical reason that at the start of the day $\Delta\theta_{v,0} \neq \left(\frac{\beta}{1+2\beta}\right)\gamma_{\theta_v} h_0$, is the lower potential temperature in the boundary layer compared to the free troposphere due to radiative cooling during the night. This results in $\Delta\theta_{v,0} > \left(\frac{\beta}{1+2\beta}\right)\gamma_{\theta_v} h_0$. From Eq. (3.23) it can be seen that in that case for $h > h_0$, $h < \sqrt{h_0^2 + \left(\frac{2+4\beta}{\gamma_{\theta_v}}\right)\int_{t_0}^{t} \overline{w'\theta'_{v0}}\,\mathrm{d}t} = \hat{h}$. Therefore, $\hat{h}^{\frac{-1}{\beta}} < h^{\frac{-1}{\beta}}$, which means that by substituting $\hat{h}$ in the second term of Eq. (3.23), this term is no longer put to zero, but its magnitude will still be less than if the true h were used. The resulting hybrid explicit expression for the boundary-layer height is

$$h_{\mathrm{hybrid}} = \sqrt{h_0^2 + \left(\frac{2+4\beta}{\gamma_{\theta_v}}\right)\left(\Delta\theta_{v,0} h_0^{\frac{1+\beta}{\beta}} - \left(\frac{\beta}{1+2\beta}\right)\gamma_{\theta_v} h_0^{\frac{1+2\beta}{\beta}}\right)\left(\hat{h}^{-\frac{1}{\beta}} - h_0^{-\frac{1}{\beta}}\right) + \left(\frac{2+4\beta}{\gamma_{\theta_v}}\right)\int_{t_0}^{t} \overline{w'\theta'_{v0}}\,\mathrm{d}t}. \tag{3.38}$$

For practical everyday use, we propose to use this representation of h if $\Delta\theta_{v,0} \geq \left(\frac{\beta}{1+2\beta}\right)\gamma_{\theta_v} h_0$, as it captures the evolution of h for both relatively small and relatively large h. A comparison between the different expressions for h is discussed in Sect. 3.3.3.

3.3.3 Comparison between solutions

In this section, four different representations of the boundary-layer height are compared: the *implicit*, *linear explicit*, *new explicit* and *explicit hybrid* solution. The *implicit* expression describes the exact boundary-layer height evolution, which is equal to the one that results from numerically solving Eqs. (3.20-3.22). This equivalence is tested for multiple situations (not shown) by comparing the l.h.s. of Eq. (3.23) to the corresponding output of a numerical

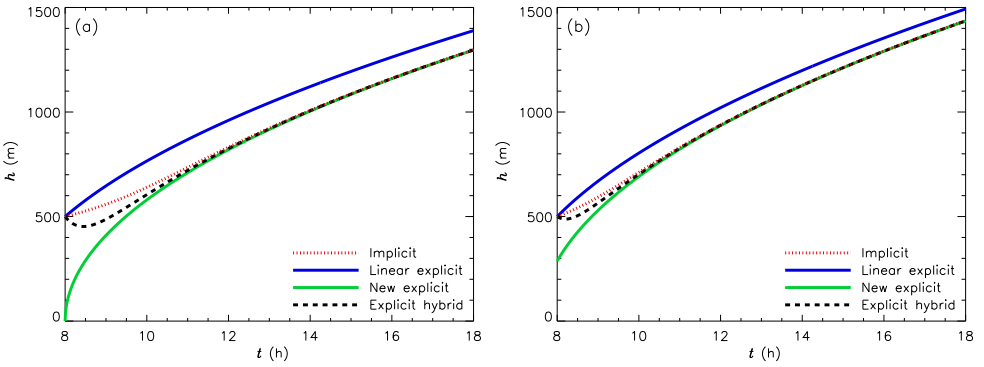

Figure 3.3: Boundary-layer height evolution representations for, **a)** *a situation without, and* **b)** *a situation with moisture present. Each panel shows the implicit solution for h, the old explicit solution that assumes $\Delta\theta$ to be linearly dependent on h and the new explicit simplification, which ignores the second term of the l.h.s. of the implicit expression (Eq.* (3.23)*). This term falls with $h^{\frac{-1}{\beta}}$. Finally, the black line shows the hybrid explicit solution, which is obtained by substituting the linear explicit solution into the h of the aforementioned term of Eq.* (3.23)*.*

Table 3.1: Initial and boundary conditions that are used for the comparison of the different boundary-layer height expressions in Fig. 3.3. For this evaluation, the surface fluxes are kept constant with time, disregarding diurnal variability.

Property		Without moisture	With moisture
h_0	(m)	500	500
$\langle\theta\rangle_0$	(K)	290	290
$\Delta\theta_0$	(K)	1.5	1.5
γ_θ	(K m^{-1})	0.006	0.006
$\overline{w'\theta'}_0$	(K m s^{-1})	0.1	0.1
$\langle q\rangle_0$	(g kg^{-1})	0	6
Δq_0	(g kg^{-1})	0	-2
γ_q	(g kg^{-1} m^{-1})	0	0
$\overline{w'q'}_0$	(g kg^{-1} m s^{-1})	0.0	0.1
β		0.2	0.2

mixed-layer model. Since the results were equal and the l.h.s. of Eq. (3.23) is bijective with h (Appendix 3A.6), the corresponding evolutions of h are equal as well. The *linear explicit* expression is the common solution for the boundary-layer height that assumes $\Delta\theta_v$ to be linearly dependent on h (e.g., Garratt, 1992). The *new explicit* expression is Eq. (3.24), which takes all initial conditions into account. Note that, due to being a simplification of the *implicit* expression, the initial state for the *new explicit* expression is not equal to the initial conditions (see Eq. (3.35)). Finally, the *explicit hybrid* expression is the combined explicit approximation that is derived in Sect. 3.3.2.

All four representations are presented in Fig. 3.3 for a boundary layer with an initial height of 500 m. Two situations are considered: one without and one with moisture present. The initial and boundary conditions are presented in Table 3.1.

The figures show the importance of the non-linear term of $\Delta\theta_v$ in reproducing the evolution of the ABL height. The difference after 10 hours between the *linear explicit* representation and the true boundary-layer height is 90 m for the case without moisture and 60 m for the case with moisture. The *new explicit* expression of Eq. (3.24) performs poorly in the initial stage. However, it matches the implicit height better with increasing h. The new expression already performs better than the linear expression for $h = 600$ m and is indistinguishable from the implicit solution for $h = 700$ m. According to the relations of Sect. 3.3.1, the differences with the true boundary-layer height for the dry and the moist situation are 5 % at 662 m and 626 m, respectively, and only 1 % at 866 m and 818 m, respectively. Finally, Fig. 3.3 shows that the hybrid explicit expression for the boundary-layer height of Eq. (3.38) does approximate the implicit representation of the boundary-layer height best. It retains the accurate representativeness of the new explicit expression for large h and solves the initial mismatch. Note that the *hybrid* expression only significantly improves on the *new explicit* expression if the *linear explicit* expression returns a boundary-layer height similar to the actual boundary-layer height. If the height according to the *new explicit* expression is much higher, $\hat{h}^{-\frac{1}{\beta}}$ in Eq. (3.38) becomes too insignificant and the *hybrid* solution will become similar to the *new explicit* expression. This occurs for strong initial potential temperature jumps.

As expressed by Eq. (3.31), the evolution of the scalars in the boundary layer depends on the ABL height evolution. To show the relevance of an accurate expression, Fig. 3.4 presents the diurnal evolution of $\langle q \rangle$ for the situation with moisture from Table 3.1. The four different lines are the evolutions that result from substituting the four different boundary-layer height evolutions of Fig. 3.3b in Eq. (3.31). Substituting the *implicit* expression for h results in the true expression of $\langle q \rangle (t)$. The evolution of $\langle q \rangle$ that is based on the explicit *hybrid* expression for h is more accurate than that calculated with the original *linear explicit* expression. After 1 hour of simulated time, using the *new explicit* expression, which is accurate for large h, results in a better representation of the evolution of $\langle q \rangle$ than using the original *linear explicit* expression as well. Near the end of the day, the value of $\langle q \rangle$ as obtained by the *linear explicit*

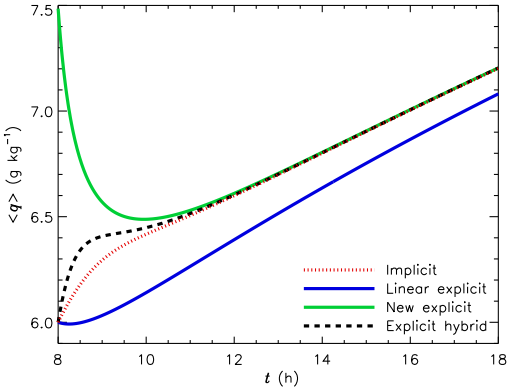

Figure 3.4: Evolution of $\langle q \rangle$ as calculated by Eq. (3.31) *using the different expressions for the boundary-layer height evolution that are shown in Fig. 3.3b. These expressions are the implicit solution for h, the old explicit solution that assumes $\Delta\theta$ to be linearly dependent on h and the new explicit simplification. Finally, the black line shows the evolution if the hybrid explicit solution for h is used.*

expression is an underestimation of 0.12 g kg^{-1}, which is 10 % of the total increase in $\langle q \rangle$ during the day, 1.2 g kg^{-1}. This underestimation can significantly affect ABL representations (Vilà-Guerau de Arellano, 2007), e.g. by inaccurately predicting the timing of saturation at the top of the boundary layer and the subsequent formation of clouds.

To predict the final boundary-layer height using the different expressions, only the integrated value of the surface heat flux is of importance and not its specific distribution over the day. This is shown in Fig. 3.5. In Fig. 3.5a, the situation without moisture from Table 3.1 is repeated. In Fig. 3.5b, this case is adapted to consider a more realistic, sinus-shaped evolution of the surface heat flux. For fair comparison the maximum value of this sinus is selected such that over the 10 hours of simulation, the integrated surface heat flux is equal to the original situation. To this end, we prescribe a surface heat flux of

$$\overline{w'\theta'}_{0,\text{Sine}}(t) = \frac{\pi}{2}\overline{w'\theta'}_0 \sin\left(\frac{\pi t}{T}\right), \tag{3.39}$$

where t is the elapsed time since the start of the simulation and T is the simulated period, both of which should be expressed in the same units. Due to the different distribution in time of the surface heat flux, the timing of the boundary-layer height evolution changed, but the final boundary-layer properties are identical. Because of the low heat fluxes at the start and at the end of the day, the ABL growth is much slower in these phases, resulting in more curved shapes for the boundary-layer height evolutions.

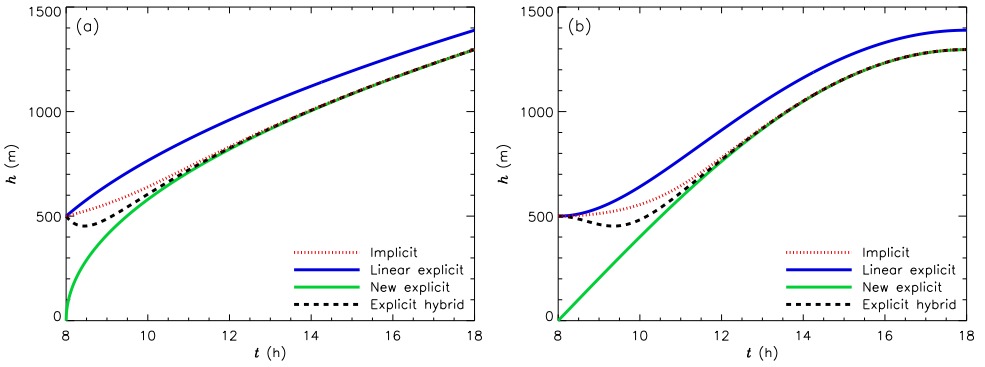

Figure 3.5: Boundary-layer height evolution representations for, **a)** *a constant, and* **b)** *a sinus-shaped surface heat flux. Each panel shows the implicit solution for h, the old explicit solution that assumes $\Delta\theta$ to be linearly dependent on h and the new explicit simplification, which ignores the second term of the l.h.s. of the implicit expression (Eq.* (3.23)*). This term falls with $h^{\frac{1}{\beta}}$. Finally, the black line shows the hybrid explicit solution, which is obtained by substituting the linear explicit solution into the h of the aforementioned term of Eq.* (3.23)*.*

3.3.4 Sensitivity of h

An advantage of having the analytical solution for h (Eq. (3.24)) is the possibility of studying its sensitivity to different initial and boundary conditions. h depends on five variables: β, γ_{θ_v}, h_0, $\Delta\theta_{v,0}$ and I, where I is the time-integrated surface buoyancy flux.

$$I = \int_{t_0}^{t} \overline{w'\theta'_{v0}} \mathrm{d}t. \tag{3.40}$$

Defining the initial virtual temperature deficit, $D_{v,0}$, as

$$D_{v,0} = \Delta\theta_{v,0} h_0 - \frac{1}{2}\gamma_{\theta_v} h_0^2, \tag{3.41}$$

squaring Eq. (3.24) results in

$$h^2 = \frac{2+4\beta}{\gamma_{\theta_v}} \left(I - D_{v,0}\right). \tag{3.42}$$

Similar to previous work by Driedonks (1982b) for β, γ_{θ_v} and I, by differentiating this expression to the five different governing variables of Eq. (3.24) we can derive

$$\frac{\partial h}{h} = \left(\frac{\beta}{1+2\beta}\right)\frac{\partial \beta}{\beta} \qquad \text{for } \beta, \tag{3.43}$$

$$\frac{\partial h}{h} = -\left(\frac{1}{2} - \frac{\gamma_{\theta_v} h0^2}{4\,(I - D_{v,0})}\right)\frac{\partial \gamma_{\theta_v}}{\gamma_{\theta_v}} \qquad \text{for } \gamma_{\theta_v}, \tag{3.44}$$

$$\frac{\partial h}{h} = \frac{I}{2\,(I - D_{v,0})}\frac{\partial I}{I} \qquad \text{for } I, \tag{3.45}$$

$$\frac{\partial h}{h} = \frac{\gamma_{\theta_v} h_0^2 - \Delta\theta_{v,0} h_0}{2\,(I - D_{v,0})}\frac{\partial h_0}{h_0} \qquad \text{for } h_0, \tag{3.46}$$

$$\frac{\partial h}{h} = -\frac{\Delta\theta_{v,0} h_0}{2\,(I - D_{v,0})}\frac{\partial \Delta\theta_{v,0}}{\Delta\theta_{v,0}} \qquad \text{for } \Delta\theta_{v,0}. \tag{3.47}$$

Note that in this analysis one should consider that $D_{v,0}$ is also dependent on $\Delta\theta_{v,0}$, h_0 and γ_{θ_v}. This consideration explains the difference between the presented Eq. (3.44) and Eq. (16) of Driedonks (1982b).

The sensitivity of h to a change in any arbitrary variable, ψ is expressed as $\left(\frac{\partial h}{h}\right) / \left(\frac{\partial \psi}{\psi}\right)$. To evaluate the importance of the different variables, these sensitivities are evaluated for the conditions of Table 3.1 with moisture. Similar to Driedonks (1982b), for each of the five variables a range of possible values is determined, which is expressed as a percentage of the original value from Table 3.1. By multiplying this range with the sensitivity, the resulting range in h compared to the original value of 1436 m is found. β is assumed to be between 0.1 and 0.3 (Stull, 1988) and γ_{θ_v} is estimated to be between 3×10^{-3} and 7×10^{-3} K m^{-1}. The influence of the integrated heat flux is evaluated for a positive or negative change of 30 % (Driedonks, 1982b). Values for h_0 are considered to be higher than 300 m and lower than 700 m. Finally, $\Delta\theta_{v,0}$ is assumed to deviate at most 1 K compared to the original value. The results are summarized in Table 3.2. This shows that if all variables were to be perturbed by the same percentage, the changes in γ_{θ_v} and I would influence h most with their absolute sensitivities of 42 % and 48 %, respectively. For the chosen typical values, the resulting relative ranges in h are largest for these two variables as well, even though their own relative ranges are smaller than those of the other variables.

Further extending on the sensitivity analysis performed by Driedonks (1982b), the calculated sensitivities are presented as dashed lines in Fig. 3.6. Additionally, the true relative deviations in the boundary-layer height, determined by Eq. (3.24), are drawn with solid lines. The solid lines deviate from the linear dashed lines, since for all initial and boundary conditions, ψ, the sensitivities are dependent on ψ itself. For example, Eq. (3.43) shows $\left(\frac{\partial h}{h}\right) / \left(\frac{\partial \beta}{\beta}\right) = \frac{\beta}{1+2\beta}$. However, even for γ_{θ_v}, where this deviation of the solid line from the

Table 3.2: Sensitivity of the boundary-layer height, h, after 10 hours of simulation to the different initial and boundary conditions. The sensitivity of h to a change in any arbitrary variable, ψ, is expressed as $\left(\frac{\partial h}{h}\right) / \left(\frac{\partial \psi}{\psi}\right)$. The property range expresses for every variable, ψ, the range $\max_\psi - \min_\psi$ as a percentage of the standard value of ψ, which is based on Table 3.1. The standard values that cannot be read directly from that table are $\gamma_{\theta_v} = 6{\times}10^{-3}$ K m^{-1}, $I = 4250$ K m and $\Delta\theta_{v,0} = 1.15$ K. The last column presents the resulting relative range in h.

Property		Sensitivity	Min	Max	Property range	*h* range
β	(−)	0.14	0.1	0.3	100 %	14 %
γ_{θ_v}	$\left(\text{K m}^{-1}\right)$	-0.42	$3 \cdot 10^{-3}$	$7 \cdot 10^{-3}$	67 %	28 %
I	(K m)	0.48	2975	5525	60 %	29 %
h_0	(m)	0.10	300	700	80 %	8 %
$\Delta\theta_{v,0}$	(K)	-0.06	0.15	2.15	174 %	11 %

dashed line is most present, the effect is insignificant as long as the relative deviation in the condition remains < 20 %.

To conclude, Fig. 3.6 displays the application of Eq. (3.24) to study the response of h to a wide range of initial and boundary conditions by two different methods. For the first method the equation is used to determine a sensitivity to these conditions, which can be used to relate changes in the conditions to changes in the boundary-layer height with a single number. The second method is to plot the solution as a function of these conditions to study the exact response of h for a larger range. The same analyses can be applied to study the sensitivity of other variables, such as $\langle\theta\rangle$, by using Eq. (3.31) or (3.34).

3.3.5 Subsidence

In this study, cases with large-scale atmospheric subsidence are not considered. The analytical solutions, which were originally derived for a basic situation without subsidence, could not be extended to include this effect. To understand why this is not possible with the currently applied mathematical method, one needs to consider a basic, dry situation with subsidence, a certain boundary-layer height, $h = h_0$, and a certain potential temperature jump, $\Delta\theta = \Delta\theta_0$. In this situation, it can be deduced that $\Delta\theta$ is not only dependent on h, but also on time. If the effect of subsidence can be ignored and the boundary-layer height changes due to entrainment, $\Delta\theta$ changes with height, independent of the time it takes to reach the new height. Therefore, if the changes in the boundary-layer height occur in a very short time period, so that the effects of subsidence are infinitesimally small, in general $\Delta\theta \neq \Delta\theta_0$ if $h \neq h_0$. However, if the entrainment process is slow compared to subsidence, the boundary-layer height decreases due to the subsidence. During this process, $\Delta\theta$ remains equal to $\Delta\theta_0$ as the subsiding motions do not alter the potential temperatures below and just above the inversion. In

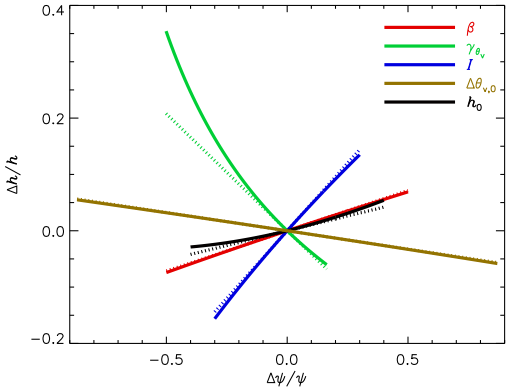

Figure 3.6: Sensitivity of the final boundary-layer height, h, to different initial and boundary conditions, ψ. The horizontal axis denotes the relative change in these conditions compared to the standard case (Table 3.1 with moisture). The vertical axis denotes the resulting relative change in h. Solid lines show the true deviations, which are determined using Eq. (3.24)*. Dashed lines are linearisations based on* $\frac{\mathrm{d}h}{\mathrm{d}\psi}$ *for the standard case, multiplied by* $\Delta\psi$*.*

this case $\Delta\theta = \Delta\theta_0$ for a certain $h < h_0$. If then (a sudden burst of) entrainment compensates the decrease in the boundary-layer height, the potential temperature jumps again changes, resulting in a different value than $\Delta\theta_0$. Therefore $\Delta\theta \neq \Delta\theta_0$ for $h = h_0$ if $t > t_0$.

This thought experiment shows that, if subsidence is present, $\Delta\theta$ is not only a function of h, but also of time. To solve Eq. (3A.22), resulting in Eq. (3A.43) through Eq. (3A.41), separation of variables is applied. $\Delta\theta$ is expressed as a function of h, $f(h)$, and h is expressed as a function of t, $g(t)$. Equation (3A.22) then results in $f(h)\frac{\mathrm{d}h}{\mathrm{d}t} = g(t)$ and, subsequently, $f(h)\mathrm{d}h = g(t)\mathrm{d}t$. This latter expression can be solved by simple integration. However, since $\Delta\theta$ is also dependent on time, $\Delta\theta = f(h,t)$. The resulting $f(h,t)\frac{\mathrm{d}h}{\mathrm{d}t} = g(t)$ could only be solved by separation of variables if $f(h,t)$ could be split into $f_1(h)\cdot f_2(t)$, which is not possible because h is dependent on t as well.

To the authors' knowledge, in the previous literature only Carson (1973) presents an analytical solution that accounts for subsidence. However, to arrive at his solution he assumes that $\Delta\theta$ scales linearly with h. Next to the influence of the initial conditions, they therefore directly ignore the dependence of $\Delta\theta$ on time. As such, this results in a first approximation of the boundary-layer height evolution rather than an exact solution.

3.4 Conclusions

The prognostic equations for a diurnal convective boundary layer are analytically solved. Compared to the most advanced solution in the literature, the results are expanded upon by including the effects of specific humidity. The resulting equations are an implicit expression for the boundary-layer height, due to the non-linear dependence of h on $\Delta\theta$, and explicit expressions for boundary-layer averaged scalars that are a function of the boundary-layer height and the time integral of their respective surface fluxes. As the ABL height cannot be directly derived from the implicit solution, an explicit simplification is presented that exactly captures the ABL height evolution for relatively large h. The differences between this expression and expressions for h of previous studies are clear for the cases under study. However, for relatively small h the mismatch between this simplification and the true boundary-layer height can be significant.

We therefore introduce an expression that enables us to determine the height at which a certain accuracy has been reached compared to the true boundary-layer height. To complete our analysis, a hybrid expression for h is derived. For this expression, the solution presented in the previous literature is substituted into the term of the implicit expression for h that becomes negligible for relatively large h. By doing so, an expression is obtained that represents the boundary-layer height evolution reasonably well for relatively small h and becomes the exact solution for larger h. Therefore, this expression could be used to predict the diurnal ABL height evolution without numerical solving the governing equations. As a result, evolutions of boundary-layer properties and dependencies of the height on other variables can be analytically determined, as demonstrated with our sensitivity analysis.

Sensitivity analyses by numerical solutions are always restricted to a limited amount of samples of the driving variable in question, while they are continuous expressions when using analytical solutions. As such, compared to previously obtained numerical solutions, the analytical solutions enable us to improve our understanding and discussion of the evolution of boundary-layer dynamics. This is very useful for research and educational purposes. Here, we explored the dependence of h on the five driving variables identified from the exact implicit expression. Next to using sensitivity analyses, the evolution of the boundary-layer height is expressed with dimensionless groups. This expression clearly shows that the growth of the boundary layer is governed by the difference between the scaled time-integrated surface buoyancy flux and the relative strength of the initial virtual potential temperature jump compared to the free tropospheric virtual potential temperature profile. Possible applications for an analytical expression of the boundary-layer height evolution include calculating the potential temperature deficit and resulting latent and sensible heat fluxes (e.g., Raupach, 2000), and analyzing the uncertainties in the determination of the CO2 budget that are associated with the boundary-layer dynamics (Pino et al., 2012).

3A Appendix: Analytical derivation

3A.1 Governing equations

We derive the governing equations for the mixed-layer slab model without subsidence from the conservation equation for heat with a budget analysis. The resulting equations are equal to the ones that are derived by integrating over height between the surface and a position at an infinitesimally small distance below the boundary-layer height and integrating over a infinitesimally thin layer around the interface between the mixed layer and the free troposphere (e.g., Lilly, 1968; Garratt, 1992).

The following derivation is executed for a situation in which specific humidity, q, is 0. In Sect. 3A.5, the equations are expanded to account for the effects of q.

We assume the vertical profiles of scalars to be characterized with a constant value in the boundary layer, a discontinuity at the top of the boundary layer (at the inversion height) and a linear profile in the free troposphere (Tennekes, 1973; Tennekes and Driedonks, 1981; Garratt, 1992). Mixed-layer slab averaged values of any arbitrary scalar, ϕ, are denoted by $\langle\phi\rangle$.

$$\langle\phi\rangle = \frac{1}{h - z_0} \int_{z_0}^{h} \phi(z) \mathrm{d}z, \tag{3A.1}$$

where z_0 and h are the roughness length and the boundary-layer height, respectively. The potential temperature jump at the inversion, $\Delta\theta$, is defined by

$$\Delta\theta = \theta_{\mathrm{FT}}(h) - \langle\theta\rangle\,. \tag{3A.2}$$

In this equation, θ_{FT} is the potential temperature in the free troposphere, h is the mixed-layer height and, therefore, the position of the interface with the free troposphere, and $\langle\theta\rangle$ is the potential temperature in the mixed layer. The potential temperature of the free troposphere follows a linear profile, expressed by

$$\theta_{\mathrm{FT}}\,(z) = \gamma_\theta\,(z - h_0) + \theta_{\mathrm{FT}}\,(h_0)\,, \tag{3A.3}$$

in which h_0 is the initial height of the mixed layer and γ_θ is the free tropospheric lapse rate for potential temperature. Taking the time derivative of Eq. (3A.2) results in

$$\frac{\mathrm{d}\Delta\theta}{\mathrm{d}t} = \frac{\mathrm{d}\theta_{\mathrm{FT}}(h)}{\mathrm{d}t} - \frac{\mathrm{d}\,\langle\theta\rangle}{\mathrm{d}t}, \tag{3A.4}$$

$$= \frac{\partial\theta_{\mathrm{FT}}(h)}{\partial h}\frac{\mathrm{d}h}{\mathrm{d}t} - \frac{\mathrm{d}\,\langle\theta\rangle}{\mathrm{d}t}. \tag{3A.5}$$

Substituting θ_{FT} by Eq. (3A.2),

$$\frac{\mathrm{d}\Delta\theta}{\mathrm{d}t} = \gamma_\theta \frac{\mathrm{d}h}{\mathrm{d}t} - \frac{\mathrm{d}\langle\theta\rangle}{\mathrm{d}t}. \tag{3A.6}$$

Since no sources or sinks of heat are present in the mixed layer itself, the conservation of heat is expressed by

$$\frac{\mathrm{d}Q}{\mathrm{d}t} = Q_{\mathrm{in,bottom}} + Q_{\mathrm{in,top}}. \tag{3A.7}$$

The total heat, Q, is defined by

$$Q = \rho c_p V \langle\theta\rangle \tag{3A.8}$$

$$= \rho c_p A h \langle\theta\rangle, \tag{3A.9}$$

where ρ is the air density, c_p is the specific heat capacity of air, V is the volume of the mixed layer and A is the surface area over which the mixed layer is evaluated. In mixed-layer theory, ρ is approximated to be a constant value (Stull, 1988). For any arbitrary variable, ϕ, its Reynolds averaged value is expressed by $\overline{\phi}$ and its deviations from the average by ϕ', so that $\phi = \overline{\phi} + \phi'$. $Q_{\mathrm{in,bottom}}$ is the incoming heat through the interface near the surface. $Q_{\mathrm{in,bottom}} = \rho c_p A \overline{w\theta}_0$ where $\overline{w} = 0$ so $Q_{\mathrm{in,bottom}} = \rho c_p A \overline{w'\theta'}_0$ for Reynolds averaged fluxes. At the interface between the mixed layer and the free troposphere, the incoming heat is due to the transport of air from the free troposphere into the mixed layer by entrainment. The rate with which this air enters is linked to the evolution of the boundary-layer height by $A\frac{\mathrm{d}h}{\mathrm{d}t}$ and the heat per volume of air is expressed by $\rho c_p \theta_{\mathrm{FT}}(h)$. This results in $Q_{\mathrm{in,top}} = \rho c_p A \frac{\mathrm{d}h}{\mathrm{d}t} \theta_{\mathrm{FT}}(h)$. In total,

$$\frac{\mathrm{d}\rho c_p A h \langle\theta\rangle}{\mathrm{d}t} = \rho c_p A \overline{w'\theta'}_0 + \rho c_p A \frac{\mathrm{d}h}{\mathrm{d}t} \theta_{\mathrm{FT}}(h). \tag{3A.10}$$

Since A, ρ and c_p are constant,

$$\frac{\mathrm{d}h\langle\theta\rangle}{\mathrm{d}t} = \overline{w'\theta'}_0 + \frac{\mathrm{d}h}{\mathrm{d}t}\theta_{\mathrm{FT}}(h), \tag{3A.11}$$

$$\frac{\mathrm{d}h}{\mathrm{d}t}\langle\theta\rangle + h\frac{\mathrm{d}\langle\theta\rangle}{\mathrm{d}t} = \overline{w'\theta'}_0 + \frac{\mathrm{d}h}{\mathrm{d}t}\theta_{\mathrm{FT}}(h), \tag{3A.12}$$

$$h\frac{\mathrm{d}\langle\theta\rangle}{\mathrm{d}t} = \overline{w'\theta'}_0 + \frac{\mathrm{d}h}{\mathrm{d}t}\left(\theta_{\mathrm{FT}}(h) - \langle\theta\rangle\right). \tag{3A.13}$$

As the introduced heating at the top of the boundary layer due to $Q_{\mathrm{in,top}}$, is further transported downward, the turbulent flux at the top of the boundary layer, $\overline{w'\theta'}_h$, is equal to the transport

of energy through the interface between the two atmospheric layers and

$$\rho c_p A \frac{\mathrm{d}h}{\mathrm{d}t} \left(\theta_{\mathrm{FT}}\left(h\right) - \left\langle\theta\right\rangle\right) = -\rho c_p A \overline{w'\theta'}_h. \tag{3A.14}$$

By using Eq. (3A.2), Eq. (3A.14) becomes

$$\overline{w'\theta'}_h = -\Delta\theta \frac{\mathrm{d}h}{\mathrm{d}t}, \tag{3A.15}$$

and Eq. (3A.13) results in

$$\frac{\mathrm{d}\left\langle\theta\right\rangle}{\mathrm{d}t} = \frac{\overline{w'\theta'}_0 - \overline{w'\theta'}_h}{h}. \tag{3A.16}$$

Summarizing, the final system consists of 3 governing equations,

$$\frac{\mathrm{d}h}{\mathrm{d}t} = -\frac{\overline{w'\theta'}_h}{\Delta\theta}, \tag{3A.17}$$

$$\frac{\mathrm{d}\left\langle\theta\right\rangle}{\mathrm{d}t} = \frac{\overline{w'\theta'}_0 - \overline{w'\theta'}_h}{h}, \tag{3A.18}$$

$$\frac{\mathrm{d}\Delta\theta}{\mathrm{d}t} = \gamma_\theta \frac{\mathrm{d}h}{\mathrm{d}t} - \frac{\mathrm{d}\left\langle\theta\right\rangle}{\mathrm{d}t}, \tag{3A.19}$$

with 4 unknowns $\left(h, \left\langle\theta\right\rangle, \Delta\theta, \overline{w'\theta'}_h\right)$ as γ_θ and $\overline{w'\theta'}_0$ are prescribed. A common closure assumption (Stull, 1988) to solve this is

$$\overline{w'\theta'}_h = -\beta \overline{w'\theta'}_0. \tag{3A.20}$$

β is the entrainment constant, which is usually assumed to be equal to $\beta = 0.2$. Equation (3A.18) then becomes

$$\frac{\mathrm{d}\left\langle\theta\right\rangle}{\mathrm{d}t} = \left(1 + \beta\right) \frac{\overline{w'\theta'}_0}{h} \tag{3A.21}$$

3A.2 Dependence of potential temperature on ABL height

In this section the dependency of the mixed-layer slab averaged potential temperature, $\langle\theta\rangle$, and the potential temperature jump at the inversion, $\Delta\theta$, on the boundary-layer height are

determined. First, the dependence of $\Delta\theta$ on h is derived. Based on Eqs. (3.1), (3.5) and (3.6),

$$\begin{aligned}\Delta\theta\frac{\mathrm{d}h}{\mathrm{d}t} &= \beta\overline{w'\theta'}_0 \\ &= \left(\frac{\beta}{1+\beta}\right)h\frac{\mathrm{d}\langle\theta\rangle}{\mathrm{d}t}.\end{aligned} \tag{3A.22}$$

Combined with Eq. (3.3), this results in

$$\begin{aligned}\Delta\theta\frac{\mathrm{d}h}{\mathrm{d}t} &= \left(\frac{\beta}{1+\beta}\right)h\left(\gamma_\theta\frac{\mathrm{d}h}{\mathrm{d}t} - \frac{\mathrm{d}\Delta\theta}{\mathrm{d}t}\right), \\ (1+\beta)\,\Delta\theta\frac{\mathrm{d}h}{\mathrm{d}t} &= \beta\gamma_\theta h\frac{\mathrm{d}h}{\mathrm{d}t} - \beta h\frac{\mathrm{d}\Delta\theta}{\mathrm{d}t}.\end{aligned} \tag{3A.23}$$

In this equation, the dependency on time can be removed by using $\frac{\mathrm{d}\Delta\theta}{\mathrm{d}t} = \frac{\partial\Delta\theta}{\partial h}\frac{\mathrm{d}h}{\mathrm{d}t}$ and dividing by $\frac{\mathrm{d}h}{\mathrm{d}t}$.

$$(1+\beta)\,\Delta\theta = \beta\gamma_\theta h - \beta h\frac{\mathrm{d}\Delta\theta}{\mathrm{d}h}, \tag{3A.24}$$

$$\frac{\mathrm{d}\Delta\theta}{\mathrm{d}h} = \gamma_\theta - \left(\frac{1+\beta}{\beta}\right)\frac{\Delta\theta}{h}. \tag{3A.25}$$

To solve this equation, a substitution is performed by $f \equiv \frac{\mathrm{d}\Delta\theta}{\mathrm{d}h}$, resulting in

$$f = \gamma_\theta - \left(\frac{1+\beta}{\beta}\right)\frac{\Delta\theta}{h}, \tag{3A.26}$$

$$\frac{\mathrm{d}f}{\mathrm{d}h} = -\left(\frac{1+\beta}{\beta}\right)\left(-\frac{\Delta\theta}{h^2} + \frac{1}{h}\frac{\mathrm{d}\Delta\theta}{\mathrm{d}h}\right), \tag{3A.27}$$

$$\frac{\mathrm{d}\Delta\theta}{\mathrm{d}h} = \frac{\Delta\theta}{h} - \left(\frac{\beta}{1+\beta}\right)h\frac{\mathrm{d}f}{\mathrm{d}h}. \tag{3A.28}$$

Combined with Eq. (3A.25) this leads to

$$\begin{aligned}\frac{\Delta\theta}{h} - \left(\frac{\beta}{1+\beta}\right)h\frac{\mathrm{d}f}{\mathrm{d}h} &= \gamma_\theta - \left(\frac{1+\beta}{\beta}\right)\frac{\Delta\theta}{h}, \\ \left(\frac{\beta}{1+\beta}\right)h\frac{\mathrm{d}f}{\mathrm{d}h} &= -\gamma_\theta - \left(\frac{1+2\beta}{\beta}\right)\frac{\Delta\theta}{h}.\end{aligned} \tag{3A.29}$$

By using the relation from Eq. (3A.26) it is found that

$$\left(\frac{\beta}{1+\beta}\right) h \frac{\mathrm{d}f}{\mathrm{d}h} = -\gamma_\theta + \left(\frac{1+2\beta}{\beta}\right)\left(\frac{\beta}{1+\beta}\right)(\gamma_\theta - f)\,, \tag{3A.30}$$

$$\beta h \frac{\mathrm{d}f}{\mathrm{d}h} = \beta\gamma_\theta - (1+2\beta)\, f. \tag{3A.31}$$

This can be rewritten as

$$\frac{\mathrm{d}f}{f - \left(\frac{\beta}{1+2\beta}\right)\gamma_\theta} = -\left(\frac{1+2\beta}{\beta}\right)\frac{\mathrm{d}h}{h}, \tag{3A.32}$$

$$\ln\left(f - \left(\frac{\beta}{1+2\beta}\right)\gamma_\theta\right) = -\left(\frac{1+2\beta}{\beta}\right)\ln(h) + c_1, \tag{3A.33}$$

in which c_1 is a constant that is still undetermined. This results in

$$f - \left(\frac{\beta}{1+2\beta}\right)\gamma_\theta = c_2 h^{-\frac{1+2\beta}{\beta}}. \tag{3A.34}$$

In this equation, $c_2 = \mathrm{e}^{c_1}$. Combined with Eq. (3A.26) it is found that

$$\left(\frac{1+\beta}{1+2\beta}\right)\gamma_\theta - \left(\frac{1+\beta}{\beta}\right)\frac{\Delta\theta}{h} = c_2 h^{-\frac{1+2\beta}{\beta}},$$

$$\frac{\Delta\theta}{h} = \left(\frac{\beta}{1+2\beta}\right)\gamma_\theta - \left(\frac{\beta}{1+\beta}\right)c_2 h^{-\frac{1+2\beta}{\beta}}. \tag{3A.35}$$

In total,

$$\Delta\theta = \left(\frac{\beta}{1+2\beta}\right)\gamma_\theta h + c_3 h^{-\frac{1+\beta}{\beta}}, \tag{3A.36}$$

where $c_3 = -\left(\frac{\beta}{1+\beta}\right)c_2$. The value of c_3 can be derived by evaluating the initial state where $(t, h, \Delta\theta, \langle\theta\rangle) = (t_0, h_0, \Delta\theta_0, \langle\theta\rangle_0)$. It follows that

$$c_3 = h_0^{\frac{1+\beta}{\beta}}\left(\Delta\theta_0 - \left(\frac{\beta}{1+2\beta}\right)\gamma_\theta h_0\right) \tag{3A.37}$$

and

$$\Delta\theta = \left(\frac{\beta}{1+2\beta}\right)\gamma_\theta h + \left(\Delta\theta_0 h_0^{\frac{1+\beta}{\beta}} - \left(\frac{\beta}{1+2\beta}\right)\gamma_\theta h_0^{\frac{1+2\beta}{\beta}}\right)h^{-\frac{1+\beta}{\beta}}. \tag{3A.38}$$

By integrating Eq. (3.3) over time, the dependency of the mixed-layer averaged potential temperature, $\langle\theta\rangle$, on h is found.

$$\begin{aligned}\Delta\theta - \Delta\theta_0 &= \gamma_\theta\,(h - h_0) - (\langle\theta\rangle - \langle\theta\rangle_0)\,,\\ \langle\theta\rangle &= \langle\theta\rangle_0 - \gamma_\theta h_0 + \Delta\theta_0 + \gamma_\theta h - \Delta\theta.\end{aligned} \tag{3A.39}$$

By substituting Eq. (3A.38), this results in

$$\langle\theta\rangle = \langle\theta\rangle_0 - \gamma_\theta h_0 + \Delta\theta_0 + \left(\frac{1+\beta}{1+2\beta}\right)\gamma_\theta h - \left(\Delta\theta_0 h_0^{\frac{1+\beta}{\beta}} - \left(\frac{\beta}{1+2\beta}\right)\gamma_\theta h_0^{\frac{1+2\beta}{\beta}}\right)h^{-\frac{1+\beta}{\beta}}. \tag{3A.40}$$

3A.3 Evolution of the boundary-layer height

With the previously determined relations, the time evolution of the boundary-layer height is derived. Equations (3A.22) and (3A.38) combine to

$$\left(\left(\frac{\beta}{1+2\beta}\right)\gamma_\theta h + \left(\Delta\theta_0 h_0^{\frac{1+\beta}{\beta}} - \left(\frac{\beta}{1+2\beta}\right)\gamma_\theta h_0^{\frac{1+2\beta}{\beta}}\right)h^{-\frac{1+\beta}{\beta}}\right)\frac{\mathrm{d}h}{\mathrm{d}t} = \beta\overline{w'\theta'}_0, \tag{3A.41}$$

$$\frac{\mathrm{d}}{\mathrm{d}t}\left(\left(\frac{\beta}{1+2\beta}\right)\frac{\gamma_\theta}{2}h^2 - \beta\left(\Delta\theta_0 h_0^{\frac{1+\beta}{\beta}} - \left(\frac{\beta}{1+2\beta}\right)\gamma_\theta h_0^{\frac{1+2\beta}{\beta}}\right)h^{-\frac{1}{\beta}}\right) = \beta\overline{w'\theta'}_0. \tag{3A.42}$$

Integrating this equation over time results in

$$\left(\frac{\gamma_\theta}{2+4\beta}\right)\left(h^2 - h_0^2\right) - \left(\Delta\theta_0 h_0^{\frac{1+\beta}{\beta}} - \left(\frac{\beta}{1+2\beta}\right)\gamma_\theta h_0^{\frac{1+2\beta}{\beta}}\right)\left(h^{-\frac{1}{\beta}} - h_0^{-\frac{1}{\beta}}\right) = \int_{t_0}^{t}\overline{w'\theta'}_0\mathrm{d}t. \tag{3A.43}$$

This is rewritten to the implicit analytical solution

$$\begin{aligned}h^2 - \left(\frac{2+4\beta}{\gamma_\theta}\right)\left(\Delta\theta_0 h_0^{\frac{1+\beta}{\beta}} - \left(\frac{\beta}{1+2\beta}\right)\gamma_\theta h_0^{\frac{1+2\beta}{\beta}}\right)h^{-\frac{1}{\beta}} =\\ h_0^2 - \left(\frac{2+4\beta}{\gamma_\theta}\right)\left(\Delta\theta_0 h_0 - \left(\frac{\beta}{1+2\beta}\right)\gamma_\theta h_0^2\right) + \left(\frac{2+4\beta}{\gamma_\theta}\right)\int_{t_0}^{t}\overline{w'\theta'}_0\mathrm{d}t.\end{aligned} \tag{3A.44}$$

Limit for large h

Equation (3A.44) can be denoted as

$$\begin{aligned}h^2\left(1 - \left(\frac{2+4\beta}{\gamma_\theta}\right)\left(\Delta\theta_0 h_0^{\frac{1+\beta}{\beta}} - \left(\frac{\beta}{1+2\beta}\right)\gamma_\theta h_0^{\frac{1+2\beta}{\beta}}\right)h^{-\frac{1+2\beta}{\beta}}\right) =\\ h_0^2 - \left(\frac{2+4\beta}{\gamma_\theta}\right)\left(\Delta\theta_0 h_0 - \left(\frac{\beta}{1+2\beta}\right)\gamma_\theta h_0^2\right) + \left(\frac{2+4\beta}{\gamma_\theta}\right)\int_{t_0}^{t}\overline{w'\theta'}_0\mathrm{d}t.\end{aligned} \tag{3A.45}$$

For 'large' h, the term with $h^{-\frac{1+2\beta}{\beta}}$ on the l.h.s. can be neglected. This is the case if

$$h \gg \left[\left(\frac{2+4\beta}{\gamma_\theta}\right)\left(\Delta\theta_0 h_0^{\frac{1+\beta}{\beta}} - \left(\frac{\beta}{1+2\beta}\right)\gamma_\theta h_0^{\frac{1+2\beta}{\beta}}\right)\right]^{\frac{\beta}{1+2\beta}}. \tag{3A.46}$$

For these situations, Eq. (3A.45) simplifies to

$$h \approx \sqrt{h_0^2 - \left(\frac{2+4\beta}{\gamma_\theta}\right)\left(\Delta\theta_0 h_0 - \left(\frac{\beta}{1+2\beta}\right)\gamma_\theta h_0^2\right) + \left(\frac{2+4\beta}{\gamma_\theta}\right)\int_{t_0}^{t}\overline{w'\theta'}_0 \mathrm{d}t} \tag{3A.47}$$

The accuracy of this expression is dependent on the initial conditions. It can be derived that Eq. (3A.47) is valid within an accuracy of α if

$$\begin{cases} h \geq (1-\alpha)\left(\left(\frac{2+4\beta}{\gamma_\theta}\right)\frac{\Delta\theta_0 h_0^{\frac{1+\beta}{\beta}} - \left(\frac{\beta}{1+2\beta}\right)\gamma_\theta h_0^{\frac{1+2\beta}{\beta}}}{\alpha(2-\alpha)}\right)^{\frac{\beta}{1+2\beta}} & \text{if} \quad \Delta\theta_0 > \left(\frac{\beta}{1+2\beta}\right)\gamma_\theta h_0, \\ h \geq (1+\alpha)\left(\left(\frac{2+4\beta}{\gamma_\theta}\right)\frac{\left(\frac{\beta}{1+2\beta}\right)\gamma_\theta h_0^{\frac{1+2\beta}{\beta}} - \Delta\theta_0 h_0^{\frac{1+\beta}{\beta}}}{\alpha(2+\alpha)}\right)^{\frac{\beta}{1+2\beta}} & \text{if} \quad \Delta\theta_0 < \left(\frac{\beta}{1+2\beta}\right)\gamma_\theta h_0, \end{cases}$$

where h is the boundary-layer height that is calculated using this simplified equation.

3A.4 Evolution of scalars

Consider any scalar, ϕ, without sources and sinks in the boundary layer. These scalars include potential temperature, θ, specific humidity, q, and mixing ratios of inert chemical species (e.g., c_{CO_2}, c_{CH_4}). If the initial vertical profile is characterized by a constant value in the mixed layer, $\langle\phi\rangle_0$, a jump at the top of this layer, $\Delta\phi_0$, and a linear profile in the free troposphere aloft. If the increase with height in the free troposphere is expressed by the tropospheric lapse rate, γ_ϕ, and the surface flux is denoted as $\overline{w'\phi'}_0$, then a mass budget below the current boundary-layer height, $h(t)$, leads to

$$A\int_0^{h(t)}\phi_0(z)\,\mathrm{d}z + \int_{t_0}^{t}A\overline{w'\phi'}_0\mathrm{d}t = A\int_0^{h(t)}\phi(z)\,\mathrm{d}z, \tag{3A.48}$$

where A is the surface area under consideration.

$$h\langle\phi\rangle_0 + \int_{h_0}^{h}\left(\Delta\phi_0 + \gamma_\phi(z-z_0)\right)\mathrm{d}z + \int_{t_0}^{t}\overline{w'\phi'}_0\mathrm{d}t = h\langle\phi\rangle. \tag{3A.49}$$

Therefore, if the initial profile, the current boundary-layer height and the surface exchange as function of time are known, the current mixed-layer averaged scalar is expressed as

$$\langle\phi\rangle = \langle\phi\rangle_0 + \frac{h-h_0}{h}\Delta\phi_0 + \frac{\gamma_\phi}{2}\frac{(h-h_0)^2}{h} + \frac{1}{h}\int_{t_0}^{t}\overline{w'\phi'}_0 \mathrm{d}t. \tag{3A.50}$$

3A.5 Including specific humidity effects

If the specific humidity, q in kg kg^{-1}, is non-zero, the driving variable for convection is not the standard potential temperature, θ, but the virtual potential temperature, θ_v, (Stull, 1988).

$$\theta_v = \theta\,(1 + 0.61q)\,, \tag{3A.51}$$

$$\overline{w'\theta'_v} \approx 0.61\,\overline{\theta}\,\overline{w'q'} + (1 + 0.61\,\overline{q})\,\overline{w'\theta'}, \tag{3A.52}$$

and Eq. (3.5) is replaced by

$$\overline{w'\theta'_v}_h = -\beta\overline{w'\theta'_v}_0. \tag{3A.53}$$

Similar to the potential temperature, it is assumed that the vertical profile of the specific humidity is constant in the mixed layer with a jump on top and a linear profile in the free tropospheric layer aloft. Similar to Eqs. (3.1), (3.2) and (3.3), q is governed by

$$\overline{w'q'}_h = -\frac{\mathrm{d}h}{\mathrm{d}t}\Delta q, \tag{3A.54}$$

$$\frac{\mathrm{d}\langle q\rangle}{\mathrm{d}t} = \frac{\overline{w'\theta'}_0 - \overline{w'\theta'}_h}{h}, \tag{3A.55}$$

$$\frac{\mathrm{d}\Delta q}{\mathrm{d}t} = \gamma_q\frac{\mathrm{d}h}{\mathrm{d}t} - \frac{\mathrm{d}\langle q\rangle}{\mathrm{d}t}. \tag{3A.56}$$

These equations can be combined to find the governing equations for θ_v.

$$\begin{aligned}\Delta\theta_v &= \theta_{v,\mathrm{FT}} - \langle\theta_v\rangle\,, \\ &= \theta_{\mathrm{FT}}\,(1 + 0.61q_{\mathrm{FT}}) - \langle\theta\rangle\,(1 + 0.61\,\langle q\rangle)\,, \\ &= (\langle\theta\rangle + \Delta\theta)\,(1 + 0.61\,(\langle q\rangle + \Delta q)) - \langle\theta\rangle\,(1 + 0.61\,\langle q\rangle)\,,\end{aligned} \tag{3A.57}$$

$$\Delta\theta_v = \Delta\theta + 0.61\,(\langle\theta\rangle\,\Delta q + \Delta\theta\,\langle q\rangle + \Delta\theta\Delta q)\,. \tag{3A.58}$$

Further, according to Eqs. (3.1), (3A.54) and (3A.52),

$$\begin{aligned}\overline{w'\theta'_{vh}} &= 0.61\ \langle\theta\rangle\ \overline{w'q'}_h + (1 + 0.61\ \langle q\rangle)\,\overline{w'\theta'}_h,\\ &= -0.61\,\langle\theta\rangle\,\Delta q\frac{\mathrm{d}h}{\mathrm{d}t} - (1 + 0.61\,\langle q\rangle)\,\Delta\theta\frac{\mathrm{d}h}{\mathrm{d}t},\\ &= -\left(\Delta\theta + 0.61\,(\langle\theta\rangle\,\Delta q + \Delta\theta\,\langle q\rangle + \Delta\theta\Delta q) - 0.61\Delta\theta\Delta q\right)\frac{\mathrm{d}h}{\mathrm{d}t}. \end{aligned} \tag{3A.59}$$

In contrast to the case without moisture, an approximation has to be made to reach an analytical solution. By assuming that $|\Delta\theta\Delta q| \ll \Delta\theta_v$ ($|\Delta\theta| \sim |\Delta\theta_v|$ and Δq is of the order of 10^{-3} kg kg^{-1}) and using the expression for $\Delta\theta_v$ from Eq. (3A.58), Eq. (3A.59) becomes

$$\overline{w'\theta'_{vh}} = -\Delta\theta_v\frac{\mathrm{d}h}{\mathrm{d}t}, \tag{3A.60}$$

$$\frac{\mathrm{d}h}{\mathrm{d}t} = -\frac{\overline{w'\theta'_{vh}}}{\Delta\theta_v}. \tag{3A.61}$$

This is the first governing equation for θ_v. From Eqs. (3.2), (3A.51), (3A.52) and (3A.55) the second governing equation follows:

$$\begin{aligned}\frac{\mathrm{d}\,\langle\theta_v\rangle}{\mathrm{d}t} &= \frac{\mathrm{d}\,(\langle\theta\rangle\,(1 + 0.61\,\langle q\rangle))}{\mathrm{d}t},\\ &= (1 + 0.61\,\langle q\rangle)\,\frac{\mathrm{d}\,\langle\theta\rangle}{\mathrm{d}t} + 0.61\,\langle\theta\rangle\,\frac{\mathrm{d}\,\langle q\rangle}{\mathrm{d}t},\\ &= (1 + 0.61\,\langle q\rangle)\,\frac{\overline{w'\theta'}_0 - \overline{w'\theta'}_h}{h} + 0.61\,\langle\theta\rangle\,\frac{\overline{w'q'}_0 - \overline{w'q'}_h}{h}, \end{aligned} \tag{3A.62}$$

$$\frac{\mathrm{d}\,\langle\theta_v\rangle}{\mathrm{d}t} = \frac{\overline{w'\theta'_{v0}} - \overline{w'\theta'_{vh}}}{h}. \tag{3A.63}$$

Finally,

$$\begin{aligned}\gamma_{\theta_v}(z) &= \frac{\mathrm{d}\theta_{v,\mathrm{FT}}(z)}{\mathrm{d}z},\\ &= \frac{\mathrm{d}\,(\theta_{\mathrm{FT}}(z)\,(1 + 0.61\ q_{\mathrm{FT}}(z)))}{\mathrm{d}z},\\ &= (1 + 0.61\ q_{\mathrm{FT}}(z))\,\frac{\mathrm{d}\theta_{\mathrm{FT}}(z)}{\mathrm{d}z} + 0.61\theta_{\mathrm{FT}}(z)\,\frac{\mathrm{d}q_{\mathrm{FT}}(z)}{\mathrm{d}z},\\ &= (1 + 0.61\ q_{\mathrm{FT}}(z))\,\gamma_\theta + 0.61\theta_{\mathrm{FT}}(z)\,\gamma_q. \end{aligned} \tag{3A.64}$$

A second assumption that is made is that γ_{θ_v} is approximately constant with height, since $0.61\ |q_{\mathrm{FT}}(h) - q_{\mathrm{FT}}(h_0)| \ll 1 + 0.61\ q_{\mathrm{FT}}(h)$ and $|\theta_{\mathrm{FT}}(h) - \theta_{\mathrm{FT}}(h_0)| \ll \theta_{\mathrm{FT}}(h)$. Therefore,

$$\gamma_{\theta_v} = (1 + 0.61\ q_{\mathrm{FT}}(h_0))\,\gamma_\theta + 0.61\theta_{\mathrm{FT}}(h_0)\,\gamma_q. \tag{3A.65}$$

By taking the derivative to time of Eq. (3A.57),

$$\begin{aligned}\frac{\mathrm{d}\Delta\theta_v}{\mathrm{d}t} &= \frac{\mathrm{d}\theta_{v,\mathrm{FT}}}{\mathrm{d}t} - \frac{\mathrm{d}\langle\theta_v\rangle}{\mathrm{d}t},\\ &= \frac{\mathrm{d}\theta_{v,\mathrm{FT}}}{\mathrm{d}h}\frac{\mathrm{d}h}{\mathrm{d}t} - \frac{\mathrm{d}\langle\theta_v\rangle}{\mathrm{d}t}, \qquad (3A.66)\\ \frac{\mathrm{d}\Delta\theta_v}{\mathrm{d}t} &= \gamma_{\theta_v}\frac{\mathrm{d}h}{\mathrm{d}t} - \frac{\mathrm{d}\langle\theta_v\rangle}{\mathrm{d}t}. \qquad (3A.67)\end{aligned}$$

As Eqs. (3A.61), (3A.63), (3A.67) and (3A.53) replace Eqs. (3.1), (3.2), (3.3) and (3.5), the analytical solution for the boundary-layer height evolution is derived in a similar fashion as for the case without moisture. In accordance to Eq. (3A.44), the implicit analytical solution is

$$\begin{aligned}h^2 - \left(\frac{2+4\beta}{\gamma_{\theta_v}}\right)\left(\Delta\theta_{v,0}h_0^{\frac{1+\beta}{\beta}} - \left(\frac{\beta}{1+2\beta}\right)\gamma_{\theta_v}h_0^{\frac{1+2\beta}{\beta}}\right)h^{-\frac{1}{\beta}} =\\ h_0^2 - \left(\frac{2+4\beta}{\gamma_{\theta_v}}\right)\left(\Delta\theta_{v,0}h_0 - \left(\frac{\beta}{1+2\beta}\right)\gamma_{\theta_v}h_0^2\right) + \left(\frac{2+4\beta}{\gamma_{\theta_v}}\right)\int_{t_0}^{t}\overline{w'\theta'_{v0}}\mathrm{d}t,\end{aligned} \tag{3A.68}$$

while the approximation for 'large' h, based on Eq. (3A.47), is

$$h \approx \sqrt{h_0^2 - \left(\frac{2+4\beta}{\gamma_{\theta_v}}\right)\left(\Delta\theta_{v,0}h_0 - \left(\frac{\beta}{1+2\beta}\right)\gamma_{\theta_v}h_0^2\right) + \left(\frac{2+4\beta}{\gamma_{\theta_v}}\right)\int_{t_0}^{t}\overline{w'\theta'_{v0}}\mathrm{d}t}. \tag{3A.69}$$

3A.6 Check on bijection

When evaluating Eqs. (3A.44) and (3A.68), note that these expressions can be written as $f(h(t)) = g(t)$. To verify that $f(h(t))$ is an implicit analytical solution for $h(t)$, it has to be checked whether there is bijection: each value for $f(h)$ always corresponds to a unique value of h and for every value of h there is an existing value for $f(h)$ when $h > h_0$. This is the case if $f(h)$ is a continuous function and

$$\frac{\mathrm{d}f(h)}{h} > 0 \qquad \text{for} \qquad h > h_0. \tag{3A.70}$$

In the case of Eq. (3A.68),

$$\begin{aligned}\frac{\mathrm{d}f(h)}{\mathrm{d}h} &= 2h + \left(\frac{2+4\beta}{\beta\gamma_{\theta_v}}\right)\left(\Delta\theta_{v,0}h_0^{\frac{1+\beta}{\beta}} - \left(\frac{\beta}{1+2\beta}\right)\gamma_{\theta_v}h_0^{\frac{1+2\beta}{\beta}}\right)h^{-\frac{1+\beta}{\beta}}, \\ &= \left(2\left(h^{\frac{1+2\beta}{\beta}} - h_0^{\frac{1+2\beta}{\beta}}\right) + \left(\frac{2+4\beta}{\beta\gamma_{\theta_v}}\right)\Delta\theta_{v,0}h_0^{\frac{1+\beta}{\beta}}\right)h^{-\frac{1+\beta}{\beta}}. \end{aligned} \tag{3A.71}$$

For $h > h_0$, $h^{-\frac{1+\beta}{\beta}} > 0$ and $h^{\frac{1+2\beta}{\beta}} > h_0^{\frac{1+2\beta}{\beta}}$. Additionally, β, γ_{θ_v} and $\Delta\theta_{v,0}$ have positive values. Therefore $\frac{\mathrm{d}f(h)}{h} > 0$ and Eqs. (3A.44) and (3A.68) are analytical implicit solutions for $h(t)$.

Every addition to true knowledge is an addition to human power.

Horace Mann

4

Amendment to "Analytical Solution for the Convectively-Mixed Atmospheric Boundary Layer": Inclusion of Subsidence

In Ouwersloot and Vilà-Guerau de Arellano (2013a), the analytical solutions for the boundary-layer height and scalar evolutions are derived for the convective boundary layer, based on the prognostic equations of mixed-layer slab models without taking subsidence into account. Here, we include and quantify the added effect of subsidence if the subsidence velocity scales linearly with height throughout the atmosphere. This enables analytical analyses for a wider range of observational cases. As a demonstration, the sensitivity of the boundary-layer height and the potential temperature jump to subsidence and the free tropospheric stability is graphically presented. The new relations show the importance of the temporal distribution of the surface buoyancy flux in determining the evolution if there is subsidence.

This chapter is published as Ouwersloot and Vilà-Guerau de Arellano (2013b).

Symbols

h	Boundary-layer height
θ_v	Virtual potential temperature
$\overline{w'\theta'_v}$	Buoyancy flux
D	Divergence of horizontal wind
t	Time
u	Coordinate transform for time
β	Entrainment constant
ϕ	Conserved scalar
$\langle\psi\rangle$	Mixed-layer average of arbitrary variable ψ
$\Delta\psi$	Jump of ψ at the inversion, $\psi_{\mathrm{FT}} - \langle\psi\rangle$
γ_ψ	Free tropospheric gradient of ψ
$\overline{w'\psi'}_0$	Vertical kinematic surface flux of ψ
$\overline{w'\psi'}_h$	Vertical kinematic entrainment flux of ψ
w_e	Entrainment velocity
w_s	Large-scale vertical velocity
P	Production
τ	Lifetime of (chemical) scalar

4.1 Introduction

Ouwersloot and Vilà-Guerau de Arellano (2013a) (from now on OV13) presented and discussed the prognostic equations of mixed-layer theory for a convective boundary layer (CBL), assuming a zeroth-order virtual potential temperature jump at the entrainment zone. They derived the analytical solutions for the CBL where subsidence was absent, while accounting for the influence of the initial conditions. Here, we amend these solutions by including the effect of subsidence. Previous studies have shown the influence of subsidence on the analytical solutions in case the initial conditions are not taken into account (Carson, 1973). Assuming fixed free tropospheric gradients, it was stated by OV13 that combining both was not possible using their employed analytical evaluation, based on the argument that in the case of subsidence the separation of variables was no longer possible. However, we show here that the combination is possible if another representation for subsidence is used (Carson, 1973). This representation implies that free tropospheric gradients of scalars are affected by subsidence and not restored by additional sources or sinks (e.g. radiative cooling or warming).

First, the derivation of the boundary-layer height evolution is explained. Then, the importance of the temporal distribution of the surface buoyancy flux is demonstrated for a case with subsidence present. To complete the study, we introduce and discuss the time evolution

of scalars under the influence of subsidence.

4.2 Results

Similar to Carson (1973), the large-scale vertical velocity associated with subsidence is throughout the lower troposphere,

$$w_s(z) = -Dz, \tag{4.1}$$

where D is the divergence of the horizontal wind. In particular, $w_s(h) = -Dh$. In the case of subsidence, $D > 0$. Free tropospheric gradients of any arbitrary scalar, ϕ, are then characterized by

$$\gamma_\phi(t) = \gamma_\phi(0)\mathrm{e}^{Dt}, \tag{4.2}$$

noting that for $D = 10^{-5}$ s^{-1}, which can be considered a typical value, this results in an increase of the free tropospheric gradients by 54 % after 12 hours. These gradients include the (virtual) potential temperature lapse rate that governs the boundary-layer height evolution. The set of governing equations (Eqs. 20-22 from OV13) becomes

$$w_e = -\frac{\overline{w'\theta'_{vh}}}{\Delta\theta_v}, \tag{4.3}$$

$$\frac{\mathrm{d}\langle\theta_v\rangle}{\mathrm{d}t} = \frac{\overline{w'\theta'_{v0}} - \overline{w'\theta'_{vh}}}{h}, \tag{4.4}$$

$$\frac{\mathrm{d}\Delta\theta_v}{\mathrm{d}t} = \gamma_{\theta_v}(t)w_e - \frac{\mathrm{d}\langle\theta_v\rangle}{\mathrm{d}t}, \tag{4.5}$$

$$\frac{\mathrm{d}h}{\mathrm{d}t} = w_e + w_s(h), \tag{4.6}$$

while retaining the closure assumption

$$\overline{w'\theta'_{vh}} = -\beta\overline{w'\theta'_{v0}}. \tag{4.7}$$

Using the knowledge that $w_e = \frac{\mathrm{d}h}{\mathrm{d}t} + Dh = \mathrm{e}^{-Dt}\frac{\mathrm{d}\left(h\mathrm{e}^{Dt}\right)}{\mathrm{d}t}$, Eqs. (4.2-4.7) can be combined to

$$\frac{\mathrm{d}\left(h\mathrm{e}^{Dt}\right)}{\mathrm{e}^{Dt}\mathrm{d}t} = \beta\frac{\overline{w'\theta'_v}_0}{\Delta\theta_v}, \tag{4.8}$$

$$\frac{\mathrm{d}\left\langle\theta_v\right\rangle}{\mathrm{e}^{Dt}\mathrm{d}t} = (1+\beta)\,\frac{\overline{w'\theta'_v}_0}{h\mathrm{e}^{Dt}}, \tag{4.9}$$

$$\frac{\mathrm{d}\Delta\theta_v}{\mathrm{e}^{Dt}\mathrm{d}t} = \gamma_{\theta_v}(0)\frac{\mathrm{d}\left(h\mathrm{e}^{Dt}\right)}{\mathrm{e}^{Dt}\mathrm{d}t} - \frac{\mathrm{d}\left\langle\theta_v\right\rangle}{\mathrm{e}^{Dt}\mathrm{d}t}. \tag{4.10}$$

If a coordinate transformation is applied, considering $u = \frac{1}{D}\mathrm{e}^{Dt}$, then $\mathrm{d}u = \mathrm{e}^{Dt}\mathrm{d}t$. Additionally, consider $\tilde{h} = h\mathrm{e}^{Dt}$. In that case the three governing equations become

$$\frac{\mathrm{d}\tilde{h}}{\mathrm{d}u} = \beta\frac{\overline{w'\theta'_v}_0}{\Delta\theta_v}, \tag{4.11}$$

$$\frac{\mathrm{d}\left\langle\theta_v\right\rangle}{\mathrm{d}u} = (1+\beta)\,\frac{\overline{w'\theta'_v}_0}{\tilde{h}}, \tag{4.12}$$

$$\frac{\mathrm{d}\Delta\theta_v}{\mathrm{d}u} = \gamma_{\theta_v}(0)\frac{\mathrm{d}\tilde{h}}{\mathrm{d}u} - \frac{\mathrm{d}\left\langle\theta_v\right\rangle}{\mathrm{d}u}. \tag{4.13}$$

These equations are equal in structure to Eqs. 20-22 of OV13, albeit with different variables. Therefore, the solution is known to be

$$\begin{aligned}\tilde{h}^2 - \left(\frac{2+4\beta}{\gamma_{\theta_v}(0)}\right)\left(\Delta\theta_{v,0}\tilde{h}_0^{\frac{1+\beta}{\beta}} - \left(\frac{\beta}{1+2\beta}\right)\gamma_{\theta_v}(0)\tilde{h}_0^{\frac{1+2\beta}{\beta}}\right)\tilde{h}^{-\frac{1}{\beta}} = \\ \tilde{h}_0^2 - \left(\frac{2+4\beta}{\gamma_{\theta_v}(0)}\right)\left(\Delta\theta_{v,0}\tilde{h}_0 - \left(\frac{\beta}{1+2\beta}\right)\gamma_{\theta_v}(0)\tilde{h}_0^2\right) + \left(\frac{2+4\beta}{\gamma_{\theta_v}(0)}\right)\int_{u(t_0)}^{u(t)}\overline{w'\theta'_v}_0\mathrm{d}u'.\end{aligned} \tag{4.14}$$

Since $h_0 = h\left(t_0\right)$ and $\gamma_{\theta_v}\left(0\right) = \gamma_{\theta_v}\left(t_0\right)\mathrm{e}^{-Dt_0}$, substituting u by $D^{-1}\mathrm{e}^{Dt}$ and multiplying the entire equation by e^{-2Dt} results in

$$\begin{aligned}h^2 - \left(\frac{2+4\beta}{\gamma_{\theta_v}\left(t_0\right)}\right)\left(\Delta\theta_{v,0}h_0^{\frac{1+\beta}{\beta}} - \left(\frac{\beta}{1+2\beta}\right)\gamma_{\theta_v}\left(t_0\right)h_0^{\frac{1+2\beta}{\beta}}\right)h^{-\frac{1}{\beta}}\mathrm{e}^{-\left(2+\frac{1}{\beta}\right)D(t-t_0)} = \\ h_0^2\mathrm{e}^{-2D(t-t_0)} - \left(\frac{2+4\beta}{\gamma_{\theta_v}\left(t_0\right)}\right)\left(\Delta\theta_{v,0}h_0 - \left(\frac{\beta}{1+2\beta}\right)\gamma_{\theta_v}\left(t_0\right)h_0^2\right)\mathrm{e}^{-2D(t-t_0)} + \\ \left(\frac{2+4\beta}{\gamma_{\theta_v}\left(t_0\right)}\right)\mathrm{e}^{-D(t-t_0)}\int_{t_0}^{t}\overline{w'\theta'_v}_0\mathrm{e}^{-D(t-t')}\mathrm{d}t'.\end{aligned} \tag{4.15}$$

To arrive at an explicit approximation, the second term on the left-hand side is ignored for relatively large h, similar to OV13. However, note that, in this situation, this approximation can also be made for relatively small h, but large $D\left(t-t_0\right)$, since the second term falls with

$h^{-\frac{1+2\beta}{\beta}} \mathrm{e}^{-\left(2+\frac{1}{\beta}\right)D(t-t_0)}$ compared to the first term on the left-hand side. Using this assumption,

$$h \approx \mathrm{e}^{-D(t-t_0)} \sqrt{h_0^2 - \left(\frac{2+4\beta}{\gamma_{\theta_v}(t_0)}\right)\left(\Delta\theta_{v,0} h_0 - \left(\frac{\beta}{1+2\beta}\right)\gamma_{\theta_v}(t_0)\, h_0^2\right) + \left(\frac{2+4\beta}{\gamma_{\theta_v}(t_0)}\right)\int_{t_0}^{t} \overline{w'\theta'_{v0}}\, \mathrm{e}^{D(t'-t_0)}\mathrm{d}t'}. \tag{4.16}$$

The influence of the initial conditions fall exponentially with time with a rate equal to D. Note that also the influence of the recent ($t - t' \ll D^{-1}$) surface buoyancy flux is reduced due to the altered free tropospheric gradient, $\gamma_{\theta_v}(t) > \gamma_{\theta_v}(t_0)$. This becomes more apparent presenting Eqs. (4.15) and (4.16) as

$$\begin{aligned} h^2 - \left(\frac{2+4\beta}{\gamma_{\theta_v}(t_0)}\right)\left(\Delta\theta_{v,0} h_0^{\frac{1+\beta}{\beta}} - \left(\frac{\beta}{1+2\beta}\right)\gamma_{\theta_v}(t_0)\, h_0^{\frac{1+2\beta}{\beta}}\right) h^{-\frac{1}{\beta}} \mathrm{e}^{-\left(2+\frac{1}{\beta}\right)D(t-t_0)} = \\ h_0^2 \mathrm{e}^{-2D(t-t_0)} - \left(\frac{2+4\beta}{\gamma_{\theta_v}(t_0)}\right)\left(\Delta\theta_{v,0} h_0 - \left(\frac{\beta}{1+2\beta}\right)\gamma_{\theta_v}(t_0)\, h_0^2\right)\mathrm{e}^{-2D(t-t_0)} + \\ \left(\frac{2+4\beta}{\gamma_{\theta_v}(t)}\right)\int_{t_0}^{t} \overline{w'\theta'_{v0}}\, \mathrm{e}^{-D(t-t')}\mathrm{d}t' \end{aligned} \tag{4.17}$$

and

$$h \approx \sqrt{h_0^2 \mathrm{e}^{-2D(t-t_0)} - \left(\frac{2+4\beta}{\gamma_{\theta_v}(t_0)}\right)\left(\Delta\theta_{v,0} h_0 - \left(\frac{\beta}{1+2\beta}\right)\gamma_{\theta_v}(t_0)\, h_0^2\right)\mathrm{e}^{-2D(t-t_0)} + \left(\frac{2+4\beta}{\gamma_{\theta_v}(t)}\right)\int_{t_0}^{t} \overline{w'\theta'_{v0}}\, \mathrm{e}^{D(t'-t)}\mathrm{d}t'}. \tag{4.18}$$

In the presence of subsidence, the final boundary-layer height is no longer only dependent on the value of the time-integrated surface buoyancy flux, but also on the temporal distribution of this flux. This is demonstrated in Fig. 4.1, which is based on the standard case without moisture of OV13 (their Table 1). The dashed line represents the boundary-layer height approximation of Eq. (4.16) between $t = 8$ h and $t = 18$ h for a constant surface buoyancy flux and no subsidence. The other lines represent the approximation in the presence of subsidence for four different temporal distributions of this flux: *constant* in time, shaped as a *sinus*, concentrated at $t = 8$ h (*start*) and concentrated at $t = 18$ h (*end*). The subsidence is prescribed by setting the constant horizontal velocity divergence, D, to 10^{-5} s^{-1}. Note that the approximations are not representative for relatively small h and t (OV13). For the cases displayed in Fig. 4.1, the approximation can be considered the true boundary-layer height for all cases if $h \geq 700$ m. As demonstrated by Eq. (4.18), the recent ($t - t' \ll D^{-1}$) surface buoyancy flux has a larger contribution to the current boundary-layer height than the initial flux. When con-

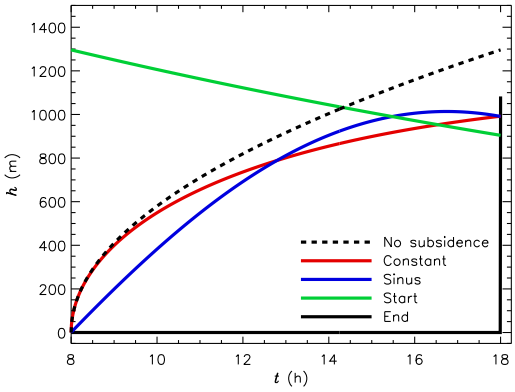

Figure 4.1: Dependency of the boundary-layer height approximation (Eq. (4.16)) on the distribution of the surface buoyancy flux in the presence of subsidence ($D = 10^{-5}\,\mathrm{s}^{-1}$). The integrated surface buoyancy flux between 8 and 18 h is equal for all cases. As a reference, the dashed line shows the approximation for a constant surface buoyancy flux and no subsidence.

tributions to the time-integrated flux are concentrated at the initial time, the resulting height just after the introduction of heat is equal to the final boundary-layer height as calculated in the case without subsidence (1296 m). However, from that moment on, the boundary-layer height decays exponentially. In the situations where the contributions to the time-integrated surface flux are concentrated in the later period, the final boundary-layer height is higher. The final boundary-layer heights for the constant and sinusoidal fluxes are respectively 992 m and 991 m. If contributions to the time-integrated heat flux are concentrated at $t = 8\,\mathrm{h}$, the final height is only 904 m and if they are concentrated at $t = 18\,\mathrm{h}$, the final height is 1083 m.

The equations also show that steady-state solutions cannot be reached with constant surface forcings if subsidence behaves no different in the free troposphere than in the boundary layer. For $t - t' \gg D^{-1}$, the integral in Eq. (4.16) becomes constant if the surface forcings are constant, resulting in a constant value in the square root of that equation. However, the exponential function in front of this square root then prevents a constant boundary-layer height and it will decay with a rate of D.

After determining the boundary-layer height evolution, the evolution of scalars can be diagnosed. Note that, due to the corresponding lateral transport, subsidence affects the expression for the evolution of conserved scalars (Eq. 34 of OV13) in more ways than only altering $h(t)$. The resulting expression for the temporal evolution of a scalar that is characterized by constant production, P, and a loss term that scales linearly with the scalar itself by a

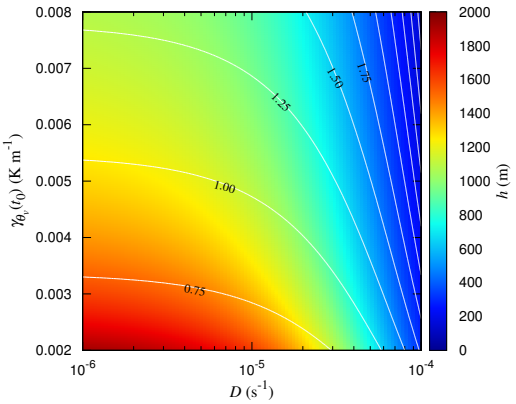

Figure 4.2: Boundary-layer height and potential temperature jump at the inversion at 16 h as a function of the horizontal wind divergence and free tropospheric stability. The other boundary and initial conditions are based on Table 1 of OV13 and a surface buoyancy flux that follows a sinusoidal temporal evolution. White contour lines, drawn at 0.25 K intervals, denote $\Delta\theta$.

factor of $1/\tau$ (as presented by OV13), is

$$\begin{aligned}\langle\phi\rangle(t) = \langle\phi\rangle_0 \, \mathrm{e}^{-\frac{(t-t_0)}{\tau}} + \frac{h(t) - h_0 \mathrm{e}^{-D(t-t_0)}}{h(t)} \Delta\phi_0 \mathrm{e}^{-D(t-t_0)} + \\ \frac{\gamma_\phi(t_0)}{2} \frac{\left(h(t) - h_0 \mathrm{e}^{-D(t-t_0)}\right)^2}{h(t)} \mathrm{e}^{(D-\frac{1}{\tau})(t-t_0)} + \\ P\tau\left(1 - \mathrm{e}^{-\frac{(t-t_0)}{\tau}}\right) + \frac{1}{h(t)} \int_{t_0}^{t} \overline{w'\phi'}_0 \mathrm{e}^{-(D+\frac{1}{\tau})(t-t')} \mathrm{d}t' . \end{aligned} \tag{4.19}$$

This shows that subsidence and chemical loss have an opposing effect on the influence of the initial free tropospheric gradient. Subsidence enhances the gradient with time, while chemical loss decreases the gradient. However, subsidence and chemical loss affect the influence of surface emissions in the same way. Both diminish the impact of early ($t - t' \gg \tau/(D\tau + 1)$) emissions by modulation with the factor $\mathrm{e}^{-(\frac{D\tau+1}{\tau})(t-t')}$ in the integral of those emissions.

The potential of the derived expressions is demonstrated in Fig. 4.2 by presenting a sensitivity analysis that does not require a numerical model analysis, extending on previous studies (e.g. Carson, 1973). Here, the boundary-layer height and $\Delta\theta$ are depicted as a function of D, which is related to subsidence through Eq. (4.1), and the initial $\gamma_{\theta_v}(t_0)$, based on the same conditions as for Fig. 4.1 and the *sinus* surface buoyancy-flux temporal distribution. Subsidence and free tropospheric stability exert a significant influence on the development of the boundary-layer height. It can be seen that both stronger subsidence and larger free

tropospheric gradients in θ_v lead to a shallower boundary layer. These effects do not add linearly. For example, the influence of subsidence becomes larger for low values of γ_{θ_v}. The dependence of $\Delta\theta$ on these two driving variables is not identical to that of h, because the potential temperature jump additionally scales with $\gamma_{\theta_v}(t)$, which in turn is affected by both driving variables ($\gamma_{\theta_v}(t_0)$ and D) as well. However, the dependencies are qualitatively similar for both h and $\Delta\theta$. An advantage of mapping h and $\Delta\theta$ as a function of initial and boundary conditions is that it enables the identification of different regimes. For instance, in the exemplary Fig. 4.2 a regime can be identified for $D > 5 \times 10^{-5}\,\mathrm{s}^{-1}$ where h and $\Delta\theta$ are less sensitive to $\gamma_{\theta_v}(t_0)$, due to their being dominated by the effect of subsidence.

4.3 Conclusions

The analytical solutions to the prognostic equations for a diurnal convective boundary layer, as presented by Ouwersloot and Vilà-Guerau de Arellano (2013a), are expanded to include the effects of subsidence. These solutions, for the boundary-layer height evolution and the associated evolution of conserved scalars, are valid for situations in which the horizontal velocity divergence is constant with height throughout the lower troposphere and no additional sources or sinks affect the free tropospheric gradients. Based on these new solutions we discuss and quantify the possibility of attaining steady-state solutions and the influence of the temporal distribution of the surface buoyancy flux. It is demonstrated that, in the case of subsidence, the boundary-layer height is governed by the recent surface buoyancy flux, whereas the total time-integrated flux is important if there is no subsidence. Finally, the resulting evolution of an arbitrary conserved scalar (in the case of a chemical species, inert or first-order decaying and with a constant production) in the boundary layer is presented.

If you have a procedure with 10 parameters, you probably missed some.

Alan Perlis

5

On the segregation of chemical species in a clear boundary layer over heterogeneous land surfaces

Using a Large-Eddy Simulation model, we have systematically studied the inability of boundary layer turbulence to efficiently mix reactive species. This creates regions where the species are accumulated in a correlated or anti-correlated way, thereby modifying the mean reactivity. We quantify this modification by the intensity of segregation, I_S, and analyse the driving mechanisms: heterogeneity of the surface moisture and heat fluxes, various background wind patterns and non-uniform isoprene emissions. The heterogeneous surface conditions are characterized by cool and wet forested patches with high isoprene emissions, alternated with warm and dry patches that represents pasture with relatively low isoprene emissions. For typical conditions in the Amazon rain forest, applying homogeneous surface forcings and in the absence of free tropospheric NO_x, the isoprene-OH reaction rate is altered by less than 10 %. This is substantially smaller than the previously assumed I_S of 50 % in recent large-scale model analyses of tropical rain forest chemistry. Spatial heterogeneous surface emissions enhance the segregation of species, leading to alterations of the chemical reaction rates up to 20 %. The intens-

This chapter is published as Ouwersloot et al. (2011).

ities of segregation are enhanced when the background wind direction is parallel to the borders between the patches and reduced in the case of a perpendicular wind direction. The effects of segregation on trace gas concentrations vary per species. For the highly reactive OH, the differences in concentration averaged over the boundary layer are less than 2 % compared to homogeneous surface conditions, while the isoprene concentration is increased by as much as 12 % due to the reduced chemical reaction rates. These processes take place at the sub-grid scale of chemistry transport models and therefore need to be parameterized.

5.1 Introduction

The Amazonian region is an area of great interest for the global climate, since the rain forest exchanges large quantities of carbon containing species with the atmosphere. This area is steadily changing from a natural environment to a human-controlled environment associated with deforestation (Andreae et al., 2002; Soares-Filho et al., 2006), causing changes in surface conditions and, consequently, boundary layer characteristics (Fisch et al., 2004) and trace gas exchanges (Ganzeveld et al., 2010). To evaluate these changes and their influence on atmospheric chemistry and global climate, the understanding of the boundary layer dynamics and atmospheric chemistry over the Amazonian system needs to be improved.

We present a numerical model study that focuses on the effects of surface heterogeneity on atmospheric dynamics and chemistry. Both are affected by mesoscale circulations induced by spatial differences in sensible and latent heat fluxes and additionally, chemistry is affected by non-uniform reactant emissions at the surface. Therefore, because of spatial variations of surface properties, chemical reactants can either be separated more strongly or be more efficiently mixed by circulations, as we will investigate. Other dynamical aspects relevant for chemistry, like the boundary layer height development or turbulent mixing, are dependent on the surface heterogeneity as well. Although many studies have been performed on the effects on the dynamics (Avissar and Liu, 1996; Patton et al., 2005; van Heerwaarden and Vilà-Guerau de Arellano, 2008), the effects on atmospheric chemistry have been investigated much less intensively (Krol et al., 2000; Auger and Legras, 2007). To our knowledge a systematic study on the impact of surface heterogeneities on simultaneously boundary layer dynamics and chemistry has not yet been performed.

Tropical rain forest chemistry is driven by the exchange of biogenic compounds, dynamic processes like turbulent mixing, and the diurnal variability of the atmospheric boundary layer (ABL). The influence of ABL dynamics on chemistry is often crudely described in large-scale atmospheric models and in models that are used to analyse experimental observations (Ganzeveld et al., 2008; Vilà-Guerau de Arellano et al., 2009). A list of the most important influences is presented in Table 5.1.

Recently, one of these processes, the segregation of species due to inefficient turbulent mixing, has been recognized as a possible relevant process to take into account in the observational analyses and models (Butler et al., 2008; Pugh et al., 2010a,b). This segregation of species was previously studied for idealized cases (Schumann, 1989; Sykes et al., 1992; Vilà-Guerau de Arellano et al., 1993). The inability of turbulence to uniformly mix the emitted and entrained species creates sub-regions where the species are non-uniformly distributed in a correlated or anti-correlated way, thereby modifying the mean chemical reaction rate in the boundary layer. The early studies focused on the boundary layer dynamics and did not consider complex chemistry. Krol et al. (2000) conducted a study for more complex chemistry using a Large-Eddy Simulation (LES) model and investigated the effect of heterogeneous surface emissions of biogenic reactive compounds on the intensity of segregation. They found that non-uniform emissions significantly enhance the segregation of reactants.

The acquired knowledge of these studies has only rarely been applied to atmospheric chemistry models and measurement analyses. Auger and Legras (2007) investigated the segregation effects for urban air chemistry for both homogeneous and heterogeneous reactant emissions while keeping the surface conditions that drive the dynamics uniform over the domain. The intensity of segregation is also considered as a potential contributor to large discrepancies between observations and model results of reactive trace gas concentrations over the tropical forest, particularly for the biogenic volatile organic compound isoprene and the hydroxyl radical (OH) (Butler et al., 2008).

In the analysis of observations ad hoc values of the intensity of segregation have been assumed that correspond to a substantial decrease in the isoprene-OH reaction rate, while not taking the governing physical and chemical processes into account (e.g. Butler et al., 2008; Pugh et al., 2010a). Observations on the intensity of segregation between OH and isoprene, by relatively fast simultaneous measurements of both compounds over a German deciduous forest, were made by Dlugi et al. (2010). However, they only measured at one location and one height, 7 m above the forest canopy. Therefore their result, a decrease in the chemical reaction rate of 15 %, is representative for the surface layer of the atmospheric boundary layer. Butler et al. (2008) made use of averaged aircraft measurements taken with a low frequency (5 s) compared to the flight speed. Their result, which corresponds to a decrease in the chemical reaction rate of 13 % compared to perfect mixing conditions, is therefore a first indication for the segregation within the Amazonian atmospheric boundary layer. However, their measurements do not capture the fine dynamical structures associated to the small scales of convective turbulence. It can not be inferred whether the total intensity of segregation is weaker or stronger, since these fine structures can lead to either positive or negative contributions.

The aim of the present work is to systematically study the intensity of segregation for the isoprene-OH reaction under conditions representative for the Amazon rain forest using

Table 5.1: Influence of ABL dynamics, radiation and surface conditions on atmospheric chemistry.

Influence	Effect on chemistry
Boundary layer growth	Lowering concentrations by dilution
	Entrainment of air from the free troposphere
Clouds	Photolysis rate modification by radiation scattering
	Impact on photosynthetically active radiation
	Enhancement of the vertical transport of chemical compounds
	Venting chemical compounds to the free troposphere
Turbulence	Driver of the mixing of air: organized in coherent structures leading to inefficient turbulent mixing that can create a segregation of species which alters the mean reactivity
Temperature	Modification of reaction rate coefficients
Moisture	Influence on reactivity as a catalyst or reactant (e.g. the formation of OH)
Atmosphere-vegetation-soil interaction	Emission and deposition fluxes of chemical compounds (isoprene, ozone) depending on the radiation, canopy characteristics and both atmospheric and soil conditions concerning temperature and moisture
Surface heterogeneity	Modification of the dynamics by induction of mesoscale circulations and the chemistry by non-uniform emission or deposition fluxes of reactants. In consequence, potential enhancement of spatial reactant segregation

a LES model. This reaction is of interest since OH chemistry largely controls the oxidizing capacity of the atmosphere, both worldwide and above the Amazon rain forest (Zimmerman et al., 1988; Karl et al., 2007; Lelieveld et al., 2008). The intensity of segregation can be calculated explicitly in the LES, in contrast to mesoscale models and global climate models where segregation is a sub-grid scale process. In consequence, the LES experiments enable us to determine the governing processes, which will be combined with investigating the impact of surface heterogeneities on the segregation effect and the boundary layer growth under different conditions.

The next section introduces the model and the numerical experiments. Subsequently, the method of calculating the intensity of segregation is explained. The first results presented are the dynamical and chemical characteristics of the cases with the standard homogeneous and heterogeneous surface conditions. This is followed by a sensitivity analysis for several governing variables affecting the impact of the surface heterogeneities.

Table 5.2: Chemical reaction scheme solved in the numerical experiments by the chemistry module of DALES (Vilà-Guerau de Arellano et al., 2011). T is the absolute temperature in K. The unit of first-order reaction rate coefficients is s^{-1} and that of second-order reaction rate coefficients is $cm^3\ molec^{-1}\ s^{-1}$. Reaction (R15) has a more difficult expression for its reaction rate. Reactions (R1), (R5) and (R6) are photolysis reactions which only occur if photons interact with the reactants. REST stands for products and/or secondary fast reactions with reactants in the ambient air that are not directly evaluated.*

Name	Chemical equation			Reaction rate constant
R1	$O_3 + h\nu$	$\rightarrow$	$O^{1D} + O_2$	$6.62 \times 10^{-5} \cdot e^{-0.575}$
R2	$O^{1D} + H_2O$	$\rightarrow$	2 OH	$1.63 \times 10^{-10} \cdot e^{\frac{60}{T}}$
R3	$O^{1D} + N_2$	$\rightarrow$	O_3 + REST	$2.15 \times 10^{-11} \cdot e^{\frac{110}{T}}$
R4	$O^{1D} + O_2$	$\rightarrow$	O_3	$3.30 \times 10^{-11} \cdot e^{\frac{55}{T}}$
R5	$NO_2 + h\nu$	$\rightarrow$	NO + O_3 + REST	$1.67 \times 10^{-2} \cdot e^{-0.575}$
R6	$CH_2O + h\nu$	$\rightarrow$	HO_2 + REST	$5.88 \times 10^{-5} \cdot e^{-0.575}$
R7	OH + CO	$\rightarrow$	$HO_2 + CO_2$ + REST	2.40×10^{-13}
R8	OH + CH_4	$\rightarrow$	CH_3O_2 + REST	$2.45 \times 10^{-12} \cdot e^{\frac{-1775}{T}}$
R9	OH + C_5H_8	$\rightarrow$	RO_2	1.00×10^{-10}
R10	OH + MVK	$\rightarrow$	$HO_2 + CH_2O$ + REST	2.40×10^{-11}
R11	HO_2 + NO	$\rightarrow$	OH + NO_2	$3.50 \times 10^{-12} \cdot e^{\frac{250}{T}}$
R12	CH_3O_2 + NO	$\rightarrow$	$HO_2 + NO_2 + CH_2O$ + REST	$2.80 \times 10^{-12} \cdot e^{\frac{300}{T}}$
R13	RO_2 + NO	$\rightarrow$	$HO_2 + NO_2 + CH_2O$+ MVK	1.00×10^{-11}
R14	OH + CH_2O	$\rightarrow$	HO_2 + REST	$5.50 \times 10^{-12} \cdot e^{\frac{125}{T}}$
R15	2 HO_2	$\rightarrow$	$H_2O_2 + O_2$	k[1]
R16	$CH_3O_2 + HO_2$	$\rightarrow$	REST	$4.10 \times 10^{-13} \cdot e^{\frac{750}{T}}$
R17	$RO_2 + HO_2$	$\rightarrow$	REST	1.50×10^{-11}
R18	OH + NO_2	$\rightarrow$	HNO_3	$3.50 \times 10^{-12} \cdot e^{\frac{340}{T}}$
R19	NO + O_3	$\rightarrow$	$NO_2 + O_2$	$3.00 \times 10^{-12} \cdot e^{-\frac{1500}{T}}$

[1] $k = (k_1 + k_2)\, k_3,\ k_1 = 2.2{\times}10^{-13} \cdot \mathrm{e}^{\frac{600}{T}},\ k_2 = 1.9{\times}10^{-33} \cdot \mathrm{e}^{\frac{980}{T}} \cdot c_{\mathrm{air}},\ k_3 = 1 + 1.4{\times}10^{-21} \cdot \mathrm{e}^{\frac{2200}{T}} \cdot c_{\mathrm{H_2O}}$

5.2 Methodology

5.2.1 Model

This study makes use of a modified version 3.2 of the Dutch Atmospheric Large-Eddy Simulation (DALES) model (Heus et al., 2010). This LES model originates from Nieuwstadt and Brost (1986) and has been further developed and improved since (e.g. Cuijpers and Duynkerke, 1993; Dosio, 2005). DALES explicitly resolves processes on a relatively large scale using the filtered Navier-Stokes equations in combination with the Boussinesq approximation (Heus et al., 2010). In general, the filter size is set equal to the grid size of the simulations. Subfilter-scale processes are parameterized using one-and-a-half-order closure. The boundary conditions in the horizontal directions are periodic. DALES 3.2 is extended with a chemistry module, thus allowing for simultaneous simulation of both boundary layer dynamics and chemistry (Vilà-Guerau de Arellano et al., 2005).

Our model is modified with respect to the standard DALES 3.2 to the extent that the domain can be divided in patches for which the boundary conditions at the surface can be generically set instead of assuming uniform surface conditions. For these patches, the number of grid points in each horizontal dimension is required to be equal to the total number of grid points in that dimension divided by a power of 2. The kinematic surface fluxes for heat and moisture are prescribed for each patch.

5.2.2 Model setup

For all cases in this study the resolution of the LES domain is set to 50 m × 50 m×20 m in the x, y and z directions respectively. The standard grid size is $256 \times 256 \times 128$, resulting in a simulated domain of 12 800 m×12 800 m×2560 m. The simulations are run for 4 h with a maximum time step of 1 s. This time step is small enough to prevent instabilities in the chemical solver. With these settings the relevant temporal and spatial scales for both atmospheric dynamics and chemistry are resolved. Output is generated every minute and the first hour is considered as spin-up of the model. The chemical and dynamical input data of the control cases are based on measurements in the Amazonian rain forest during the TROFFEE campaign that was conducted 14–29 September 2004 (Karl et al., 2007; Vilà-Guerau de Arellano et al., 2011).

In order to investigate the effects of surface heterogeneity without the effects of the diurnal variability, the cases are based on noon conditions characterized by a well-developed boundary layer. The initial boundary layer height is set to 1000 m. We assume no large scale subsidence and, in the control cases, no background wind as well (i.e. local free convection). The surface roughness length, z_0, is set to 0.1 m. The initial potential temperature profile is constant at 300 K in the boundary layer with a temperature jump of 0.8 K at 1000 m. In the

free troposphere, the potential temperature, θ, rises by $6 \times 10^{-3}\,\mathrm{K\,m^{-1}}$. The initial humidity profile, q, is set constant at $6 \times 10^{-3}\,\mathrm{kg\,kg^{-1}}$ in the boundary layer and $3 \times 10^{-3}\,\mathrm{kg\,kg^{-1}}$ in the free troposphere. The chosen humidity is lower than the characteristic values for the Amazonian rain forest to prevent cloud formation and maintain a clear boundary layer during the numerical experiments. The drawback of this choice is its impact on the HO_x production. Consequently, the intensity of segregation for the isoprene-OH reaction is affected as well and quantitative results should be considered as first order estimates. The surface kinematic heat flux and moisture flux are set to $0.15\,\mathrm{K\,m\,s^{-1}}$ and $1 \times 10^{-4}\,\mathrm{kg\,kg^{-1}\,m\,s^{-1}}$ respectively. This corresponds to a sensible heat flux of approximately $185\,\mathrm{W\,m^{-2}}$ and a latent heat flux of approximately $300\,\mathrm{W\,m^{-2}}$.

As well as a passive tracer, 18 reactant species are simulated in the numerical experiments. The applied chemical scheme contains the 19 essential reactions for the O_3-NO_x-VOC-HO_x system during daytime in the Amazonian rain forest (Vilà-Guerau de Arellano et al., 2011) and is shown in Table 5.2. Concentrations are converted from ppb to molec cm^{-3} before applying the chemical scheme and back afterwards. The simulated reactants correspond to the species listed in this scheme, although it should be noted that all first generation oxidation products of isoprene (C_5H_8), through Reactions (R9) and (R13), are lumped into methyl vinyl ketone (MVK). For 10 reactants the surface fluxes and initial concentrations are assumed to be 0, but the other 9 reactants have non zero emissions or initial concentrations. O_3, CH_4, CO, O_2 and N_2 are assigned initial concentrations over the whole domain of 10 ppb, 1724 ppb, 124 ppb, 2×10^8 ppb and 8×10^8 ppb, respectively. The initial concentrations of NO_2 and MVK are 1 ppb and 1.3 ppb below the initial boundary layer height and both 0 ppb in the free troposphere. The emission of NO is set to $5 \times 10^{-4}\,\mathrm{ppb\,m\,s^{-1}}$. For isoprene the emission is set to $0.65\,\mathrm{ppb\,m\,s^{-1}}$ and the initial concentration profile is set to 2 ppb in the boundary layer and 0 ppb in the free troposphere. In this idealized setup NO_x is not completely realistically represented. Sensitivity studies have shown that under the chosen set of conditions the NO_x emissions have very limited impact on the isoprene-OH segregation. However, entrainment of NO_x from the free troposphere can significantly alter the boundary layer chemistry as will be shown in Sect. 5.3.6.

As mentioned before, this study is based on two control cases: one with homogeneous and one with heterogeneous surface conditions. The control case with heterogeneous surface conditions is split into 4 patches in the x-direction. The first and third patch correspond to a forest, while the second and fourth patch have typical savannah surface properties. Because of the periodic boundary conditions (i.e. opposing borders of the domain are connected) used by DALES, this configuration represents an infinite sequence of alternating forest and savannah patches. A scheme of the setup of the numerical experiments is shown in Fig. 5.1.

Over the whole domain the total emissions of reactants, moisture and heat are kept equal to the case with homogeneous surface conditions, and only the distribution is changed. Over

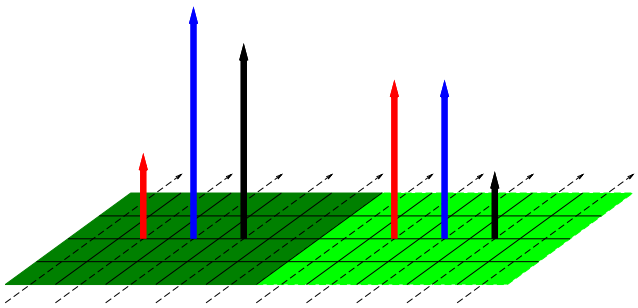

*Figure 5.1: Schematic overview of the heterogeneous surface conditions for the numerical experiments performed by DALES. The simulated domain is split into **forest** and **savannah** patches. Over the relatively cold and wet forest patch the **sensible heat flux** is lower than over the relatively warm and dry savannah patch, but the **latent heat flux** is higher. The **emission of isoprene** is highest over the forest. Over the whole domain the total isoprene emission and surface heat fluxes are kept the same as the case with homogeneous surface conditions. For both terrains the sum of the latent and sensible heat fluxes is the same. Generated statistics are averaged in the direction perpendicular to the direction of heterogeneity.*

the forested patch the kinematic moisture flux is enhanced from $1 \times 10^{-4}\,\mathrm{kg\,kg^{-1}\,m\,s^{-1}}$ to $1.2 \times 10^{-4}\,\mathrm{kg\,kg^{-1}\,m\,s^{-1}}$ due to extra evapotranspiration in the forest compared to the savannah. For compensation the kinematic moisture flux is decreased to $0.8 \times 10^{-4}\,\mathrm{kg\,kg^{-1}\,m\,s^{-1}}$ for the savannah patch. These changes correspond to approximately $60\,\mathrm{W\,m^{-2}}$. To keep the total energy budget equal for both patches, the sum of sensible and latent heat fluxes is kept constant too. This results in a change of the kinematic heat flux to $0.1\,\mathrm{K\,m\,s^{-1}}$ for the forest patch and $0.2\,\mathrm{K\,m\,s^{-1}}$ for the savannah patch. The biogenic emission of isoprene over the forest patch is higher than over the savannah patch (Kesselmeier and Staudt, 1999; Garcia-Carreras et al., 2010). An emission of $1.0\,\mathrm{ppb\,m\,s^{-1}}$ is set for the forest and $0.3\,\mathrm{ppb\,m\,s^{-1}}$ for the savannah configuration. Other emissions and the initial concentration, temperature and specific humidity profiles are kept equal to the case with homogeneous surface conditions. As will be shown in Sect. 5.3.1, the changes in kinematic heat and moisture fluxes cause a difference in buoyancy flux between the forest and savannah patches. This difference generates mesoscale circulations in the xz-plane. To enable visualisation of these circulations and to study the different atmospheric conditions over the two terrain types, average statistics are calculated in the y-direction (Patton et al., 2005; van Heerwaarden and Vilà-Guerau de Arellano, 2008).

Next to the two control cases, we perform sensitivity analyses. These simulations are based on the control case with heterogeneous surface properties. An overview of all per-

formed numerical experiments with their altered input variables is shown in Table 5.3. To study the influence of wind on the dynamics and chemistry, the large scale background wind profiles, u_g and v_g in $\mathrm{m\,s^{-1}}$, are varied in Sect. 5.3.2. For some simulations the grid size is doubled in the x-direction, resulting in a larger domain size. For these simulations, the total number of patches in which the surface is divided in the x-direction, N_{patches}, is varied to determine the impact of the length scale of heterogeneous surface properties. The odd numbered patches represent forest areas and the even numbered patches represent savannah. These results are discussed in Sect. 5.3.3. The dependence on the magnitude of the difference in emissions between the two land types is studied for heat fluxes and isoprene emissions separately. In Sect. 5.3.4 the difference in isoprene emission by the forest relative to the savannah, $\Delta E_{\mathrm{isoprene},f-s}$ in $\mathrm{ppb\,m\,s^{-1}}$, is varied. The sensitivity analysis presented in Sect. 5.3.5 treats the dependences on the differences between the forest and the savannah in kinematic heat flux, $\Delta\overline{w'\theta'}_{f-s}$ in $\mathrm{K\,m\,s^{-1}}$, and kinematic moisture flux, $\Delta\overline{w'q'}_{f-s}$ in $\mathrm{kg\,kg^{-1}\,m\,s^{-1}}$. The impact of NO_x is discussed in Sect. 5.3.6.

5.2.3 Formulation and interpretation of the segregation

We derive the intensity of segregation for a generic second-order chemical reaction,

$$A + B \rightarrow C. \tag{5.1}$$

For a 3-dimensional field of filtered atmospheric variables, as generated by Large-Eddy Simulations, the concentration of a chemical compound C satisfies the conservation equation

$$\frac{\partial c_C}{\partial t} + \frac{\partial u_i c_C}{\partial x_i} + \mathrm{SGF} = R \tag{5.2}$$

with

$$R = k \cdot c_A \cdot c_B. \tag{5.3}$$

A, B and C are indicators for chemical compounds, u_i and x_i are respectively the wind velocity and the coordinate in the i-direction, SGF is the parameterized sub-grid flux (see Heus et al. (2010) for a complete description), k is the reaction constant, R is the chemical reaction rate and c_A, c_B and c_C are the concentrations of respectively the chemicals A, B and C.

Equations (5.1), (5.2) and (5.3) describe processes for a 3-D field. However, numerical calculations are often performed using spatially averaged values. In order to compare box models, mesoscale models or climate models with measurements, the averages for the 3-D field should be calculated over the complete mixing volume. Every possible variable, ϕ, can be expressed as

$$\phi = [\phi] + \phi', \tag{5.4}$$

Table 5.3: Description of the different simulations. Variables not listed in this table are kept the same as the control cases treated in Sect. 5.2.2. u_g and v_g are the large scale background wind profiles. N_{patches} represents the total number of patches in which the surface is divided in the x-direction. $\Delta\overline{w'\theta'}_{f-s}$ is the difference in kinematic heat flux over the forest patch, f, relative to the savannah patch, s, and $\Delta\overline{w'q'}_{f-s}$ is the difference in kinematic moisture flux. $\Delta E_{\text{isoprene},f-s}$ represents the difference in isoprene emission between the forest and the savannah. c_{NO_2} is the initial free tropospheric NO_2 concentration. The input variables that are altered with respect to the heterogeneous control numerical experiment, HET, are printed in bold.

Name	Grid	$\mathbf{u_g}$	$\mathbf{v_g}$	$\mathbf{N_{patches}}$	$\mathbf{\Delta\overline{w'\theta'}_{f-s}}$	$\mathbf{\Delta\overline{w'q'}_{f-s}}$	$\mathbf{\Delta E_{isoprene,f-s}}$	$\mathbf{c_{NO_2}}$
[−]	[− × − × −]	[m s^{-1}]	[m s^{-1}]	[−]	[K m s^{-1}]	[10^{-3} kg kg^{-1} m s^{-1}]	[ppb m s^{-1}]	[ppb]
Control numerical experiments								
HOM	256 × 256 × 128	0.0	0.0	4	**0.0000**	**0.000**	**0.0**	0.0
HET	256 × 256 × 128	0.0	0.0	4	−0.1000	0.040	0.7	0.0
Impact of background wind								
WU1	256 × 256 × 128	0.0	**2.5**	4	**0.0000**	**0.000**	**0.0**	0.0
WU2	256 × 256 × 128	0.0	**5.0**	4	**0.0000**	**0.000**	**0.0**	0.0
WU3	256 × 256 × 128	0.0	**7.5**	4	**0.0000**	**0.000**	**0.0**	0.0
WX1	256 × 256 × 128	**2.5**	0.0	4	−0.1000	0.040	0.7	0.0
WX2	256 × 256 × 128	**5.0**	0.0	4	−0.1000	0.040	0.7	0.0
WX3	256 × 256 × 128	**7.5**	0.0	4	−0.1000	0.040	0.7	0.0
WY1	256 × 256 × 128	0.0	**2.5**	4	−0.1000	0.040	0.7	0.0
WY2	256 × 256 × 128	0.0	**5.0**	4	−0.1000	0.040	0.7	0.0
WY3	256 × 256 × 128	0.0	**7.5**	4	−0.1000	0.040	0.7	0.0
Impact of the length scale of heterogeneity								
LS1	256 × 256 × 128	0.0	0.0	**2**	−0.1000	0.040	0.7	0.0
LS2	256 × 256 × 128	0.0	0.0	**8**	−0.1000	0.040	0.7	0.0
LS3	256 × 256 × 128	0.0	0.0	**16**	−0.1000	0.040	0.7	0.0
LSB1	**1024 × 512** × 128	0.0	0.0	4	**0.0000**	**0.0000**	0.7	0.0
LSB2	**1024 × 512** × 128	0.0	0.0	**2**	−0.1000	0.040	0.7	0.0
LSB3	**1024 × 512** × 128	0.0	0.0	4	−0.1000	0.040	0.7	0.0
LSB4	**1024 × 512** × 128	0.0	0.0	**8**	−0.1000	0.040	0.7	0.0
LSB5	**1024 × 512** × 128	0.0	0.0	**16**	−0.1000	0.040	0.7	0.0
Impact of the spatial variation of isoprene emissions								
IS1	256 × 256 × 128	0.0	0.0	4	−0.1000	0.040	**1.3**	0.0
IS2	256 × 256 × 128	0.0	0.0	4	−0.1000	0.040	**0.0**	0.0
IS3	256 × 256 × 128	0.0	0.0	4	−0.1000	0.040	**−0.7**	0.0
Impact of the spatial variation of surface heat fluxes								
HF1	256 × 256 × 128	0.0	0.0	4	**0.0000**	**0.000**	0.7	0.0
HF2	256 × 256 × 128	0.0	0.0	4	**−0.0125**	**0.005**	0.7	0.0
HF3	256 × 256 × 128	0.0	0.0	4	**−0.0250**	**0.010**	0.7	0.0
HF4	256 × 256 × 128	0.0	0.0	4	**−0.0375**	**0.015**	0.7	0.0
HF5	256 × 256 × 128	0.0	0.0	4	**−0.0500**	**0.020**	0.7	0.0
HF6	256 × 256 × 128	0.0	0.0	4	**−0.1500**	**0.060**	0.7	0.0
HF7	256 × 256 × 128	0.0	0.0	4	**−0.2000**	**0.080**	0.7	0.0
Sensitivity to free tropospheric NO_2								
UNO	256 × 256 × 128	0.0	0.0	4	**0.0000**	**0.000**	**0.0**	**0.5**
HNO	256 × 256 × 128	0.0	0.0	4	−0.1000	0.040	0.7	**0.5**

in which the rectangular brackets correspond to a spatial average and the prime corresponds to a deviation from the spatial average. The spatial average is calculated over a horizontal plane or over a volume. If the reaction rate constant is considered to be equal throughout the boundary layer, the spatial average of the reaction rate is equal to

$$[R] = k \cdot [c_A \cdot c_B] \,. \tag{5.5}$$

By applying a Reynolds decomposition (Eq. 5.4) with its properties, Eq. (5.5) becomes

$$[R] = k \cdot ([c_A] \cdot [c_B] + [c'_A \cdot c'_B]) \,. \tag{5.6}$$

The physical interpretation of the intensity of segregation is the relative deviation of the total chemical reaction rate from the reaction rate due to the mean concentrations,

$$R_{\text{mean}} = k \cdot [c_A] \cdot [c_B] \,. \tag{5.7}$$

This is expressed as

$$I_{\text{S}} \equiv \frac{[R] - R_{\text{mean}}}{R_{\text{mean}}}. \tag{5.8}$$

I_{S} is the intensity of segregation. Substituting Eqs. (5.6) and (5.7) in Eq. (5.8) yields

$$I_{\text{S}} = \frac{\left[c'_A \cdot c'_B\right]}{[c_A] \cdot [c_B]} \tag{5.9}$$

and the average chemical reaction rate reads:

$$[R] = k \cdot (1 + I_{\text{S}}) \cdot [c_A] \cdot [c_B] = k_{\text{eff}} \cdot [c_A] \cdot [c_B] \,. \tag{5.10}$$

Equation (5.9) shows that the intensity of segregation is equal to the covariance of the two reacting chemicals divided by their mean concentrations. Since DALES explicitly resolves turbulence, including quantities like covariances, the intensities of segregation are calculated directly. Ouwersloot et al. (2010) validated the DALES results, confirming the dependence of segregation on the ratio of the turbulent time scale versus the chemical time scales and on the reactant concentration ratio (Schumann, 1989) and giving results in agreement with measurements (Butler et al., 2008; Dlugi et al., 2010) and previous simulations (Krol et al., 2000; Vinuesa and Vilà-Guerau de Arellano, 2003).

We further discuss the dependence of the intensity of segregation on the physical and chemical processes. For instance, for perfectly mixed conditions I_{S} is 0, though its value can range from -1 to infinity. More insight on the sign of the intensity of segregation is obtained by analysing I_{S} as a function of the correlation and the concentration variances. The intensity

of segregation for 2 reacting species is related with the correlation factor, r, where

$$r = \frac{\sigma_{AB}}{\sigma_A \cdot \sigma_B}. \tag{5.11}$$

The standard deviations of the concentrations of compounds A and B are expressed by σ_A and σ_B and their covariance is expressed by σ_{AB}. The variance of c_A is defined as $\sigma_A^2 = \left[c'_A \cdot c'_A\right]$ and the covariance between c_A and c_B is equal to $\left[c'_A \cdot c'_B\right]$. Equations (5.9) and (5.11) show that

$$I_S = r \cdot \frac{\sigma_A \cdot \sigma_B}{[c_A] \cdot [c_B]}. \tag{5.12}$$

This can be denoted as

$$I_S = r \cdot i_A \cdot i_B, \tag{5.13}$$

where i_X is the concentration fluctuation intensity of compound X, defined as

$$i_X \equiv \frac{\sigma_X}{[c_X]}. \tag{5.14}$$

Since concentrations and standard deviations are always positive if non-zero, the sign of I_S equals the sign of r. This correlation factor is controlled by transport and chemistry. First we will briefly address the influence of transport. Inert species that are transported together are positively correlated, $r > 0$. This is the case for two compounds which are both entrained from the free troposphere or both emitted from the surface. If one compound is emitted from the surface and the other is entrained from the free troposphere, then the species are negatively correlated, $r<0$. Further, chemistry has an impact on the correlation factor since two reacting compounds are negatively correlated. For two reactants that are transported, the overall sign of the correlation factor therefore depends on the interaction between the dynamics and chemistry. The correlation between isoprene and OH as a function of height will be treated in Sect. 5.3.1.

Definition of the boundary layer height

To calculate the intensities of segregation in the boundary layer, the boundary layer height needs to be defined. For a heterogeneous surface forcing, it varies over the domain. In order to determine the boundary layer heights as a function of time and the x-coordinate, an adaptation of the maximum gradient method (Sullivan et al., 1998) is applied to the averages in the y-direction of the virtual potential temperature, θ_v:

$$\theta_v = \theta \cdot (1 + 0.61 \cdot q) \tag{5.15}$$

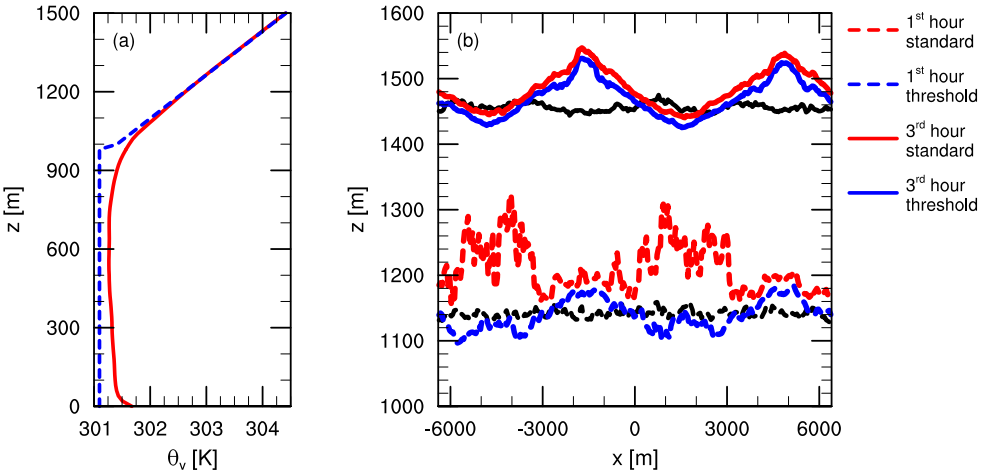

Figure 5.2: **(a)** *The **initial** profile in blue and the profile **after 30 min** in red for the virtual potential temperature as a function of height. The profile is calculated for an arbitrary position in the area towards which warm air is advected in the top of the boundary layer. In* **(b)** *the boundary layer heights as determined by the **maximum gradient** and the **threshold gradient** methods are shown as a function of the x-position in respectively red and blue. As a reference, the boundary layer height over a **homogeneous** surface, as determined by the maximum gradient method, is shown in black. The dashed and solid lines show the boundary layer heights averaged over the first and third hour of the simulation, respectively. The relatively cold forest patches are located at −6400 m< x < −3200 m and 0 m< x <3200 m. Here, the boundary layer is shallower than over the relatively warm savannah patches.*

Differences in θ_v between air parcels and the air surrounding them drive the buoyancy (Stull, 1988). The buoyancy flux in a clear boundary layer is

$$\overline{w'\theta'_v} \cong (1 + 0.61\overline{q})\,\overline{w'\theta'} + 0.61\,\overline{\theta}\,\overline{w'q'}, \tag{5.16}$$

emphasizing the importance of the surface energy partitioning into sensible heat and moisture flux for buoyancy. Considering the difference in orders of magnitude of the different terms, this equation shows that the buoyancy flux is dominated by the kinematic sensible heat flux, $\overline{w'\theta'}$. Note that in the case of a uniform sensible surface heat flux, differences in the kinematic surface moisture flux, $\overline{w'q'}$, result in buoyancy flux differences and the generation of turbulence and mesoscale circulations. Hence, analyses that only take into account the amplitude of the sensible surface heat flux heterogeneity would be erroneous.

Mesoscale circulations lead to advection of warm air at the top of the boundary layer over a patch with relatively cool air. This results in a virtual potential temperature profile as shown

Table 5.4: Main properties of the different numerical experiments averaged over the fourth hour of simulated time. h_{BL} represents the boundary layer height. $\langle\theta\rangle$ and $\langle q\rangle$ are respectively the potential temperature and specific humidity averaged over the whole boundary layer. w_* is the convective velocity scale. The boundary layer averaged concentrations of isoprene and OH are denoted by respectively $\left\langle c_{\mathrm{Isoprene}}\right\rangle$ and $\langle c_{\mathrm{OH}}\rangle$. Is_{R9} is the intensity of segregation for Reaction (R9) (Table 5.2).

Case	h_{BL}	$\langle\theta\rangle$	$\langle q\rangle$	w_*	$\left\langle c_{\mathrm{Isoprene}}\right\rangle$	$\langle c_{\mathrm{OH}}\rangle$	$\mathrm{Is}_{\mathrm{R9}}$
[−]	[m]	[K]	[10^{-3} kg kg^{-1}]	[m s^{-1}]	[ppb]	[ppt]	[−]
HOM	1550	302.11	5.74	2.04	1.28	0.142	−0.070
HET	1587	302.16	5.68	2.05	1.33	0.142	−0.126
WU1	1538	302.10	5.76	2.03	1.30	0.142	−0.077
WU2	1528	302.08	5.78	2.03	1.32	0.142	−0.087
WU3	1527	302.08	5.78	2.03	1.32	0.142	−0.093
WX1	1534	302.09	5.77	2.03	1.34	0.143	−0.110
WX2	1529	302.09	5.77	2.03	1.33	0.142	−0.104
WX3	1530	302.09	5.77	2.03	1.33	0.142	−0.104
WY1	1587	302.16	5.68	2.05	1.33	0.142	−0.132
WY2	1576	302.15	5.69	2.05	1.35	0.142	−0.143
WY3	1576	302.15	5.69	2.05	1.37	0.143	−0.154
LS1	1557	302.12	5.73	2.04	1.42	0.143	−0.176
LS2	1606	302.19	5.64	2.06	1.29	0.142	−0.114
LS3	1568	302.14	5.71	2.05	1.30	0.141	−0.090
LSB1	1549	302.11	5.74	2.04	1.28	0.142	−0.070
LSB2	1528	302.11	5.78	2.03	1.61	0.168	−0.405
LSB3	1547	302.12	5.75	2.04	1.54	0.153	−0.308
LSB4	1552	302.12	5.74	2.04	1.43	0.143	−0.177
LSB5	1587	302.16	5.68	2.06	1.33	0.142	−0.126
IS1	1587	302.16	5.68	2.05	1.41	0.142	−0.183
IS2	1587	302.16	5.68	2.05	1.28	0.142	−0.087
IS3	1587	302.16	5.68	2.05	1.30	0.141	−0.095
HF1	1550	302.11	5.74	2.04	1.43	0.145	−0.196
HF2	1546	302.11	5.75	2.04	1.41	0.141	−0.148
HF3	1545	302.10	5.75	2.04	1.38	0.140	−0.114
HF4	1548	302.11	5.75	2.04	1.36	0.140	−0.110
HF5	1556	302.12	5.73	2.04	1.35	0.141	−0.111
HF6	1622	302.21	5.62	2.07	1.32	0.142	−0.146
HF7	1650	302.26	5.58	2.08	1.33	0.143	−0.174
UNO	1550	302.11	5.74	2.04	1.04	0.192	−0.124
HNO	1587	302.16	5.68	2.05	1.10	0.197	−0.209

in Fig. 5.2a. It shows the initial profile together with a profile after half an hour of simulation. The location is an arbitrary position in the area towards which warm air is advected. In the inversion zone, $z \approx 1000$ m, no clear θ_v gradient is present. This would result in a flawed determination of the boundary layer height using the maximum gradient method. To circumvent this, an alternative method is proposed: a threshold gradient method. This method sets the boundary layer height equal to the lowest height for which the gradient of the considered variable, in our case the virtual potential temperature, exceeds a certain percentage of the maximum gradient. In the case no sharp inversion is present, this maximum gradient will be equal to the lapse rate in the free troposphere. In the treatment of the numerical experiments presented in this paper, the threshold percentage is set to 90 %. This threshold percentage is chosen such that the erratic boundary layer height determinations are suppressed, but the determined heights for profiles with a clear inversion remain similar. The result is shown in Fig. 5.2b. This graph is based on the numerical experiment HET. During the first hour the threshold gradient method results in smoother and less random boundary layer heights as a function of the x-position. In the third hour the gradient is more well defined at all locations and both methods result in similar boundary layer heights.

5.3 Results

The main properties of the numerical experiments during the fourth hour of simulated time are summarized in Table 5.4. The dynamical properties include the boundary layer height, the averages over the whole boundary layer of the potential temperature and the specific humidity, and the convective velocity scale. The convective velocity scale is almost unaffected by the differences between the numerical experiments. The listed chemical properties represent the volume averages of the isoprene and hydroxyl radical concentrations over the entire boundary layer and the intensity of segregation of the isoprene-OH reaction. The mean concentration of OH is less strongly affected by the differences between the simulations compared to the intensity of segregation and the mean isoprene concentration. A more detailed analysis of the results follows in the next paragraphs.

5.3.1 Influence of heterogeneous surface conditions

Dynamics

In Fig. 5.3, the dynamical characteristics are shown for the cases with standard homogeneous, HOM, and standard heterogeneous, HET, surface forcing. The savannah patches are located at $-\frac{\lambda}{2} < x < 0$ and $\frac{\lambda}{2} < x < 1$. The depicted variables are averaged both over the fourth hour of the numerical experiments (1 h average) and over the y-coordinate, which is the horizontal

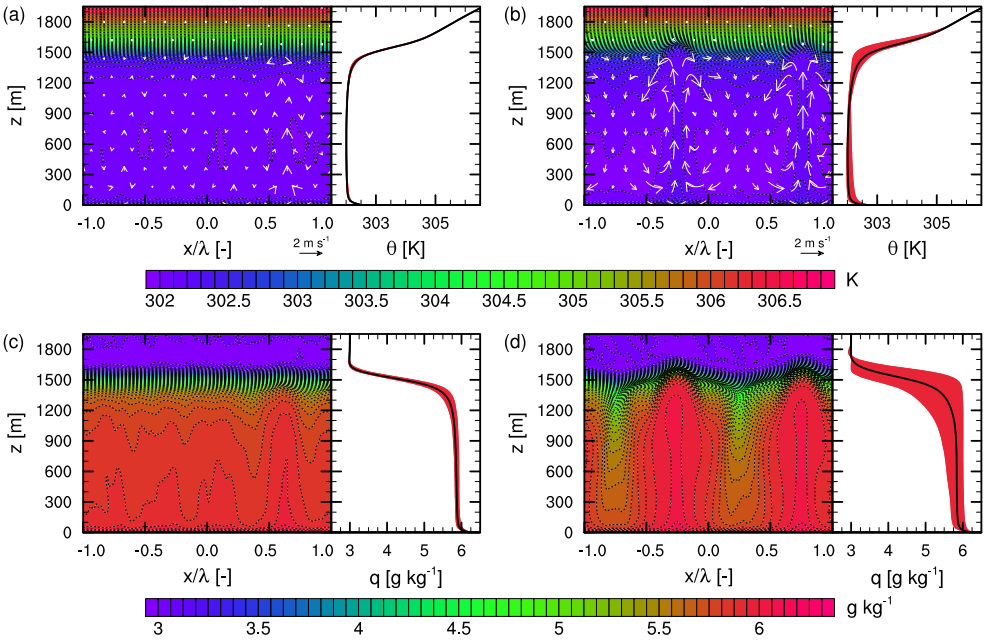

Figure 5.3: Potential temperature and moisture for the homogeneous case **(a, c)** *and the heterogeneous case* **(b, d)**. *Each figure consists of two panels. The first panel shows these variables averaged over the fourth hour of simulated time and the y-direction, while the second panel shows an additional average in the x-direction. The red area in the second panel shows the variability in the x-direction of the temporal and y averaged values. The potential temperature, θ, is shown on top* **(a, b)** *and the specific humidity, q, at the bottom* **(c, d)**. *Wind direction and magnitude are indicated by vectors* **(a, b)**. *The x-coordinate is scaled by the length scale of heterogeneity, λ, which is twice the patch size.*

direction perpendicular to the direction of heterogeneity. The flow of air within the boundary layer is indicated by the arrows in Fig. 5.3a and b. From these graphs it is clear that a heterogeneous surface forcing influences the mixing in the atmospheric boundary layer. While the potential temperature and specific humidity are well-mixed throughout the boundary layer for the homogeneous case, a mesoscale structure appears for the heterogeneous case. The differences in surface buoyancy fluxes between the forest and savannah patches induce mesoscale circulations. Over the warm and dry savannah patches air is transported to the top of the boundary layer, while air is transported downward over the colder and wetter forested patches. This is in accord with the findings of Patton et al. (2005) and van Heerwaarden and Vilà-Guerau de Arellano (2008). The rising air moves faster (with a velocity of more than $2\,\mathrm{m\,s^{-1}}$ in the core of the rising plume halfway up the boundary layer) and is spread over

a smaller area than the descending air (with an average velocity of approximately $0.5\,\mathrm{m\,s^{-1}}$ halfway up the boundary layer). Due to this pattern, turbulent mixing is stronger over the savannah patches than over the forest patches.

For the heterogeneous case the average boundary layer height is higher than for the homogeneous case, but also more variability is observed in the x-direction. This effect is explained by van Heerwaarden and Vilà-Guerau de Arellano (2008). At the top of the buoyant thermals, the entrainment is enhanced, because the relatively warm air with more kinetic energy can penetrate the inversion layer relatively easily. The entrained air is horizontally advected towards the forest patches where it is transported downwards. Over the forest patches, thermals are suppressed by the subsiding branch of the mesoscale circulations, reducing entrainment over these areas. This process leads to higher boundary layer heights over the savannah patches than over the forest patches. The average boundary layer height of the numerical experiment HET is higher than that of HOM, however this difference is less than 40 m. The minimum boundary layer height in the numerical experiment HET is approximately equal to the average boundary layer height in the numerical experiment HOM. A more detailed explanation of the dependence of the boundary layer height on the surface energy partitioning is presented in Sect. 5.3.5.

The right panels of Fig. 5.3 show that the variability of the dynamic variables in the x-direction is increased significantly by a heterogeneous surface forcing. This is caused by entrained air and the mesoscale circulations. In the lower half of the boundary layer, the air over the savannah is warmer due to the higher sensible heat fluxes. The mesoscale circulations caused by this difference transport emitted moisture from the forest to the savannah. Therefore the air over the savannah, which is transported upward, is warmer and more moist than over the forest. In the upper half of the boundary layer, entrainment is of importance. The entrained air is warmer and drier than the air in the boundary layer and is transported to the forest patch by a mesoscale circulation. Therefore, also the air in the upper half of the boundary layer is drier over the forested patch than over the savannah patch. However, due to the relatively warm air parcels that are entrained, the temperature in the upper half of the boundary layer is higher over the forest patch than over the savannah patch. The processes near the surface and the entrainment zone have the same effect on the horizontal distribution of moisture in the boundary layer, while the effects are opposed for the distribution of the potential temperature. Because of this, the variability in the potential temperature is much lower than the variability in the specific humidity if normalized by the differences between the free troposphere and the boundary layer for the respective variables.

In contrast to the increased variability of the dynamic variables, the horizontally averaged vertical profiles are very similar. The maximum differences in potential temperature and specific humidity are located at approximately 1350 m and 1600 m height, which are, respectively, in the upper part and just above the average top of the boundary layer. For the

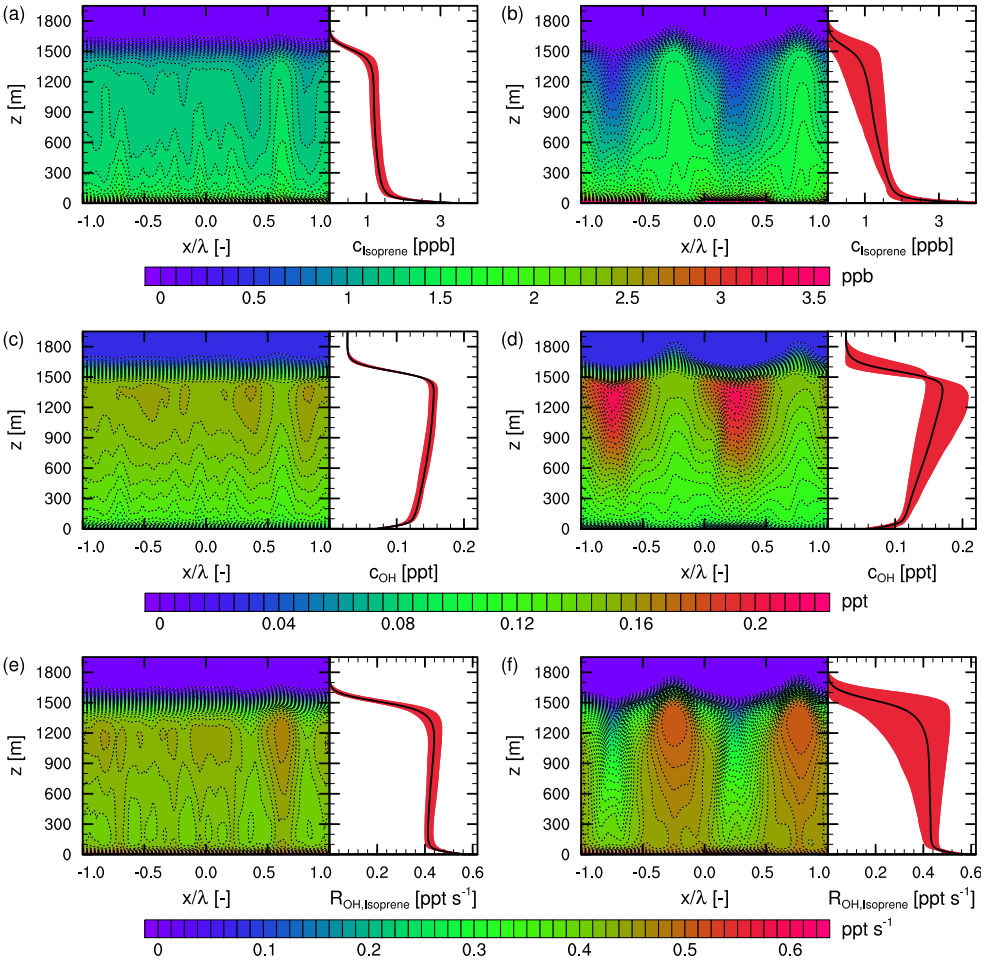

Figure 5.4: Isoprene and OH concentrations and chemical reaction rates for the homogeneous case **(a, c, e)** *and the heterogeneous case* **(b, d, f)**. *Each figure consists of two panels. The first panel shows these variables averaged over the fourth hour of simulated time and the y-direction, while the second panel shows an additional average in the x-direction. The red area in the second panel shows the variability in the x-direction of the temporal and y averaged values. The concentration of Isoprene, $c_{Isoprene}$, is shown on top* **(a, b)**, *followed by the concentration of the hydroxyl radical, c_{OH}, in the middle* **(c, d)**. *At the bottom* **(e, f)** *the chemical reaction rates for Reaction (R9), $R_{OH,Isoprene}$, are displayed. The x-coordinate is scaled by the length scale of heterogeneity, λ, which is twice the patch size.*

heterogeneous case the potential temperature at these heights are respectively 0.1 K warmer and 0.3 K colder, while the specific humidity at these heights are respectively 0.1 g kg^{-1} lower and 0.3 g kg^{-1} higher. The small decrease in average potential temperature and the small increase in specific humidity for the heterogeneous surface forcing are due to the intrusion of the buoyant thermals towards the free troposphere. Since the air in the boundary layer is more humid and colder than the free troposphere, this leads to the deviation in averaged quantities. The changes at a height of 1350 m are due to entrained air from the free troposphere.

Atmospheric chemistry

The spatial distributions of the concentrations and reaction rates of isoprene with the hydroxyl radical are displayed in Fig. 5.4 for the numerical experiments HOM and HET. As we specifically study the isoprene-OH reaction, the concentrations of these two reactants are shown together with their chemical reaction rate. Due to the induced mesoscale circulations, the isoprene is advected near the earth's surface from the forest towards the savannah patches, where it is transported upwards. After emission, the isoprene reacts with OH. Due to these interactions, above the surface layer the concentration of isoprene is significantly higher over the savannah patches than over the forested patches. This is shown in more detail in Fig. 5.5. Since isoprene depletes OH, the chemical reaction rates are highest and the OH concentrations are lowest over the savannah patches. At the top of the rising thermals a region appears with a relatively high reaction rate, because the chemical reaction rate depends on the product of both concentrations. These features are governed by the spatial distribution of isoprene. Dynamics have an impact on chemistry, because in the thermals the lifetime of isoprene (approximately 50 min) is of the same order of magnitude as the transport time from the surface to the top of the boundary layer (approximately 15 min). For both the homogeneous and heterogeneous surface forcings the reaction rate is highest near the surface, where isoprene concentrations are highest.

Due to the mesoscale circulations, the boundary layer over the forest is strongly influenced by the entrained air, while the boundary layer over the savannah is mainly affected by the surface turbulent fluxes. Therefore, a heterogeneous surface forcing leads to an enhancement of the variability of the chemical variables. In addition, the mean variables as a function of height, shown in the right panels of Fig. 5.4, as well as the averages over the entire domain are affected. For the uniform surface forcing the relatively long-lived species like isoprene are well-mixed, which results in a concentration that is approximately constant with height. However, for a heterogeneous surface forcing the slope of the isoprene concentration profile with height is strongly enhanced due to the entrained air that is transported towards the forested areas. Over the forest, turbulent mixing is less effective for a heterogeneous surface forcing, which results in a significant concentration gradient. Since OH is depleted

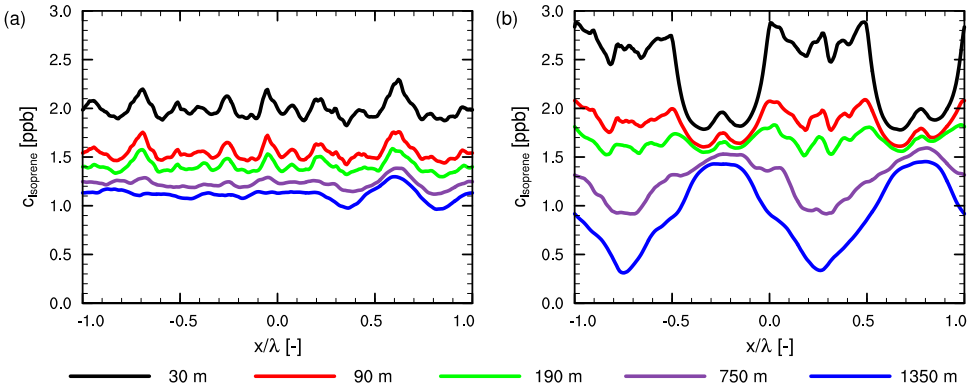

Figure 5.5: Isoprene concentrations for the homogeneous case **(a)** *and the heterogeneous case* **(b)** *at different heights. The concentrations are averaged over the fourth hour of simulated time and the y-direction. The x-coordinate is scaled by the length scale of heterogeneity, λ, which is twice the patch size. The forest patches are located at $-1 < \frac{x}{\lambda} < -0.5$ and $0 < \frac{x}{\lambda} < 0.5$ and the savannah patches are located elsewhere.*

by isoprene, also the OH concentration profile is influenced by this process. The altered concentration profiles result in a differently shaped profile of the isoprene-OH reaction rate. The average concentrations over the entire domain are enhanced by 1.3 % and 5.1 % for OH and isoprene, respectively, while the resulting average chemical reaction rate is reduced by 0.68 %. This counter-intuitive combination of effects that shows a non-linear response, is caused by increased segregation ($1 + I_S$ over the entire domain is decreased by 6.7 %), as outlined in Sect. 5.2.3.

Figure 5.4 shows that the y-averages of the concentrations of OH and isoprene as well as the chemical reaction rate vary both in the x-direction and in height. To calculate the average reaction rate, the different rates have to be determined locally and then averaged spatially, as shown in Eq. (5.5). For this calculation spatially averaged concentrations cannot be used without knowledge of the covariance of the reacting species (Eq. 5.6). This poses a problem for the interpretation of observations that cover only one point in space at a time, e.g. aircraft observations. To interpret these data, one needs to know the intensity of segregation or perform simultaneous observations of all relevant reactants at a high frequency in order to determine the covariances between those reactants.

Processes driving segregation

For the numerical experiments HOM and HET the intensities of segregation in the boundary layer during the 4th hour are −0.07 and −0.13, respectively. This corresponds to effective

chemical reaction rates (k_{eff} in Eq. 5.10) of 93 % and 87 % compared to the chemical reaction rates that are calculated from boundary layer averaged concentrations. This shows that atmospheric chemistry is influenced by dynamics and that a heterogeneous surface forcing might enhance this influence. In this section the processes that drive the segregation are explored.

The intensity of segregation profiles, for the reaction in which OH and isoprene form RO_2, are shown in Fig. 5.6a, b. To produce this figure, the instantaneous intensities of horizontal segregation are determined for each height at 1 min intervals. The mean and variability for these profiles during the fourth hour are depicted with the solid lines and shading. The dashed lines represent the averages over the fourth hour of the instantaneous intensities of segregation over the entire boundary layer at 1 min intervals. Since the intensity of segregation is used to relate the boundary layer averaged chemical reaction rate to the reaction rate which would be calculated using boundary layer averaged concentrations, the intensities of segregation over the entire boundary layer are of most interest. However, the profiles of the intensities of horizontal segregation enable us to identify processes driving the segregation.

Figure 5.6a and b show that the average horizontal segregation can be divided into 3 regions. The lowest region is the surface layer in which the intensity is most negative. Near the top of the boundary layer, the intensity of segregation increases to large positive values. The largest region is in-between, representing the bulk value of the intensity of horizontal segregation. The intensities differ from each other and all are different from the intensity of total boundary layer segregation.

To understand these profiles, the two terms of Eq. (5.12) are plotted separately in Fig. 5.6c and e for the numerical experiment HOM and in Fig. 5.6d and f for the numerical experiment HET. It is shown that for both numerical experiments the horizontal correlation factors behave similar. In the boundary layer, isoprene and the hydroxyl radical are almost perfectly anti-correlated. This indicates that the correlation is strongly influenced by chemistry (Reaction R9). For the heterogeneous surface forcing this anti-correlation is lower in the lower part of the boundary layer. This is probably caused by the generation of regions characterized by low isoprene concentrations. In those regions the importance of Reaction (R9) to OH is relatively low compared to other chemical reactions.

Above the boundary layer, isoprene and OH are strongly positively correlated, indicating that OH producing compounds and isoprene are transported together into the free troposphere (Sect. 5.2.3). In the free troposphere, the concentrations of these compounds are initially very low, as shown in Fig. 5.4. Therefore, at locations where thermals have transported compounds to the free troposphere, the concentrations of both OH and isoprene are higher than the surroundings. This results in a positive correlation. The figures show that the only height at which the magnitude of the intensity of segregation is influenced by the correlation factor, is near the entrainment zone. There the correlation factor changes sign over approximately 100 m, decreasing and increasing again in magnitude in the process. The correlation factor

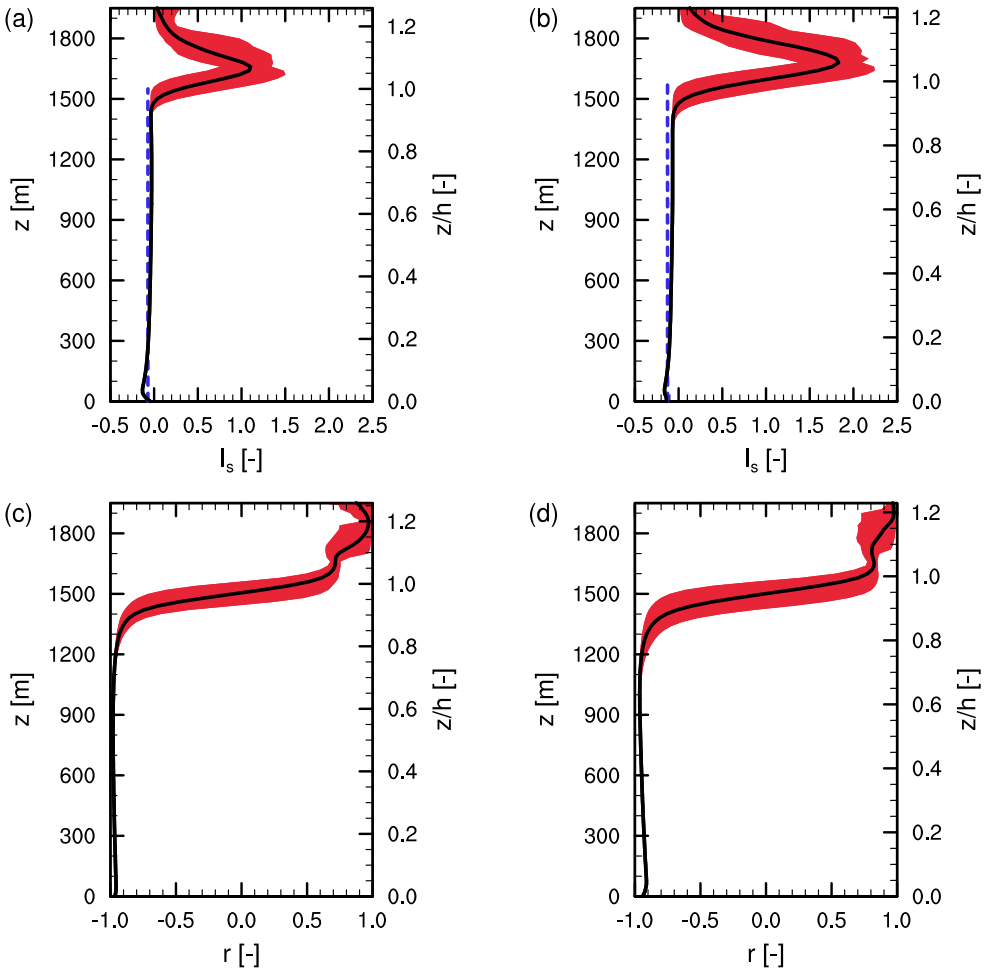

Figure 5.6: Horizontal intensities of segregation and the contributing components, evaluating the isoprene-OH reaction. The fourth hour of the numerical experiments HOM **(a, c, e)** *and HET* **(b, d, f)** *is evaluated. At every height the instantaneous intensity of segregation over the horizontal plane is determined at intervals of 1 min. Its averages are shown in* **(a)** *and* **(b)** *with the* ***variability in time*** *depicted using the red shading. The intensity of segregation over the* ***entire boundary layer*** *is shown by the blue dashed line. In* **(c)** *and* **(d)** *the horizontal spatial correlations between isoprene and OH are shown with their temporal variability. In* **(e)** *and* **(f)** *this is also done for the product of the concentration fluctuation intensities of OH and isoprene, i.e. the second term in Eq. (5.12). In blue and purple dashed lines the separate concentration fluctuation intensities are shown for* ***isoprene*** *and* ***OH****, respectively. The numbers in* **(e)** *and* **(f)** *denote their unnormalized maximum values.*

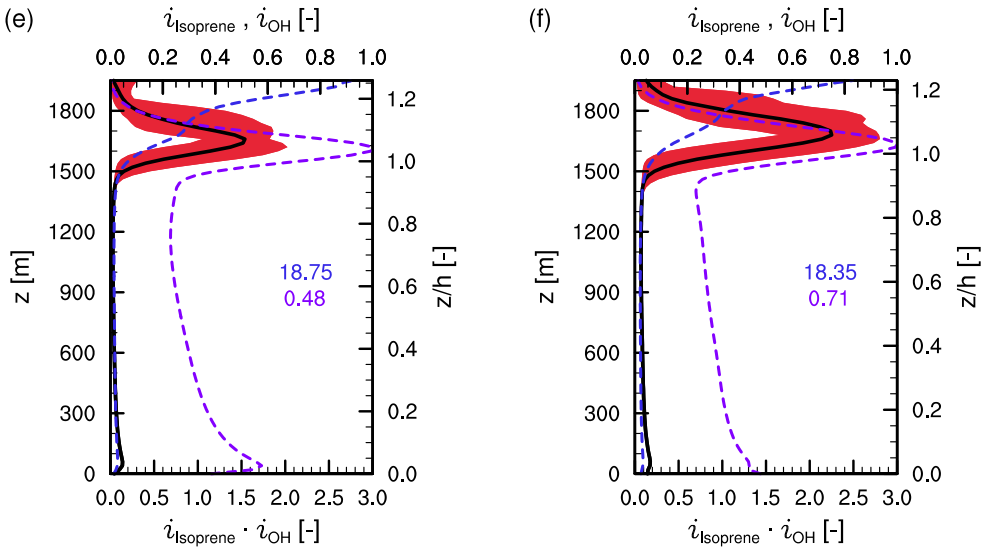

Figure 5.6: (continued)

does determine the sign of the intensity of segregation, since the concentration fluctuation intensities are positive by definition. In the case of isoprene and the hydroxyl radical, the intensity of segregation is therefore negative in the whole boundary layer and positive above.

The products of the concentration fluctuation intensities for isoprene and OH, $i_{\text{Isoprene}} \cdot i_{\text{OH}}$, drawn with the black lines in Fig. 5.6e and f, are shaped similar for both a homogeneous and heterogeneous surface forcing. Near the surface a small peak is present, which is caused by a relatively high concentration fluctuation intensity of OH. This is caused by the high isoprene concentrations near the surface, resulting in rapid depletion of the hydroxyl radical. Above the boundary layer, the relative variabilities of both compounds peak. This is due to local transport through the inversion layer. While the average concentrations decrease with height, the standard deviations slightly increase in that region. Above this layer, also the standard deviations drop with height. Since the area of transport by thermals grows smaller with increasing height, the concentration fluctuation intensity for isoprene still increases with height. Due to fast depletion, OH is characterized by a more uniform concentration in the free troposphere. For the heterogeneous surface forcing the product of the concentration fluctuation intensities for isoprene and OH is enhanced, mostly due to OH. In turn, this leads to an increase in magnitude of the horizontal segregation intensity.

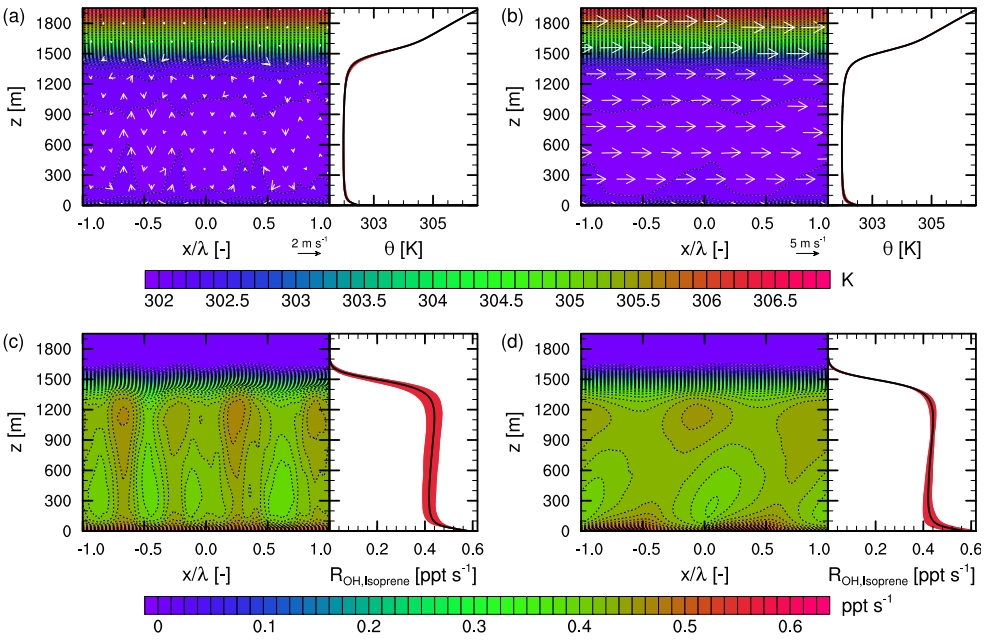

Figure 5.7: Potential temperature and chemical reaction rate for Reaction (R9) for the numerical experiments WU2 **(a, c)** *and WX2* **(b, d)**. *WU2 evaluates a homogeneous surface forcing with a background wind of 5 m s^{-1} in the positive y-direction. In the numerical experiment WX2 a heterogeneous surface forcing is applied with a background wind of 5 m s^{-1} in the positive x-direction. The potential temperature, θ, is shown on top* **(a, b)** *and the chemical reaction rate, $R_{OH,Isoprene}$, below* **(c, d)**. *Each figure consists of two panels. The first panel shows these variables averaged over the fourth hour of simulated time and the y-direction, while the second panel shows an additional average in the x-direction. The red area in the second panel shows the variability in the x-direction of the temporal and y averaged values. Wind direction in the xz-plane and its magnitude are indicated by vectors* **(a, b)**. *The x-coordinate is scaled by the length scale of heterogeneity, λ, which is twice the patch size.*

5.3.2 Influence of background wind

In the previous simulations background wind was not present (i.e. local free convection). In this section its influence will be discussed. For the numerical experiments presented here, the roughness length, z_0, is kept constant to 0.1 m. The validity of this parameter for our numerical experiments is checked by applying a roughness length of 1 m for the forest areas and 0.03 m for the savannah areas. The resulting differences in the main properties are very small for the conditions studied (not shown). Another effect not taken into account in this study is the possibility of differences in the background wind between the boundary layer and the free troposphere. The wind shear generates additional turbulence near the inversion layer, thereby increasing entrainment (e.g. Pino et al., 2003). In turn, this enhanced entrainment would influence both dynamics and chemistry. However, in all simulations presented here, the wind profiles are set constant with height.

In Fig. 5.7 the potential temperature and chemical reaction rate of Reaction (R9) are shown for the numerical experiments WU2 and WX2. Both experiments have a background wind of $5\,\mathrm{m\,s^{-1}}$ (constant with height). In the case of WU2 a homogeneous surface forcing is applied with a background wind pointing in the y-direction. WX2 is characterized by a heterogeneous surface forcing and a background wind pointing in the x-direction. This corresponds to wind blowing perpendicular to the borders between the savannah and forest patches. In Fig. 5.7a it is visible that with a uniform surface forcing, mesoscale circulations are induced in the plane orthogonal to the direction of the background wind. These structures are called horizontal roll vortices (e.g. Stull, 1988; Young et al., 2002). At locations where the air is rising, the potential temperature in the lower part of the boundary layer is higher due to transport of air from the relatively warm surface layer. Chemistry is influenced by these circulations too, due to the horizontally heterogeneous vertical transport of chemical species. The rising branches of the circulations transport isoprene from the surface layer to the upper part of the boundary layer, which is where the hydroxyl radical mixing ratio is highest. Therefore, the chemical reaction rate of Reaction (R9) is higher in the upward moving air than in the downward moving air and has an increased horizontal variability compared to the numerical experiment without background wind (HOM), as shown in Fig. 5.7c. Due to the uneven distribution of isoprene and its depleting effect on the hydroxyl radical, the segregation between isoprene and OH is enhanced.

The influence of background wind on the turbulent coherent structures and the vertical wind velocity is shown in Fig. 5.8. The mesoscale circulations that are characteristic for a heterogeneous surface forcing are slightly enhanced by the horizontal roll vortices if both circulations exist in the same plane. The rising air in the core of the thermals is slower (with a velocity of approximately $1.8\,\mathrm{m\,s^{-1}}$ halfway up the boundary layer), but the structure of the thermals is wider. However, if the background wind blows across the boundaries between sur-

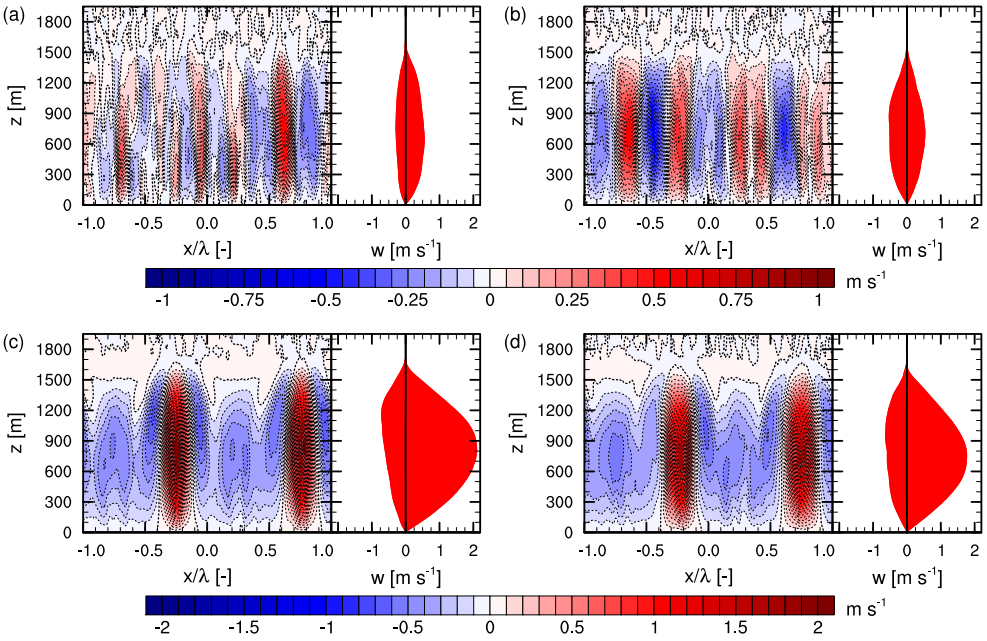

Figure 5.8: Vertical wind velocity for the numerical experiments HOM **(a)**, *HET* **(c)**, *WU2* **(b)** *and WY2* **(d)**. *The upper figures are based on a homogeneous surface forcing while the lower figures are connected to a heterogeneous surface forcing. The background wind was set to* $0\,m\,s^{-1}$ *for the numerical experiments shown in the left column and* $5\,m\,s^{-1}$ *in the positive y-direction for the numerical experiments shown on the right. Each figure consists of two panels. The first panel shows these variables averaged over the fourth hour of simulated time and the y-direction. The red area in the second panel shows the variability in the x-direction of the temporal and y averaged values. The x-coordinate is scaled by the length scale of heterogeneity,* λ*, which is twice the patch size.*

face types, it inhibits the mesoscale circulations due to the extra mixing because of advection. Figure 5.7b shows this suppresses the heterogeneous distribution of the potential temperature, compared to the local free convective case (Fig. 5.3b). Because of this the horizontal variability in the boundary layer height decreases. Consequently, the chemicals are more effectively mixed as well, resulting in more uniform chemical reaction rates in the boundary layer as illustrated by Fig. 5.7d. The dependence on wind direction and the significance of a background wind of $5\,m\,s^{-1}$ is in accordance with previous studies (Raasch and Harbusch, 2001; Kim et al., 2004).

Multiple numerical experiments have been performed with background wind for both kinds of surface forcing. The magnitudes were set to 2.5, 5.0 and $7.5\,m\,s^{-1}$ and in the case of

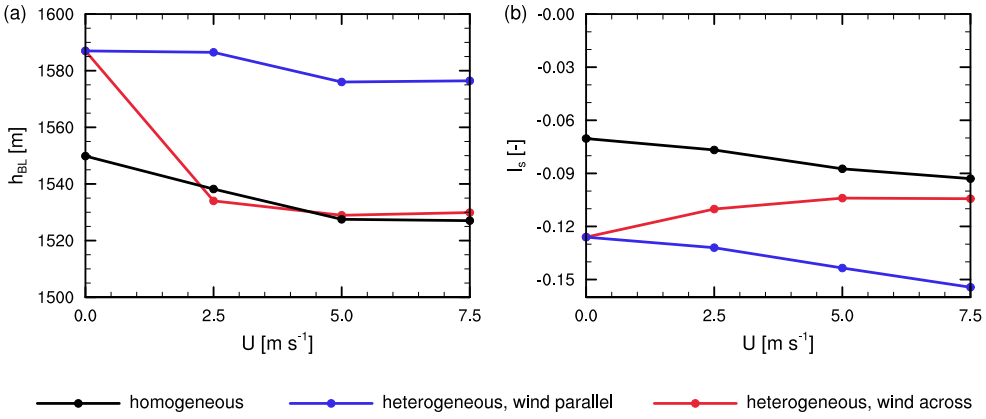

Figure 5.9: Dependency of the boundary layer height **(a)** *and the intensity of segregation in the boundary layer for Reaction (R9)* **(b)** *on horizontal wind. The plotted variables are averages over the fourth hour of simulated time. The boundary layer heights are additionally averaged in the x-direction. The black lines represent the numerical experiments with a* ***homogeneous surface forcing****, while the other two lines are based on cases with a heterogeneous surface forcing. For these cases, the wind can have two directions. The blue lines correspond to* ***wind blowing parallel*** *to the borders between the grass and savannah patches, i.e. in the y-direction, and the red lines correspond to* ***wind blowing across*** *these borders, i.e. in the x-direction.*

a heterogeneous surface forcing the wind direction was set either parallel or perpendicular to the borders. Figure 5.9 summarizes the effects on the boundary layer height and the intensity of segregation for the isoprene-OH reaction, Reaction (R9) (Table 5.2). The average boundary layer height slightly decreases for increasing wind velocities.

This seems to be caused by the lower vertical wind velocity maxima near the inversion layer with stronger background winds. For the cases with heterogeneous surface forcing and wind across the boundaries of the patches, the mixing effect of the background wind dominates the effect of surface heterogeneity. Therefore, the characteristics tend towards values representative for a homogeneous surface and the decrease in boundary layer height is strongest for these numerical experiments.

In general, chemicals are segregated more if a background wind is present, resulting in the heterogeneous chemical reaction rate of Fig. 5.7c. Figure 5.9b shows that this effect increases with the wind velocity. However, in the case of a heterogeneous surface forcing and advection across the patch borders, the magnitude of the intensity of segregation decreases. Again, this is due to the background wind smoothing the effect of surface heterogeneity: by enhancing the mixing of chemical species, the reactants are segregated less.

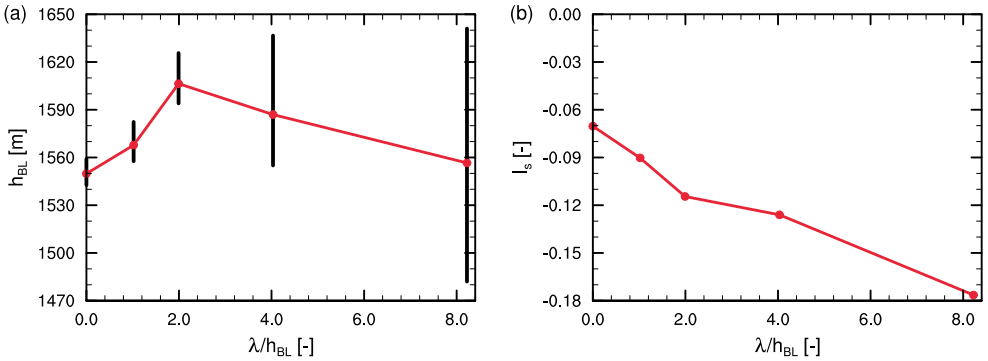

Figure 5.10: Dependency of the boundary layer height **(a)** *and the intensity of segregation in the boundary layer for the isoprene-OH Reaction (R9)* **(b)** *on the length scale of heterogeneity (i.e. twice the patch size). The homogeneous surface forcing corresponds to a heterogeneous surface forcing with a length scale of 0 m. The plotted variables are averages over the fourth hour of simulated time. The boundary layer heights are additionally averaged in the x-direction. The length scales on the bottom axes are normalized by the corresponding averaged boundary layer heights, h_{BL}. In* **(a)** *the black vertical lines represent the variability in the hourly averaged boundary layer height in the x-direction.*

5.3.3 Influence of the length scale of heterogeneity

Previous studies have shown that the impact of a heterogeneous surface forcing on dynamics is highly dependent on the length scale of heterogeneity (e.g. Avissar and Schmidt, 1998; Raasch and Harbusch, 2001; Patton et al., 2005). Also the effects on atmospheric chemistry depend on this length scale. Figure 5.10 shows the sensitivities of the boundary layer height and the intensity of segregation of the isoprene-OH Reaction (R9). Note that in this analysis, length scales are scaled by the boundary layer height. When analysing the TKE, scaled by the convective velocity, as a function of the normalized length scale in a similar way as Patton et al. (2005), we qualitatively find the same sensitivity (not shown), but the maxima of TKE occur at $\lambda \approx 16\ h_{BL}$ instead of $\lambda \approx 8\ h_{BL}$. Therefore a more appropriate scaling might exist.

In the case of the shorter length scales ($\lambda < 2\ h_{BL}$), stronger mesoscale motions are induced for an increase in length scale. Consequently, the upward moving thermals are more localized over the savannah and therefore stronger. Due to the more vigorous thermals over the savannah patches, entrainment becomes stronger, which leads to enhanced boundary layer heights over the savannah, explaining the increase in the maxima. At larger length scales, the cores of the thermals increase in size if the length scale increases. Therefore, entrainment does not intensify and the boundary layer height maxima over the savannah remain the same. For very large length scales ($\lambda > 16\ h_{BL}$) the boundary layer over the centre of the savannah

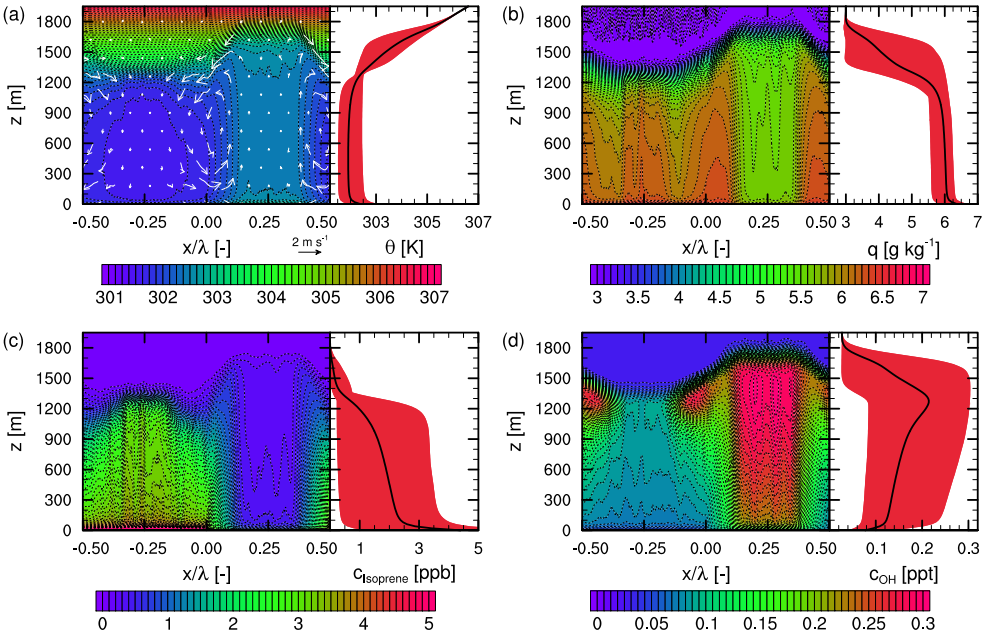

Figure 5.11: The potential temperature **(a)**, *specific humidity* **(b)**, *isoprene concentration* **(c)** *and OH concentration* **(d)** *for the fourth hour of the numerical experiment LSB2. The length scale of heterogeneity, λ, is 51.2 km, which is equal to 33.5 times the averaged boundary layer height during this period. Each figure consists of two panels. The first panel shows the variables averaged over the fourth hour of simulated time and the y-direction, while the second panel shows an additional average in the x-direction. The red area in the second panel shows the variability in the x-direction of the temporal and y averaged values. Wind direction and magnitude are indicated by vectors* **(a)**.

(forest) patch is not affected by the surface forcing of the forest (savannah), which is visible in Fig. 5.11. This shows a separation of the combined boundary layer into separate boundary layers over the forest and savannah areas. The only interaction occurs near the interface (for our cases approximately 10 km wide) where a circulation still exists. If the boundary layers are fully separated, increasing the length scale of heterogeneity will not have any effect.

In the case of induced mesoscale circulations, hot air at the top of the boundary layer is transported from the savannah to the forest patches. Since no distinct temperature inversion is present over the forests (see Fig. 5.2a), the resulting heating enables more rapid boundary layer growth by generating a more gradual transition in temperature to the free tropospheric lapse rate. Therefore, for the smaller length scales, also over the forest areas the boundary layer heights increase with increasing length scale. However, in the case of larger length

scales ($\lambda > 2\ h_{\mathrm{BL}}$), direct entrainment of air from the free troposphere does not occur over the forests due to the mesoscale circulations, in accord with the findings of van Heerwaarden and Vilà-Guerau de Arellano (2008). In addition, in those cases the relative amount of transported heat from the savannah areas compared to the size of the forest areas decreases with an increasing length scale, leading to a decrease in the boundary layer heights over the forests. The domain-averaged boundary layer height decreases due to this more uneven distribution of entrained air as well.

The distribution of reactive species is also affected by the length scale. In this analysis the focus is on isoprene and OH. For the shorter length scales ($\lambda < 2\ h_{\mathrm{BL}}$), the non-uniformly distributed isoprene, due to heterogeneous surface emissions, is mixed within the surface layer (Mahrt, 2000). Therefore the strongest effect on the chemistry is an enhancement of the horizontal segregation in the surface layer. For increasing length scales, the mesoscale circulations become stronger, transporting isoprene from the forests to the savannah. The combination of the induced transport by the mesoscale circulations and the depletion by OH leads to increasing concentrations of isoprene over the savannah areas and lower concentrations in the upper part of the boundary layer over the forest areas. Since OH and isoprene react efficiently, the distribution of OH is affected in an opposite direction, leading to additional segregation.

For even larger length scales ($\lambda \geq 16\ h_{\mathrm{BL}}$, not shown), separation of the boundary layer between forest and savannah sets in (Avissar and Schmidt, 1998). Almost no isoprene emitted from the forest will be transported to the savannah areas. The concentration of OH over the savannah will therefore be much higher than over the forest, resulting in a spatial segregation of the reactive species between the boundary layer over the forest and over the savannah. In atmospheric chemistry models the intensity of segregation is sometimes used to account for the changed chemical reaction rates (Eq. 5.10) (e.g. Butler et al., 2008). However, for these length scales, both areas can have completely different dynamical and chemical characteristics, and the intensity of segregation concept can no longer be applied over the entire domain. Therefore, both areas should be treated separately instead of considering a single mixed boundary layer if $\lambda \geq 16\ h_{\mathrm{BL}}$. This corresponds to a length scale of approximately 25 km, which is of the same magnitude as the grid size of meso-scale chemistry-transport models and smaller compared to global climate models. For regions with surface heterogeneity length scales of that magnitude, chemistry-transport models should use a finer grid or nested models to accurately resolve the boundary layer chemistry.

All numerical experiments performed in this study consider 1D-heterogeneity of the land surface. Courault et al. (2007) found that 2-D-heterogeneity leads to weaker induced circulations. Relating these findings with the quantification in Table 5.4 suggests that in those cases the absolute value of the intensity of segregation will be lower. Further research on this subject is required, but this lies beyond the scope of this study.

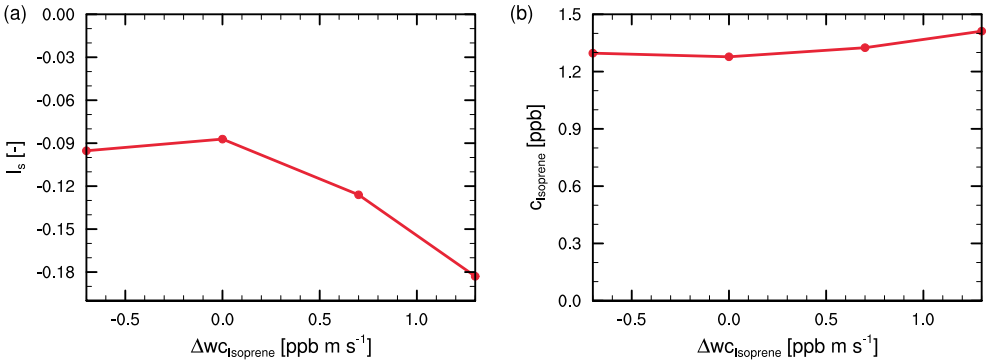

Figure 5.12: Dependency of the intensity of segregation in the boundary layer for Reaction (R9) **(a)** *and the boundary layer averaged concentration of isoprene* **(b)** *on the difference in isoprene emissions between forest and savannah areas. The average isoprene emission is 0.65 ppb m s^{-1}. The plotted variables are averages over the fourth hour of simulated time and the whole boundary layer. The values on the bottom axis are equal to* $\overline{w'c'}_{\text{Isoprene,forest}} - \overline{w'c'}_{\text{Isoprene,savannah}}$.

5.3.4 Influence of the difference in isoprene emissions

In our model, the heterogeneity of isoprene emissions does not affect boundary layer dynamics, but it does influence atmospheric chemistry. The numerical experiments that are discussed in this section are characterized by the heterogeneous surface heat fluxes of case HET. Figure 5.12a shows that with heterogeneous surface heat fluxes the intensity of segregation is enhanced compared to the numerical experiment HOM ($I_s = -0.07$), even if the isoprene emission from the surface is uniformly distributed. This segregation is caused by the transport (near the surface) of isoprene from the forest to the savannah by the induced mesoscale circulations and the following upward transport. During transport, isoprene is depleted by OH. The isoprene concentration is lower by the time the air is advected to the forest area at the top of the boundary layer. Consequently, in the bulk of the boundary layer high isoprene concentrations are found over the savannah and low isoprene concentrations over the forest. Since the hydroxyl radical concentrations respond to the isoprene concentrations, the reverse is true for OH. This leads to horizontal segregation. In the case where the isoprene emission from the savannah is higher than from the forest ($\Delta wc_{\text{Isoprene}} = -0.7$ ppb m s^{-1} in Fig. 5.12), this effect is slightly enhanced.

Not all isoprene is transported to the savannah by the induced mesoscale circulations. The horizontal transport is strongest near the borders between savannah and forest. If more isoprene is emitted over the forest, the average transport time of isoprene to the savannah area and then to the upper part of the boundary layer increases. Therefore, the concentration of

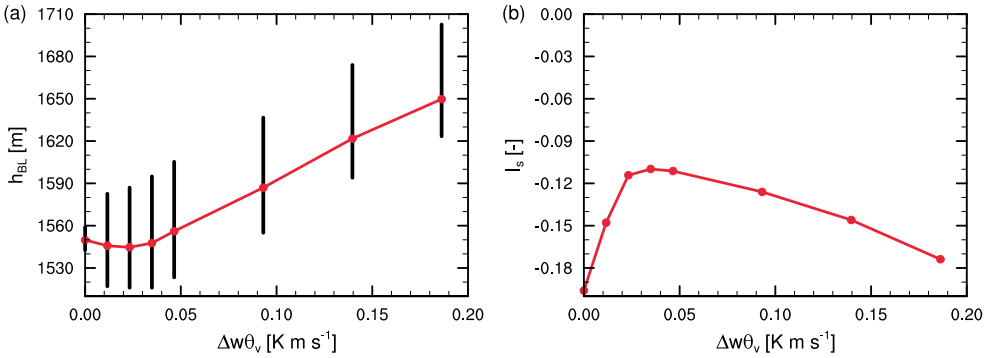

Figure 5.13: Dependency of the boundary layer height **(a)** *and the intensity of segregation in the boundary layer for Reaction (R9)* **(b)** *on the difference in surface buoyancy flux between forest and savannah areas. The plotted variables are averages over the fourth hour of simulated time. The boundary layer heights are additionally averaged in the x-direction. The values on the bottom axis are equal to* $\overline{w'\theta'_v}_{\text{savannah}} - \overline{w'\theta'_v}_{\text{Isoprene,forest}}$. *In* **(a)** *the black vertical lines represent the variability in the hourly averaged boundary layer height in the x-direction.*

isoprene over the forest increases relative to conditions with uniform emissions and, due to the ongoing chemical reaction with OH, most isoprene will be located in the lower part of the boundary layer. Again, OH responds to the concentration of isoprene, resulting in higher concentrations in the top of the boundary layer and lower concentrations near the surface. This introduces additional segregation in the vertical direction.

The concentration of isoprene is plotted in Fig. 5.12b. The effective chemical reaction rate coefficient when using boundary layer averaged concentrations is equal to $k \cdot (1 + I_S)$ according to Eq. (5.10). In the case of stronger (more negative) segregation effects, the effective coefficient of Reaction (R9) is reduced, resulting in higher concentrations in the boundary layer. Isoprene is most strongly affected, with a concentration increase of up to 10.5 % compared to the case with homogeneous isoprene emissions. After the build up of isoprene in the lower part of the boundary layer, a new chemical balance is reached. Therefore, the boundary layer averaged total chemical reaction rate is reduced only by 0.6 %. While the lifetime of isoprene is increased significantly by the increase in segregation, the lifetime of the short-lived hydroxyl radical remains short due to other chemical reactions. Therefore the concentration of isoprene will build up more than that of OH and consequently OH is also affected much less (only 0.5 %).

5.3.5 Influence of the surface energy partitioning

The effects of the surface energy partitioning on the boundary layer height and the intensity of segregation for Reaction (R9) (Table 5.2) are summarized in Fig. 5.13. The boundary layer height has a non-linear dependency on the difference in surface buoyancy flux between the forest and savannah. This is due to two competing effects of the induced mesoscale circulations. The circulations that are imposed on the boundary layer dynamics intensify with larger surface buoyancy flux differences. Therefore, more turbulence is generated over the savannah areas and entrainment is increased, leading to higher boundary layers. By transport of air from the savannah to forest areas at the top of the boundary layer, the air over the forest is heated, resulting in the growth of the local boundary layer. For stronger circulations, the maximum boundary layer height is larger and entrained air has a higher potential temperature. Therefore the heating of the boundary layer over the forest is also stronger, which results in higher boundary layer height minima. The domain-averaged boundary layer height also increases due to this warmer entrained air.

The second effect is the suppression of turbulence over the forest by the downward moving branch of the induced circulations. Consequently, direct entrainment over the forest is reduced for increasing surface buoyancy flux differences and the local boundary layer height is lower. Therefore the boundary layer height minima decrease. This effect is relatively strong for weak mesoscale introductions which are related to small buoyancy flux differences ($\Delta\overline{w'\theta_v'} < 0.04\,\mathrm{K\,m\,s^{-1}}$). For larger differences, all entrainment over the forest is suppressed and increasing the strength of the circulations only impacts the first of the two effects mentioned above. As a result the boundary layer height minima decrease with growing buoyancy flux differences as long as those differences are small ($\Delta\overline{w'\theta_v'} < 0.023\,\mathrm{K\,m\,s^{-1}}$) and increase in the case of larger differences.

Atmospheric chemistry depends strongly on the partitioning of the surface buoyancy flux. The effect on the intensity of segregation of Reaction (R9) is shown in Fig. 5.13b. Two regimes can be identified. For the regime with lower buoyancy flux differences, the segregation is governed by local emissions. In the case of larger buoyancy flux differences, the segregation is governed by mesoscale effects.

If the buoyancy flux is uniformly distributed, mixing in the vertical direction takes place due to thermals, but horizontal mixing is limited. The isoprene emitted by the forest stays in the boundary layer over the forest and the concentration of isoprene over the savannah is much lower. Consequently, the hydroxyl radical is mainly present in the boundary layer over the savannah. This leads to strong horizontal segregation that is approximately constant with height. For increasing differences in surface buoyancy fluxes, the mesoscale circulations become stronger. Near the surface, isoprene is transported from the forest to the savannah where vertical transport sets in. As a result, the horizontal mixing is stronger and the segreg-

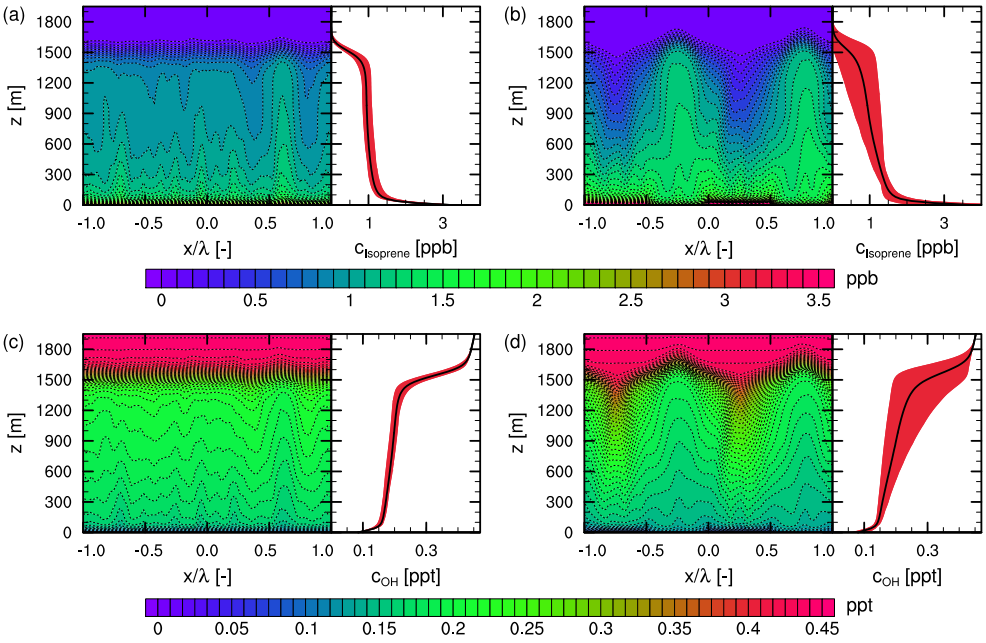

Figure 5.14: Isoprene and OH concentrations for numerical experiments UNO **(a, c)** *and HNO* **(b, d)**. *They are identical to HOM and HET, respectively, except for the initial NO_2 concentration above 1000 m (free troposphere). Each figure has two panels. The first shows the variables averaged over the fourth hour of simulation time and the y-direction, while the second panel shows the additional average in the x-direction. The red area in the second panel shows the variability in the x-direction of the temporal and y averaged values. The concentration of isoprene, c_{Isoprene}, is shown on top* **(a, b)** *and the concentration of the hydroxyl radical, c_{OH}, at the bottom* **(c, d)**. *The x-coordinate is scaled by the length scale of heterogeneity, λ, which is twice the patch size.*

ation is reduced. Depletion by OH limits the concentrations of isoprene in the upper part of the boundary layer, resulting in vertical segregation. The induced vertical segregation is weaker than the horizontal segregation, and the magnitude of the total intensity of segregation is reduced. For our numerical experiments this holds until $\Delta\overline{w'\theta'_v} \approx 0.035\,\mathrm{K\,m\,s^{-1}}$.

For even larger buoyancy flux differences, stronger induced circulations transport more isoprene from the forest to the savannah. The highest isoprene concentrations are now located over the savannah and in the lower part of the boundary layer over the forest. The OH concentration is therefore highest in the upper part of the boundary layer over the forest. For stronger circulations, the part of the boundary layer over the forest with high isoprene concentrations grows thinner, resulting in conditions with more negative horizontal segregation. In

such cases the isoprene is more concentrated over the savannah and the hydroxyl radical over the forest. This corroborates the importance of a correct partitioning of the energy budget into surface moisture and heat fluxes when modelling atmospheric chemistry.

5.3.6 Sensitivity to NO_x

As mentioned in Sect. 5.2.2, sensitivity studies are performed on the role of NO_x. In particular we focus on the impact of biogenic NO_x emissions and initial free tropospheric NO_2. According to these numerical experiments, a one order of magnitude change in the prescribed NO emissions and changes in their distribution have limited impact on the isoprene-OH segregation under the chosen set of conditions. However, entrainment of NO_x from the free troposphere, driven by the boundary layer growth in the morning hours, can significantly alter the boundary layer chemistry conditions. The presented numerical experiments (UNO and HNO) are based on cases HOM and HET, respectively, but have their initial free tropospheric NO_2 concentration set to 0.5 ppb.

The temporal and y averaged profiles of the hydroxyl radical and isoprene concentrations are displayed in Fig. 5.14. OH is strongly affected by the free tropospheric NO_x. Note that in the free troposphere, the chemistry is characterized by higher hydroxyl radical concentrations due to the lower abundance of reduced species like isoprene. Therefore, air masses that are entrained from the free troposphere into the boundary layer are relatively rich in NO_x and lead to higher OH concentrations. Since this process occurs at the top of the boundary layer, the spatial distribution of OH is changed and the gradients of the additional x averaged OH profiles indicate enhancements as well. The increase in OH subsequently depletes isoprene. Therefore, the isoprene concentration is lower compared to the cases without free tropospheric NO_x. However, the spatial pattern of isoprene remains similar to the cases without initial free tropospheric NO_2.

The intensity of segregation for the isoprene-OH reaction is enhanced for the cases UNO and HNO. As mentioned, the free tropospheric air has a chemical composition that generates relatively high OH concentrations. This air enters the boundary layer at those edges of the layer that are positioned opposed to the locations of isoprene emissions. For example, for homogeneous surface forcings, isoprene is emitted at the surface and the entrained air is introduced at the top of the boundary layer. For heterogeneous surface forcings, i.e. when isoprene is mainly emitted by the forest (at $-1 < \frac{x}{\lambda} < -0.5$ and $0 < \frac{x}{\lambda} < 0.5$ in Fig. 5.14), it is subsequently horizontally transported to the savannah region (at $-0.5 < \frac{x}{\lambda} < 0$ and $0.5 < \frac{x}{\lambda} < 1$) by the induced mesoscale circulations. There, the air is transported upwards. The entrained air, which is relatively enriched in NO_x and consequently characterized by higher OH concentrations, is introduced at the top of the boundary layer over the savannah area and transported by the upper branch of a mesoscale circulation to the top of the bound-

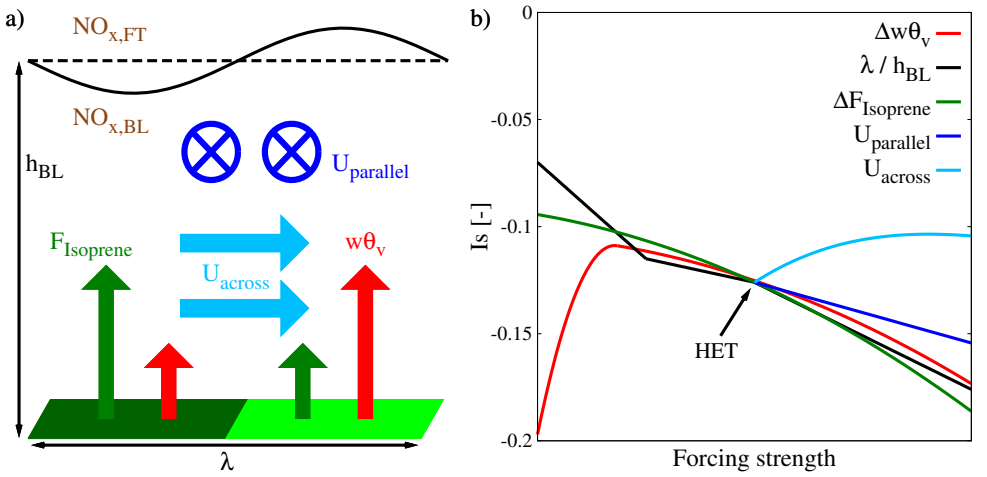

Figure 5.15: Governing variables which affect the segregation of chemical species **(a)** *and the resulting intensity of segregation for Reaction (R9) as a function of the magnitude of those variables (see descriptions of sensitivity analysis experiments in Table 5.3 and their results in Table 5.4)* **(b)**. *The governing variables are the* ***surface buoyancy flux difference****, the* ***length scale of heterogeneity****, the* ***isoprene emission difference****,* ***wind blowing parallel*** *to the borders between forest and grass and* ***wind blowing across*** *those borders. The control numerical experiment with heterogeneous surface forcing, HET, is indicated with an arrow. Not shown in panel* **(b)** *is the impact of* ***NO_x*** *mixing ratios and their distribution within the boundary layer and free troposphere on the intensity of segregation for Reaction (R9).*

ary layer over the forest. There it is transported downwards by the subsiding branch of the induced mesoscale circulation. Consequently, the updrafts are rich in isoprene and poor in OH, while in the downdrafts, which are poor in isoprene, the abundance of OH is enhanced due to the relatively high NO_x concentration in the entrained air. This leads to enhanced spatial segregation compared to the cases without initial free tropospheric NO_2. We find that averaged over the fourth hour of simulated time, the intensity of segregation is changed from −0.070 (HOM) to −0.124 (UNO) in the case of homogeneous surface forcings and from −0.126 (HET) to −0.209 (HNO) in the case of heterogeneous surface forcings.

These results show that NO_x mixing ratios and their distribution within the boundary layer and free troposphere significantly influence the intensity of segregation for the isoprene-OH reaction. It stresses the need to take the VOC and NO_x conditions into account in future studies that aim at segregation parameterizations.

5.4 Conclusions

Numerical experiments with DALES, a model that simultaneously resolves turbulence and atmospheric chemistry at the most energetic and relevant scales, are used to systematically study boundary layer dynamics and mixing over a land surface characterized by heterogeneous conditions. Particular emphasis is put on the structure of the boundary layer and the intensity of segregation for the isoprene-OH reaction. The numerical experiments are based on conditions representative for the Amazon rain forest.

Figure 5.15 summarizes the main driving variables including a quantification of the intensity of segregation as a function of the magnitude of those variables. The results indicate that in the absence of free tropospheric NO_x the intensity of segregation for the isoprene-OH reaction is normally in the range $-0.07 > I_S > -0.20$. The difference in surface buoyancy flux between the forest and savannah induces circulations that affect segregation. The impacts depend on the regime under study. For low buoyancy flux differences between savannah and forest, isoprene is mainly concentrated over the forest and an increase in the horizontal transport between the forest and savannah due to a larger difference leads to a lower magnitude of the intensity of segregation. For high buoyancy flux differences, most isoprene is located over the savannah and an increase of the surface buoyancy flux difference enhances this segregation. This non-linearity is visible in Fig. 5.15b. An increase in the length scale of heterogeneity always results in stronger segregation. However, for length scales of heterogeneity much larger than the boundary layer height ($\lambda > 16\ h_{BL}$) the centres of the boundary layers above each patch are hardly affected by the induced circulations that only occur in a narrow zone near the surface discontinuities. In these cases the intensity of segregation becomes more negative than -0.20, but separation of the boundary layers can occur.

For larger differences in isoprene emissions between forest and savannah, more negative intensities of segregation are found. The intensity and direction of the background wind is of importance too. Wind parallel to the borders between forest and savannah enhances the induced circulations and the resulting intensity of segregation. Wind traversing these borders smoothens the effects of a heterogeneous surface forcing, which results in a weaker intensity of segregation.

In general, the results suggest that the intensity of segregation cannot be taken as a constant number based on averaged emissions and moisture and heat fluxes. It strongly depends on the background wind conditions and the partitioning of the emissions and surface fluxes.

The intensity of segregation for the isoprene-OH reaction varies significantly between the different simulated conditions. However, with the exception of the cases in which the boundary layers become separated or NO_x is entrained from the free troposphere, the boundary layer average concentration of OH is hardly modified. This is caused by an increase in the isoprene concentration, compensating for the segregation effect. The increase in isoprene

concentration for these cases reaches values up to 12 %, which is actually within the 15 % uncertainty in isoprene measurements (Karl et al., 2007). Consequently, the chemical reaction rates remain almost equal, which explains the satisfactory performance of mixed layer models that assume instantaneous mixing for atmospheric chemistry in the planetary boundary layer during diurnal convective conditions (e.g. Vilà-Guerau de Arellano et al., 2011).

The usual mismatch between OH observations and current state of the art atmospheric model by factors over 2 (Tan et al., 2001; Lelieveld et al., 2008) cannot be fully explained by the intensity of segregation. Since the difference in concentrations due to segregation is comparable to the measurement uncertainties and uncertainties in the reaction rate coefficients (5–15 %, Atkinson et al., 2006), representing the segregation is not the final solution to reconcile modelled and observed OH concentrations. Therefore, the implementation of parameterizations for the intensity of segregation for the sub-grid scale processes in large scale atmospheric chemistry-transport may not have first priority. However, parameterizations are needed when striving for the best possible model performance. This study shows dependences on the length scale of heterogeneity, the differences in surface buoyancy fluxes and isoprene emissions between forest and savannah and the intensity and direction of the background wind. These governing processes are interacting non-linearly. Therefore, future research on representations of the intensity of segregation in chemistry-transport models needs to take these interactions between the different processes into account. An effort should be made to obtain observational data that can verify the results obtained from numerical experiments. Finally, our study shows that in order to help reconcile modelling with observations, it is recommendable to combine future measurements of atmospheric chemistry and boundary layer dynamics with a characterization of the heterogeneity of the land surface conditions and the direction and magnitude of the background wind.

A cloud does not know why it moves in just such a direction and at such a speed...It feels an impulsion...this is the place to go now. But the sky knows the reasons and the patterns behind all clouds, and you will know, too, when you lift yourself high enough to see beyond horizons.

Richard Bach

6

Quantifying the transport of sub-cloud layer reactants by shallow cumulus clouds over the Amazon

We investigate the vertical transport of atmospheric chemical reactants from the sub-cloud layer to the cumulus cloud layer driven by shallow convection over the Amazon during the dry season. The dynamical and chemical assumptions needed for mesoscale and global chemistry-transport model parametrizations are systematically analysed using a Large-Eddy Simulation model. We quantify the mass-flux transport contribution to the temporal evolution of reactants. Isoprene, a key atmospheric compound over the tropical rain forest, decreases by 8.5 % hr^{-1} on average and 15 % hr^{-1} at maximum due to mass-flux induced removal. We apply mass-flux parametrizations for the transport of chemical reactants and obtain satisfactory agreement with numerically resolved transport, except for some reactants like O_3, NO and NO_2. The latter is caused by the local partitioning of reactants, influenced by UV radiation extinction by clouds and small-scale variability of ambient atmospheric compounds. By considering the longer lived NO_x (NO + NO_2), the transport is well represented by the parametrization. Finally, by considering

This chapter is submitted to J. Geophys. Res. with Jordi Vilà-Guerau de Arellano, Bart van Stratum, Maarten Krol and Jos Lelieveld.

heterogeneous surface exchange conditions, it is demonstrated that the parametrizations are sensitive to boundary conditions due to changes in the boundary-layer dynamics.

6.1 Introduction

The Amazon rain forest plays an important role in regulating the regional and global atmospheric composition (Zimmerman et al., 1988; Karl et al., 2007), particularly due to high biogenic volatile organic compound (BVOC) emissions. However, to accurately represent and predict the atmospheric chemistry over this ecosystem, the role of dynamics (Butler et al., 2008; Ganzeveld et al., 2008) and chemical processes (e.g., Lelieveld et al., 2008) need to be better understood. Since atmospheric chemistry depends on the surface exchange of biogenic compounds, the reactivity is controlled by processes that occur in the atmospheric boundary layer (ABL). The ABL dynamics have multiple effects on the atmospheric chemistry. Here, we investigate the transport by shallow cumulus (SCu) convection and its implications for the sub-cloud layer chemistry, using a Large-Eddy Simulation (LES) model. The focus is primarily on the sub-cloud atmospheric properties since the conditions there are directly linked to the Earth's surface. Therefore, knowledge of the processes that occur in the sub-cloud region is important for interpreting observational data. This study quantifies the fluxes from the sub-cloud to the cloud layer and their impact on the reactant mixing ratios. We aim to contribute to parametrizations that represent this transport in chemistry-transport and climate models. This is of importance considering that SCu cloud processes occur at scales that are not resolved in such models (Kim et al., 2012). We also analyse the effects of heterogeneous surface forcings.

In the Amazon region, daytime shallow cumulus (fair weather) clouds are present during approximately 50 % of the time in the period June-August (Hahn and Warren, 2007). Shallow cumulus clouds affect the atmospheric dynamics and chemistry in multiple ways. Next to regulating the growth of the convectively mixed sub-cloud layer, clouds affect radiation (Madronich, 1987), thereby changing the chemical reaction rates and surface heat fluxes. Previous LES studies have shown that the attenuation of UV radiation has a profound impact on the instantaneous below-cloud chemistry, resulting in changes up to 10 % (for NO_2) in the spatial averaged sub-cloud layer mixing ratios of reactants (Vilà-Guerau de Arellano et al., 2005; Kim et al., 2012). Related to the ABL dynamics, the SCu clouds transport atmospheric constituents from the mixed layer to the free troposphere (FT), enhance entrainment of free tropospheric air into the boundary layer and can trigger deep convection (Zhang and Klein, 2010). The sub-cloud layer height, below which chemical reactants are well-mixed, is lowered by air masses that are transported by the thermals from the sub-cloud layer into the cloud layer, the so-called mass flux (Siebesma and Cuijpers, 1995). This height impacts the mixing ratios of chemical species in the sub-cloud layer, as demonstrated with concep-

tual mixed-layer models (van Stratum et al., 2012; Ouwersloot et al., 2012). The feedbacks between mixed-layer height, mass flux and entrainment rate is explored in more detail by van Stratum et al. (Submitted). SCu clouds also give rise to large-scale structures in the sub-cloud layer (Kim et al., 2012) similar to those induced by surface heterogeneity (Patton et al., 2005) and affecting atmospheric chemistry (Ouwersloot et al., 2011). An additional effect of clouds on atmospheric chemistry is related to chemical reactions within the cloud droplets. This aqueous phase chemistry is not considered here as it mainly affects the atmospheric composition in the cloud layer and not the temporal evolution of mixing ratios in the sub-cloud layer.

In this study, we investigate the impact of mass-flux transport on the mixing ratios of atmospheric reactants. We address Amazonian conditions, inspired by the Tropical Forest and Fire Emission Experiment (TROFFEE) (Karl et al., 2007; Vilà-Guerau de Arellano et al., 2011). We quantify the influence of the mass flux on the budget of chemical species using two different expressions. One considers the additional effect of the mass flux compared to boundary layer growth and the other considers the additional effect of the mass flux compared to entrainment. These two approaches are complementary and can be applied for different analyses, as will be discussed in detail. Furthermore we discuss how the impact of mass flux depends on the spatial distribution of the chemical species as a first step towards a parametrization in large-scale models. This is complemented by an evaluation of the impact of the altered UV radiation below clouds on the transport by SCu convection. The analysis is completed by discussing how heterogeneous surfaces can modify the mass flux.

The next section introduces the theory of mass flux and its impact on the chemistry budget. This is followed by a description of the LES model and the numerical experiments. Then, the dynamical effects of the mass flux are compared to values reported in literature to affirm if they are consistent. Next, the spatial distributions of dynamical variables and reactant mixing ratios and their influence on cloud transport are discussed and the mass-flux contribution to the mixing ratio budgets is quantified. Subsequently, we investigate representative expressions for the mass-flux transport contributions to the budgets, showing difference between different types of chemical species. Finally, we demonstrate that surface heterogeneity influences the results.

6.2 Methodology

6.2.1 Mass flux

Here we define the framework that will be used to develop and test a parametrization for the mass-flux transport of atmospheric constituents, including specific humidity. In Sect. 6.2.1 the definitions for the mass flux are presented. Subsequently, the impact of the cloud-base

mass flux on the boundary-layer growth and scalar evolutions are presented in Sect. 6.2.1. Finally, the analysis of the mass-flux transport from the LES data and its parametrization are discussed in Sect. 6.2.1. The parametrizations are based on numerical data sampled from the Large-Eddy Simulation.

Mass-flux definition

In convectively mixed ABLs that are topped by SCu clouds, transport of air occurs from the (well-mixed) sub-cloud layer to the free atmosphere by thermals that become active cumulus clouds above the lifting condensation level. To identify transport by these thermals, we are limited to analysing the active clouds that are rooted into them (LeMone and Pennell, 1976), since the organized transport below the clouds cannot be discriminated from the upward moving air parcels caused by entrainment related turbulence. The transport, quantified as the kinematic convective mass flux (hereafter referred to as mass flux), M (Siebesma and Cuijpers, 1995), depends on the vertical velocity in and the area fraction of the active clouds. These active clouds, which are positively buoyant (Stull, 1988), are referred to as the cloud cores (Heus and Jonker, 2008). The corresponding mass flux is defined as

$$M = a_{cc}\left(w_{cc} - \overline{w}\right), \tag{6.1}$$

where a_{cc} is the (horizontal) area fraction, a, of the cloud cores, $\overline{w}$ is the Reynolds averaged vertical wind velocity, w, and w_{cc} is the average w sampled over the cloud cores. These properties are all height dependent. Note that the cloud core area fraction is not equal to the total cloud core cover, c_{cc}, since that quantity is determined using vertically integrated values. The index c is used for samples over all SCu clouds.

Similar to Siebesma and Cuijpers (1995), the total vertical transport of an arbitrary scalar, ϕ, is partitioned in advective and turbulent fluxes for clouded areas and the environmental air by

$$\overline{w'\phi'} = a_{cc}\left(\left(w_{cc} - \overline{w}\right)\left(\phi_{cc} - \overline{\phi}\right) + \overline{w'\phi'}^{cc}\right) + \left(1 - a_{cc}\right)\left(\left(w_{en} - \overline{w}\right)\left(\phi_{en} - \overline{\phi}\right) + \overline{w'\phi'}^{en}\right), \tag{6.2}$$

where the subscripts cc and en indicate cloud core and environmental averages, respectively. The cloud and environment indexed overlines ($\overline{\cdot}^{cc}$ and $\overline{\cdot}^{en}$) denote that the considered fluctuations are relative to the cloud and environment averages. Within the two pairs of brackets that are linked to the area fraction of a sampling criterion (i.e. cloud core or environment) in Eq. (6.2), the first term is related to the corresponding organized transport and the second term quantifies the corresponding turbulent flux. As will be corroborated in this study, within the cloud cores the organized transport dominates the total flux (Siebesma and

Cuijpers, 1995). Further, since $\overline{\phi} = a_{cc}\phi_{cc} + (1 - a_{cc})\phi_{en}$,

$$(1 - a_{cc})(w_{en} - \overline{w})(\phi_{en} - \overline{\phi}) = \frac{a_{cc}}{1 - a_{cc}} a_{cc}(w_{cc} - \overline{w})(\phi_{cc} - \overline{\phi}),$$

so the organized transport in the environment is only $\frac{a_{cc}}{1-a_{cc}}$ times the organized transport in the cloud cores. In the cases under study, the factor $\frac{a_{cc}}{1-a_{cc}}$ is small (4.7 % at maximum) and the organized transport in the environment is negligible. In case of SCu convection, the mass flux is much larger than the turbulent transport in the environment and dominates the total vertical transport in the cloud layer. Therefore,

$$\overline{w'\phi'} \approx M\left(\phi_{cc} - \overline{\phi}\right). \tag{6.3}$$

The validity of this approximation was already demonstrated for potential temperature and specific humidity (e.g., Siebesma and Cuijpers, 1995), and chemical species (Vilà-Guerau de Arellano et al., 2005) and will be confirmed by the results presented in Sect. 6.3. In the remainder of this paper, we investigate this organized transport in the cloud cores.

Even though the decomposition into cloud core areas and environment is based on dynamical arguments, the choice for two areas is arbitrary. One could think of different divisions, e.g. cloud cores, remaining clouds and environment (Siebesma and Cuijpers, 1995; Heus and Jonker, 2008), as will be discussed in Sect. 6.3.6.

Impact of mass flux

Mixed-layer theory (Lilly, 1968) is used to quantify the impact of the cloud-base mass flux on the sub-cloud layer height. The evolution of the sub-cloud layer (or mixed-layer) height, h, is expressed (Neggers et al., 2006) as

$$\frac{\partial h}{\partial t} = w_e + \overline{w}(h) - M, \tag{6.4}$$

where w_e is the entrainment velocity and $\overline{w}(h)$ is the large-scale vertical velocity at height h. Here, M is shorthand for the mass flux that escapes the sub-cloud layer, $M(h)$. According to a budget analysis (van Stratum et al., Submitted), the mixing ratio of an arbitrary atmospheric compound, ϕ, with chemical production P and loss L is governed by

$$\frac{\mathrm{d}\langle\phi\rangle}{\mathrm{d}t} = \frac{\overline{w'\phi'}_0 + w_e\Delta\phi - M\left(\phi_{cc} - \langle\phi\rangle\right)}{h} + P - L, \tag{6.5}$$

where $\langle\phi\rangle$ is the mixed-layer averaged value and $\Delta\phi$ is the concentration jump at the top of the mixed layer. The latter is equal to $\overline{\phi}(h^+) - \langle\phi\rangle$, where $\overline{\phi}(h^+)$ is the average value of ϕ just above the sub-cloud layer. $\overline{w'\phi'}_0$ is the turbulent flux at the surface. Equation (6.5) shows that, in contrast to previously stated (Neggers et al., 2006), the mass flux can directly change

mixed-layer averaged properties if ϕ_{cc} differs from $\langle\phi\rangle$. Next to the enhanced entrainment (van Stratum et al., Submitted), this contributes to the reduction of mixing ratios of emitted passive tracers in the sub-cloud layer that was found by Kim et al. (2012).

Even if the growth of the mixed layer is negligible, the entrainment and the mass flux may still exchange air between the sub-cloud and the cloud layer. With constant height, all air mass that leaves the sub-cloud layer with property ϕ_{cc} returns with property $\overline{\phi}(h^+)$ due to the compensating entrainment. This effect can be recognized more easily by rearranging Eq. (6.5). Using Eq. (6.4) to split the entrainment velocity in mixed-layer growth and compensation for the loss of mixed-layer air by the mass flux, yields

$$\frac{\mathrm{d}\langle\phi\rangle}{\mathrm{d}t} = \frac{\overline{w'\phi'}_0 + \frac{\mathrm{d}h}{\mathrm{d}t}\Delta\phi - M\left(\phi_{cc} - \overline{\phi}(h^+)\right)}{h} + P - L. \tag{6.6}$$

This shows that, next to surface exchange and chemical production and loss, two additional contributions to the mixing ratio budget are (*i*) the mixing of sub-cloud and cloud layer air due to the mixed-layer growth (second term in the fraction), and (*ii*) the aforementioned circulation of air at the top of the sub-cloud layer with a flow rate M (third term in the fraction). While Eq. (6.5) can be used to analyse the contributions of different dynamical processes (such as entrainment and venting of air by mass flux), Eq. (6.6) is more straightforward when evaluating the mixing ratio budget based on data from observations or numerical experiments with turbulence resolving models (e.g. LES). Using LES data, the mixed-layer height evolution and the mass flux can be quantified directly. Additionally, according to Eq. (6.3), the mass-flux contribution in Eq. (6.6) can be compared directly to the total vertical scalar transport in the cloud layer. Therefore we will mainly focus on this budget equation in our analysis.

Mass-flux parametrization

The cloud-base height, z_b, at which the mass flux is evaluated, is actually higher than the sub-cloud layer height. Even though the mass flux out of the mixed layer, $M(h)$, is under investigation, $M(z_b)$ is a good proxy since all the air that escapes the sub-cloud layer is transported by the SCu convection. To determine the mass flux in the dry thermals at h instead, one would have to separate the contributions of organized transport and turbulent motions to the total vertical transport of air at this height. Then ϕ_{cc} could be determined by sampling in the upward organized transport. However, this was computationally not attainable in this study. Here, the cloud-base height is diagnosed as the height with maximum a_{cc} (Neggers et al., 2007) and the sub-cloud layer height as the inversion height, z_i, determined by the vertical profile of the virtual potential temperature, θ_v. The inversion height is calculated using the treshold gradient method (Ouwersloot et al., 2011), diagnosing z_i as the lowest level where

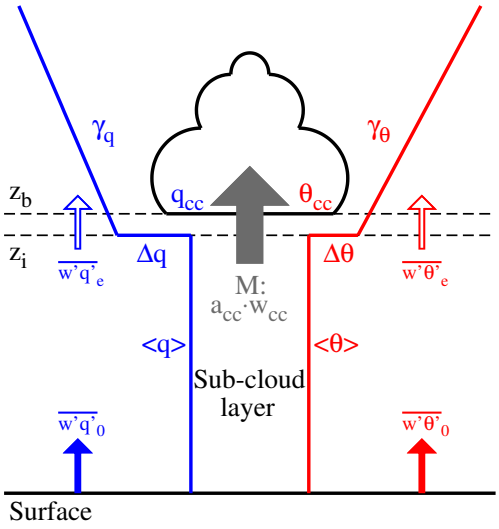

Figure 6.1: Schematic overview of the vertical structure of the convectively mixed layer topped by shallow cumulus clouds. The variables are defined in Sect. 6.2.1.

$\frac{d\theta_v}{dz} > \left(0.5 \max \frac{d\theta_v}{dz}\right)$. An illustration of the structure of the SCu cloud topped mixed layer is presented in Fig. 6.1. The symbol e indicates entrainment and γ_ϕ is the vertical gradient of ϕ in the cloud layer (free troposphere) for cloudy (clear sky) conditions.

For models that do not (fully) resolve the cloud processes, the values for w_{cc}, a_{cc} and ϕ_{cc} have to be parametrized. Building on Neggers et al. (2006), van Stratum et al. (Submitted) state, based on LES analyses for different cases with SCu convection over land, that w_{cc} scales with the convective velocity scale, w_*, as

$$w_{cc} = \lambda w_*, \tag{6.7}$$

where $\lambda = 0.84$. The cloud core value of q is prescribed by

$$q_{cc} - < q >= \zeta \sigma_{q,h}, \tag{6.8}$$

in which $\zeta = 0.51$ and $\sigma_{q,h}$ is the standard deviation of q at the top of the sub-cloud layer. These parametrizations for w_{cc} and q_{cc} are evaluated in Sect. 6.3. Here we additionally study the parametrizations for ϕ_{cc} considering scalars other than q. Since Eqs. (6.5) and (6.6) express the mixed-layer budget of $< \phi >$, we analyse the parametrizations for $\phi_{cc} - < \phi >$ and $\phi_{cc} - \overline{\phi}(h^+)$. To prevent the sampling of sub-cloud layer air when calculating the value for ϕ at the bottom of the cloud layer, $\overline{\phi}(z_b)$ is used as a proxy for $\overline{\phi}(h^+)$. This value is only evaluated if $c_{cc} \geq 0.05$, because then enough active clouds are present to accurately determine

z_b.

6.2.2 LES model

The LES model that is employed is based on version 3.2 of the Dutch Atmospheric Large-Eddy Simulation (DALES) model (Heus et al., 2010), extended with a chemistry module (Vilà-Guerau de Arellano et al., 2005) and expanded to enable studies of ABLs that are characterized by heterogeneous boundary conditions at the surface (Ouwersloot et al., 2011). This LES code has been introduced by Nieuwstadt and Brost (1986). Further developments and improvements were made (e.g., Cuijpers and Duynkerke, 1993; Dosio et al., 2003) prior to resulting in DALES 3.2.

DALES solves dynamical and chemical processes in the ABL explicitly on a computational grid resolution (typically 100 m or less) that is much finer than that of mesoscale and global models, but still requires parametrization of the smaller scale turbulence. For this parametrization, the filtered Navier-Stokes equations are applied, using the one-and-a-half-order closure assumption (Deardorff, 1973), in combination with the Boussinesq approximation (Heus et al., 2010). The corresponding filter size is generally set equal to the grid resolution, which is chosen such that less than 10 % of the total turbulent energy is parametrized. In the horizontal directions the domain is constrained by periodic boundary conditions. Related to the interaction of clouds with UV radiation, the photolysis rates are multiplied with separate factors below and above the clouds in each vertical column of the computational grid (only taking into account the one-dimensional effects). This multiplication is described by Vilà-Guerau de Arellano et al. (2005). The second-order effect of adjusted surface heat and moisture fluxes due to the altered radiation is not applied.

6.2.3 Numerical experiments

The $256 \times 256 \times 300$ grid applied in the LES experiments spans $12\,800\,\text{m} \times 12\,800\,\text{m} \times 6\,000\,\text{m}$ with a resolution of $50\,\text{m} \times 50\,\text{m} \times 20\,\text{m}$. The numerical experiments start at 5 local time (LT) and are run for 11.5 hour, using a time step of 1 s. Larger time steps lead to instabilities in the chemical solver. These temporal and spatial resolutions suffice to resolve the most relevant processes for both the atmospheric dynamics and chemistry. Statistics are calculated and stored every minute.

The numerical experiments are aimed at investigating the role of shallow cumulus convection for Amazonian sub-cloud layer reactants. The evaluated case is based on the TROFFEE campaign (Karl et al., 2007; Vilà-Guerau de Arellano et al., 2011) that took place 14–29 September 2004 (dry season) in the Amazonian rain forest. The dynamical and chemical surface conditions are set equal to those prescribed by Vilà-Guerau de Arellano et al. (2011).

However, the upper atmospheric conditions were less well known. Therefore we prescribe initial vertical profiles based on the previous study, but slightly changed. While doing so, we paid attention to reproduce a situation in which SCu convection occurred that did not evolve into deep convection and to keep the profiles realistic and representative for Central Amazonia. We consider local free convection (i.e. no mean horizontal wind velocity).

The initial boundary layer height was set to 200 m. Below, the initial potential temperature, θ, is 300 K and the initial specific humidity, q, is 16×10^{-3} kg kg^{-1}. The respective jumps in these values from the mixed-layer to the free troposphere are 1 K and -3×10^{-3} kg kg^{-1}. Above this height, there are two regimes in which θ changes with a different vertical gradient each, as is commonly observed (e.g., Brown et al., 2002). It rises by 3×10^{-3} K m^{-1} until 4 km height and 6×10^{-3} K m^{-1} above 4 km height. The specific humidity drops by -3×10^{-3} kg kg^{-1} m^{-1} until it is equal to 0 (at $\sim$ 4.5 km height). The surface kinematic heat flux is prescribed by

$$\overline{w'\theta'}_0 = 0.19 \sin\left(\frac{\pi\,(t - 8100)}{28800}\right) \text{K m s}^{-1}$$

between 0715 and 1515 LT and 0 at any other time, where t is the time in s since 5 LT. The surface kinematic moisture flux is

$$\overline{w'q'}_0 = 0.13 \times 10^{-3} \sin\left(\frac{\pi\,(t - 8100)}{28800}\right) \text{kg kg}^{-1} \text{ m s}^{-1}$$

between 0600 and 1630 LT and 0 at any other time.

When investigating the impact of surface heterogeneities on the transport by shallow cumulus convection, the surface is subdivided into 4 patches in one horizontal direction (Ouwersloot et al., 2011), resulting in a length scale of heterogeneity (the width of a forest and savannah patch combined) of 6.4 km. The first and the third patch are characteristic for forest and the other two for savannah. In the forest areas the sensible heat flux is lower and the latent heat flux is higher. In this study, the sum of sensible and latent heat fluxes is kept constant per patch. Additionally, the average sensible and latent heat fluxes over the entire domain are kept equal to the conditions with a homogeneous surface. Similar to Ouwersloot et al. (2011), the change in sensible and latent heat flux is set to a third of the sensible heat flux over the homogeneous surface. This results in an amplitude of 0.125 (0.255) K m s^{-1} in the kinematic heat flux for the forest (savannah) patches and an amplitude of 0.156 (0.104) $\times 10^{-3}$ kg kg^{-1} m s^{-1} in the kinematic moisture flux. The resulting sensible and latent heat fluxes correspond to maximum Bowen ratios of 0.32 (0.99) for the forest (savannah) areas, which are representative values for the dry season (da Rocha et al., 2009). For homogeneous surface conditions, the maximum Bowen ratio during the day is 0.59. Over a heterogeneous surface with this length scale and this distribution of sensible and latent heat fluxes, coherent

mesoscale circulations are induced that affect the distribution of scalars within the mixed-layer as well as the evolution of the ABL height and mixed-layer averaged properties (e.g., Patton et al., 2005; Ouwersloot et al., 2011), facilitating cloud formation (van Heerwaarden et al., 2010).

The chemical mechanism is based on the one proposed by Vilà-Guerau de Arellano et al. (2009), which contains the basic reactions for the O_3-NO_x-VOC-HO_x mechanism that represents daytime chemistry over the Amazon rain forest. After some expansions (Vilà-Guerau de Arellano et al., 2011; Ouwersloot et al., 2011; van Stratum et al., 2012), the current mechanism was presented by Ouwersloot et al. (2012). In this chemical scheme, 20 reactant species are included. Note that methyl vinyl ketone (MVK) is here a lumped species with all first generation oxidation products of isoprene (C_5H_8). The chemical reactions and the expressions for the reaction rates are presented in Table 6.1. The mixing ratios of the reactants are first converted to concentrations (in molec cm^{-3}) before applying the chemical production and loss and back again afterwards. Apart from the 20 reactant species listed in this table, 3 passive tracers are considered: an emitted tracer (INERT), an inert species that is initially only present in the mixed-layer (BLS) and an inert species that is initially only present in the free troposphere (FTS). For the latter two species there is no surface exchange. INERT and BLS/FTS are inspired on the classical "bottom-up" and "top-down" tracers (Wyngaard and Brost, 1984), respectively.

For 11 tracers, the vertical profile is initialized to 0 ppb. The exceptions to this profile are as follows. The chemical species H_2O is linked to and governed by q. O_3, CH_4, MVK, C_5H_8, CO, O_2 and N_2 are initialized with respectively 10, 1724, 1.3, 2, 124, 0.2×10^9 and 0.8×10^9 ppb at all heights. NO_2 is 1 ppb in the mixed layer and 0.5 ppb aloft. Tracer BLS (FTS) is initialized only in (above) the mixed layer with 1 ppb. Since the sum of the initial BLS and FTS mixing ratios is 1 ppb everywhere and they do not experience surface exchange or chemical transformations, the tracers are complementary.

The surface exchange of the atmospheric tracers is prescribed. INERT and NO are emitted with 1 ppb m s^{-1} and 0.5×10^{-3} ppb m s^{-1}, respectively. The emission for isoprene, E_{Iso}, is based on observations (Karl et al., 2007) and prescribed as

$$E_{\mathrm{Iso}} = 0.65 \exp\left(-\frac{\left(\frac{t-24705}{7999}\right)^2}{2} \right) \mathrm{ppb\,m\,s^{-1}},$$

where again t is the time in seconds since 5 LT. When heterogeneous surface conditions are considered, the isoprene emission is higher (lower) in the forest (savannah) patches and the value 0.65 is replaced by 1.0 (0.3).

Table 6.1: Chemical reaction scheme solved by DALES, the same as in **Ouwersloot et al. (2012)** *(Table 2.1 in this thesis). T is the absolute temperature in K and χ is the solar zenith angle. The unit of first-order reaction rate coefficients is* s^{-1} *and that of second-order reaction rate coefficients is* $cm^3\,molec^{-1}\,s^{-1}$*. Reaction (R15), (R24) and (R25) have more comprehensive expressions for their reaction rates*[1,2,3]*. For these expressions, c_{air} and c_{H_2O} are the concentrations in* $molec\,cm^{-3}$ *for air and* H_2O*, respectively. MVK represents methyl vinyl ketone and REST represents products and/or secondary fast reactions with reactants that are not specified.*

Name	Chemical equation			Reaction rate constant
R1	$O_3 + h\nu$	$\rightarrow$	$O(^1D) + O_2$	$3.83\times10^{-5} \cdot e^{-\frac{0.575}{\cos(\chi)}}$
R2	$O(^1D) + H_2O$	$\rightarrow$	2 OH	$1.63\times10^{-10} \cdot e^{\frac{60}{T}}$
R3	$O(^1D) + N_2$	$\rightarrow$	O_3 + REST	$2.15\times10^{-11} \cdot e^{\frac{110}{T}}$
R4	$O(^1D) + O_2$	$\rightarrow$	O_3	$3.30\times10^{-11} \cdot e^{\frac{55}{T}}$
R5	$NO_2 + h\nu$	$\rightarrow$	NO + O_3 + REST	$1.67\times10^{-2} \cdot e^{-\frac{0.575}{\cos(\chi)}}$
R6	$CH_2O + h\nu$	$\rightarrow$	HO_2 + REST	$1.47\times10^{-4} \cdot e^{-\frac{0.575}{\cos(\chi)}}$
R7	OH + CO	$\rightarrow$	$HO_2 + CO_2$ + REST	2.40×10^{-13}
R8	OH + CH_4	$\rightarrow$	CH_3O_2 + REST	$2.45\times10^{-12} \cdot e^{\frac{-1775}{T}}$
R9	OH + C_5H_8	$\rightarrow$	RO_2	1.00×10^{-10}
R10	OH + MVK	$\rightarrow$	$HO_2 + CH_2O$ + REST	2.40×10^{-11}
R11	HO_2 + NO	$\rightarrow$	OH + NO_2	$3.50\times10^{-12} \cdot e^{\frac{250}{T}}$
R12	CH_3O_2 + NO	$\rightarrow$	$HO_2 + NO_2 + CH_2O$ + REST	$2.80\times10^{-12} \cdot e^{\frac{300}{T}}$
R13	RO_2 + NO	$\rightarrow$	$HO_2 + NO_2 + CH_2O$+ MVK	1.00×10^{-11}
R14	OH + CH_2O	$\rightarrow$	HO_2 + REST	$5.50\times10^{-12} \cdot e^{\frac{125}{T}}$
R15	2 HO_2	$\rightarrow$	$H_2O_2 + O_2$	k^1
R16	$CH_3O_2 + HO_2$	$\rightarrow$	REST	$4.10\times10^{-13} \cdot e^{\frac{750}{T}}$
R17	$RO_2 + HO_2$	$\rightarrow$	REST	1.50×10^{-11}
R18	OH + NO_2	$\rightarrow$	HNO_3	$3.50\times10^{-12} \cdot e^{\frac{340}{T}}$
R19	NO + O_3	$\rightarrow$	$NO_2 + O_2$	$3.00\times10^{-12} \cdot e^{-\frac{1500}{T}}$
R20	OH + HO_2	$\rightarrow$	$H_2O + O_2$	$4.80\times10^{-11} \cdot e^{\frac{250}{T}}$
R21	OH + H_2O_2	$\rightarrow$	$H_2O + HO_2$	$2.90\times10^{-12} \cdot e^{\frac{-160}{T}}$
R22	NO + NO_3	$\rightarrow$	2 NO_2	$1.80\times10^{-11} \cdot e^{\frac{110}{T}}$
R23	$NO_2 + O_3$	$\rightarrow$	$NO_3 + O_2$	$1.40\times10^{-13} \cdot e^{\frac{-2470}{T}}$
R24	$NO_2 + NO_3$	$\rightarrow$	N_2O_5	k^2
R25	N_2O_5	$\rightarrow$	$NO_2 + NO_3$	k^3
R26	$N_2O_5 + H_2O$	$\rightarrow$	2 HNO_3	2.50×10^{-22}
R27	N_2O_5 + 2 H_2O	$\rightarrow$	2 $HNO_3 + H_2O$	1.80×10^{-39}
R28	$HO_2 + O_3$	$\rightarrow$	OH + 2 O_2	$2.03\times10^{-16} \cdot \left(\frac{T}{300}\right)^{4.57} \cdot e^{\frac{693}{T}}$

[1] $k = (k_1 + k_2)\,k_3,\ k_1 = 2.2\times10^{-13} \cdot e^{\frac{600}{T}},\ k_2 = 1.9\times10^{-33} \cdot e^{\frac{980}{T}} \cdot c_{air},\ k_3 = 1 + 1.4\times10^{-21} \cdot e^{\frac{2200}{T}} \cdot c_{H_2O}$

[2] $k = 0.35 \cdot (k_1 \cdot k_2)\,/\,(k_1 + k_2),\ k_1 = 3.6\times10^{-30} \cdot \left(\frac{T}{300}\right)^{-4.1} \cdot c_{air},\ k_2 = 1.9\times10^{-12} \cdot \left(\frac{T}{300}\right)^{0.2}$

[3] $k = 0.35 \cdot (k_1 \cdot k_2)\,/\,(k_1 + k_2),\ k_1 = 1.3\times10^{-3} \cdot \left(\frac{T}{300}\right)^{-3.5} \cdot e^{\frac{-11000}{T}} \cdot c_{air},\ k_2 = 9.7\times10^{14} \cdot \left(\frac{T}{300}\right)^{0.1} \cdot e^{\frac{-11080}{T}}$

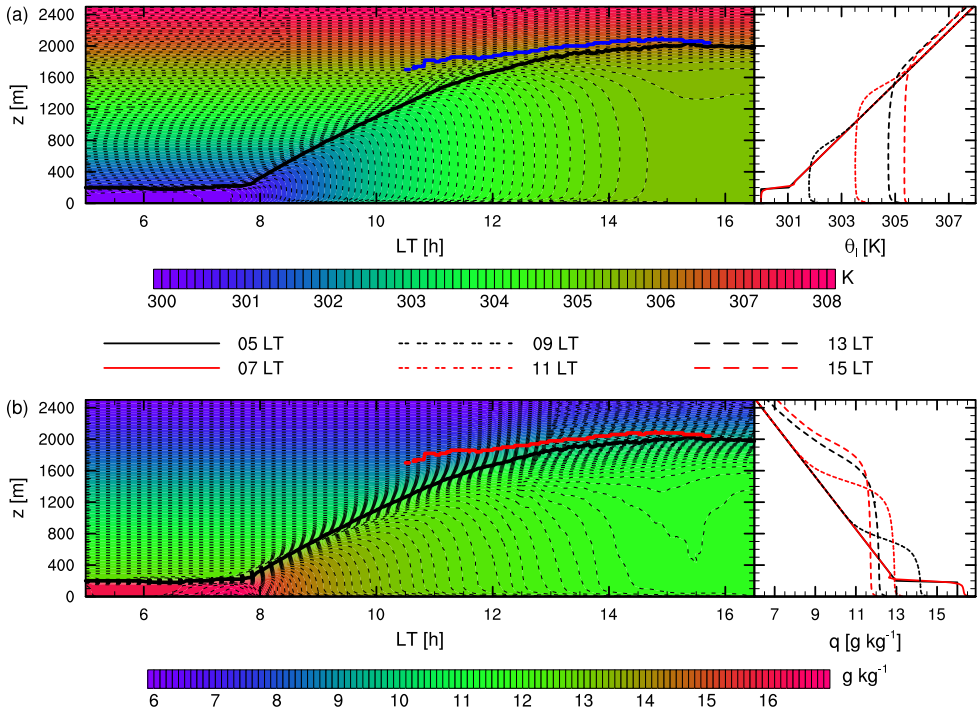

Figure 6.2: The vertical profile evolution of **(a)** *liquid water potential temperature, θ_l, and* **(b)** *specific humidity, q. The left panels show horizontal averages as a function of local time and height. The diagnosed mixed-layer height is indicated by the black line. The cloud-base height, z_b, is presented as a blue line in figure* **(a)** *and a red line in* **(b)**. *The right panels show the horizontally averaged instantaneous vertical profiles at intervals of 2 hours.*

6.3 Results

6.3.1 Dynamics

The temporal evolution of liquid water potential temperature, θ_l, and specific humidity, q, is presented in Figure 6.2 for the duration of the numerical experiment. Both variables are horizontally averaged. Additionally, the evolutions of the diagnosed mixed-layer height and cloud-base height are depicted. Here, z_b is only determined if $c_{cc} > 0.1\,\%$. Note that the latent heat flux is 0 before 0600 LT and the sensible heat flux is 0 before 0715 LT. After the breaking of the morning capping inversion, the mixed layer begins to deepen near 0800 LT. The first active clouds appear around 1030 LT and start to increase in number and depth near 1130 LT (see Fig. 6.3a). All active clouds have dissipated by 1530 LT, 15 minutes after the

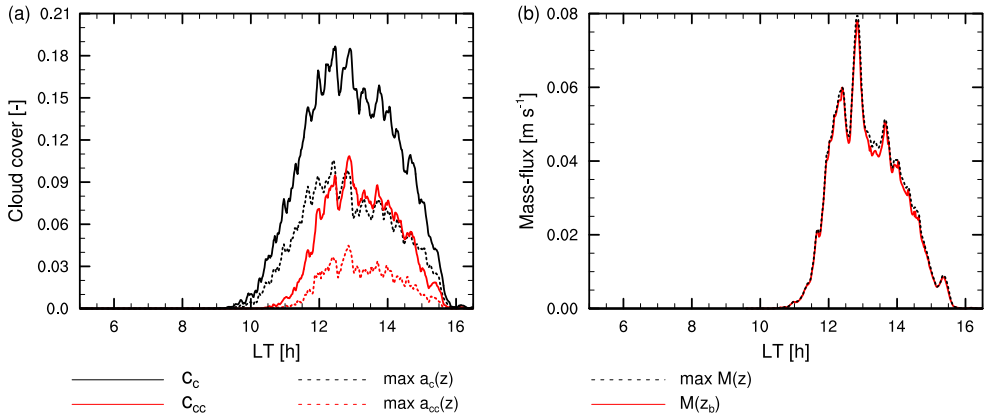

Figure 6.3: The evolution of **(a)** *the cover and area fraction of SCu clouds and cloud cores, and* **(b)** *the mass fluxes by SCu convection. For the latter, the values at height z_b and the maximum mass flux are presented.*

sensible heat flux has dropped to zero. The vertical relative humidity profile as determined by using the horizontally averaged temperature, specific humidity and pressure, does not exceed 85 %. The maximum relative humidity is located directly below the mixed-layer top.

These figures show that, even though it is often assumed from a mixed-layer approach that the cloud-layer characteristics are not affected by the SCu convection (Neggers et al., 2006; van Stratum et al., Submitted), the horizontally averaged vertical profiles of q and θ_l in the cloud-layer can be affected by the air that is vented from the sub-cloud layer. Future parametrizations in conceptual mixed-layer models or in large-scale atmospheric models could possibly be improved by incorporating this second-order effect, as recently implemented by Gentine et al. (2013).

The evolution of the cloud presence is depicted in Fig. 6.3a. In this figure, the cover and the maximum value of the area fraction for clouds and cloud cores are shown at 1-minute intervals. Here, we show that one should not take the total cloud cover as a proxy for the area of SCu convective transport. The active transport depends on the area fraction of the cloud cores at cloud-base height. Since this is determined as the height at which the cloud core area fraction reaches its maximum, the used variable is the maximum cloud-core area fraction. As introduced above, a denotes the height dependent area fraction and c denotes the cover, considering cloud presence anywhere in the column at a horizontal position. The indices c and cc indicate sampling over all clouds and sampling over the cloud cores, respectively. Since c considers the presence of clouds in the entire column, $a(z) \leq c$ for any z, resulting in the lower max $a(z)$ compared to c. In our numerical experiment, the value of c_{cc} is on average only 33 % of the value of c_c and the maximum $\frac{c_{cc}}{c_c}$ ratio is 60 %. Additionally, max $a_{cc}(z)$

is on average 36 % compared to c_{cc}. Therefore in total, $\max a_{cc}(z)$ divided by c_c reaches a maximum of only 30 % and is, when active clouds are present, on average only 12 %.

The resulting mass flux by active SCu transport is shown in Fig. 6.3b. To smooth extremes, the mass flux is averaged over 10 minutes. The figure shows that the mass flux at z_b is usually equal to the maximum mass flux and very close otherwise, agreeing with the vertical mass-flux profiles presented in previous studies (Siebesma and Cuijpers, 1995; Vilà-Guerau de Arellano et al., 2005). In this numerical experiment, the mass flux is strongest between 12 and 14 LT. In that period, M is on average 5.0 cm s^{-1}, while the average is only 2.1 cm s^{-1} when averaging over all moments during which there is a mass flux. The mass flux peaks at a value of 7.8 cm s^{-1}. These magnitudes of the mass flux correspond well to the profiles presented in the aforementioned studies. During this period, the average liquid water path is 16 g m^{-2} and the time averaged maximum relative humidity is 81 %.

In this study, we further investigate the impact of mass-flux transport on atmospheric reactant mixing ratios in the sub-cloud layer. Before quantifying this transport, we test our model and analysis by evaluating our resulting parametrizations for w_{cc} and q_{cc} and comparing them with the current state-of-the-art parametrizations for SCu mass flux over land (van Stratum et al., Submitted). To obtain representative values that are sampled over a sufficiently large number of data points, this analysis is only performed at times that $c_{cc} > 5\,\%$. Here, Eqs. (6.7) and (6.8) are used. However, two new adaptations are made as we found they improved the representativeness of the parametrizations. First, next to evaluating Eq. (6.8) with $\sigma_{q,h}$ we evaluated this equation using σ_q as determined over the entire sub-cloud layer. Second, to generalize the parametrization to include conditions where the sub-cloud layer value of q (or, later on, a reactant) is lower than the value at z_b, we multiplied by the sign of $-\Delta q$. In our study this is not needed for q, since Δq is always negative as the mixed-layer q is higher than the free tropospheric value and the surface moisture flux is never negative. However, this addition makes the parametrization more general and it will be needed to represent atmospheric reactant transport using the same framework. The resulting dependencies of w_{cc} and q_{cc} (compared to $< q >$) are displayed in Fig. 6.4. The linear fit for both graphs is forced through the origin, corresponding to the expressions in Eqs. (6.7) and (6.8). To evaluate the quality of the fit, we make use of the index of agreement, d (Willmott, 1981). This statistical diagnostic expresses the degree to which an observed variable (e.g. w_{cc}) can be accurately estimated by a predicted variable (e.g. λw_*), rather than the correlation between the variables. The use of the common R^2 can yield biased values, because the used linear fit is forced through the origin, so that even the averages of the observed and predicted values do not have to be equal. In total, this can even lead to negative R^2 for some of the tested parametrizations. In accord with van Stratum et al. (Submitted) for three different cases over land, we find

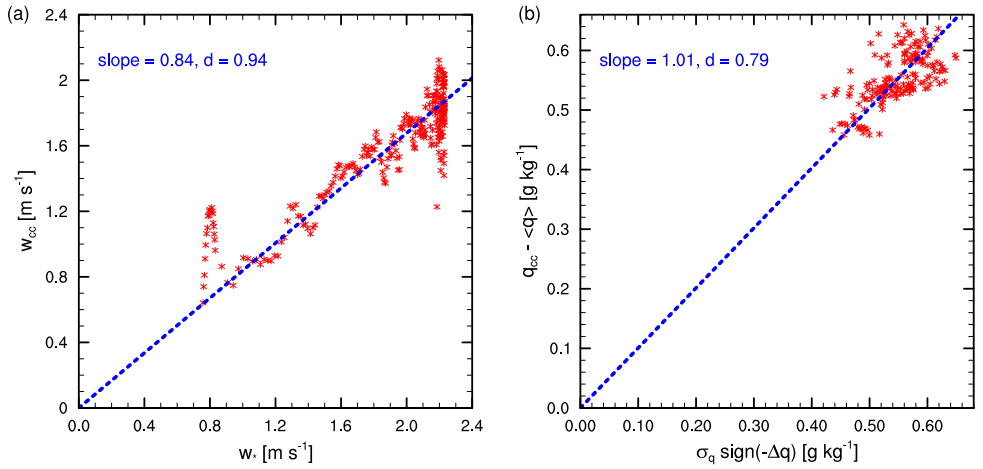

Figure 6.4: Parametrization for **(a)** w_{cc} *and* **(b)** $q_{cc}- < q >$. *The blue dashed lines indicate the linear regression fits, forced through (0,0). The red asterisks are model data sampled at 1-minute intervals. The slopes and indexes of agreement, d, are indicated.*

$$w_{cc} = 0.84 w_* \tag{6.9}$$

with $d = 0.94$. For the representation of q we find only a minor difference. Instead of a factor 0.51, our results show

$$q_{cc}- < q >= 0.53 \sigma_{q,h} \tag{6.10}$$

with $d = 0.73$. A better index of agreement, $d = 0.79$, is found relating q_{cc} to the total σ_q. This results in

$$q_{cc}- < q >= \zeta_2 \sigma_q, \quad \zeta_2 = 1.01. \tag{6.11}$$

In short, our results show that we can reproduce the parametrizations for the mass flux of moisture, even though the numerical experiment is not similar to the ones presented before. These previous studies, which include the Atmospheric Radiation Measurement - Southern Great Plains (Brown et al., 2002), Small Cumulus and Microphysics Study (Neggers et al., 2003) and Gulf of Mexico Atmospheric Composition and Climate Study (Angevine et al., 2010) experiments, were situated at temperate latitudes with maximum mixed-layer heights below 1500 m, while the case under study is situated near the equator and has a maximum mixed-layer height of 2000 m. The fact that analyses of different cases yield similar parametrizations confirms the validity and robustness of the proposed expressions. However, our

results also suggest that a more representative parametrization might exist for q_{cc} by using the standard deviation that is calculated over the entire sub-cloud layer. Future studies could investigate whether this improvement is general or case dependent.

6.3.2 Spatial distribution of atmospheric compounds in the sub-cloud layer

As shown by the budget equations (Eqs. (6.5) and (6.6)), the contribution of the mass flux to the evolution of an arbitrary scalar, ϕ, is determined by the deviation of the cloud core averaged value compared to a reference value, i.e. respectively $\phi_{cc} - < \phi >$ and $\phi_{cc} - \overline{\phi}(z_b)$ (as z_b is used as a proxy for h^+). To parametrize these contributions, first the source of these differences should be understood. Even if the sub-cloud layer were perfectly well mixed, the contribution of $\phi_{cc} - \overline{\phi}(z_b)$ would be expected to be non-zero. After all, in that case the value of ϕ_{cc} is equal to the value of ϕ in the thermals that originate from the sub-cloud layer and therefore equal to $< \phi >$. In turn, $\overline{\phi}(z_b)$ is the value for ϕ in the cloud layer, being unequal to $< \phi >$. However, if the sub-cloud layer were perfectly well mixed, the contribution in the other budget, governed by $\phi_{cc} - < \phi >$, would be 0. Why this is not the case can be deduced from Fig. 6.5. In this figure, the hourly and y-direction averaged mixing ratios are shown for three different simulated chemical species and two different time periods. The two chosen periods are between 1200 LT and 1300 LT, and between 1300 LT and 1400 LT, since the mass flux is relatively largest (see Fig. 6.3b). In Figs. 6.5a and b the projections are shown for the atmospheric compound BLS. This inert tracer has no active surface exchange and was initialized at 0 ppb above the mixed layer. Even though the compound was initially well-mixed throughout the sub-cloud layer, in this figure clear spatial patterns can be discerned. This spatial distribution is driven by the turbulence characteristics of the sub-cloud layer. The air flow is shown superimposed on the BLS mixing ratio contour plots. As mentioned in Sect. 6.1, the SCu clouds stimulate large-scale structures in the sub-cloud layer (Kim et al., 2012), which are very similar in shape compared to the circulations induced by land surface heterogeneity (Patton et al., 2005; Ouwersloot et al., 2011). Higher mixing ratios are found near the $\frac{x}{\lambda}$ positions -0.25, 0.5 and 1. At these locations, upward moving thermals are present that drive the SCu convection. While the thermals become narrower in the period 1300 – 1400 LT compared to 1200 – 1300 LT, their positions do not change significantly. As the clouds on top of the thermals vent the air from the sub-cloud layer, air in that layer will tend to converge to those locations, strengthening the thermals and fixing their positions, a process which was hinted at in observational studies (LeMone and Pennell, 1976). In the cloudless regions, the air descends (with a velocity of maximum 0.5 m s^{-1}), transporting the air that is entrained at the top of the sub-cloud layer towards the surface. This air is characterized by lower (cloud-layer) mixing ratios of BLS. The sub-cloud layer averaged mixing ratio, $\langle \phi \rangle$, is

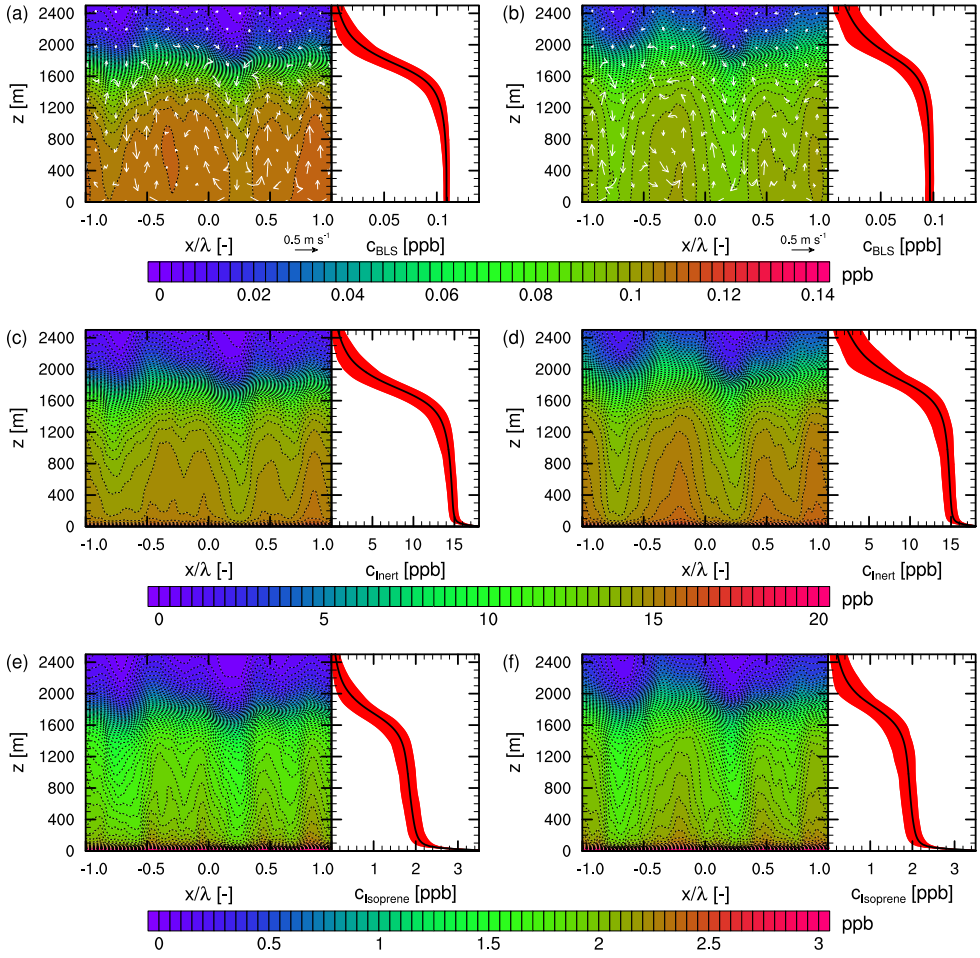

Figure 6.5: Mixing ratios of the chemical species BLS **(a,b)**, *INERT* **(c,d)** *and isoprene* **(e,f)**. *The left panels with color contours show the mixing ratios averaged over the y-direction and over time. The period of averaging is between 1200 LT and 1300 LT* **(a,c,e)** *and between 1300 LT and 1400 LT* **(b,d,f)**. *In the right panels the mixing ratios are additionally averaged in the x-direction. The red ranges in the right panels show the spread in the x-direction of the temporal and y-direction averaged values. The x-coordinate is scaled over a distance of 6.4 km. The wind direction and magnitude are indicated by vectors* **(a,b)**.

a value between the mixing ratios in the upward moving thermals, ϕ_{cc}, and in the downward moving motions. As a consequence, in Eq. (6.5), $\phi_{cc} > \langle\phi\rangle$ for the BLS mixing ratio.

Figures 6.5c and d show that the same structure is present for the mixing ratio of INERT. This inert chemical species is initialized with a mixing ratio of 0 ppb everywhere and is continuously emitted from the surface. Since the emitted species are transported to the upper part of the sub-cloud layer by thermals, the difference between the mixing ratio in the thermals compared to the mixed-layer averaged mixing ratio is increased. However, even though the spatial segregation is enhanced, in general the same effects occur as for the BLS mixing ratio. As evidenced by Figs. 6.5e and f, the same structures also appear for the chemically active species isoprene, which is also released from the surface.

In short, the combination of entrained cloud-layer air and the induced large-scale structures causes the difference between ϕ_{cc}, which is characterized by ϕ in the thermals, and $< \phi >$. As the organized variance in ϕ, related to the spatial distribution, dominates the total variance of ϕ in the boundary-layer, the magnitude of σ_ϕ, calculated either over the entire sub-cloud layer or just below the inversion, seems a good proxy to estimate $\phi_{cc} - < \phi >$, confirming the assumption of van Stratum et al. (Submitted). In turn, this variance is caused by the entrainment of cloud-layer air into the sub-cloud layer, as first suggested by Neggers et al. (2007). Here, we should note that $\phi_{cc} - \overline{\phi}(z_b)$ is mainly governed by $\overline{\phi}(z_b) - < \phi >$, since $\phi_{cc} - \overline{\phi}(z_b) = \phi_{cc} - < \phi > -(\overline{\phi}(z_b) - < \phi >)$ and $\left|\overline{\phi}(z_b) - < \phi >\right|$ is significantly larger than $|\phi_{cc} - < \phi >|$. For parametrizing the budget expressed by Eq. (6.6), $\phi_{cc} - \overline{\phi}(z_b)$ therefore scales best with $\overline{\phi}(z_b) - < \phi >$, rather than with σ_ϕ.

6.3.3 Importance of SCu convection

Here, we focus on the direct contribution of the mass flux to the evolution of ϕ, i.e. $\frac{-M(\phi_{cc} - \langle\phi\rangle)}{h}$ and $\frac{-M\left(\phi_{cc} - \overline{\phi}(h^+)\right)}{h}$ for Eqs. (6.5) and (6.6), respectively. Note that related to the mass flux, the sub-cloud layer height development, $\frac{\mathrm{d}h}{\mathrm{d}t}$, is affected as well (see Eq. (6.4)). Budget equation (6.5), hereafter referred to as 'venting budget', divides the exchange at the top of the sub-cloud layer into air that is entrained with flow rate w_e and air that escapes the sub-cloud layer with flow rate M, therefore representing the air flows across the interface between cloud and sub-cloud layer. Budget equation (6.6), hereafter referred to as 'pumping budget', divides this exchange into incorporating air from the cloud-layer into the sub-cloud layer by growth of the sub-cloud layer, and an additional circulation of air with flow rate M. This circulation transports air characterized by ϕ_{cc} out of the sub-cloud layer and replaces it with air characterized by $\overline{\phi}(h^+)$, acting like a pump. An advantage of this expression is that, in contrast to the entrainment velocity, the tendency of the mixed-layer height ($\frac{\mathrm{d}h}{\mathrm{d}t}$) can be determined directly from observational or numerical data. While we will evaluate the parametrizations of the mass-flux transport for both budgets (Sect. 6.3.4), only the more applicable 'pump-

ing budget' is considered when analysing the vertical transport profiles from LES data (Sect. 6.3.5).

To determine the importance of the mass-flux transport, we calculate its contributions to the temporal evolutions of q and the mixing ratios. They are divided by q or the mixing ratios themselves to result in a contribution that is expressed as a percentage change per hour. In general, the contribution of the 'pumping budget' mass-flux term is higher than the contribution of the 'venting budget' mass-flux term. For example, the 'pumping' contribution for q is $-2.5\,\%\,\mathrm{hr}^{-1}$, while the 'venting' contribution is $-0.4\,\%\,\mathrm{hr}^{-1}$. The reason is that at the interface between the cloud and sub-cloud layer, the most important contribution to the budget equations is the air that is entrained in surplus of $\frac{dh}{dt}$, i.e. with flow rate M (see Eq. (6.4)). This contribution ($-M\Delta\phi$) is incorporated in the entrainment term in the 'venting budget', and in the mass-flux term in the 'pumping budget'. Even for the 'pumping budget', the contributions to the mixing ratio tendencies are of the order of 1 % hr^{-1} and therefore not significant. In our analysis, based on TROFFEE data, there are a few exceptions that change mixing ratios on average more than 5 % per hour due to the mass-flux circulation ('pumping budget'). Focusing on those reactants whose chemical lifetime is not shorter than the turbulent time scale ($\sim$ 15 min), this is the case for the INERT species ($-6.4\,\%\,\mathrm{hr}^{-1}$), isoprene ($-8.5\,\%\,\mathrm{hr}^{-1}$) and the inert tracer BLS ($-5.9\,\%\,\mathrm{hr}^{-1}$). These contributions can be considered minor but nevertheless significant. The corresponding maximum contributions during the presence of active SCu clouds are for the respective species -11.4 (INERT), -15.1 (isoprene) and -10.6 $\%\,\mathrm{hr}^{-1}$ (BLS).

Note that the BLS and FTS tracers were initialized such that at every location the sum of their mixing ratios was 1 ppb. Additionally, they are not influenced by any surface exchange or chemical transformations. Therefore, the mass-flux contributions for these two tracers are equal in magnitude and only differ in sign. However, at the time the active clouds appear, the mixed-layer height is much larger than its initial value. Therefore, the mixing ratios of BLS and FTS approach their initial free tropospheric mixing ratios (i.e. 0 and 1 ppb, respectively). During the most active SCu convection (1200 – 1400 LT) their mixed-layer averaged mixing ratios are, respectively, 0.1 and 0.9 ppb. As a result, the same mass-flux contribution to the budget yields a much lower relative change per hour for FTS than for BLS.

6.3.4 Parametrizing reactant transport

Similar to q in Sect. 6.3.1, the mixing ratios of the atmospheric compounds in the cloud core are parametrized compared to a reference value, being either $< \phi >$ or $\overline{\phi}(z_b)$. We analyse the resulting expressions for two cases: the standard case (SC) that is described in Sect. 6.2.3 and a numerical setup in which the scattering of UV radiation by clouds has been turned off, effectively resulting in transparent clouds (TC). As will be discussed later in this

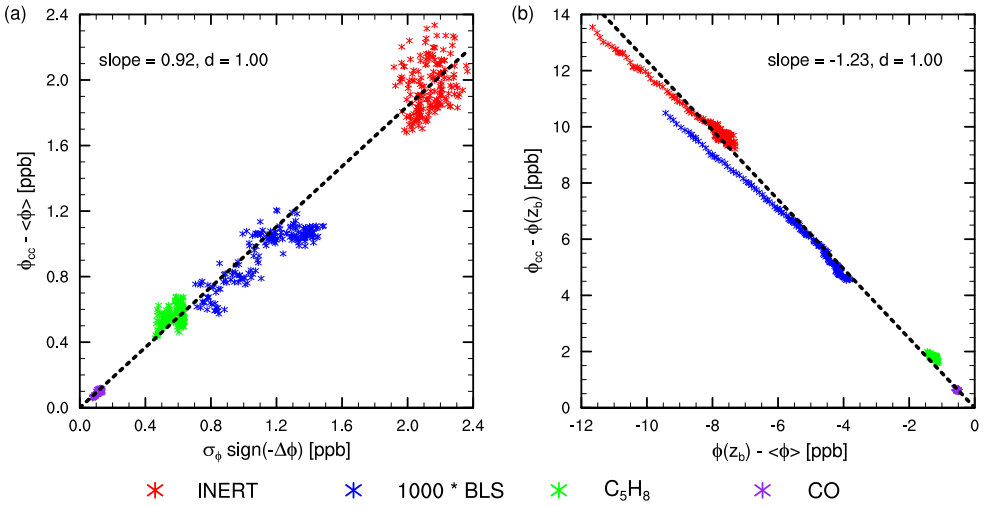

Figure 6.6: Parametrization for **(a)** $\phi_{cc} - <\phi>$ *(related to Eq. (6.5)) as a function of* σ_ϕ *times the sign of* $-\Delta\phi$ *and* **(b)** $\phi_{cc} - \overline{\phi}(z_b)$ *(related to Eq. (6.6)) as a function of* $\overline{\phi}(z_b) - <\phi>$*. The evaluated numerical experiment is the standard case (SC). The values for* ϕ *represent the mixing ratios of INERT, BLS,* C_5H_8 *and CO. The black dashed lines indicate the linear regression fits through all (unscaled) data, forced through (0,0). The asterisks are data sampled at 1-minute intervals. The slopes and indexes of agreement, d, are indicated.*

section, several chemical species (especially O_3, NO and NO_2) are particularly sensitive to this modification of the UV radiation below the clouds. We tested different parametrizations for both $\phi_{cc} - <\phi>$ and $\phi_{cc} - \overline{\phi}(z_b)$, using linear functions. For $\phi_{cc} - <\phi>$, the most realistic results were obtained by expressions as a function of $\sigma_\phi \, \mathrm{sign}\,(-\Delta\phi)$. This agrees with the discussion in Sect. 6.3.2. $\phi_{cc} - \overline{\phi}(z_b)$ is best parametrized as a function of $\overline{\phi}(z_b) - \langle\phi\rangle$. Here, σ_ϕ is the standard deviation of scalar ϕ that is calculated over the entire sub-cloud layer. This differs from previous studies (van Stratum et al., Submitted), where $\sigma_{\phi,h}$ is used. In this study, using $\sigma_{\phi,h}$ resulted in slightly lower values for d and slopes approximately $\frac{1}{2}$ times the slopes found for expressions based on the total σ_ϕ.

The relations between σ_ϕ and $\phi_{cc} - <\phi>$, and between $\overline{\phi}(z_b) - \langle\phi\rangle$ and $\phi_{cc} - \overline{\phi}(z_b)$ are visualized for different atmospheric compounds in Figs. 6.6 and 6.7. The presented results are a first step in developing a general expression for the mass-flux transport of atmospheric reactants. Figure 6.6 shows the parametrization based on isoprene, CO and the inert tracers INERT and BLS for the standard case. For visualization purposes, the BLS mixing ratios are multiplied by 1000. For these atmospheric compounds, the perturbation of UV radiation by clouds has no significant impact on the parametrization, producing nearly identical results for the TC numerical experiment (not shown). Additionally, the constants for the expressions

that are derived from these four compounds are very similar to those derived for q. For the 'venting budget', the slope is found to be 0.92, while it was 1.01 for q. For the 'pumping budget' the match is even closer with a slope of -1.23 for the atmospheric compounds and -1.20 for q (not shown). Even though not all data points lay perfectly on the regression line, Fig. 6.6 corroborates that $\phi_{cc} - < \phi >$ and $\phi_{cc} - \overline{\phi}(z_b)$ can be adequately represented for these atmospheric compounds.

However, not all reactants comply that well with the expressions that were derived. The parametrizations for O_3, NO_2, OH and H_2O_2 are shown in Fig. 6.7. These four reactants all respond quickly to changes in UV radiation through reactions R1, R5 and R6 in Table 6.1. Note that the chemical lifetimes of NO_2 ($\sim$ 3 min) and OH ($\sim$ 0.15 s) are short compared to the turbulent time scale. OH is multiplied by 1000 in the figure for visualization. In the sub-cloud layer, the coherent thermals to which the SCu clouds are rooted are located exactly at these shaded positions. Therefore the mixing ratios of the UV dependent reactants in those thermals, and subsequently in the cloud cores, are shifted from their equilibria (Vilà-Guerau de Arellano et al., 2005). Subsequently, the transported air by SCu convection is more representative for lower UV conditions than for the average sub-cloud layer conditions. For the 'venting budget', the atmospheric compounds cannot be parametrized using the proposed linear relationship (e.g., for H_2O_2 the slope in Fig. 6.7a should rather be 0.02). However, the compounds do satisfy a linear relationship for the 'pumping' budget, albeit with a different slope than derived before. This slope, mainly governed by O_3 due to the magnitude of its differences in mixing ratio between cloud and sub-cloud layer, is much closer to -1 and actually implies that ϕ_{cc} is closer to $\langle\phi\rangle$. When these reactants are eventually transported out of the coherent thermals or clouds towards an area above which no cloud is present, the equilibria are quickly restored. Therefore this misrepresentation has no significant impact on our results. However, the results also show that the actual mass-flux transport of individual chemical species to the cloud-layer depends on a more complex combination of dynamics, the UV radiation modification by clouds, and the chemical pathways.

Using the TC numerical experiment, we demonstrate that the standard expressions can indeed be applied if the modification of the UV radiation by clouds is not active. In this case, the temporary departure of the UV dependent reactants, compared to their equilibrium mixing ratios under sub-cloud layer averaged conditions, does not occur. In Figs. 6.7c and d the resulting parametrizations are shown. The slopes for the 'venting budget' and 'pumping budget' are, with respectively 0.89 and -1.19, very close to the slopes found in Fig. 6.6 for the non UV dependent atmospheric compounds. This confirms that the original deviations found for chemical reactive species in the SC numerical experiment are indeed caused by temporary modifications induced by UV radiation and that consequently the parametrizations for transport by SCu convection are valid.

Apart from clustering atmospheric compounds, parametrizations are determined per in-

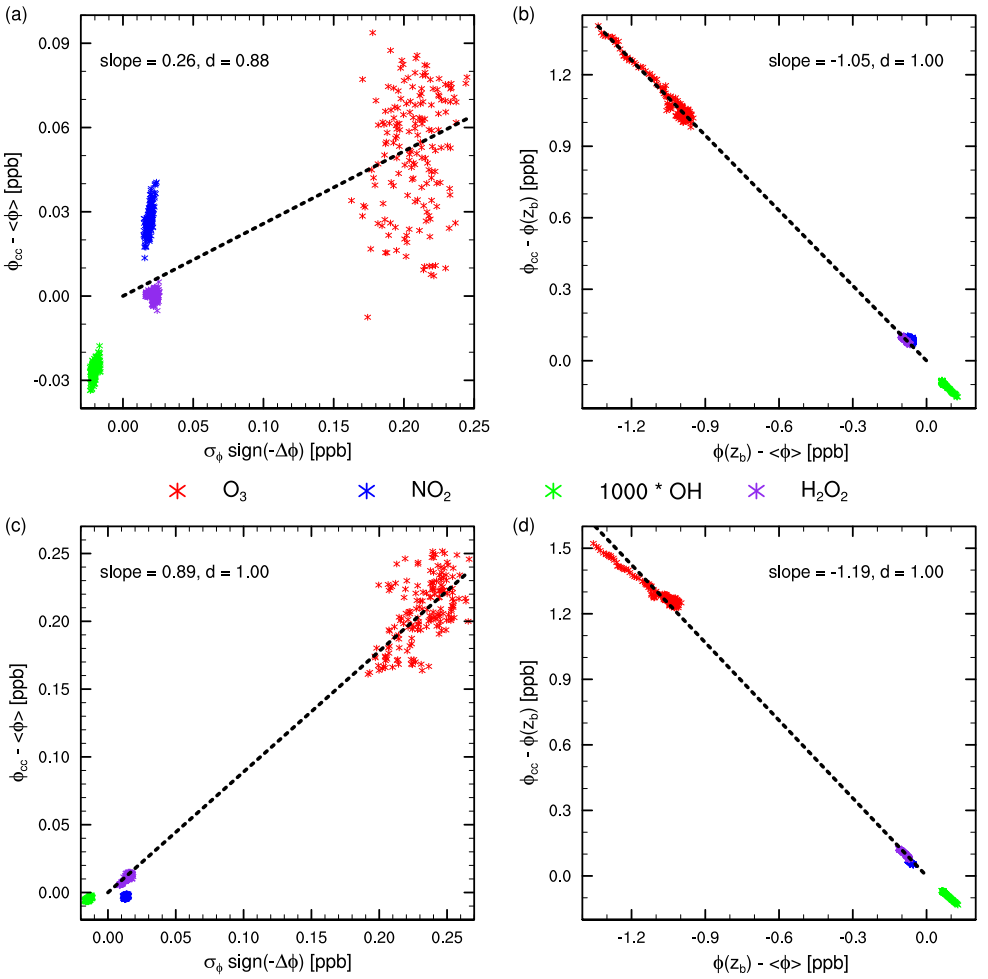

Figure 6.7: Parametrization for **(a,c)** $\phi_{cc} - <\phi>$ *(related to Eq. (6.5)) as a function of* σ_ϕ *times the sign of* $-\Delta\phi$ *and* **(b,d)** $\phi_{cc} - \overline{\phi}(z_b)$ *(related to Eq. (6.6)) as a function of* $\overline{\phi}(z_b) - <\phi>$*. Two different numerical experiments are evaluated, the standard case* **(a,b)** *and one in which the UV scattering by clouds has been disabled* **(c,d)***. The values for* ϕ *represent the mixing ratios of* O_3*,* NO_2*,* OH *and* H_2O_2*. The black dashed lines indicate the linear regression fits through all (unscaled) data, forced through (0,0). The asterisks are data sampled at 1-minute intervals. The slopes and indexes of agreement, d, are indicated.*

Table 6.2: Parametrizations of mixing ratios, denoted by ϕ, in the cloud cores. The parametrization for $\phi_{cc} - <\phi>$, linked to Eq. (6.5), is a slope times $\sigma_\phi \,\mathrm{sign}\,(-\Delta\phi)$. The parametrization for $\phi_{cc} - \overline{\phi}(z_b)$, linked to Eq. (6.6), is a slope times $\overline{\phi}(z_b) - \langle\phi\rangle$. These parametrizations are derived using the standard case (SC) and the Transparent Clouds (TC) case. Listed are the slopes with their corresponding indices of agreement in parentheses.

Reactant	$\phi_{cc} - <\phi>$ vs. $\sigma_\phi \,\mathrm{sign}\,(-\Delta\phi)$		$\phi_{cc} - \overline{\phi}(z_b)$ vs. $\overline{\phi}(z_b) - \langle\phi\rangle$	
	SC	TC	SC	TC
INERT	0.92 (0.50)	0.92 (0.50)	-1.23 (0.98)	-1.23 (0.98)
O_3	0.25 (0.26)	0.89 (0.72)	-1.05 (0.99)	-1.19 (0.95)
O^{1D}	1.66 (0.64)	-2.51 (0.93)	-5.13 (0.52)	0.44 (0.15)
NO	1.23 (0.46)	-1.97 (0.02)	-8.06 (0.52)	5.09 (0.02)
NO_2	1.45 (0.74)	-0.23 (0.08)	-1.45 (0.87)	-0.95 (0.99)
CH_4	0.94 (0.87)	0.86 (0.87)	-1.21 (0.85)	-1.18 (0.89)
CH_2O	0.75 (0.75)	0.84 (0.79)	-1.14 (0.95)	-1.16 (0.92)
CH_3O_2	2.12 (0.58)	1.74 (0.45)	-1.53 (0.94)	-1.40 (0.96)
MVK	0.79 (0.73)	0.89 (0.78)	-1.16 (0.96)	-1.19 (0.94)
C_5H_8	0.96 (0.64)	0.86 (0.70)	-1.46 (0.84)	-1.41 (0.91)
RO_2	-0.58 (0.33)	1.43 (0.58)	-0.84 (0.93)	-1.34 (0.97)
OH	1.31 (0.75)	0.34 (0.60)	-1.34 (0.97)	-1.06 (1.00)
HO_2	-1.56 (0.25)	-0.30 (0.18)	5.30 (0.17)	-0.60 (0.76)
CO	0.84 (0.91)	0.84 (0.88)	-1.18 (0.94)	-1.16 (0.95)
REST	0.59 (0.88)	0.85 (0.91)	-1.13 (0.99)	-1.18 (0.98)
HNO_3	0.93 (0.94)	0.87 (0.92)	-1.21 (0.96)	-1.18 (0.96)
H_2O_2	0.02 (0.02)	0.77 (0.91)	-1.00 (1.00)	-1.13 (1.00)
NO_3	0.34 (0.47)	-1.53 (0.99)	-1.37 (0.39)	-0.21 (0.20)
N_2O_5	-3.59 (0.86)	-2.56 (0.99)	9.02 (0.69)	1.88 (0.10)
BLS / FTS	0.83 (0.92)	0.83 (0.92)	-1.17 (1.00)	-1.17 (1.00)

dividual species, except for the background atmospheric compounds N_2, O_2 and H_2O. The resulting slopes and corresponding indices of agreement are listed in Table 6.2. Even though Figs. 6.6 and 6.7 show that multiple atmospheric compounds approximately follow one derived parametrization, this table indicates that the derived slopes differ depending on which compound is used. For individual species (e.g. NO), the scaling can be completely different from the general derived expression. The scaling even differs between the inert atmospheric compounds INERT and BLS / FTS. These species only differ in initial profiles and surface exchange. However, when grouping all atmospheric compounds, generic expressions are derived that read

$$\phi_{cc} - \langle\phi\rangle \approx \xi\sigma_\phi \mathrm{sign}\,(-\Delta\phi)\,, \quad \xi = 0.91 \tag{6.12}$$

and

$$\phi_{cc} - \overline{\phi}(z_b) \approx \xi_2 \left(\overline{\phi}(z_b) - \langle\phi\rangle\right), \quad \xi_2 = -1.23. \tag{6.13}$$

Some significant deviations from this line can be found for the 'venting budget' for the standard case (not shown), but these disappear for the TC numerical experiment, implying that these excursions are caused by local deviations from chemical equilibria related to UV radiation. To represent ϕ_{cc}, these scalings would give satisfactory results for the individual reactant mixing ratios under the investigated dynamical conditions. However, the slopes in the expressions, both for the dynamical variables (w_{cc} and q_{cc}) and for the mixing ratios, can change if specific conditions are altered. This will be demonstrated for heterogeneous surface forcings in Sect. 6.3.6. Therefore, it is recommended in future research to test the parametrizations for different regions and under different dynamical and chemical conditions.

Finally, since the slopes of the regression line are determined using the least squares method, the derived slopes for the parametrizations are mainly governed by the atmospheric compounds with the largest difference between ϕ_{cc} and the reference value, which is INERT in this study. Additionally, due to the different orders of magnitude in the mixing ratios of the atmospheric compounds, statistical variables, like R^2 and the index of agreement, that describe the regression lines for these combined compounds are artificially forced to 1. In short, this is because these statistical variables describe how much of the variance in the dataset can be explained by the regression and they therefore increase if the variance in the dataset increases.

6.3.5 Capturing vertical transport

The previously determined expressions to parametrize ϕ_{cc} were derived to represent the vertical transport of specific humidity and atmospheric reactants. In Sect. 6.2.1 it was stated (after Siebesma and Cuijpers (1995)) that in the cloud layer the vertical transport is dominated by transport in the cloud cores. Furthermore, in these cloud cores, turbulent transport is considered to be negligible compared to the the organized transport, which is governed by the mass flux. Here, we study the ability of the parametrization for ϕ_{cc} to reproduce the vertical transport. To directly compare the mass-flux transport to the total vertical transport, as expressed by Eq. (6.3) and discussed in Sect. 6.2.1, the transport as used in the 'pumping' budget is evaluated. To predict the organized SCu transport of any scalar, the parametrization of Eq. (6.13) and the diagnosed M are multiplied, $M\left(\phi_{cc} - \overline{\phi}\,(z_b)\right)$.

The representativeness of the organized transport in the SCu cloud cores for the total vertical transport in the cloud layer has already been demonstrated for θ_l and q by Siebesma and Cuijpers (1995). This has been confirmed in our numerical experiments (not shown). The focus is to represent the vertical transport of atmospheric reactants. In contrast to the dynamical variables, the reactant mixing ratios do not affect M. Additionally, the transported

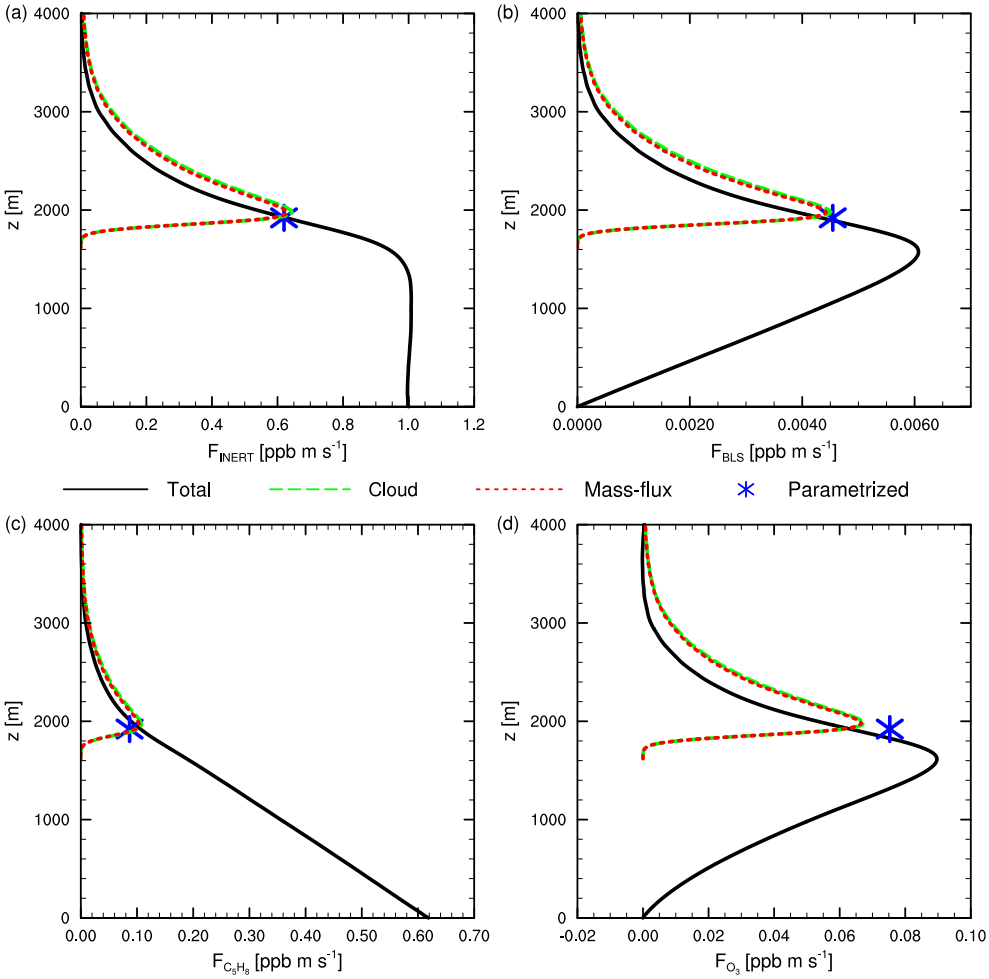

Figure 6.8: Vertical transport of the atmospheric compounds **(a)** *INERT,* **(b)** *BLS,* **(c)** C_5H_8 *and* **(d)** O_3*. The data is averaged between 1200 and 1300 LT. The black lines show the total vertical fluxes. The vertical transport in the cloud cores is depicted by the dashed green lines and the organized transport in the cloud cores through the mass flux by the red dashed lines. The blue asterisks represent the parametrized (mass-flux) vertical transport using the diagnosed M and the parametrization of Eq. (6.13) according to Eq. (6.3).*

mixing ratios are influenced by extra factors (e.g., chemistry and UV radiation). Therefore, differences can be expected. For the evaluation of the vertical transport in DALES, the vertical fluxes are averaged between 1200 and 1300 LT. Organized transport by SCu convection is most active in the numerical experiment during this hour. In Fig. 6.8, the vertical transport of INERT, BLS, C_5H_8 and O_3 is presented. The parametrized mass flux is plotted at the height of the hourly averaged z_b. Figure 6.8 confirms that the transport in the cloud cores makes up for the majority of the total vertical transport in the cloud layer, the two quantities being very similar in magnitude. Additionally, this figure shows that the organized (mass-flux) transport is virtually equal to the total transport in the clouds, justifying the assumption that the turbulent transport in the clouds is negligible compared to the organized transport. Furthermore, the predicted vertical transport, using Eq. (6.3) and the parametrization of Eq. (6.13), agrees very well with the actual transport by SCu convection. This is especially the case for INERT **(a)**, BLS **(b)** and isoprene **(c)**, while also the ozone flux **(d)** is captured satisfactorily. For the simulation in which the UV radiation is not modified by clouds, TC, the match for ozone is similar to INERT, BLS and isoprene (not shown).

As mentioned in Sect. 6.3.4, the aforementioned assumptions about vertical transport do not comply with all reactants. Here, we analyse two interconnected atmospheric compounds in particular: NO and NO_2. Similar to Fig. 6.8, the vertical transport for NO and NO_2 is presented in Fig. 6.9 for both the SC and TC numerical experiments. For the standard case **(a,b)**, the vertical transport is again dominated by the transport in the cloud cores. However, the mass-flux transport is not equal to the total transport in the cloud cores. As these differences do not occur for most atmospheric compounds in the model and since the differences for the short-lived NO and NO_2 seem to cancel each other, this feature is most likely caused by the NO/NO_2 partitioning, which is influenced by the UV radiation modification below the SCu clouds. Due to the resulting lower photolysis rate in reaction R5 (see Table 6.1), the NO/NO_2 ratio is shifted to smaller values below the clouds (Vilà-Guerau de Arellano et al., 2005). The time scale associated with the photostationary state equilibrium is in the order of minutes. Within the turbulent motions in the cloud cores, the higher vertical velocities are associated more with air that comes from below the cloud, while the lower vertical velocities are associated more with air from above. Due to the smaller NO and larger NO_2 mixing ratios below the clouds, the turbulent motions in the cloud cores will have a negative contribution to the vertical flux of NO and a positive contribution to the vertical flux of NO_2. This agrees with the results presented in Figs. 6.9a and b. The depicted vertical fluxes reflect as well that the parametrizations are not representative for NO and NO_2 at the same level compared to the atmospheric compounds presented in Fig. 6.8. For NO_2 the parametrized mass-flux transport is of the right order, albeit an underprediction. However, the predicted transport of NO is negligible compared to the actual transport calculated by DALES.

As discussed above, the poor representation of the vertical transport of these short-lived

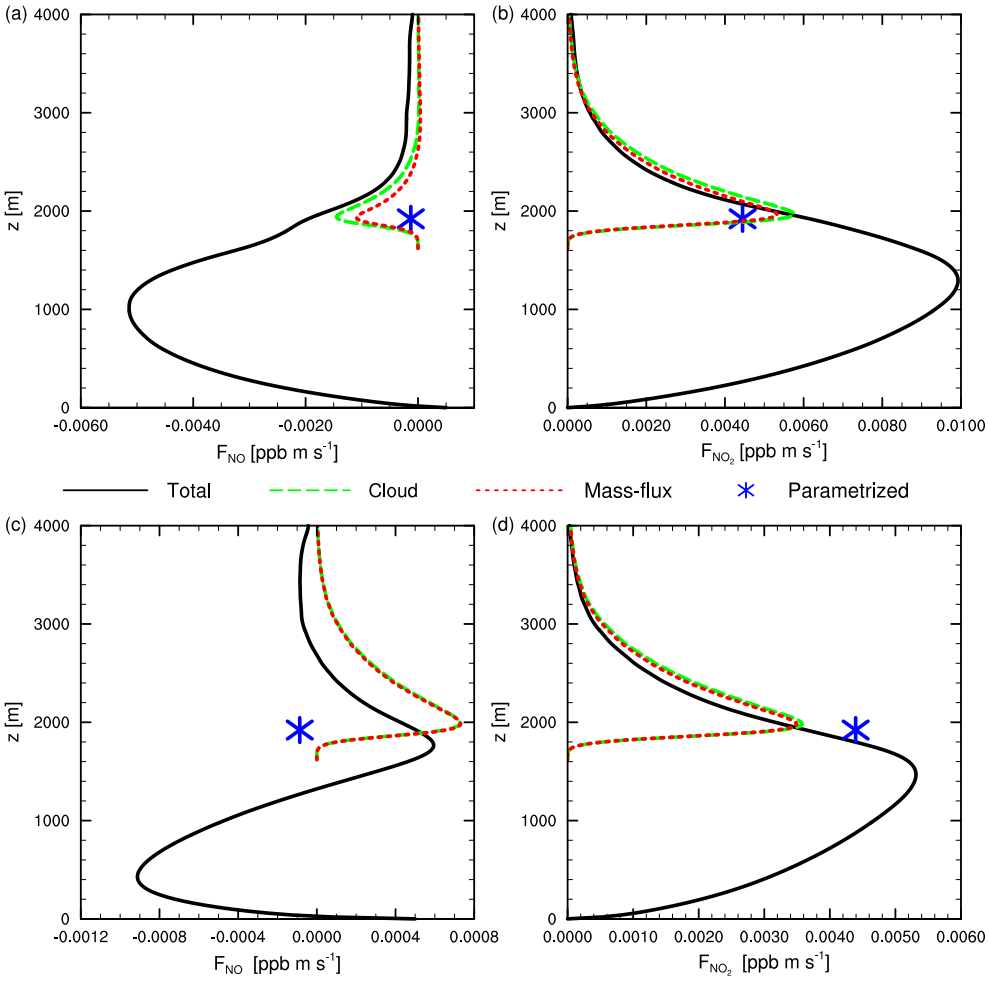

Figure 6.9: Vertical transport of the atmospheric compounds **(a,c)** *NO and* **(b,d)** *NO_2. The results are shown for the numerical experiments* **(a,b)** *SC and* **(c,d)** *TC. The data is averaged between 1200 and 1300 LT. The black lines show the total vertical fluxes. The vertical transport in the cloud cores is depicted by the dashed green lines and the organized transport in the cloud cores through the mass-flux by the red dashed lines. The blue asterisks represent the parametrized (mass-flux) vertical transport using the diagnosed M and the parametrization of Eq. (6.13) according to Eq. (6.3).*

chemical compounds is likely the result of the NO/NO_2 partitioning that depends on the local concentrations of other atmospheric compounds and UV radiation. To check whether this hypothesis is the full explanation, the flux of NO_x ($NO + NO_2$) is evaluated, since this generic species has a longer lifetime ($\sim$ 15 h) and is less affected by UV radiation and concentrations of other atmospheric compounds. However, first the sole impact of the UV radiation modification by clouds on the vertical transport of NO and NO_2 is further investigated by analysing the TC numerical experiment. Figures 6.9c and d show that the absence of UV radiation modification below the clouds results in altered vertical transport of NO and NO_2 compared to the SC numerical experiment at all heights. Even though the sub-cloud layer averaged quantities of NO and NO_2 are not influenced significantly by this local difference in UV radiation below the clouds, their horizontally averaged vertical fluxes are. The transport in the cloud cores is again of the same order as the total vertical transport, but in contrast to Figs. 6.9a and b, the turbulent flux of NO and NO_2 in the cloud cores is in this numerical experiment negligible compared to the organized mass-flux transport. Thus, the UV radiation modification explains part of the different behaviour of the NO and NO_2 transport compared to the transport of chemical species that are not very sensitive to the local and instantaneous UV radiation (e.g., INERT, BLS/FT and isoprene). However, the parametrized transport still differs significantly from the vertical flux in the cloud cores that is calculated by DALES. The NO_2 mass-flux transport is overpredicted and again the predicted NO mass-flux transport is negligible compared to the actual transport. To check whether these remaining differences are caused by temporary shifts in the NO/NO_2 partitioning related to the spatial distribution of other reactants, the vertical flux of NO_x is analysed. Note that a similar analysis for O_x ($O_3 + NO_2$) yields comparable results as for O_3, due to the relatively low concentration of NO_2.

Figure 6.10 shows the vertical transport of NO_x for the SC numerical experiment. The actual and parametrized vertical transport (not shown) are almost identical for the TC numerical experiment. These results confirm that NO_x behaves like the inert atmospheric compounds depicted in Fig. 6.8. The total vertical transport in the cloud layer is dominated by the vertical transport in the cloud cores. In turn, this latter transport is virtually equal to the organized mass-flux transport. Finally, while the parametrization of the mass-flux transport, using Eqs. (6.3) and (6.13), did not result in accurate predictions for the individual NO and NO_2 fluxes, the prediction for the NO_x flux matches the actual vertical transport very well. As an illustration, using solely NO_x to derive the constant in Eq. (6.13) would result in -1.20 ($d = 0.98$) for the SC numerical experiment. This value is very similar to those derived for the inert tracers INERT and BLS/FTS (see Table 6.2).

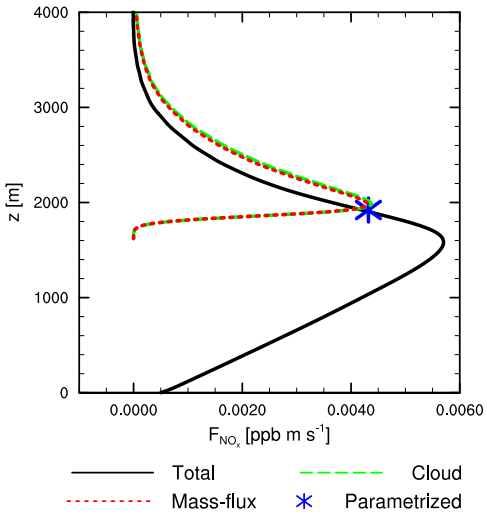

Figure 6.10: Vertical transport of NO_x for the SC numerical experiment. The data is averaged between 1200 and 1300 LT. The black line shows the total vertical flux. The vertical transport in the cloud cores is depicted by the dashed green line and the organized transport in the cloud cores through the mass flux by the red dashed line. The blue asterisk represents the parametrized (mass-flux) vertical transport using the diagnosed M and the parametrization of Eq. (6.13) according to Eq. (6.3).

6.3.6 Heterogeneous surface forcings

The results presented in the previous sections strengthen confidence in the general applicability of the derived predictive expressions to represent the reactant transport from sub-cloud layer to cloud layer. Similar to the parametrizations for q, in general the cloud core mixing ratios are shown to be accurately predicted by Eqs. (6.12) and (6.13) in our numerical experiments. Next, we investigate whether the predictive expressions still hold if initial or boundary conditions are altered. We select a situation that can have a profound impact on the cloud characteristics and therefore on SCu convection: heterogeneous surface forcings, which induce secondary circulations (Patton et al., 2005; Ouwersloot et al., 2011). This numerical experiment, which is described in Sect. 6.2.3, is referred to as the heterogeneous surface (HS) experiment.

Due to the induced mesoscale circulations, the upward (downward) motions are located over the savannah (forest) patches. Emitted reactants are transported to the savannah patches and then upwards, while entrained air is transported to the forest patches and then downwards (Ouwersloot et al., 2011). As a result, over the forest the sub-cloud layer specific humidity and mixing ratios are more characterized by their values in the (entrained) free tropospheric

air than over the savannah. Therefore, q and the mixing ratios of e.g., INERT, BLS, NO_x and C_5H_8 in the sub-cloud layer are all relatively high over savannah and low over forest (not shown). As the SCu clouds are formed at the top of thermals, they are now solely located over the savannah patches. This suggests that compared to the homogeneous SC numerical experiment the properties of the air that escapes the sub-cloud layer deviate more from the properties of both the entrained air and the average sub-cloud layer air, resulting in constants with larger magnitudes in Eqs. (6.8), (6.11), (6.12) and (6.13).

It should be noted that over the savannah patches, the coverage and area fractions of clouds and cloud cores are enhanced such that over the entire domain their magnitudes are similar to the SC numerical experiment. However, their evolution is shifted forward by approximately half an hour. As a result, the mass flux is advanced by half an hour as well. Due to the stronger positive wind velocities over the savannah patches, related to the induced mesoscale circulations (Patton et al., 2005), w in the cloud core becomes higher (maximum 56 % increase). As a result, the mass flux is enhanced as well, although the order remains similar.

Compared to the SC numerical experiment, the mixed-layer height never differs more than 118 m (7 %) and its final value differs less than 10 m. As a result, the convective velocity scale, w_*, deviates only insignificantly (maximum 2 %) compared to the SC numerical experiment, too. We find that the linear relation of Eq. (6.7) is still valid, however, related to the increased w_{cc}, $\lambda = 0.91$ (with $d = 0.93$), which is significantly different from 0.84. Additionally, we find that for the HS data, in order to accurately predict $q_{cc} - < q >$, ζ in Eq. 6.8 should be 0.63 (with $d = 0.65$) rather than the previously determined 0.51 by van Stratum et al. (Submitted) or 0.53 for the SC numerical experiment. In the alternative Eq. (6.11), ζ_2 becomes 1.06 instead of 1.01. These results underscore that, even though q_{cc} and w_{cc} can still be parametrized using the previously applied linear functions, the proportionality factors in these expressions depend on the boundary conditions of the evaluated ABL. Future studies are recommended to address how the constants λ, ζ and ζ_2 depend on the initial and boundary conditions.

Here, we evaluate the vertical transport of atmospheric reactants. Figure 6.11 shows the dependencies of Eq. (6.13) for INERT, BLS, isoprene and CO in the HS numerical experiment, using an updated value for ξ_2. The data points match the regression line well, indicating that the aforementioned equations still adequately represent the mixing ratios in the active clouds if the constant ξ_2 is adapted. For these four chemical species combined, ξ_2 changes from -1.23 to -1.42. Evaluating all chemical species together (not shown) results in $\xi = 0.99$ instead of 0.91 (in Eq. (6.12)) and $\xi_2 = -1.42$ instead of -1.23. As was the case for specific humidity, the mixing ratios in the cloud cores can thus be predicted using the previously applied linear relations if the change in slopes for Eqs. (6.12) and (6.13) are taken into account.

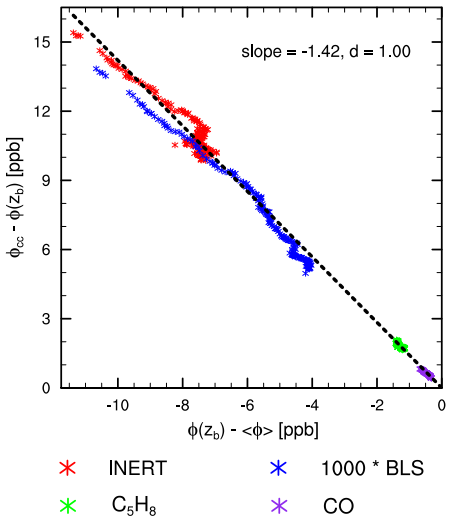

Figure 6.11: Parametrization for $\phi_{cc} - \overline{\phi}(z_b)$ (related to Eq. (6.6)) as a function of $\overline{\phi}(z_b) - <\phi>$. Here, the numerical experiment with heterogeneous surface forcings is evaluated. The values for ϕ represent the mixing ratios of INERT, BLS, C_5H_8 and CO. The black dashed line indicates the linear regression fit through all (unscaled) data, forced through (0,0). The asterisks are data sampled at 1-minute intervals. The slope and index of agreement, d, are indicated.

Similar to Fig. 6.8, the vertical transport of INERT, BLS, isoprene and ozone is depicted in Fig. 6.12 for the HS numerical experiment. The parametrized mass flux is calculated using the updated Eq. (6.12) with $\xi_2 = -1.42$. The organized mass-flux transport is still the dominant contribution to the total vertical transport in the cloud cores for all tracers. For INERT, BLS and isoprene, this transport is a satisfactory match to the total vertical flux in the cloud layer. For ozone, on the other hand, the total vertical flux significantly deviates from the transport in the cloud cores. This could be caused by transport in the cloud shells, as hypothesized by Heus and Jonker (2008) and Jonker et al. (2008). In the cloud shells, on average the air descends. As the shells are positioned between the cloud cores and the environment and partly return air downwards after it was transported upwards in the cores, they are most likely to reduce the effect of the cloud core transport. For the heterogeneous case, the clouds are concentrated over the savannah patches. Since the clouds, and the thermals they are rooted into, are concentrated over a smaller domain, the clouds become more active. These clouds grow deeper (reaching a maximum horizontally averaged thickness of 1900 m instead of 1400 m) and the transport by cloud shells increases. As mentioned in Sect. 6.2.1, to evaluate why O_3 is affected more than the other chemical species, an analysis could be per-

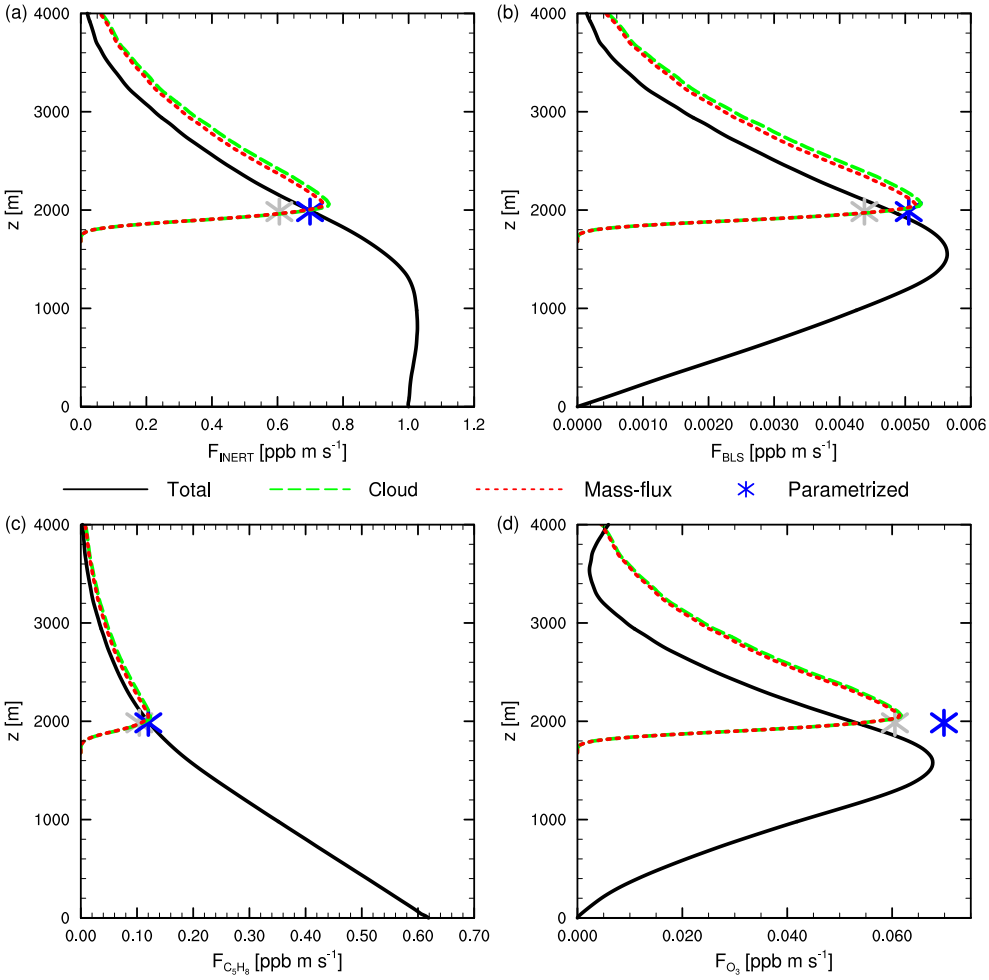

Figure 6.12: Vertical transport of atmospheric compounds **(a)** *INERT,* **(b)** *BLS,* **(c)** C_5H_8 *and* **(d)** O_3 *for the numerical experiment with heterogeneous surface forcings. The data is averaged between 1200 and 1300 LT. The black lines show the total vertical fluxes. The vertical transport in the cloud cores is depicted by the dashed green lines and the organized transport in the cloud cores through the mass flux by the red dashed lines. The blue asterisks represent the parametrized (mass-flux) vertical transport using the diagnosed M and the parametrization of Eq. (6.13) with* $\xi_2 = -1.42$ *according to Eq. (6.3). The grey asterisks represent the parametrized vertical transport using the original* $\xi_2 = -1.23$.

formed in which the transport is partitioned in advective and turbulent fluxes in three areas: cloud core, cloud shell and environment. However, as this section only aims at checking whether the concept of mass-flux transport and its parametrizations hold for all conditions, this is beyond the scope of this study. Finally, the predicted vertical transport, using Eqs. (6.3) and (6.13) with $\xi_2 = -1.42$, agrees well with the actual transport by SCu convection.

Although our analysis is not a comprehensive sensitivity study, it is clearly demonstrated that, even though the factors in the parametrizations were approximately equal between the SC numerical experiment presented in this study and the three numerical experiments presented by van Stratum et al. (Submitted), changing the applied boundary conditions can result in changes in the parameters of the expressions that predict the mass flux and the resulting transport of humidity and atmospheric reactants. Thus it is demonstrated that heterogeneous surface forcings can affect the prognostic expressions and future research will have to show in more detail which initial and boundary conditions affect the parametrizations and how the proportionality factors (λ, ζ,ζ_2, ξ, ξ_2) in the various equations (Eqs. (6.7), (6.8), (6.11), (6.12) and (6.13)) are affected by these conditions. The altered constants that are presented in this section are therefore not typical for every situation with heterogeneous surface conditions, but demonstrate the need to be cautious in applying the standard parametrization equations with factors that are derived for particular conditions. Note that even though the constants in the predictive expressions are affected by surface heterogeneity, the magnitude is still the same and the dependencies are still well represented by linear functions. Therefore, if a numerical model does not explicitly resolve transport by SCu convection, applying the parametrizations with the constants of the SC numerical experiment is still an improvement compared to not applying the parametrizations at all.

6.4 Conclusions

We studied how mass-flux transport by shallow cumulus convection, which is driven by fair weather clouds that form over the Amazon region, affects sub-cloud layer atmospheric reactants by analysing Large-Eddy Simulation data. These Amazonian conditions are based on observations in the TROFFEE campaign. For the analysis of the numerical data, two different expressions for the budget of the mixing ratio evolutions in the diurnal atmospheric boundary layer are derived using mixed layer theory. These expressions are equivalent, though correspond to different physical interpretations. Between these two budget expressions, it is found that in the expression relevant for chemistry-transport models (the 'pumping budget') the mass-flux transport makes a more significant contribution to reactant mixing ratio evolutions. This influence on the sub-cloud layer reactant mixing ratios is for most chemical species relatively small, being of the order of a few % per hour. However, for some reactants

the contribution of the mass-flux transport to the mixing ratio evolution is more significant. For example, during shallow cumulus convection isoprene decreases on average by 8.5 % per hour and at maximum (when the shallow cumulus clouds are fully developed) by 15 % per hour due to the mass-flux transport. As the influence of mass-flux transport is significant for some atmospheric reactants, it is recommended that this sub-grid process is taken into account in chemistry-transport and climate models.

To represent this transport in these models, we first evaluated the parametrizations for the dynamical variables (vertical wind and specific humidity) that were previously derived for three independent numerical LES experiments. The results corroborate that the proposed linear expressions for the parametrizations and their constants are valid over a wide range of conditions. Additionally, our LES data indicates that the specific humidity in the cloud cores is better predicted by the total (volumetric) standard deviation of moisture in the sub-cloud layer than by the horizontal standard deviation near the top of this layer. It is therefore recommended to investigate in future studies whether this is also the case for other conditions with active shallow cumulus convection. Second, the representations for the cloud core values were investigated. Assuming linear dependencies, we determined to which variables these representations scale best and with which proportionality factors. The derived linear expressions to predict the mixing ratios in the cloud cores compare well with LES data for many reactants, but not for all. The latter is especially the case for reactants whose concentrations are highly dependent on the local and instantaneous UV radiation. Due to the modification of the UV radiation distribution by the clouds, the chemical equilibrium between some species, such as NO and NO_2, is perturbed. It is demonstrated by an additional LES experiment that if UV radiation modification by clouds is not applied, also these reactants comply with the standard linear expressions. Since these UV dependent reactants are restored to their original equilibria in the regions where the UV radiation is not modified by the clouds, the standard parametrizations adequately represent the transport of reactants from the sub-cloud layer to the cloud layer by shallow cumulus convection.

It is shown that in general, in the cloud layer the vertical transport of atmospheric reactants is governed by organized shallow cumulus convection. In turn, this mass-flux transport is accurately predicted by the derived expressions. However, there are a few, but relevant exceptions, particularly NO and NO_2. By analysing the mass-flux transport of the generic species NO_x, it is shown that this is caused by departures from the chemical equilibrium that are linked to local concentrations of other atmospheric compounds, such as ozone. For NO_x, the mass-flux transport matches the total vertical flux very well and the parametrizations agree satisfactorily with the LES model. As the NO/NO_2 partitioning is locally determined, predicting the NO_x transport accurately, suffices for numerical models that aim to represent NO and NO_2.

Finally, the robustness of the parametrizations has been explored. For a situation with het-

erogeneous surface forcings it is shown that, while the prognostic expressions still have the same linear dependencies as previously determined, the proportionality factors in all expressions have to be enhanced to make them agree with the LES experiment over heterogeneous terrain. This shows that the derived parametrizations for the mass flux and corresponding transport of sub-cloud layer reactants are dependent on boundary conditions, including heterogeneous surface forcings. Further research is needed to investigate on which other conditions they depend and how these dependencies can be explicitly incorporated in the parametrizations. It should also be noted that the diagnosed constants in the various predictive expressions remain of similar magnitude for the different evaluated conditions. Therefore, until the sensitivities to the different boundary and initial conditions are identified, chemistry-transport and climate models would already benefit from applying the diagnosed expressions.

Be yourself and think for yourself; and while your conclusions may not be infallible, they will be nearer right than the conclusions forced upon you.

Elbert Hubbard

7 Summary and outlook

This chapter provides an overview of the main findings of this PhD project. As the results are discussed in detail in Chapters 2 to 6, only the most important conclusions are presented. This chapter concludes with providing an outlook for future studies.

7.1 Summary

In the analysis of chemical observations and in the representation of atmospheric chemistry in chemistry-transport and climate models, one should take into account the multiple processes that affect the various reactants. In this, various dynamic effects are often overlooked or poorly represented. The main objective of this PhD project is to identify and understand the dynamic processes that affect chemistry in atmospheric boundary layers (ABL) over forested regions. We focus on the atmospheric processes above boreal forest and the Amazon rain forest since both ecosystems have a significant impact on global atmospheric chemistry and physics. In this study we make use of numerical models of varying complexity that simultaneously solve atmospheric chemistry and boundary-layer dynamics for conditions based on observational data. A second goal is to investigate parametrizations that could be applied in chemistry-transport and climate models to account for these influences. In this thesis, special attention is paid to the influences of the evolution of the boundary-layer height, the

segregation of chemical species within an ABL and the transport of air from the sub-cloud to the cloud layer by shallow cumulus convection. Additionally, the response of these processes to heterogeneous surface properties is investigated. The impact of the boundary-layer height evolution on chemical species in a convective boundary layer is quantified using an elementary mixed-layer model. To further investigate how this boundary-layer height evolution is affected by various dynamic processes and to study the segregation of chemical species and shallow cumulus convection, a Large-Eddy Simulation model is employed, which explicitly resolved the various dynamical and chemical processes at a scale of 50 m rather than parametrizing them. These numerical experiments are based on observational data from the HUMPPA–COPEC–2010 (boreal forest) and TROFFEE (Amazon rain forest) campaigns.

7.1.1 Impact of the boundary-layer height evolution

In Chapter 2, the boundary-layer height evolution and its impact on atmospheric chemistry are evaluated for a convectively well-mixed boundary layer over boreal forest (in Finland) during summertime, based on the HUMPPA–COPEC–2010 observational campaign. The combined dynamical and chemical observations provided an opportunity to investigate the impact of dynamics on chemistry. Although various ABL types were present during daytime, a categorization of radiosonde data showed that these mixed layers below a stable free troposphere were most frequently observed. As a representative day, data of 6 August 2010 is analysed. The numerical study is constrained and validated by surface data combined with atmospheric observations. In the analysis, particular emphasis is placed on how large scale forcings (subsidence and advection) and the transition from nocturnal to daytime turbulent conditions influence the development of the ABL.

By using a numerical model that accounts for the basic dynamical and chemical processes for convectively well-mixed boundary layers, the mixed-layer model (MXL), it is shown that accurate knowledge of the ABL height evolution is necessary for the representation and interpretation of concentration evolutions of atmospheric reactants. The reason is twofold. Firstly, the boundary-layer height determines the mixing volume in which reactive atmospheric compounds are released and interact. Secondly, the growth of the ABL height determines the exchange of compounds between the free tropospheric and boundary-layer air due to entrainment. Due to the dependency of the chemical reaction rates on the concentrations of chemical species, the continuous boundary layer height evolution affects the final chemical state of the ABL. Therefore, knowledge about the initial (early morning) chemical conditions, the surface emissions/deposition and the boundary-layer height at one specific point in time does not suffice to accurately predict the concentrations of chemical species at that point in time.

It is demonstrated for the examined data that the evolution of the ABL height is satisfactorily reproduced and explained by using the relatively basic MXL model. In representing

the observational data, it is shown as well that it is important to account for a residual layer in the morning and the large-scale forcings advection and subsidence. By considering the morning transition from a shallow boundary layer merging with a residual mixed layer aloft into a combined mixed boundary layer, we were able to explain and represent the increase of O_3 concentrations with time and an observed morning peak in the NO_x concentrations. This demonstrates that analyses of chemical observations should take into account the influence of ABL dynamics and in particular the boundary-layer height evolution.

To interpret chemical observations, an alternative solution to employing models that numerically solve the boundary-layer height evolution is using analytical solutions to the applied prognostic equations. Such analytical solutions are derived and presented in Chapter 3. Compared to the most advanced solutions in the literature, the results are expanded upon by simultaneously including the effects of specific humidity and initial conditions. Due to the non-linear dependence of the boundary-layer height on the temperature inversion at the top of the mixed layer, the resulting expression for the boundary-layer height evolution is an implicit function. For applicability, also an explicit simplification is presented, which captures the evolution of the ABL height well for relatively large heights. In Chapter 4, these analytical solutions are expanded to include the effect for subsidence, a large-scale forcing that significantly affects boundary-layer growth. For this expansion, we assume that the divergence of the mean horizontal wind velocity, which is related to subsidence, is constant with height throughout the lower troposphere.

Not only the ABL height evolution can be expressed by an analytical equation. For predicting and interpreting the evolution of atmospheric reactants, additionally the (explicit) analytical expressions for mixed-layer averaged scalars are presented as a function of the ABL height and their respective surface fluxes integrated over time. These expressions are adapted to represent chemical species mixing ratios under idealized chemical conditions, i.e. a chemical production that is constant with time and height and a chemical loss that scales linearly with the mixing ratio of the chemical species under consideration.

Using the analytical solutions for the boundary-layer height and mixed-layer averaged scalars, we are able to perform sensitivity analyses that are continuous in the parameter space, since they are not restricted to a limited amount of samples, as is the case for numerical sensitivity studies. Therefore, these expressions enable us to improve our understanding of the evolution of boundary-layer properties. One example for which the analytical expressions would be useful is to assess the influence of ABL dynamics on the CO_2 budget at a diurnal scale.

The evolution of the boundary-layer height can become more complex by large-scale dynamical processes. Using the Dutch Atmospheric Large-Eddy Simulation (DALES) model, the influence of surface heterogeneity is investigated in Chapter 5. In the applied configuration, warm and dry patches are alternated with cool and wet patches in one direction by

prescribing different sensible and latent heat fluxes. As a result, mesoscale circulations appear with upward moving air over the dry patches and subsiding air over the wet patches. Subsequently, the entrainment of free tropospheric air is enhanced over the dry regions and decreased over the wet regions. We discuss how the length scale of heterogeneity and the amplitude in the surface buoyancy flux affect the final boundary-layer height. It is found that while the boundary-layer height always increases over the dry patches due to the heterogeneous surface forcings, the effect over the wet patches can be either positive or negative. The reason is that for weaker mesoscale circulations, e.g. related to smaller amplitudes in the surface buoyancy flux, the main feedback is less entrainment due to suppressed turbulence, resulting in a lower boundary-layer height. However, for stronger mesoscale circulations, the main feedback is the transport at the top of the ABL of entrained air from the dry patch to the wet patch, resulting in deeper boundary layers. As a result, the sensitivity of the domain averaged boundary-layer height to the length scale of heterogeneity and amplitude in the surface buoyancy flux is also dependent on which of these two feedbacks dominates. The further impact of these circulations on atmospheric chemistry in general, and on isoprene in particular, is summarized in Sect. 7.1.2. Additionally, as mentioned, but not further explored in Chapter 6, the kinematic mass flux has a decreasing effect on the boundary-layer height and, consequently, an increasing effect on the entrainment of free tropospheric air into the mixed layer.

7.1.2 Cause and effect of the segregation of chemical species

A secondary effect of boundary-layer dynamics on atmospheric chemistry is related to mixing within the ABL. If turbulent mixing is too inefficient to smooth concentration fluctuations in the ABL, segregation of chemical species occurs. This effect is enhanced by organized circulations in the boundary layer and non uniform surface exchange of reactants. As mentioned in the introduction of this thesis, this segregation has been suggested in the literature as a possible cause of reduced reactivity. How much it affects the chemical production rate, compared to the calculations using mixed-layer averaged properties, is quantified by the intensity of segregation. In Chapter 5 this has been systematically studied for the isoprene-OH reaction using the DALES model under dynamical and chemical conditions that are representative for the Amazon rain forest. The resolved chemical pathways describe the essential reactions for the O_3–NO_x–VOC–HO_x system that is typical for a diurnal ABL over the Amazon rain forest.

As a general finding, the intensity of segregation cannot be taken as a constant since its magnitude is driven by both dynamical and chemical variables. This even holds when evaluating a single chemical reaction while the domain-averaged surface exchange and heat and moisture fluxes at the surface are kept constant. The segregation is shown to be dependent on the background wind (both magnitude and direction), the initial vertical distribution of

NO_x and, as examined by applying heterogeneous surface conditions, the horizontal distribution of the surface exchange of chemical species and the partitioning of sensible and latent heat fluxes over the terrain. This horizontal distribution of surface exchange and heat fluxes is chosen to be representative for adjacent patches that are alternatively forested and deforested. In the absence of free tropospheric NO_x, the intensity of segregation normally lies between -0.07 and -0.20 in our analysis, corresponding to a chemical reaction rate that is 7 to 20 % lower than the reaction rate that would be calculated from boundary-layer averaged concentrations. These results agree with indications from observational studies.

The lowest intensity of segregation magnitude occurs for completely homogeneous surface conditions without background wind. Wind and/or heterogeneous terrain induce large-scale circulations that affect the distribution of isoprene and OH and, consequently, the segregation between those two chemical species. It is demonstrated that weak differences in surface buoyancy flux counteract the segregation caused by heterogeneously distributed surface emissions of isoprene. This is due to the increased horizontal mixing. However, if the former differences are strong enough, an increase in the surface buoyancy flux amplitude results in enhanced (more negative) intensity of segregation. Larger length scales of the surface heterogeneity are always linked to stronger segregation. However, if these become to large this is not longer due to transport by large-scale circulations in the ABL, but due to the emergence of completely separated boundary-layers over the respective patches with uncoupled dynamics and chemistry. According to our large-eddy simulation results, this occurs for length scales larger than 16 times the boundary-layer height.

Although the intensities of segregations vary significantly for the isoprene-OH reaction between the various analysed numerical experiments, the OH concentration is hardly modified. The only exceptions are the numerical experiments with altered initial chemical concentrations (additional NO_x in the free troposphere) or such a large length scale that the boundary layers over the wet and dry patches start to separate. That the OH is less affected is caused by the increased amount of isoprene that compensates for the enhanced segregation. Consequently, the final chemical production rates are not significantly altered, explaining the satisfactory performance of mixed-layer models in reproducing atmospheric chemistry observations during diurnal convective conditions that is reported in the literature.

Finally, since measurement uncertainties, as well as uncertainties in the reaction rate coefficients, are comparable to the segregation induced modifications to chemical species concentrations, representing the intensity of segregation in chemistry-transport or climate models is not the solution to reconcile modelled and observed OH concentrations. If in the future, parametrizations are applied to strive for best model performance, the non-linear and interacting dependencies on the various driving variables have to be further investigated and taken into account.

7.1.3 Importance and representation of transport by shallow convection

During daytime conditions, atmospheric boundary layers over boreal and tropical forest often transition from clear to cloudy conditions. These clouds modify the UV radiation (by scattering) and the boundary-layer dynamics (see Table 5.1). In turn, these affect the chemical reactants in the sub-cloud layer. In the presence of shallow cumulus clouds, air mass is transported from the sub-cloud layer to the cloud layer. The resulting flow rate, referred to as mass-flux, consequently transports dynamical and chemical tracers to the cloud layer. In Chapter 6, the effect of this transport on chemical species concentrations in the sub-cloud layer is studied using DALES under conditions that are representative for the Amazon. In the absence of complete observational data sets, this still enables us to understand the impact of cloud dynamics on the spatial distribution of atmospheric reactants and to prepare strategies for future observational campaigns in the Amazon. In this analysis, again the essential reactions for the O_3–NO_x–VOC–HO_x system for a diurnal boundary layer over the Amazon rain forest are considered. In this study we focus on the direct effect of mass-flux transport. Therefore, the well-known influence of the kinematic mass flux on the evolution of the boundary layer height and entrainment velocity is not further evaluated.

For most chemical species, the impact of the mass-flux transport on the sub-cloud layer mixing ratio is relatively small (few % per hour), but there are important exceptions. For example, during the presence of active shallow cumulus clouds the impact of mass-flux transport on isoprene is on average -8.5 % per hour and at maximum magnitude -15 % per hour. This is a significant contribution to the total diurnal budget of isoprene.

The parametrizations that are needed to represent the mass-flux transport in chemistry-transport or climate models are assessed using numerical data from DALES. The results corroborate that previously published parametrizations for the dynamical variables (in particular specific humidity) are valid for the evaluated conditions as well. As a new aspect in this study, parametrizations are proposed that describe the mass-flux transport of atmospheric reactants. Up to now, only parametrizations have been derived for specific humidity. However, in contrast to the reactants, specific humidity is not significantly affected by chemical production or loss and is directly correlated to buoyancy and cloud characteristics. Therefore, differences in the parametrizations are to be expected. For many chemical species, the derived linear expressions to predict the mixing ratios in the cloud cores compare well with LES data. Exceptions are mainly reactants whose concentrations are significantly affected by the local UV radiation. The cause is that the UV radiation modification by the clouds temporarily alters the chemical equilibrium between some species, as confirmed by a numerical experiment in which the impact of clouds on the UV radiation is disabled. However, since these reactants are restored to their original equilibria in regions with undisturbed UV radiation, the derived parametrizations also suffice to represent the transport of those reactants from the sub-cloud

layer to the cloud layer by shallow cumulus convection. As a special case, important for the O_3–NO_x–VOC–HO_x system, the mass-flux transport of NO and NO_2 is still not well represented in the numerical experiment without UV radiation modification. It is shown that this is again caused by the modification of the local chemical equilibrium. For NO and NO_2, this is additionally significantly affected by the small-scale variability in the concentrations of ambient atmospheric compounds. However, the parametrizations do predict the transport of the generic species NO_x very well. This suffices for numerical models that aim to represent NO and NO_2, since the chemical partitioning is locally determined and independent of the transport.

The derived parametrizations for the mass-flux transport are shown to be dependent on initial and boundary conditions. This is demonstrated by applying heterogeneous surface forcings in the numerical DALES experiment, which change the characteristics of the clouds. For the examined conditions, the linear expressions in the various parametrizations are still valid if the proportionality factors are enhanced. Furthermore, since the factors remain of similar magnitude, the results of Chapter 6 suggest that for a first-order representation in chemistry-transport and climate models, the diagnosed parametrizations for mass-flux transport would still be an improvement.

7.2 Outlook

The findings in this thesis indicate that boundary-layer dynamics have a significant contribution to the evolution of mixed-layer averaged concentrations of atmospheric reactants. Therefore, in future observational campaigns that aim at measuring and analysing atmospheric chemistry, a good balance should be maintained between chemical and dynamical observations, both at the surface and in the atmosphere. First priority should be on representing the evolution of the boundary-layer height, which can be modelled or calculated using observations of the surface sensible and latent heat fluxes and vertical radiosonde profiles of the temperature and specific humidity. A second priority that arises from this study is to characterize the heterogeneity of the terrain as well as the characteristics of the background wind, since these conditions affect both the height of the ABL and the transport of chemical species in the mixed layer. A final recommendation for observational campaigns is to determine chemical reactant concentrations in the bulk of the atmospheric boundary layer, i.e. above the canopy and the atmospheric surface layer. The reason is that most numerical models do not predict the evolution of the chemical concentrations in the atmospheric surface layer, but at higher levels. In a convective boundary layer, chemical evolutions are governed by mixed-layer averaged mixing ratios, which are virtually equal to those in the bulk of the ABL. The significance of comparisons between observational data and model results and the validity

of applying those models to interpret the observations would increase if concentrations were known at equivalent heights.

A natural conclusion from this thesis is that numerical models that do not account for the boundary-layer height evolution are inaccurate in predicting the time evolution of chemical concentrations in a diurnal convective boundary layer. Chemistry box models or chemistry-transport models in which the ABL height is set to a fixed value should therefore be updated to include a reliable representation for the boundary-layer height. As the basic equations that predict boundary-layer growth are computationally inexpensive, the elementary representation of the evolution of a convectively well-mixed ABL, equal to the one used in the mixed-layer model that is employed in this study, can be calculated by those numerical models with negligible extra computational cost.

The mathematical expressions for the evolution of the boundary-layer height presented in this thesis offer the possibility to investigate the dependence of chemical reactants in a well-mixed convective boundary layer on different dynamical conditions (e.g. surface exchange and free tropospheric gradients of potential temperature, specific humidity and atmospheric reactants) analytically instead of needing numerical mixed-layer models. If the boundary-layer height dependence to e.g. the surface buoyancy flux is analytically determined and the dependence of the reactant mixing ratio on the boundary-layer height evolution is known, the influence of the buoyancy flux on the reactant mixing ratio can be expressed analytically as well. Since these equations are continuous instead of being characterized by a limited amount of samples, there is no limit in the range of the examined driving variables. Another advantage of these derived analytical solutions is that they make it easier to identify distinct regimes in which different processes are most significant.

In contrast to the literature, this study indicates that the chemical reaction rates are not affected that much by segregation between chemical species that it can explain discrepancies between numerical models and observations. The presented results further suggest that the resulting changes in chemical concentrations are of the same order as uncertainties in the observations. Furthermore, the impact of segregation heavily depends on the evaluated conditions. Since the impacts of different dynamical and chemical conditions interact and not all dependencies are investigated, a parametrization for the intensities of segregation is not yet complete. Therefore, we do not advice to put priority on representing the intensity of segregation between chemical species in chemistry-transport and climate models. However, as shallow cumulus convection reinforces the large-scale dynamical structures in the ABL (see Chapter 6) and those structures promote segregation, an obvious extension of the research in Chapter 5 would be to evaluate the dependency of the intensity of segregation on the cloud conditions. Other possible dependencies of segregation that should be investigated include the background concentrations of the various atmospheric reactants, UV radiation and the response of interactive land surfaces on clouds and induced mesoscale circulations. Such a

sensitivity study should not be limited to varying one condition at a time, but should also investigate how the intensity of segregation behaves if multiple conditions are simultaneously changed. Under specific conditions, the impact of segregation could be strong enough that it has to be taken into account.

As a direct application of Chapter 6, the derived parametrizations for the transport of atmospheric reactants from the sub-cloud layer to the cloud layer by shallow cumulus convection can be applied to and tested in chemistry-transport and climate models. This process, which can have a significant impact on the sub-cloud layer reactant mixing ratios, is well represented by those parametrizations. As an intermediate step we propose a pilot study, implementing the representation of transport by shallow cumulus convection in the more conceptual mixed-layer model. Although this study has demonstrated that the parametrizations need different proportionality factors for heterogeneous surface conditions, the evaluated numerical experiments suggest that the changes are relatively small and that the standard parametrizations still suffice as a first order estimate. However, currently it is still an open question which dynamical and chemical conditions affect the parametrizations and how much these parametrizations can deviate. We therefore recommend sensitivity studies with a LES model, similar to those presented in Chapter 5, to investigate whether adapted expressions for the parametrizations are needed to account for the influence of the various chemical and dynamical conditions. These studies would include the sensitivities to different concentrations of chemical species and background wind and the influence of surface heterogeneity for different length scales and different distributions of reactant exchange and heat fluxes at the surface.

All analyses in this study pertain to academic conditions, albeit inspired by observational data. The advantage of this is that it enables us to investigate the influences of different processes that would be obscured for more realistic conditions. Therefore, an obvious extension of the presented study would be to stepwise increase complexity until, ultimately, realistic conditions are reached. A first step would be to include the height dependency of the air density, which is commonly considered to be constant in the ABL in the employed numerical models. This addition, which is now included in the latest version of the DALES model, is necessary to eventually study the transition from shallow to deep convection and its impact on sub-cloud layer reactants.

Other research that would be recommended based on this study relates to the interaction of processes at different scales. The analyses under heterogeneous surface conditions (Chapters 5 and 6) have demonstrated that a non-uniform distribution of surface heat and moisture fluxes induces large-scale circulations that link the boundary-layer dynamics and chemistry to their mesoscale properties. As this transport can occur at scales that are larger than the typical domain size in a large-eddy simulation model and smaller than the grid resolution in chemistry-transport or climate models, this effect is not yet studied in detail, which could

be done by employing LES models with large enough domain sizes. Knowledge about this scale interaction would improve the understanding of the segregation dependency on surface heterogeneity length scales.

Finally, considering the recent PhD dissertations of Joost aan de Brugh and Ruud Janssen, we recommend to involve the impact of aerosols in future studies. While not investigated in this study, aerosols are known to be important for UV radiation, the surface energy balance and cloud dynamics, as well as the thermal structure of the ABL. Therefore, we hypothesize that aerosols can be important for the observed large-scale structures that are observed in this study for heterogeneous surface forcings, background wind and/or shallow cumulus convection. In turn, the transport by these large-scale structures will influence the aerosol distribution. Chemical reactants are affected by these large-scale dynamics and by the aerosols, but in turn determine the aerosol configuration as well. Therefore, adding aerosols to the analyses would result in a coupled system with various feedbacks that are not yet evaluated in this project.

References

Andreae, M. O., Artaxo, P., Brandao, C., Carswell, F. E., Ciccioli, P., da Costa, A. L., Culf, A. D., Esteves, J. L., Gash, J. H. C., Grace, J., Kabat, P., Lelieveld, J., Malhi, Y., Manzi, A. O., Meixner, F. X., Nobre, A. D., Nobre, C., Ruivo, M. L. P., Silva-Dias, M. A., Stefani, P., Valentini, R., von Jouanne, J., and Waterloo, M. J.: Biogeochemical cycling of carbon, water, energy, trace gases, and aerosols in Amazonia: The LBA-EUSTACH experiments, J. Geophys. Res., 107, 8066, doi:10.1029/2001JD000524, 2002.

Angevine, W. M., Jiang, H., and Mauritsen, T.: Performance of an Eddy Diffusivity-Mass Flux Scheme for Shallow Cumulus Boundary Layers, Mon. Wea. Rev., 138, 2895–2912, doi:10.1175/2010MWR3142.1, 2010.

Atkinson, R., Baulch, D. L., Cox, R. A., Crowley, J. N., Hampson, R. F., Hynes, R. G., Jenkin, M. E., Rossi, M. J., and Troe, J.: Evaluated kinetic and photochemical data for atmospheric chemistry: Volume II - gas phase reactions of organic species, Atmos. Chem. Phys., 6, 3625–4055, doi:10.5194/acp-6-3625-2006, 2006.

Aubinet, M., Heinesch, B., and Yernaux, M.: Horizontal and vertical CO_2 advection in a sloping forest, Bound.-Lay. Meteorol., 108, 397–417, doi:10.1023/A:1024168428135, 2003.

Auger, L. and Legras, B.: Chemical segregation by heterogeneous emissions, Atmos. Environ., 41, 2302–2318, doi:10.1016/j.atmosenv.2006.11.032, 2007.

Avissar, R. and Liu, Y.: Three-dimensional numerical study of shallow convective clouds and precipitation induced by land surface forcing, J. Geophys. Res., 101(D3), 7499–7518, doi:10.1029/95JD03031, 1996.

Avissar, R. and Schmidt, T.: An Evaluation of the Scale at which Ground-Surface Heat Flux Patchiness Affects the Convective Boundary Layer Using Large-Eddy Simulations, J. Atmos. Sci., 55, 2666–2689, doi:10.1175/1520-0469(1998)055<2666:AEOTSA>2.0.CO;2, 1998.

Baldocchi, D., Falge, E., Gu, L., Olson, R., Hollinger, D., Running, S., Anthoni, P., Bernhofer, C., Davis, K., Evans, R., Fuentes, J., Goldstein, A., Katul, G., Law, B., Lee,

X., Malhi, Y., Meyers, T., Munger, W., Oechel, W., Paw U, K. T., Pilegaard, K., Schmid, H. P., Valentini, R., Verma, S., Vesala, T., Wilson, K., and Wofsy, S.: FLUXNET: A New Tool to Study the Temporal and Spatial Variability of Ecosystem-Scale Carbon Dioxide, Water Vapor, and Energy Flux Densities, B. Am. Meteorol. Soc., 82, 2415–2434, doi:10.1175/1520-0477(2001)082<2415:FANTTS>2.3.CO;2, 2001.

Barr, A. G. and Betts, A. K.: Radiosonde boundary layer budgets above a boreal forest, J. Geophys. Res., 102, 29 205–29 212, doi:10.1029/97JD01105, 1997.

Betts, A. K.: Non-precipitating cumulus convection and its parameterization, Q. J. Roy. Meteor. Soc., 99, 178–196, doi:10.1002/qj.49709941915, 1973.

Bianco, L., Djalalova, I. V., King, C. W., and Wilczak, J. M.: Diurnal Evolution and Annual Variability of Boundary-Layer Height and Its Correlation to Other Meteorological Variables in California's Central Valley, Bound.-Lay. Meteorol., 140, 491–511, doi:10.1007/s10546-011-9622-4, 2011.

Brown, A. R., Cederwall, R. T., Chlond, A., Duynkerke, P. G., Golaz, J.-C., Khairoutdinov, M., Lewellen, D. C., Lock, A. P., MacVean, M. K., Moeng, C.-H., Neggers, R. A. J., Siebesma, A. P., and Stevens, B.: Large-Eddy simulation of the diurnal cycle of shallow cumulus convection over land, Q. J. Roy. Meteor. Soc., 128, 1075–1093, doi:10.1256/003590002320373210, 2002.

Butler, T. M., Taraborrelli, D., Brühl, C., Fischer, H., Harder, H., Martinez, M., Williams, J., Lawrence, M. G., and Lelieveld, J.: Improved simulation of isoprene oxidation chemistry with the ECHAM5/MESSy chemistry-climate model: lessons from the GABRIEL airborne field campaign, Atmos. Chem. Phys., 8, 4529–4546, doi:10.5194/acp-8-4529-2008, 2008.

Carson, D. J.: The development of a dry inversion-capped convectively unstable boundary layer, Q. J. Roy. Meteor. Soc., 99, 450–467, doi:10.1002/qj.49709942105, 1973.

Courault, D., Drobinski, P., Brunet, Y., Lacarrere, P., and Talbot, C.: Impact of surface heterogeneity on a buoyancy-driven convective boundary layer in light winds, Bound.-Lay. Meteorol., 124, 383–403, doi:10.1007/s10546-007-9172-y, 2007.

Cuijpers, J. W. M. and Duynkerke, P. G.: Large Eddy Simulation of Trade Wind Cumulus Clouds, J. Atmos. Sci., 50, 3894 – 3907, doi:10.1175/1520-0469(1993)050<3894:LESOTW>2.0.CO;2, 1993.

Culf, A. D., Fisch, G., Malhi, Y., and Nobre, A. D.: The influence of the atmospheric boundary layer on carbon dioxide concentrations over a tropical forest, Agr. For. Meteorol., 85, 149–158, doi:10.1016/S0168-1923(96)02412-4, 1997.

da Rocha, H. R., Manzi, A. O., Cabral, O. M., Miller, S. D., Goulden, M. L., Saleska, S. R., R.-Coupe, N., Wofsy, S. C., Borma, L. S., Artaxo, P., Vourlitis, G., Nogueira, J. S., Cardoso, F. L., Nobre, A. D., Kruijt, B., Freitas, H. C., von Randow, C., Aguiar, R. G., and Maia, J. F.: Patterns of water and heat flux across a biome gradient from tropical forest to savanna in Brazil, J. Geophys. Res., 114, 1–8, doi:10.1029/2007JG000640, 2009.

Danckwerts, P. V.: The definition and measurement of some characteristics of mixtures, Appl. Sci. Res., 3, 279–296, doi:10.1007/BF03184936, 1952.

Davis, K. J., Lenschow, D. H., and Zimmerman, P. R.: Biogenic non-methane hydrocarbon emissions estimated from tethered balloon observations, J. Geophys. Res., 99, 25 587–25 598, doi:10.1029/94JD02009, 1994.

Davis, K. J., Lenschow, D. H., Oncley, S. P., Kiemle, C., Ehret, G., Giez, A., and Mann, J.: Role of entrainment in surface-atmosphere interactions over the boreal forest, J. Geophys. Res., 102, 29 219–29 230, doi:10.1029/97JD02236, 1997.

de Bruin, H. A. R.: A Model for the Priestley-Taylor Parameter α, J. Clim. Appl. Meteorol., 22, 572–578, doi:10.1175/1520-0450(1983)022<0572:AMFTPT>2.0.CO;2, 1983.

Deardorff, J. W.: Three-dimensional numerical modeling of the planetary boundary layer, in: Workshop on Meteorology, edited by Haugen, D. A., pp. 271–311, Amer. Meteorol. Soc., 1973.

Dlugi, R., Berger, M., Zelger, M., Hofzumahaus, A., Siese, M., Holland, F., Wisthaler, A., Grabmer, W., Hansel, A., Koppmann, R., Kramm, G., Möllmann-Coers, and Knaps, A.: Turbulent exchange and segregation of HO_x radicals and volatile organic compounds above a deciduous forest, Atmos. Chem. Phys., 10, 6215–6235, doi:10.5194/acp-10-6215-2010, 2010.

Donaldson, C. d. and Hilst, G. R.: Effect of inhomogeneous mixing on atmospheric photochemical reactions, Environ. Sci. Technol., 6, 812–816, doi:10.1021/es60068a004, 1972.

Dosio, A.: Turbulent dispersion in the Atmospheric Convective Boundary Layer, Ph.D. thesis, Wageningen University, 2005.

Dosio, A., Vilà-Guerau de Arellano, J., Holtslag, A. A. M., and Builtjes, P. J. H.: Dispersion of a Passive Tracer in Buoyancy- and Shear-Driven Boundary Layers, J. Appl. Meteor., 42, 1116–1130, doi:10.1175/1520-0450(2003)042<1116:DOAPTI>2.0.CO;2, 2003.

Driedonks, A. G. M.: Models and observations of the growth of the atmospheric boundary layer, Bound.-Lay. Meteorol., 23, 283–306, doi:10.1007/BF00121117, 1982a.

Driedonks, A. G. M.: Sensitivity analysis of the equations for a convectively mixed layer, Bound.-Lay. Meteorol., 22, 475–580, doi:10.1007/BF00124706, 1982b.

Ek, M. B. and Holtslag, A. A. M.: Influence of Soil Moisture on Boundary Layer Cloud Development, J. Hydrometeor., 5, 86–99, doi:10.1175/1525-7541(2004)005<0086:IOSMOB>2.0.CO;2, 2004.

Fisch, G., Tota, J., Machado, L. A. T., Silva Dias, M. A. F., Lyra, R. F. d. F., Nobre, C. A., Dolman, A. J., and Gash, J. H. C.: The convective boundary layer over pasture and forest in Amazonia, Theor. Appl. Climatol., 78, 47–59, doi:10.1007/s00704-004-0043-x, 2004.

Fitzjarrald, D. R. and Lenschow, D. H.: Mean concentration and flux profiles for chemically reactive species in the atmospheric surface layer, Atmos. Environ., 17, 2505–2512, doi:10.1016/0004-6981(83)90076-8, 1983.

Fuentes, J. D., Lerdau, M., Atkinson, R., Baldocchi, D., Bottenheim, J. W., Ciccioli, P., Lamb, B., Geron, C., Gu, L., Guenther, A., Sharkey, T. D., and Stockwell, W.: Biogenic Hydrocarbons in the Atmospheric Boundary Layer: A Review, Bull. Amer. Meteor. Soc., 81, 1537–1575, doi:10.1175/1520-0477(2000)081<1537:BHITAB>2.3.CO;2, 2000.

Galmarini, S., Duynkerke, P. G., and Vilà-Guerau de Arellano, J.: Evolution of Nitrogen Oxide Chemistry in the Nocturnal Boundary Layer, J. Appl. Meteor., 36, 943–957, doi:10.1175/1520-0450(1997)036<0943:EONOCI>2.0.CO;2, 1997.

Ganzeveld, L., Eerdekens, G., Feig, G., Fischer, H., Harder, H., Königstedt, R., Kubistin, D., Martinez, M., Meixner, F. X., Scheeren, H. A., Sinha, V., Taraborrelli, D., Williams, J., Vilà-Guerau de Arellano, J., and Lelieveld, J.: Surface and boundary layer exchanges of volatile organic compounds, nitrogen oxides and ozone during the GABRIEL campaign, Atmos. Chem. Phys., 8, 6223–6243, doi:10.5194/acp-8-6223-2008, 2008.

Ganzeveld, L., Bouwman, L., Stehfest, E., van Vuuren, D. P., Eickhout, B., and Lelieveld, J.: Impact of future land use and land cover changes on atmospheric chemistry-climate interactions, J. Geophys. Res., 115, D23 301, doi:10.1029/2010JD014041, 2010.

Ganzeveld, L. N., Lelieveld, J., Dentener, F. J., Krol, M. C., and Roelofs, G.-J.: Atmosphere-biosphere trace gas exchanges simulated with a single-column model, J. Geophys. Res., 107, 4297, doi:10.1029/2001JD000684, 2002.

Gao, W., Wesely, M. L., and Doskey, P. V.: Numerical Modeling of the Turbulent Diffusion and Chemistry of NO_x, O_3, Isoprene, and Other Reactive Trace Gases in and Above a Forest Canopy, J. Geophys. Res., 98, 18 339–18 353, doi:10.1029/93JD01862, 1993.

Garcia-Carreras, L., Parker, D. J., Taylor, C. M., Reeves, C. E., and Murphy, J. G.: Impact of mesoscale vegetation heterogeneities on the dynamical and thermodynamic properties of the planetary boundary layer, J. Geophys. Res., 115, D03 102, doi:10.1029/2009JD012811, 2010.

Garratt, J. R.: The atmospheric boundary layer, Cambridge University Press, 1992.

Gentine, P., Betts, A. K., Lintner, B. R., Findell, K. L., van Heerwaarden, C. C., and D'Andrea, F.: A Probabilistic Bulk Model of Coupled Mixed Layer and Convection. Part II: Shallow Convection Case, J. Atmos. Sci., 70, 1557–1576, doi:10.1175/JAS-D-12-0146.1, 2013.

Gibert, F., Schmidt, M., Cuesta, J., Ciais, P., Ramonet, M., Xueref, I., Larmanou, E., and Flamant, P. H.: Retrieval of average CO_2 fluxes by combining in situ CO_2 measurements and backscatter lidar information, J. Geophys. Res., 112, D10 301, doi:doi:10.1029/2006JD008190, 2007.

Górska, M., Vilà-Guerau de Arellano, J., LeMone, M. A., and van Heerwaarden, C. C.: Mean and Flux Horizontal Variability of Virtual Potential Temperature, Moisture, and Carbon Dioxide: Aircraft Observations and LES Study, Mon. Wea. Rev., 136, 4435–4451, doi:10.1175/2008MWR2230.1, 2008.

Gregory, D. and Rowntree, P. R.: A mass flux scheme with representation of cloud ensemble characteristics and stability-dependent closure, Mon. Wea. Rev., 118, 1483–1506, doi:10.1175/1520-0493(1990)118<1483:AMFCSW>2.0.CO;2, 1990.

Guenther, A., Karl, T., Harley, P., Wiedinmyer, C., Palmer, P. I., and Geron, C.: Estimates of global terrestrial isoprene emissions using MEGAN (Model of Emissions of Gases and Aerosols from Nature), Atmos. Chem. Phys., 6, 3181–3210, doi:10.5194/acp-6-3181-2006, 2006.

Hahn, C. J. and Warren, S. G.: A Gridded Climatology of Clouds over Land (1971-96) and Ocean (1954-97) from Surface Observations Worldwide. Numeric Data Package NDP-026E, CDIAC, Department of Energy, Oak Ridge, Tennessee, doi:10.3334/CDIAC/cli.ndp026e, 2007.

Hari, P. and Kulmala, M.: Station for measuring ecosystem-atmosphere relations (SMEAR II), Boreal Env. Res., 10, 315–322, 2005.

Heus, T. and Jonker, H. J. J.: Subsiding Shells around Shallow Cumulus Clouds, J. Atmos. Sci., 65, 1003–1018, doi:10.1175/2007JAS2322.1, 2008.

Heus, T., van Heerwaarden, C. C., Jonker, H. J. J., Siebesma, A. P., Axelsen, S., van den Dries, K., Geoffroy, O., Moene, A., Pino, D., de Roode, S. R., and Vilà-Guerau de Arellano, J.: Formulation of the Dutch Atmospheric Large-Eddy Simulation (DALES) and overview of its applications, Geosci. Model Dev., 3, 415–444, doi:10.5194/gmd-3-415-2010, 2010.

Jonker, H. J. J., Duynkerke, P. G., and Cuijpers, J. W.: Mesoscale Fluctuations in Scalars Generated by Boundary Layer Convection, J. Atmos. Sci., 56, 801–808, doi:10.1175/1520-0469(1999)056<0801:MFISGB>2.0.CO;2, 1999.

Jonker, H. J. J., Vilà-Guerau de Arellano, J., and Duynkerke, P. G.: Characteristic Length Scales of Reactive Species in a Convective Boundary Layer, J. Atmos. Sci., 61, 41–56, doi:10.1175/1520-0469(2004)061<0041:CLSORS>2.0.CO;2, 2004.

Jonker, H. J. J., Heus, T., and Sullivan, P. P.: A refined view of vertical mass transport by cumulus convection, Geophys. Res. Lett., 35, L07 810, doi:10.1029/2007GL032606, 2008.

Junninen, H., Lauri, A., Keronen, P., Aalto, P., Hiltunen, V., Hari, P., and Kulmala, M.: Smart-SMEAR: on-line data exploration and visualization tool for SMEAR stations, Boreal Env. Res., 14, 447–457, 2009.

Kaimal, J. C., Wyngaard, J. C., Haugen, D. A., Coté, O. R., and Izumi, Y.: Turbulence Structure in the Convective Boundary Layer, J. Atmos. Sci., 33, 2152–2169, doi:10.1175/1520-0469(1976)033<2152:TSITCB>2.0.CO;2, 1976.

Karl, T., Guenther, A., Yokelson, R., Greenberg, J., Potosnak, M., Blake, D. R., and Artaxo, P.: The tropical forest and fire emissions experiment: Emission, chemistry, and transport of biogenic volatile organic compounds in the lower atmosphere over Amazonia, J. Geophys. Res., 112, D18 302, doi:10.1029/2007JD008539, 2007.

Kesselmeier, J. and Staudt, M.: Biogenic Volatile Organic Compounds (VOC): An Overview on Emission, Physiology and Ecology, J. Atmos. Chem., 33, 23–88, doi:10.1023/A:1006127516791, 1999.

Kim, H.-J., Noh, Y., and Raasch, S.: Interaction between wind and temperature fields in the planetary boundary layer for a spatially heterogeneous surface heat flux, Bound.-Lay. Meteorol., 111, 225–246, doi:10.1023/B:BOUN.0000016471.75325.75, 2004.

Kim, S.-W., Barth, M. C., and Trainer, M.: Influence of fair-weather cumulus clouds on isoprene chemistry, J. Geophys. Res., 117, D10 302, doi:10.1029/2011JD017099, 2012.

Kley, D.: Tropospheric Chemistry and Transport, Science, 276, 1043–1044, doi:10.1126/science.276.5315.1043, 1997.

Krol, M. C., Molemaker, M. J., and Vilà-Guerau de Arellano, J.: Effects of turbulence and heterogeneous emissions on photochemically active species in the convective boundary layer, J. Geophys. Res., 105, 6871–6884, doi:10.1029/1999JD900958, 2000.

Kulmala, M., Hämeri, K., Aalto, P. P., Mäkelä, J. M., Pirjola, L., Douglas Nilsson, E., Buzorius, G., Rannik, U., Dal Maso, M., Seidl, W., Hoffmann, T., Janson, R., Hansson, H.-C., Viisanen, Y., Laaksonen, A., and O'Dowd, C. D.: Overview of the international project on biogenic aerosol formation in the boreal forest (BIOFOR), Tellus B, 53, 324–343, doi:10.1034/j.1600-0889.2001.530402.x, 2001.

Lelieveld, J., Butler, T. M., Crowley, J. N., Dillon, T. J., Fischer, H., Ganzeveld, L., Harder, H., Lawrence, M. G., Martinez, M., Taraborrelli, D., and Williams, J.: Atmospheric oxidation capacity sustained by a tropical forest, Nature, 452, 737–740, doi:10.1038/nature06870, 2008.

LeMone, M. A. and Pennell, W. T.: The Relationship of Trade Wind Cumulus Distribution to Subcloud Layer Fluxes and Structure, Mon. Wea. Rev., 104, 524–539, doi:10.1175/1520-0493(1976)104<0524:TROTWC>2.0.CO;2, 1976.

LeMone, M. A., Grossman, R. L., Chen, F., Ikeda, K., and Yates, D.: Choosing the Averaging Interval for Comparison of Observed and Modeled Fluxes along Aircraft Transects over a Heterogeneous Surface, J. Hydrometeor., 4, 179–195, doi:10.1175/1525-7541(2003)4<179:CTAIFC>2.0.CO;2, 2003.

Lilly, D. K.: Models of cloud-topped mixed-layer under a strong inversion, Q. J. Roy. Meteor. Soc., 94, 292–309, doi:10.1002/qj.49709440106, 1968.

Madronich, S.: Photodissociation in the atmosphere: 1. Actinic flux and the effects of ground reflections and clouds, J. Geophys. Res., 92, 9740–9752, doi:10.1029/JD092iD08p09740, 1987.

Mahrt, L.: Surface Heterogeneity and Vertical Structure of the Boundary Layer, Bound.-Lay. Meteorol., 96, 33–62, doi:10.1023/A:1002482332477, 2000.

Mammarella, I., Launiainen, S., Gronholm, T., Keronen, P., Pumpanen, J., Rannik, U., and Vesala, T.: Relative Humidity Effect on the High-Frequency Attenuation of Water Vapor Flux Measured by a Closed-Path Eddy Covariance System, J. Atmos. Ocean. Tech., 26, 1856–1866, doi:10.1175/2009JTECHA1179.1, 2009.

Neggers, R., Stevens, B., and Neelin, J. D.: A simple equilibrium model for shallow-cumulus-topped mixed layers, Theor. Comput. Fluid. Dyn., 20, 305–322, doi:10.1007/s00162-006-0030-1, 2006.

Neggers, R. A. J., Duynkerke, P. G., and Rodts, S. M. A.: Shallow cumulus convection: A validation of large-eddy simulation against aircraft and Landsat observations, Q. J. Roy. Meteor. Soc., 129, 2671–2696, doi:10.1256/qj.02.93, 2003.

Neggers, R. A. J., Siebesma, A. P., Lenderink, G., and Holtslag, A. A. M.: An evaluation of mass flux closures for diurnal cycles of shallow cumulus, Mon. Wea. Rev., 132, 2525–2538, doi:10.1175/MWR2776.1, 2004.

Neggers, R. A. J., Stevens, B., and Neelin, J. D.: Variance scaling in shallow-cumulus-topped mixed layers, Q. J. Roy. Meteor. Soc., 133, 1629–1641, doi:10.1002/qj.105, 2007.

Nieuwstadt, F. T. M. and Brost, R. A.: The Decay of Convective Turbulence, J. Atmos. Sci., 43, 532 – 545, doi:10.1175/1520-0469(1986)043<0532:TDOCT>2.0.CO;2, 1986.

Nilsson, E. D., Rannik, U., Kulmala, M., Buzorius, G., and O'Dowd, C. D.: Effets of continental boundary layer evolution, convection, turbulence and entrainment, on aerosol formation, Tellus B, 53, 441–461, doi:10.1034/j.1600-0889.2001.530409.x, 2001.

Ookouchi, Y., Segal, M., Kessler, C., and Pielke, R. A.: Evaluation of Soil Moisture Effects on the Generation and Modification of Mesoscale Circulations, Mon. Wea. Rev., 112, 2281–2292, doi:10.1175/1520-0493(1984)112<2281:EOSMEO>2.0.CO;2, 1984.

Ouwersloot, H. G. and Vilà-Guerau de Arellano, J.: Analytical Solution for the Convectively-Mixed Atmospheric Boundary Layer, Bound.-Lay. Meteorol., 148, 557–583, doi:10.1007/s10546-013-9816-z, 2013a.

Ouwersloot, H. G. and Vilà-Guerau de Arellano, J.: Amendment to "Analytical Solution for the Convectively-Mixed Atmospheric Boundary Layer": inclusion of subsidence, Bound.-Lay. Meteorol., 148, 585–591, doi:10.1007/s10546-013-9837-7, 2013b.

Ouwersloot, H. G., Vilà-Guerau de Arellano, J., van Heerwaarden, C. C., Ganzeveld, L. N., Krol, M. C., and Lelieveld, J.: The significance of species segregation for Amazonian Chemistry, in: 19th Symposium on Boundary Layers and Turbulence/29th Conference on Agricultural and Forest Meteorology, AMS, extended abstract, 2010.

Ouwersloot, H. G., Vilà-Guerau de Arellano, J., van Heerwaarden, C. C., Ganzeveld, L. N., Krol, M. C., and Lelieveld, J.: On the segregation of chemical species in a clear boundary layer over heterogeneous land surfaces, Atmos. Chem. Phys., 11, 10 681–10 704, doi:10.5194/acp-11-10681-2011, 2011.

Ouwersloot, H. G., Vilà-Guerau de Arellano, J., Nölscher, A. C., Krol, M. C., Ganzeveld, L. N., Breitenberger, C., Mammarella, I., Williams, J., and Lelieveld, J.:

Characterization of a boreal convective boundary layer and its impact on atmospheric chemistry during HUMPPA-COPEC-2010, Atmos. Chem. Phys., 12, 9335–9353, doi:10.5194/acp-12-9335-2012, 2012.

Patton, E. G., Sullivan, P. P., and Moeng, C.-H.: The Influence of Idealized Heterogeneity on Wet and Dry Planetary Boundary Layers Coupled to the Land Surface, J. Atmos. Sci., 62, 2078–2097, doi:10.1175/JAS3465.1, 2005.

Petersen, A. C., Beets, C., van Dop, H., Duynkerke, P. G., and Siebesma, A. P.: Mass-Flux Characteristics of Reactive Scalars in the Convective Boundary Layer, J. Atmos. Sci., 56, 37–56, doi:10.1175/1520-0469(1999)056<0037:MFCORS>2.0.CO;2, 1999.

Pino, D., Vilà-Guerau de Arellano, J., and Duynkerke, P. G.: The Contribution of Shear to the Evolution of a Convective Boundary Layer, J. Atmos. Sci., 60, 1913–1926, doi:10.1175/1520-0469(2003)060<1913:TCOSTT>2.0.CO;2, 2003.

Pino, D., Vilà-Guerau de Arellano, J., Peters, W., Schröter, J., van Heerwaarden, C. C., and Krol, M. C.: A conceptual framework to quantify the influence of convective boundary layer development on carbon dioxide mixing ratios, Atmos. Chem. Phys., 12, 2969–2985, doi:10.5194/acp-12-2969-2012, 2012.

Porporato, A.: Atmospheric Boundary-Layer Dynamics with Constant Bowen Ratio, Bound.-Lay. Meteorol., 132, 227–240, doi:10.1007/s10546-009-9400-8, 2009.

Pugh, T. A. M., MacKenzie, A. R., Hewitt, C. N., Langford, B., Edwards, P. M., Furneaux, K. L., Heard, D. E., Hopkins, J. R., Jones, C. E., Karunaharan, A., Lee, J., Mills, G., Misztal, P., Moller, S., Monks, P. S., and Whalley, L. K.: Simulating atmospheric composition over a South-East Asian tropical rainforest: performance of a chemistry box model, Atmos. Chem. Phys., 10, 279–298, doi:10.5194/acp-10-279-2010, 2010a.

Pugh, T. A. M., MacKenzie, A. R., Langford, B., Nemitz, E., Misztal, P. K., and Hewitt, C. N.: The influence of small-scale variations in isoprene concentrations on atmospheric chemistry over a tropical rainforest, Atmos. Chem. Phys. Discuss., 10, 18 197–18 234, doi:10.5194/acpd-10-18197-2010, 2010b.

Pugh, T. A. M., MacKenzie, A. R., Langford, B., Nemitz, E., Misztal, P. K., and Hewitt, C. N.: The influence of small-scale variations in isoprene concentrations on atmospheric chemistry over a tropical rainforest, Atmos. Chem. Phys., 11, 4121–4134, doi:10.5194/acp-11-4121-2011, 2011.

Raasch, S. and Harbusch, G.: An analysis of secondary circulations and their effects caused by small-scale surface inhomogeneities using large-eddy simulation, Bound.-Lay. Meteorol., 101, 31–59, doi:10.1023/A:1019297504109, 2001.

Raupach, M. R.: Equilibrium Evaporation and the Convective Boundary Layer, Bound.-Lay. Meteorol., 96, 107–142, doi:10.1023/A:1002675729075, 2000.

Schumann, U.: Large-Eddy Simulation of Turbulent Diffusion with Chemical Reactions in the Convective Boundary Layer, Atmos. Environ., 23, 1713–1727, doi:10.1016/0004-6981(89)90056-5, 1989.

Sellers, P. J., Hall, F. G., Kelly, R. D., Black, A., Baldocchi, D., Berry, J., Ryan, M., Ranson, K. J., Crill, P. M., Lettenmaier, D. P., Margolis, H., Cihlar, J., Newcomer, J., Fitzjarrald, D., Jarvis, P. G., Gower, S. T., Halliwell, D., Williams, D., Goodison, B., Wickland, D. E., and Guertin, F. E.: BOREAS in 1997: Experiment overview, scientific results, and future directions, J. Geophys. Res., 102, 28 731–28 769, doi:10.1029/97JD03300, 1997.

Siebesma, A. P. and Cuijpers, J. W.: Evaluation of Parametric Assumptions for Shallow Cumulus Convection, J. Atmos. Sci., 52, 650–666, doi:10.1175/1520-0469(1995)052<0650:EOPAFS>2.0.CO;2, 1995.

Sitch, S., Cox, P. M., Collins, W. J., and Huntingford, C.: Indirect radiative forcing of climate change through ozone effects on the land-carbon sink, Nature, 448, 791–794, doi:10.1038/nature06059, 2007.

Soares-Filho, B. S., Nepstad, D. C., Curran, L. M., Cerqueira, G. C., Garcia, R. A., Ramos, C. A., Voll, E., McDonald, A., Lefebvre, P., and Schlesinger, P.: Modelling conservation in the Amazon basin, Nature, 440, 520–523, doi:10.1038/nature04389, 2006.

Stensrud, D. J.: Elevated Residual Layers and Their Influence on Surface Boundary-Layer Evolution, J. Atmos. Sci., 50, 2284–2293, doi:10.1175/1520-0469(1993)050<2284:ERLATI>2.0.CO;2, 1993.

Stull, R. B.: An Introduction to Boundary Layer Meteorology, Kluwer Academic Publishers, 1988.

Sullivan, P. P., Moeng, C.-H., Stevens, B., Lenschow, D. H., and Mayor, S. D.: Structure of the Entrainment Zone Capping the Convective Atmospheric Boundary Layer, J. Atmos. Sci., 55, 3042–3064, doi:10.1175/1520-0469(1998)055<3042:SOTEZC>2.0.CO;2, 1998.

Sykes, R. I., Henn, D. S., Parker, S. F., and Lewellen, W. S.: Large-eddy simulation of a turbulent reacting plume, Atmos. Environ., 26A, 2565–2574, doi:10.1016/0960-1686(92)90109-X, 1992.

Tan, D., Faloona, I., Simpas, J. B., Brune, W., Shepson, P. B., Couch, T. L., Sumner, A. L., Carroll, M. A., Thornberry, T., Apel, E., Riemer, D., and Stockwell, W.: HO_x budgets in a

deciduous forest: Results from the PROPHET summer 1998 campaign, J. Geophys. Res., 106, 24 407–24 427, doi:10.1029/2001JD900016, 2001.

Tennekes, H.: A Model for the Dynamics of the Inversion Above a Convective Boundary Layer, J. Atmos. Sci., 30, 558–567, doi:10.1175/1520-0469(1973)030<0558:AMFTDO>2.0.CO;2, 1973.

Tennekes, H. and Driedonks, A. G. M.: Basic Entrainment Equations for the Atmospheric Boundary Layer, Bound.-Lay. Meteorol., 20, 515–531, doi:10.1007/BF00122299, 1981.

Tiedtke, M.: A comprehensive mass flux scheme for cumulus parameterization in large-scale models, Mon. Wea. Rev., 117, 1779–1800, doi:10.1175/1520-0493(1989)117<1779:ACMFSF>2.0.CO;2, 1989.

Toor, H. L.: Turbulent Mixing of Two Species with and without Chemical Reactions, Ind. Eng. Chem. Fundamen., 8, 655–659, doi:10.1021/i160032a009, 1969.

van Driel, R. and Jonker, H. J. J.: Convective Boundary Layers Driven by Nonstationary Surface Heat Fluxes, J. Atmos. Sci., 68, 727–738, doi:10.1175/2010JAS3643.1, 2011.

van Heerwaarden, C. C. and Vilà-Guerau de Arellano, J.: Relative Humidity as an Indicator for Cloud Formation over Heterogeneous Land Surfaces, J. Atmos. Sci., 65, 3263–3277, doi:10.1175/2008JAS2591.1, 2008.

van Heerwaarden, C. C., Vilà-Guerau de Arellano, J., Gounou, A., Guichard, F., and Couvreux, F.: Understanding the Daily Cycle of Evapotranspiration: A Method to Quantify the Influence of Forcings and Feedbacks, J. Hydrometeor., 11, 1405–1422, doi:10.1175/2010JHM1272.1, 2010.

van Stratum, B. J. H., Vilà-Guerau de Arellano, J., Ouwersloot, H. G., van den Dries, K., van Laar, T. W., Martinez, M., Lelieveld, J., Diesch, J.-M., Drewnick, F., Fischer, H., Hosaynali Beygi, Z., Harder, H., Regelin, E., Sinha, V., Adame, J. A., Sörgel, M., Sander, R., Bozem, H., Song, W., Williams, J., and Yassaa, N.: Case study of the diurnal variability of chemically active species with respect to boundary layer dynamics during DOMINO, Atmos. Chem. Phys., 12, 5329–5341, doi:10.5194/acp-12-5329-2012, 2012.

van Stratum, B. J. H., Vilà-Guerau de Arellano, J., van Heerwaarden, C. C., and Ouwersloot, H. G.: Sub-cloud layer feedbacks driven by the mass flux of shallow cumulus convection over land, J. Atmos. Sci., Submitted.

Verver, G. H. L., van Dop, H., and Holtslag, A. A. M.: Turbulent mixing of reactive gases in the convective boundary layer, Bound.-Lay. Meteorol., 85, 197–222, doi:10.1023/A:1000414710372, 1997.

Verver, G. H. L., van Dop, H., and Holtslag, A. A. M.: Turbulent mixing and the chemical breakdown of isoprene in the atmospheric boundary layer, J. Geophys. Res., 105, 3983–4002, doi:10.1029/1999JD900956, 2000.

Vilà-Guerau de Arellano, J.: Role of nocturnal turbulence and advection in the formation of shallow cumulus over land, Q. J. Roy. Meteor. Soc., 133, 1615–1627, doi:10.1002/qj.138, 2007.

Vilà-Guerau de Arellano, J. and Duynkerke, P. G.: Atmospheric surface layer similarity theory applied to chemically reactive species, J. Geophys. Res., 100, 1397–1408, doi:10.1029/94JD02434, 1995.

Vilà-Guerau de Arellano, J., Duynkerke, P. G., Jonker, P. J., and Builtjes, P. J. H.: An Observational Study on the Effects of Time and Space Averaging in Photochemical Models, Atmos. Environ., 27A, 353–362, doi:10.1016/0960-1686(93)90109-C, 1993.

Vilà-Guerau de Arellano, J., Kim, S.-W., Barth, M. C., and Patton, E. G.: Transport and chemical transformations influenced by shallow cumulus over land, Atmos. Chem. Phys., 5, 3219–3231, doi:10.5194/acp-5-3219-2005, 2005.

Vilà-Guerau de Arellano, J., van den Dries, K., and Pino, D.: On inferring Isoprene Emission Surface Flux from Atmospheric Boundary Layer Concentration Measurements, Atmos. Chem. Phys., 9, 3629–3640, doi:10.5194/acp-9-3629-2009, 2009.

Vilà-Guerau de Arellano, J., Patton, E. G., Karl, T., van den Dries, K., Barth, M. C., and Orlando, J. J.: The role of boundary layer dynamics on the diurnal evolution of isoprene and the hydroxyl radical over tropical forests, J. Geophys. Res., 116, D07 304, doi:10.1029/2010JD014857, 2011.

Vilà-Guerau de Arellano, J., van Heerwaarden, C. C., and Lelieveld, J.: Modelled suppression of boundary-layer clouds by plants in a CO_2-rich atmosphere, Nature Geosci., 5, 701–704, doi:10.1038/ngeo1554, 2012.

Vinuesa, J.-F. and Vilà-Guerau de Arellano, J.: Fluxes and (co-)variances of reacting scalars in the convective boundary layer, Tellus B, 55, 935–949, doi:10.1046/j.1435-6935.2003.00073.x, 2003.

Vinuesa, J.-F. and Vilà-Guerau de Arellano, J.: Introducing effective reaction rates to account for the inefficient mixing of the convective boundary layer, Atmos. Environ., 39, 445–461, doi:10.1016/j.atmosenv.2004.10.003, 2005.

Williams, J., Crowley, J., Fischer, H., Harder, H., Martinez, M., Petäjä, T., Rinne, J., Bäck, J., Boy, M., Dal Maso, M., Hakala, J., Kajos, M., Keronen, P., Rantala, P., Aalto, J.,

Aaltonen, H.and Paatero, J., Vesala, T., Hakola, H., Levula, J., Pohja, T., Herrmann, F., Auld, J., Mesarchaki, E., Song, W., Yassaa, N., Nölscher, A., Johnson, A. M., Custer, T., Sinha, V., Thieser, J., Pouvesle, N., Taraborrelli, D., Tang, M. J., Bozem, H., Hosaynali-Beygi, Z., Axinte, R., Oswald, R., Novelli, A., Kubistin, D., Hens, K., Javed, U., Trawny, K., Breitenberger, C., Hidalgo, P. J., Ebben, C. J., Geiger, F. M., Corrigan, A. L., Russell, L. M., Ouwersloot, H. G., Vilà-Guerau de Arellano, J., Ganzeveld, L., Vogel, A., Beck, M., Bayerle, A., Kampf, C. J., Bertelmann, M., Köllner, F., Hoffmann, T., Valverde, J., González, D., Riekkola, M.-L., Kulmala, M., and Lelieveld, J.: The summertime Boreal forest field measurement intensive (HUMPPA-COPEC-2010): an overview of meteorological and chemical influences, Atmos. Chem. Phys., 11, 10 599–10 618, doi:10.5194/acp-11-10599-2011, 2011.

Willmott, C. J.: On the validation of models, Phys. Geogr., 2, 184–194, 1981.

Wyngaard, J. C. and Brost, R. A.: Top-Down and Bottom-Up Diffusion of a Scalar in the Convective Boundary Layer, J. Atmos. Sci., 41, 102–112, doi:10.1175/1520-0469(1984)041<0102:TDABUD>2.0.CO;2, 1984.

Yassaa, N., Song, W., Lelieveld, J., Vanhatalo, A., Bäck, J., and Williams, J.: Diel cycles of isoprenoids in the emissions of Norway spruce, four Scots pine chemotypes, and in Boreal forest ambient air during HUMPPA-COPEC-2010, Atmos. Chem. Phys., 12, 7215–7229, doi:10.5194/acp-12-7215-2012, 2012.

Young, G. S., Kristovich, A. R., Hjelmfelt, M. R., and Foster, R. C.: Rolls, Streets, Waves, and More: A Review of Quasi-Two-Dimensional Structures in the Atmospheric Boundary Layer, B. Am. Meteorol. Soc., 83, 997–1001, doi:10.1175/1520-0477(2002)083<0997:RSWAMA>2.3.CO;2, 2002.

Zhang, Y. and Klein, S. A.: Mechanisms Affecting the Transition from Shallow to Deep Convection over Land: Inferences from Observations of the Diurnal Cycle Collected at the ARM Southern Great Plains Site, J. Atmos. Sci., 67, 2943–2959, doi:10.1175/2010JAS3366.1, 2010.

Zimmerman, P. R., Greenberg, J. P., and Westberg, C. E.: Measurement of atmospheric hydrocarbons and biogenic emission fluxes in the Amazon boundary layer, J. Geophys. Res., 93, 1407–1416, doi:10.1029/JD093iD02p01407, 1988.

Samenvatting

Om chemische waarnemingen te analyseren en atmosferische chemie in chemisch-transport- en klimaatmodellen te representeren, moet men rekening houden met de verschillende processen die de diverse reactanten beïnvloeden. Hierbij worden vaak meerdere dynamische effecten over het hoofd gezien of slecht vertegenwoordigd. Het hoofddoel van dit promotieproject is om de dynamische processen die de chemie in atmosferische grenslagen boven bebost gebied beïnvloeden, te identificeren en beter te begrijpen. We richten ons op de atmosferische processen boven boreaal bos en het Amazoneregenwoud aangezien beide ecosystemen een belangrijke invloed hebben op de mondiale atmosferische chemie en fysica. In dit onderzoek maken we gebruik van numerieke modellen van variërende complexiteit. Deze modellen lossen zowel de atmosferische chemie als de grenslaagdynamica op voor omstandigheden die op waarnemingen gebaseerd zijn. Een tweede doel is om de parameterisaties te onderzoeken die kunnen worden toegepast in chemisch-transport- en klimaatmodellen om rekening te houden met deze invloeden. In deze dissertatie is de aandacht gericht op de invloeden van de ontwikkeling van de grenslaaghoogte, de scheiding van chemische stoffen in de grenslaag en het transport van lucht van de menglaag naar de wolkenlaag door ondiepe cumulusconvectie. Daarnaast is de invloed van heterogene oppervlakte-eigenschappen op deze processen onderzocht. De invloed van de grenslaaghoogte-ontwikkeling op chemische stoffen in een convectieve grenslaag is gekwantificeerd met een elementair menglaagmodel. Om verder te onderzoeken hoe deze grenslaaggroei wordt beïnvloed door de verscheidene dynamische processen en om de scheiding van chemische stoffen en ondiepe cumulusconvectie te bestuderen, gebruiken we een grote-wervel simulatiemodel (LES). In plaats van de dynamische en chemische processen voor te schrijven, lost dit model deze expliciet op voor schalen groter dan 50 m. De numerieke experimenten zijn gebaseerd op waarnemingen van de HUMPPA–COPEC–2010 (boreaal bos) en TROFFEE (Amazoneregenwoud) campagnes.

Impact van de grenslaaggroei

In Hoofdstuk 2 zijn de grenslaaggroei en diens invloed op de atmosferische chemie geëvalueerd voor een convectief goed gemengde grenslaag in de zomer boven boreaal bos (in

Finland), gebaseerd op de HUMPPA–COPEC–2010 meetcampagne. De combinatie van dynamische en chemische waarnemingen bood de mogelijkheid om de invloed van dynamica op chemie te onderzoeken. Hoewel er overdag verschillende grenslaagtypes aanwezig waren, wees een categorisatie van radiosondedata uit dat een convectieve grenslaag onder een stabiele vrije troposfeer het meest frequent werd waargenomen. Data van 6 augustus 2010, zijnde een representatieve dag, werd geanalyseerd. De numerieke analyses zijn geforceerd en gevalideerd met waarnemingen aan het aardoppervlak en in de atmosfeer. Hierbij is er in het bijzonder nadruk gelegd op hoe grootschalige processen (subsidentie en advectie) en de overgang van nachtelijke omstandigheden naar turbulente omstandigheden overdag, invloed hebben op de ontwikkeling van de grenslaag.

Door gebruik te maken van het menglaagmodel, een numeriek model dat de dynamische en chemische basisprocessen voor convectieve menglagen oplost, is aangetoond dat nauwkeurige kennis van de grenslaaghoogte-ontwikkeling vereist is voor de representatie en interpretatie van het verloop van concentraties van atmosferische reactanten. Dit heeft twee redenen. Ten eerste bepaalt de grenslaaghoogte het mengvolume waarin reactieve atmosferische stoffen met elkaar reageren. Ten tweede bepaalt de grenslaaggroei door inmenging ("entrainment") de uitwisseling van stoffen tussen de vrije troposfeer en de grenslaag. Aangezien chemische reactiesnelheden afhankelijk zijn van de concentraties van de reagerende stoffen, heeft de gehele grenslaaghoogte-ontwikkeling invloed op de uiteindelijke chemische toestand van de grenslaag. Daarom volstaat kennis van de uitwisseling aan het landoppervlak, de initiële chemische omstandigheden en de grenslaaghoogte op een bepaald tijdstip niet om nauwkeurig de concentraties van reagerende chemische stoffen te voorspellen op dat tijdstip.

Het is voor de onderzochte gegevens gedemonstreerd dat de grenslaaggroei toereikend gereproduceerd en verklaard wordt met het relatief simpele grenslaagmodel. Bij het representeren van de waarnemingen is ook aangetoond dat het belangrijk is om rekening te houden met resterende atmosferische lagen en de grootschalige forceringen advectie en subsidentie. Door rekening te houden met de ochtendovergang van een ondiepe grenslaag die mengt met een bovenliggende resterende laag naar een gecombineerde menglaag, waren we in staat om de toename van ozon en een waargenomen ochtendpiek in NO_x te verklaren en te reproduceren. Dit toont aan dat analyses van chemische waarnemingen rekening moeten houden met de invloed van grenslaagdynamica, en voornamelijk met de grenslaaggroei.

Een alternatief voor het gebruik van modellen die de grenslaaggroei numeriek berekenen om chemische waarnemingen te interpreteren, is het gebruik van analytische oplossingen voor de toegepaste prognostische vergelijkingen. Deze oplossingen zijn afgeleid en gepresenteerd in Hoofdstuk 3. De meest geavanceerde oplossingen uit de literatuur zijn hier uitgebreid door de invloeden van zowel vocht als de begintoestand mee te nemen. Vanwege de niet-lineaire grenslaaghoogte-afhankelijkheid van de temperatuurinversie aan de menglaagtop, is de uiteindelijke uitdrukking voor de grenslaaghoogte-ontwikkeling een impliciete functie.

Om de oplossing makkelijker toe te passen is ook een expliciete vereenvoudiging gepresenteerd. Deze representeert de ontwikkeling goed voor relatief grotere hoogtes. In Hoofdstuk 4 zijn deze analytische oplossingen uitgebreid om rekening te houden met het effect van subsidentie, een grootschalige forcering die de grenslaaggroei aanzienlijk beïnvloedt. Voor deze uitbreiding hebben we aangenomen dat de divergentie van de gemiddelde horizontale windsnelheid, die gerelateerd is aan subsidentie, in de gehele lagere troposfeer op elke hoogte gelijk is.

Niet alleen de grenslaaghoogte-ontwikkeling kan worden uitgedrukt met een analytische vergelijking. Om het verloop van atmosferische reactanten te voorspellen en te verklaren, zijn ook de (expliciete) analytische uitdrukkingen voor grenslaaggemiddelde scalairen gepresenteerd als een functie van de grenslaaghoogte en hun respectievelijke over de tijd geïntegreerde uitwisseling aan het oppervlak. Deze vergelijkingen zijn aangepast om ook de mengverhoudingen van chemische stoffen te vertegenwoordigen voor geïdealiseerde chemische omstandigheden. Hiervoor wordt aangenomen dat de chemische productie constant is in de tijd en ruimte, en dat chemisch verlies lineair schaalt met de mengverhouding van de bestudeerde chemische stof.

De analytische oplossingen voor de grenslaaghoogte en de menglaaggemiddelde scalairen maakten het mogelijk om gevoeligheidsanalyses uit te voeren die niet beperkt zijn tot een bepaalde hoeveelheid datapunten (zoals bij numerieke studies), maar continu zijn in de parameterruimte. Hierdoor maken de vergelijkingen het mogelijk om de ontwikkeling van grenslaageigenschappen beter te leren begrijpen. Een voorbeeld waar analytische uitdrukkingen nuttig kunnen zijn, is bij de bepaling van de invloed van grenslaagdynamica op het CO_2 budget op een dagelijkse schaal.

De grenslaaggroei kan worden gecompliceerd door grootschalige dynamische processen. De invloed van heterogene oppervlakken is onderzocht met het Dutch Atmospheric LES (DALES) model in Hoofdstuk 5. In de toegepaste configuratie worden warme en droge vlakken in één horizontale richting afgewisseld met koele en vochtige vlakken door verschillende voelbare en latente warmtestromen voor te schrijven. Hierdoor ontstaan mesoschaalcirculaties met omhoog bewegende lucht boven de droge vlakken en neerdalende lucht boven de vochtige vlakken. Vervolgens wordt de inmenging van lucht uit de vrije troposfeer versterkt boven de droge gebieden en verzwakt boven de vochtige gebieden. We bespreken hoe de uiteindelijke grenslaaghoogte wordt beïnvloed door de heterogeniteitslengteschaal en de grootte van de warmtestromen aan het oppervlak. Deze warmtestromen zijn gerelateerd aan het drijfvermogen (“buoyancy”) van de lucht. Hoewel de grenslaaghoogte door heterogene oppervlakteforceringen altijd groter wordt boven de droge vlakken, kan het effect boven de vochtige vlakken zowel positief als negatief zijn. De reden hiervoor is dat voor zwakkere mesoschaalcirculaties, bijvoorbeeld gerelateerd aan kleinere variaties in de warmtestroom aan het oppervlak, de verminderde inmenging van vrije troposferische lucht door de onderdrukte

turbulentie de belangrijkste terugkoppeling is. Dit resulteert in een lagere grenslaagtop. Echter, voor sterkere mesoschaalcirculaties is de belangrijkste terugkoppeling gerelateerd aan het transport van ingemengde lucht vanaf het droge vlak naar het vochtige vlak dat net onder de grenslaagtop plaatsvindt. Dit veroorzaakt een diepere grenslaag. Hierdoor hangt de gevoeligheid van de domeingemiddelde grenslaaghoogte ten opzichte van de heterogeniteitslengteschaal en de verschillen in de warmtestromen aan het oppervlak af van welke van deze twee terugkoppelingen domineert. De verdere invloed van deze circulaties op de atmosferische chemie, en in het bijzonder op isopreen, is samengevat in de volgende paragraaf.

Buiten de eerder genoemde effecten heeft kinematisch massatransport van lucht door stapelwolken een verlagende invloed op de grenslaaghoogte en zodoende een verhogende werking op de inmenging van lucht uit de vrije troposfeer in de menglaag.

Oorzaak en gevolg van de scheiding van chemische stoffen

Een secundair effect van grenslaagdynamica op atmosferische chemie is gerelateerd aan menging in de grenslaag. Als turbulente menging niet efficiënt genoeg is om de concentratiefluctuaties in de grenslaag te dempen, ontstaat er een scheiding van chemische stoffen. Dit effect wordt versterkt als er georganiseerde circulaties in de grenslaag zijn of als de uitwisseling van reactanten bij het aardoppervlak heterogeen verdeeld is. Zoals vermeld in de inleiding van dit proefschrift, wordt in de literatuur gesuggereerd dat deze scheiding een mogelijke oorzaak is van waargenomen significant verminderde reactiviteit. De scheidingsintensiteit kwantificeert in welke mate de chemische productiesnelheid is veranderd ten opzichte van berekeningen met grenslaaggemiddelde concentraties. Dit is systematisch bestudeerd in Hoofdstuk 5 voor de isopreen-OH reactie met behulp van het DALES model. Dit is gedaan voor dynamische en chemische omstandigheden die representatief zijn voor het Amazoneregenwoud. De opgeloste chemische paden beschrijven de essentiële reacties voor het O_3–NO_x–VOC–HO_x stelsel dat typisch is voor een grenslaag boven het Amazoneregenwoud overdag.

Over het algemeen kan worden geconcludeerd dat de scheidingsintensiteit niet constant kan worden verondersteld aangezien zijn grootte bepaald wordt door zowel dynamische als chemische variabelen. Dit geldt zelfs wanneer de uitwisseling van reactanten, hitte en vocht aan het oppervlak constant wordt gehouden. De scheiding hangt ook af van de achtergrondwind (zowel sterkte als richting), de initiële verticale verdeling van NO_x en, zoals onderzocht door heterogene landoppervlakken voor te schrijven, de horizontale verdeling van de uitwisseling van reactanten, hitte en vocht over het gebied. De gekozen horizontale verdeling van oppervlakte-uitwisseling van reactanten en warmtestromen is representatief voor aangrenzende vlakken die afwisselend bebost en onbebost zijn. In de afwezigheid van NO_x in de vrije troposfeer, ligt de scheidingsintensiteit in onze analyse normaal gesproken tussen -0.07

en -0.20. Dit komt overeen met een chemische reactiesnelheid die 7 tot 20 % lager is dan de snelheid die berekend zou worden met grenslaaggemiddelde concentraties. Deze resultaten komen overeen met indicaties uit meetonderzoeken.

De zwakste scheidingsintensiteit is gevonden voor een compleet homogeen landoppervlak zonder achtergrondwind. Wind en/of heterogeen terrein leiden tot grootschalige circulaties die de ruimtelijke verdeling van isopreen en OH, en zodoende de scheiding tussen die twee chemische stoffen, beïnvloeden. Het is aangetoond dat kleine verschillen in het drijfvermogentransport aan de grond, door de toenemende horizontale menging de scheiding teniet kunnen doen die is veroorzaakt door heterogeen verdeelde oppervlakte-uitwisseling van isopreen. Als deze verschillen echter sterk genoeg zijn, dan leidt een toename in de plaatsafhankelijke uitwijkingen in de warmtestromen tot een sterkere (negatievere) scheidingsintensiteit. Grotere heterogeniteitslengteschalen resulteren altijd in sterkere stoffenscheiding. Echter, wanneer deze lengteschalen te groot worden, komt de scheiding niet meer door het transport in grootschalige grenslaagcirculaties, maar door het ontstaan van volledig gescheiden grenslagen boven de verschillende oppervlakken. Hierbij raken de dynamica en chemie tussen de verschillende gebieden ontkoppeld. In onze LES resultaten gebeurt dit voor lengteschalen die groter zijn dan 16 keer de grenslaaghoogte.

Hoewel de scheidingsintensiteit voor de isopreen-OH reactie aanzienlijk varieert tussen de verschillende geanalyseerde numerieke experimenten, varieert de OH concentratie nauwelijks. De enige uitzonderingen hierop zijn de numerieke experimenten met aangepaste chemie (extra NO_x in de vrije troposfeer) of met zulke grote heterogeniteitslengteschalen dat de grenslagen over de droge en vochtige vlakken ontkoppeld raken. Dat de OH concentratie minder wordt beïnvloed, komt door de toename in isopreen die de versterkte stoffenscheiding compenseert. Hierdoor zijn de uiteindelijke chemische reactiesnelheden niet significant anders. Dit verklaart ook de in de literatuur gerapporteerde toereikende resultaten van menglaagmodellen die waarnemingen van de atmosferische chemie weten te reproduceren gedurende convectieve omstandigheden overdag.

Ten slotte zijn zowel meetonzekerheden als onzekerheden in de bepaling van reactiesnelheidscoëfficiënten vergelijkbaar met de aan stoffenscheiding gerelateerde verandering van concentraties van chemische stoffen. Daarom is het rekening houden met de scheidingsintensiteit in chemisch-transportmodellen en klimaatmodellen niet de uiteindelijke oplossing om gemodelleerde en waargenomen OH concentraties met elkaar overeen te laten komen. Als in de toekomst parameterisaties voor de stoffenscheiding worden toegepast om tot een optimaal modelresultaat te komen, dan moeten de niet-lineaire en interagerende afhankelijkheden van de verschillende aandrijvende factoren verder worden onderzocht en worden meegenomen.

Belang en representatie van transport door ondiepe convectie

Gedurende de dag gaan atmosferische grenslagen boven boreaal en tropisch bos vaak over van een heldere naar een bewolkte toestand. Deze wolken veranderen de UV-straling (door verstrooiing) en de grenslaagdynamica (zie Tabel 5.1), welke vervolgens de chemische stoffen in de menglaag beïnvloeden. Wanneer ondiepe cumuluswolken aanwezig zijn, wordt luchtmassa getransporteerd vanuit de menglaag naar de wolkenlaag. Het debiet, ook wel massatransport genoemd, zorgt er vervolgens voor dat vocht en chemische stoffen naar de wolkenlaag worden verplaatst. In Hoofdstuk 6 is de invloed van dit transport op de concentraties van chemische stoffen in de menglaag bestudeerd, gebruikmakend van DALES onder omstandigheden die representatief zijn voor de Amazone. Bij gebrek aan complete verzamelingen van waarnemingen, maakt dit het ons toch mogelijk om de invloed van wolkendynamica op de ruimtelijke verdeling van atmosferische reactanten te begrijpen en om strategieën te ontwikkelen voor toekomstige meetcampagnes in de Amazone. In deze analyse worden weer de essentiële reacties van het O_3–NO_x–VOC–HO_x stelsel voor een grenslaag boven het Amazoneregenwoud in acht genomen. In dit onderzoek richten we ons op de directe invloed van massatransport. Daarom worden de welbekende invloeden van het kinematische massatransport op de grenslaaghoogte-ontwikkeling en op de inmengingssnelheid niet verder bestudeerd.

Voor de meeste chemische stoffen is de impact van het massatransport op de grenslaaggemiddelde mengverhouding relatief klein (enkele % per uur), maar er zijn belangrijke uitzonderingen. Voor isopreen bijvoorbeeld is de invloed van massatransport gedurende de aanwezigheid van actieve ondiepe cumuluswolken gemiddeld -8.5 % per uur en maximaal -15 % per uur. Dit is een significante bijdrage aan het totale dagelijkse isopreenbudget.

De benodigde parameterisaties om het massatransport in chemisch-transport- en klimaatmodellen te representeren, zijn onderzocht met numerieke data van DALES. De resultaten bevestigen dat eerder gepubliceerde parameterisaties voor dynamische variabelen (voornamelijk vocht) ook geldig zijn voor de hier onderzochte omstandigheden. Als vernieuwend aspect in het onderzoek, hebben we parameterisaties voor het massatransport van atmosferische reactanten voorgesteld. In tegenstelling tot vocht, worden die reactanten beïnvloed door chemische productie en/of verlies en zijn ze niet direct gekoppeld aan drijfvermogen en wolkeneigenschappen. Daarom kunnen er logischerwijs verschillen in de parameterisaties worden verwacht. Voor vele chemische stoffen komt de afgeleide lineaire uitdrukking om de mengverhouding in de wolkenkern te voorspellen, goed overeen met de LES gegevens. Uitzonderingen hierop zijn hoofdzakelijk reactanten waarvan de concentratie significant beïnvloed wordt door de plaatselijke UV-straling. Dit komt doordat de door wolken veranderde UV-straling tijdelijk het chemisch evenwicht tussen sommige stoffen verandert. Dit is bevestigd in een numeriek experiment waar de invloed van wolken op de UV-straling uitgeschakeld

is. Aangezien de reactanten weer in hun originele evenwicht komen in gebieden waar de UV-straling niet verstoord is, voldoen de afgeleide parameterisaties alsnog om het transport van die reactanten vanuit de menglaag naar de wolkenlaag door ondiepe cumulusconvectie te beschrijven. Als belangrijke uitzondering voor het O_3–NO_x–VOC–HO_x stelsel, wordt het massatransport van NO en NO_2 nog steeds niet goed voorspeld in het numerieke experiment waar de UV-straling niet wordt beïnvloed door wolken. Dit komt wederom door een veranderd chemisch evenwicht. In het geval van NO en NO_2 wordt dit evenwicht ook aanzienlijk veranderd door de concentraties van overige atmosferische stoffen. Echter, de parameterisaties kunnen het totale transport van de generieke stof NO_x goed voorspellen. Dit is voldoende voor numerieke modellen die het verloop van NO en NO_2 proberen te voorspellen, aangezien de chemische verdeling van deze twee stoffen lokaal bepaald is en niet afhangt van de vorm waarin het getransporteerd wordt.

Het is aangetoond dat de afgeleide parameterisaties voor het massatransport afhankelijk zijn van de randvoorwaarden door een heterogeen landoppervlak voor te schrijven in een numeriek experiment. De niet-uniform verdeelde warmte- en vochtstromen veranderen namelijk de eigenschappen van de wolken. Voor de onderzochte omstandigheden zijn de lineaire uitdrukkingen van de diverse parameterisaties nog steeds geldig, al zijn wel de proportionaliteitsfactoren versterkt. Aangezien de factoren van ongeveer dezelfde grootte blijven, suggereren de resultaten van Hoofdstuk 6 ten slotte dat het toepassen van de gediagnosticeerde massatransportparameterisaties nog altijd een verbetering zou zijn voor een eerste orde representatie in chemisch-transport- en klimaatmodellen.

Dankwoord / Acknowledgments

Het werk voor dit proefschrift zit erop. Nu ik vier jaar van mijn leven heb doorgebracht als een promovendus is het tijd voor een nieuwe uitdaging. Echter, eerst wil ik nog terugdenken aan deze periode die in mijn beleving tegelijkertijd zeer kort en zeer lang was.

Tijdens dit project waren er veel stimulansen aanwezig en hoefde ik me geen moment te vervelen. Tegelijkertijd ben ik een schat aan ervaringen rijker en verbaas ik me erover dat zelfs de eerste herinneringen aan mijn tijd in Wageningen nog maar vier jaar oud zijn. Deze mooie combinatie heb ik mogen ervaren door vele mensen die ik niet allemaal bij naam zal noemen, maar aan wie ik wel denk. Ook dit boekje zou nooit het huidige niveau hebben gehaald zonder al hun steun. Voor dit dankwoord zal ik proberen een selectie te maken van diegenen die het meest direct hebben bijgedragen aan dit proefschrift. In alinea's waar mensen worden bedankt die de Nederlandse taal niet of minder machtig zijn, zal ik overschakelen naar het Engels.

It should be clear for all who are even a bit familiar with my project that Jordi is the first person I have to thank. It has always been (and surely will remain) a pleasure to work with you. Your simultaneous support and stimulation have been very important in furthering my project, while your unrelenting enthusiasm for education and research serve as an example. Also my other supervisors I would like to thank. Maarten, your straight and acute comments significantly improved the quality of the dissertation. Laurens, I appreciated your suggestions for alternative research directions. Finally, I am very grateful to Jos for providing me with the opportunity to perform this PhD study. Thank you for the trust you showed during the process and for your feedback that was always constructive and relevant. Additionally, I really appreciate all the opportunities you have given me to broaden my research.

Na mijn begeleiders wil ik graag Bert bedanken voor de ontvangst die ik heb gekregen bij de vakgroep. Waar mijn officiële status als gastmedewerker mij soms apart zette, heb jij je er altijd voor ingezet om dat te veranderen. Ook het vertrouwen dat je gaf wanneer er dingen georganiseerd werden versterkte bij mij het gevoel een volwaardige MAQ'er te zijn.

Then I would like to acknowledge three important persons for the start and end of my PhD program. Joel, thank you very much for seeing the potential and suggesting my name as a candidate for this project. Also afterwards I have enjoyed your company and the various

discussions that came with it. Then I arrive at my paranymphs, Peter and Michał. Your support and willingness to speak your minds make you very suitable for the job. I am very glad that you have agreed to support me during the big finale.

Next on the list are all the PhD students, temporary employees and visitors of the MAQ department. I really have enjoyed the atmosphere at our (various) offices due to you. Also the drinks, dinners, sports, holidays and other activities that I have experienced with subsets of you were all greatly appreciated. Moreover, from all of you I asked input or information on subjects that were unfamiliar to me at one time or another. Thank you again for your willingness to help me learn. Although I will not mention you all by name, I will not need this acknowledgements chapter to remember you in the future. As an exception, I would like to specifically acknowledge the people that were involved in the organization of our SENSE A2 project. Eduardo and Ivar, it was a pleasure to work with you. That we managed to organize such a project without any hiccups or conflict says enough.

Gerelateerd aan deze onderneming wil ik ook Caroline, Gerrie en Kees bedanken voor alle keren dat ik 'even' binnen kwam lopen met een vraag of verzoek. Jullie gingen altijd gelijk aan de slag en zorgden ervoor dat dingen voor elkaar kwamen. Ook Gert-Jan wil ik nog even bij naam noemen. Voor praktische informatie kon ik altijd bij je langslopen. Hartelijk dank voor de verscheidene tips.

De rest van de staf droeg voor mij ook altijd bij aan een fijne werksfeer. Ook al kwam ik uit een iets andere omgeving, ik voelde me al snel op mijn gemak. Ik zal deze vakgroep zeker gaan missen.

Even though I did not have that much interaction with my colleagues from Mainz, it was always a pleasure to meet them and collaborate. Whether it was in Mainz, Finland, Cyprus, Wageningen or Brazil. Thank you all for the nice experience.

Very important to me during my development as a researcher was the opportunity to teach and supervise students. I especially enjoyed the contact with the students that worked on their BSc and MSc theses. Next to that, both your questions and findings resulted in an increase in my knowledge. Thank you Yonas, Thirza, Roanne and Martin.

I am also grateful to my friends outside MAQ. Thank you for all the moments of leisure and for your support when I needed it. Thanks to you I could always carry on.

En tenslotte een (veel te kort) dankwoord voor mijn familie. Mijn zusjes, ouders en grootouders zijn er altijd voor me zodat ik een veilige basis heb om op terug te vallen als het nodig is. Bedankt voor al jullie steun en ik ben er trots op dat ik jullie als familie heb.

List of journal publications

Kroon, P. S., Hensen, A., Jonker, H. J. J., **Ouwersloot, H. G.**, Vermeulen, A. T., and Bosveld, F. C.: Uncertainties in eddy co-variance flux measurements assessed from CH_4 and N_2O, Agr. For. Meteorol., 150, 806–816, doi:10.1016/j.agrformet.2009.08.008, 2010.

Williams, J., Crowley, J., Fischer, H., Harder, H., Martinez, M., Petäjä, T., Rinne, J., Bäck, J., Boy, M., Dal Maso, M., Hakala, J., Kajos, M., Keronen, P., Rantala, P., Aalto, J., Aaltonen, H.and Paatero, J., Vesala, T., Hakola, H., Levula, J., Pohja, T., Herrmann, F., Auld, J., Mesarchaki, E., Song, W., Yassaa, N., Nölscher, A., Johnson, A. M., Custer, T., Sinha, V., Thieser, J., Pouvesle, N., Taraborrelli, D., Tang, M. J., Bozem, H., Hosaynali-Beygi, Z., Axinte, R., Oswald, R., Novelli, A., Kubistin, D., Hens, K., Javed, U., Trawny, K., Breitenberger, C., Hidalgo, P. J., Ebben, C. J., Geiger, F. M., Corrigan, A. L., Russell, L. M., **Ouwersloot, H. G.**, Vilà-Guerau de Arellano, J., Ganzeveld, L., Vogel, A., Beck, M., Bayerle, A., Kampf, C. J., Bertelmann, M., Köllner, F., Hoffmann, T., Valverde, J., González, D., Riekkola, M.-L., Kulmala, M., and Lelieveld, J.: The summertime Boreal forest field measurement intensive (HUMPPA-COPEC-2010): an overview of meteorological and chemical influences, Atmos. Chem. Phys., 11, 10 599–10 618, doi:10.5194/acp-11-10599-2011, 2011.

Ouwersloot, H. G., Vilà-Guerau de Arellano, J., van Heerwaarden, C. C., Ganzeveld, L. N., Krol, M. C., and Lelieveld, J.: On the segregation of chemical species in a clear boundary layer over heterogeneous land surfaces, Atmos. Chem. Phys., 11, 10 681–10 704, doi:10.5194/acp-11-10681-2011, 2011.

van Stratum, B. J. H., Vilà-Guerau de Arellano, J., **Ouwersloot, H. G.**, van den Dries, K., van Laar, T. W., Martinez, M., Lelieveld, J., Diesch, J.-M., Drewnick, F., Fischer, H., Hosaynali Beygi, Z., Harder, H., Regelin, E., Sinha, V., Adame, J. A., Sörgel, M., Sander, R., Bozem, H., Song, W., Williams, J., and Yassaa, N.: Case study of the diurnal variability of chemically active species with respect to boundary layer dynamics during DOMINO, Atmos. Chem. Phys., 12, 5329–5341, doi:10.5194/acp-12-5329-2012, 2012.

Nölscher, A. C., Williams, J., Sinha, V., Custer, T., Song, W., Johnson, A. M., Axinte, R.,

Bozem, H., Fischer, H., Pouvesle, N., Phillips, G., Crowley, J. N., Rantala, P., Rinne, J., Kulmala, M., Gonzales, D., Valverde-Canossa, J., Vogel, A., Hoffmann, T., **Ouwersloot, H. G.**, Vilà-Guerau de Arellano, J., and Lelieveld, J.: Summertime total OH reactivity measurements from boreal forest during HUMPPA-COPEC 2010, Atmos. Chem. Phys., 12, 8257–8270, doi:10.5194/acp-12-8257-2012, 2012.

Ouwersloot, H. G., Vilà-Guerau de Arellano, J., Nölscher, A. C., Krol, M. C., Ganzeveld, L. N., Breitenberger, C., Mammarella, I., Williams, J., and Lelieveld, J.: Characterization of a boreal convective boundary layer and its impact on atmospheric chemistry during HUMPPA-COPEC-2010, Atmos. Chem. Phys., 12, 9335–9353, doi:10.5194/acp-12-9335-2012, 2012.

Aan de Brugh, J. M. J., **Ouwersloot, H. G.**, Vilà-Guerau de Arellano, J., and Krol, M. C.: A large-eddy simulation of the phase transition of ammonium nitrate in a convective boundary layer, J. Geophys. Res., 118, 826–836, doi:10.1002/jgrd.50161, 2013.

Ouwersloot, H. G. and Vilà-Guerau de Arellano, J.: Analytical solution for the convectively-mixed atmospheric boundary layer, Bound.-Lay. Meteorol., 148, 557–583, doi:10.1007/s10546-013-9816-z, 2013a.

Ouwersloot, H. G. and Vilà-Guerau de Arellano, J.: Amendment to "Analytical solution for the convectively-mixed atmospheric boundary layer": inclusion of subsidence, Bound.-Lay. Meteorol., 148, 585–591, doi:10.1007/s10546-013-9837-7, 2013b.

Ouwersloot, H. G., Vilà-Guerau de Arellano, J., van Stratum, B. J. H., Krol, M. C., and Lelieveld, J.: Quantifying the transport of sub-cloud layer reactants by shallow cumulus clouds over the Amazon, J. Geophys. Res., Submitted.

van Stratum, B. J. H., Vilà-Guerau de Arellano, J., van Heerwaarden, C. C., and **Ouwersloot, H. G.**: Sub-cloud layer feedbacks driven by the mass flux of shallow cumulus convection over land, J. Atmos. Sci., Submitted.

Barbaro, E., Vilà-Guerau de Arellano, J., **Ouwersloot, H. G.**, Schröter, J. S., and Krol, M. C.: Aerosols in the convective boundary layer: radiation effects on the coupled land-atmosphere system, J. Geophys. Res., Submitted.

International Max Planck Research School for
Atmospheric Chemistry and Physics

Max Planck Institute for Chemistry Mainz
Johannes Gutenberg University Mainz
University of Heidelberg
Johann Wolfgang Goethe University Frankfurt

Certificate

Huig Gerrit Ouwersloot

born May 4th, 1985 in Leiden (Netherlands)

has successfully attended the programme of the International Max Planck Research School for Atmospheric Chemistry and Physics

Overall grading: Excellent

Subjects:	Credits:
Atmospheric Chemistry incl. Exam	2
Boundary Layer Processes incl. Exam	2
An introduction to the atmospheric boundary layer for chemists, Block course with modeling exercises	1
Various Research Schools, Oral and Poster Presentations as listed	12
	17*

* minimum 12 credit points

PhD Thesis: *The impact of dynamic processes on chemistry in atmospheric boundary layers over tropical and boreal forest*

Mainz, 13.8.2013

Chair of the Scientific Board

Additional activities of *Huig Gerrit Ouwersloot* within the framework of the International Max Planck Research School included:

Research Schools

- Autumn School on *Biogeochemistry and -physics of the lower atmosphere*, Paphos (Cyprus), 9th – 17th October 2010
- *Bridging the Gap between Atmospheric Scales*, Wageningen University (The Netherlands), 8th – 12th October 2012

Oral presentations

- *Urban The significance of species segregation for Amazonian Chemistry*, Conference of the American Meteorological Society, Keystone (Colorado, USA), 5th August 2010
- *The significance of species segregation for Amazonian Chemistry*, SENSE/BBOS seminar, Callantsoog (The Netherlands), 28th October 2010
- *On the segregation of chemical species in a clear boundary layer over heterogeneous conditions*, ITM - NATO/SPS International Technical Meeting on Air Pollution Modelling and its Application, Utrecht (The Netherlands), 11th May 2012,
- *The response of atmospheric chemistry to dynamical boundary layer processes associated to temporal transitions and surface heterogenes*, 20th Symposium on Boundary Layers and Turbulence, Boston (USA), 13th July 2012

Organization

- Organization of the School "Bridging the Gap between Atmospheric Scales", Wageningen University (The Netherlands), 8th – 12th October 2012

Teaching Assistance

- Teaching assistance "Boundary-Layer Processes" given by Jordi Vilà (3 years)
- 2 times assisting in lecture "An introduction to the atmospheric boundary layer" (Mainz (Germany), September 2011 and Nicosia (Cyprus), February 2013)
- Co-Supervision of 2 BSc students
- Co-Supervision of 2 MSc-students

Publications

- Ouwersloot, H. G., Vilà-Guerau de Arellano, J., van Heerwaarden, C. C., Ganzeveld, L. N., Krol, M. C., and Lelieveld, J.: *On the segregation of chemical species in a clear boundary layer over heterogeneous land surfaces*, Atmos. Chem. Phys., 11, 10681-10704, doi:10.5194/acp-11-10681-2011, 2011
- Ouwersloot, H. G., Vilà-Guerau de Arellano, J., Nölscher, A. C., Krol, M. C., Ganzeveld, L. N., Breitenberger, C., Mammarella, I., Williams, J., and Lelieveld, J.: *Characterization of a boreal convective boundary layer and its impact on atmospheric chemistry during HUMPPA-COPEC-2010*, Atmos. Chem. Phys., 12, 9335-9353, doi:10.5194/acp-12-9335-2012, 2012
- Ouwersloot, H. G., and Vilà-Guerau de Arellano: *Analytical solution for the convectively-mixed atmospheric boundary layer*, Boundary-Layer Meteorol, doi:10.1007/s10546-013-9816-z, 2013
- Ouwersloot, H. G., and Vilà-Guerau de Arellano: Amendment to "Analytical solution for the convectively-mixed atmospheric boundary layer": inclusion of subsidence, Boundary-Layer Meteorol, doi: 10.1007/s10546-013-9837-7, 2013
- Kroon, P. S., Hensen, A., Jonker, H. J. J., Ouwersloot, H. G., Vermeulen, A. T., and Bosveld, F. C.: *Uncertainties in eddy co-variance flux measurements assessed from CH_4 and N_2O*, Agr. For. Meteorol., 150, 806–816, doi:10.1016/j.agrformet.2009.08.008, 2010.
- Williams, J., Crowley, J., Fischer, H., Harder, H., Martinez, M., Petäjä, T., Rinne, J., Bäck, J., Boy, M., Dal Maso, M., Hakala, J., Kajos, M., Keronen, P., Rantala, P., Aalto, J., Aaltonen, H.and Paatero, J., Vesala, T., Hakola, H., Levula, J., Pohja, T., Herrmann, F., Auld, J., Mesarchaki, E., Song, W., Yassaa, N., Nölscher, A., Johnson, A. M., Custer, T., Sinha, V., Thieser, J., Pouvesle, N., Taraborrelli, D., Tang, M. J., Bozem, H., Hosaynali-Beygi, Z., Axinte, R., Oswald, R., Novelli, A., Kubistin, D., Hens, K., Javed, U., Trawny, K., Breitenberger, C., Hidalgo, P. J., Ebben, C. J., Geiger, F.M., Corrigan, A. L., Russell, L.M., Ouwersloot, H. G., Vilà-Guerau de Arellano, J., Ganzeveld, L., Vogel, A., Beck, M., Bayerle, A., Kampf, C. J., Bertelmann, M., Köllner, F., Hoffmann, T., Valverde, J., González, D., Riekkola, M.-L., Kulmala,M., and Lelieveld, J.: *The summertime Boreal forest field measurement intensive (HUMPPA-COPEC-2010): an overview of meteorological and chemical influences*, Atmos. Chem. Phys., 11, 10 599–10 618, doi:10.5194/acp-11-10599-2011, 2011.

- van Stratum, B. J. H., Vilà-Guerau de Arellano, J., Ouwersloot, H. G., van den Dries, K., van Laar, T. W., Martinez, M., Lelieveld, J., Diesch, J.-M., Drewnick, F., Fischer, H., Hosaynali Beygi, Z., Harder, H., Regelin, E., Sinha, V., Adame, J. A., Sörgel, M., Sander, R., Bozem, H., Song,W.,Williams, J., and Yassaa, N.: *Case study of the diurnal variability of chemically active species with respect to boundary layer dynamics during DOMINO*, Atmos. Chem. Phys., 12, 5329–5341, doi:10.5194/acp-12-5329-2012, 2012.
- Nölscher, A. C., Williams, J., Sinha, V., Custer, T., Song, W., Johnson, A. M., Axinte, R., Bozem, H., Fischer, H., Pouvesle, N., Phillips, G., Crowley, J. N., Rantala, P., Rinne, J., Kulmala, M., Gonzales, D., Valverde-Canossa, J., Vogel, A., Hoffmann, T., Ouwersloot, H. G., Vilà-Guerau de Arellano, J., and Lelieveld, J.: *Summertime total OH reactivity measurements from boreal forest during HUMPPA-COPEC 2010*, Atmos. Chem. Phys., 12, 8257–8270, doi:10.5194/acp-12-8257-2012, 2012.
- Aan de Brugh, J. M. J., Ouwersloot, H. G., Vilà-Guerau de Arellano, J., and Krol, M. C.: *A large-eddy simulation of the phase transition of ammonium nitrate in a convective boundary layer*, J. Geophys. Res., 118, 826–836, doi:10.1002/jgrd.50161, 2013.

Netherlands Research School for the
Socio-Economic and Natural Sciences of the Environment

C E R T I F I C A T E

The Netherlands Research School for the
Socio-Economic and Natural Sciences of the Environment
(SENSE), declares that

Huig Gerrit Ouwersloot

born on 4 May 1985 in Leiden, The Netherlands

has successfully fulfilled all requirements of the
Educational Programme of SENSE.

Wageningen, 8 November 2013

the Chairman of the SENSE board	the SENSE Director of Education
Prof. dr. Rik Leemans	Dr. Ad van Dommelen

The SENSE Research School has been accredited by the Royal Netherlands Academy of Arts and Sciences (KNAW)

KONINKLIJKE NEDERLANDSE
AKADEMIE VAN WETENSCHAPPEN

The SENSE Research School declares that **Mr. Huug Ouwersloot** has successfully fulfilled all requirements of the Educational PhD Programme of SENSE with a work load of 65 ECTS, including the following activities:

SENSE PhD Courses

- Environmental Research in Context
- Research Context Activity: Co-organizing 1 week PhD course and developing best practices, based on the organization of the course: Bridging the gap between atmospheric scales, Wageningen, 8-12 October 2012
- Autumn School: biogeochemistry and –physics of the lower atmosphere
- Bridging the scale gap between atmospheric scales

Advanced MSc Courses

- Boundary-Layer Processes
- Atmospheric Chemistry and Air Quality

Management and Didactic Skills Training

- Organizing, developing and teaching a computer practical related to the PhD course *Bridging the gap between atmospheric scales*
- Practical assistant for the PhD course *An introduction to the atmospheric boundary layer*
- Co-supervision of four BSc and MSc students
- Teaching assistant for the BSc course *Boundary-Layer Processes*

Oral Presentations

- *The significance of species segregation for Amazonian chemistry*. Conference of the American Meteorological Society, 2-6 August 2010, Keystone, Colorado, United States
- *On the segregation of chemical species in a clear boundary layer over heterogeneous conditions.* ITM - NATO/SPS International Technical Meeting on Air Pollution Modelling and its Application, 7-11 May 2012, Utrecht, Netherlands
- *The response of atmospheric chemistry to dynamical boundary layer processes associated to temporal transitions and surface heterogeneities*. Conference of the American Meteorological Society, 9-13 July 2012, Boston, United States

SENSE Coordinator PhD Education

Drs. Serge Stalpers

This project was financially supported by the Max Planck Institute for Chemistry, Mainz.

The modelling part of this study was sponsored by the National Computing Facilities Foundation (NCF project SH-060) for the use of supercomputer facilities.

Financial support from Wageningen University for printing this thesis is gratefully acknowledged.